



Forschungszentrum Karlsruhe
in der Helmholtz-Gemeinschaft

Wissenschaftliche Berichte
FZKA 6970

**Experimental and
Computational Results
of the QUENCH-08
Experiment
(Reference to QUENCH-07)**

**J. Stuckert, A.V. Boldyrev, A. Miassoedov,
A.V. Palagin, G. Schanz, L. Sepold,
V.E. Shestak, U. Stegmaier, L. Steinbock,
M. Steinbrück, H. Steiner, M.S. Veshchunov**
Institut für Materialforschung
Institut für Kern- und Energietechnik
Programm Nukleare Sicherheitsforschung

August 2005

Forschungszentrum Karlsruhe

in der Helmholtz-Gemeinschaft

Wissenschaftliche Berichte

FZKA 6970

Experimental and Computational Results
of the QUENCH-08 Experiment
(Reference to QUENCH-07)

J. Stuckert, A.V.Boldyrev*, A. Miassoedov, A.V. Palagin*, G. Schanz,
L. Sepold, V.E. Shestak*, U. Stegmaier, L. Steinbock, M. Steinbrück,
H. Steiner, M.S. Veshchunov*

Institut für Materialforschung
Institut für Kern- und Energietechnik
Programm Nukleare Sicherheitsforschung

*Russian Academy of Science, Nuclear Safety Institute (IBRAE),
Moscow

Forschungszentrum Karlsruhe GmbH, Karlsruhe

2005

Impressum der Print-Ausgabe:

**Als Manuskript gedruckt
Für diesen Bericht behalten wir uns alle Rechte vor**

**Forschungszentrum Karlsruhe GmbH
Postfach 3640, 76021 Karlsruhe**

**Mitglied der Hermann von Helmholtz-Gemeinschaft
Deutscher Forschungszentren (HGF)**

ISSN 0947-8620

urn:nbn:de:0005-069705

Zusammenfassung

Ergebnisse des Experiments QUENCH-08

In den QUENCH-Versuchen wird der Wasserstoffquellterm bei der Einspeisung von Notkühlwasser in einen trockenen, überhitzten Reaktorkern eines Leichtwasserreaktors (LWR) untersucht. Die Testbündel bestehen aus 21 Brennstabsimulatoren mit einer Gesamtlänge von ca. 2,50 m.

Der Test QUENCH-08 (ohne B_4C -Absorber), der am 24. Juli 2003 im Forschungszentrum Karlsruhe durchgeführt wurde, war als Referenzversuch zu QUENCH-07 (mit B_4C -Absorber) geplant. Deshalb war das Hauptziel des Versuchs die Untersuchung des B_4C -Absorber-Einflusses auf die Oxidation bzw. H_2 -Erzeugung und die Bündelzerstörung.

Die einzelnen Versuchsphasen, wie Hochheizen, Voroxidation (eine quasi-stationäre Phase bei ~ 1700 - 1760 K mit einer Dauer von ~ 15 - 16 min), Transiente und Abkühlung (mittels eines Dampf-Mengenstroms von 15 g/s) verliefen in beiden Experimenten ähnlich. Die Temperaturen während der transienten und der Abkühl-Phase des Versuchs QUENCH-08 waren jedoch etwas niedriger als diejenigen des Tests QUENCH-07.

Innerhalb der beheizten Zone zeigten alle Temperaturen eine sofortige Abkühlung nach der Dampfeinspeisung an. Einige Messebenen am oberen Ende und oberhalb der beheizten Zone erlebten jedoch zum Beginn der Kühlphase eine starke Temperatureskalation mit maximalen Temperaturen von ~ 2100 K in der 950 mm-Ebene und ~ 2300 K in der 1150 mm-Ebene während der Kühlphase. In Verbindung mit dieser Eskalation wurde eine erhöhte Freisetzung von Wasserstoff, die etwa zwei Minuten ab Beginn der Kühlung dauerte, beobachtet.

Die Auswertung der QUENCH-08-Massenspektrometer-Daten ergab ~ 84 g an gesamt freigesetztem H_2 (verglichen mit einer H_2 -Gesamtmenge von ~ 180 g im Versuch QUENCH-07).

Gemäß der Nachuntersuchung des Bündels bestimmte zunächst die Dampfoxidation der Hüllrohre und ihr Kontakt mit den Pellets das Fortschreiten der Schädigung. Die Verteilung freigesetzter Hüllmaterial-Restschmelzen war unerheblich, aber ausgelöst durch Aufschmelzen des Shrouds konnte weitere Schmelze in das Bündel eindringen und sich verlagern. Die Überhitzung des oberen Bündelbereichs, die sich in der Abkühlphase fortsetzte, verursachte massive Bildung und Verlagerung von Schmelze.

Abstract

The QUENCH experiments are to investigate the hydrogen source term resulting from the water injection into an uncovered core of a Light-Water Reactor (LWR). The QUENCH test bundle consists of 21 fuel rod simulators with a total length of approximately 2.5 m.

The QUENCH-08 test (without B₄C absorber), performed at the Karlsruhe Research Center on July 24, 2003, was set up as a reference test to be compared to the QUENCH-07 experiment (with B₄C absorber). So, the major objective of the test was to investigate the impact of B₄C absorber on oxidation and H₂ generation, respectively, and bundle degradation.

The test phases of both experiments were similar, as there were heatup, preoxidation (a quasi-stationary phase at ~1700-1760 K for ~15-16 min), transient, and cooldown by steam with a flow rate of 15 g/s. Temperatures during the transient and cooldown phases of QUENCH-08, however, were somewhat lower than during those phases of QUENCH-07.

All the observations within the heated zone indicated immediate cooling upon steam injection. Several locations toward the top of and above the heated zone, however, experienced a strong escalation with maximum temperatures of ~2100 K at the 950 mm level at the beginning of cooling and ~2300 K at the 1150 mm level during the cooling phase. Associated with this escalation an increased release of hydrogen was observed during the cooling phase for a period of about 2 minutes.

The evaluation of the QUENCH-08 mass spectrometer data resulted in ~84 g of hydrogen release in total compared to ~180 g during test QUENCH-07.

According to the posttest examination, the bundle damage progression was initially dominated by rod cladding conversion due to steam oxidation and pellet contact. The distribution of some released molten cladding residues was unimportant, but relocation took place due to shroud melting, penetration of additional melt into the bundle, and candling. Overheating of upper elevations in the transient, continuing during the steam cooling phase, gave rise to massive cladding melt formation and relocation.

Contents

| | |
|---|-----|
| List of Tables..... | 1 |
| List of Figures..... | 2 |
| Introduction | 9 |
| 1 Description of the Test Facility | 11 |
| 2 Test Bundle Assembly | 12 |
| 3 Test Bundle Instrumentation | 13 |
| 4 Hydrogen Measurement Devices..... | 14 |
| 5 Data Acquisition and Process Control..... | 16 |
| 6 Test Conduct and Pertinent Results..... | 16 |
| 7 Posttest Examination | 19 |
| 7.1 QUENCH-08 Posttest Appearance Prior to Bundle Sectioning | 19 |
| 7.2 Sectioning of the Test Bundle..... | 19 |
| 7.3 Metallographic Examination | 20 |
| 7.3.1 Investigation Procedures | 20 |
| 7.3.2 Axial Oxidation Profile of Corner Rod B..... | 20 |
| 7.3.3 Bundle Documentation and Microstructure Interpretation | 20 |
| 7.3.4 Lateral and Axial Oxide Scale Thickness Distribution | 25 |
| 7.3.5 Summary and Conclusions..... | 26 |
| 7.4 Hydrogen Absorption by Zircaloy | 27 |
| 8 Analytical support..... | 27 |
| 8.1 Analytical Support Using the FZK/IRS Version of the SCDAP/RELAP5 Code..... | 27 |
| 8.2 Calculations of the QUENCH-08 test with the FZK Bundle Code CALUMO | 28 |
| 8.3 Application of the SVECHA/QUENCH Code to the Simulation of the QUENCH Bundle Test QUENCH-08..... | 31 |
| 8.3.1 Introduction | 31 |
| 8.3.2 Processing of the QUENCH-08 Bundle Test Temperature Data..... | 32 |
| 8.3.3 Experimental Data Analysis..... | 34 |
| 8.3.4 QUENCH-08 Bundle Test Simulation | 39 |
| 8.3.5 QUENCH-08 bundle test simulation with B ₄ C central rod | 43 |
| 8.3.6 Summary and Conclusions..... | 45 |
| References..... | 47 |
| Acknowledgements | 49 |
| Appendix | 187 |

List of Tables

- Table 1: QUENCH test matrix
- Table 2: Design characteristics of the QUENCH-08 test bundle
- Table 3: List of instrumentation for the QUENCH-08 test
- Table 4: QUENCH-08; Failure of thermocouples
- Table 5: QUENCH-08; Sequence of events
- Table 6: QUENCH-08; Maximum measured test rod temperature of each elevation
- Table 7: QUENCH-08; Maximum measured shroud temperature of each elevation
- Table 8: Hydrogen accumulated up to characteristic events of the QUENCH-07, -08, and -09 experiments [g]
- Table 9: QUENCH-08; Cross sections for the metallographic examination
- Table 10: QUENCH-08; Oxide scale thickness of corner rod B (withdrawn from the bundle prior to the transient phase)
- Table 11: QUENCH-08; Oxide scale thickness
- Table 12: QUENCH-08; Hydrogen absorbed by the remaining Zr(O) metal phases
- Table 13: Locations of the TCs used for the temperature measurements of the fuel rod simulators of the QUENCH-08 bundle
- Table 14: Locations of the TCs used for the shroud temperature measurement in the QUENCH-08 bundle test
- Table 15: Calculated total amount of different components released from a B₄C absorber rod during tests QUENCH-07 and QUENCH-08 (with virtual absorber)

List of Figures

- Fig. 1: Flow diagram of the QUENCH test facility
- Fig. 2: QUENCH Facility; Main components
- Fig. 3: QUENCH Facility; containment and test section
- Fig. 4: QUENCH test section; flow lines
- Fig. 5: QUENCH-08; Fuel rod simulator bundle
- Fig. 6: Heated fuel rod simulator
- Fig. 7: Unheated fuel rod simulator
- Fig. 8: QUENCH-08; Test bundle, TC instrumentation and rod designation
- Fig. 9: Axial temperature measurement locations in the QUENCH test section
- Fig. 10: QUENCH; High-temperature thermocouple
- Fig. 11: QUENCH; Concept for the TC fastening at the test rod
- Fig. 12: QUENCH-08; TC instrumentation of the unheated fuel rod simulator at level 7 (350 mm) and 9 (550 mm).
- Fig. 13: QUENCH-08; TC instrumentation of the unheated fuel rod simulator at all levels
- Fig. 14: QUENCH-08; Arrangement of the thermocouples inside the corner rods
- Fig. 15: QUENCH-08; Routing of the shroud thermocouples (TSH)
- Fig. 16: QUENCH-08; H₂ measurement with the GAM 300 mass spectrometer
- Fig. 17: QUENCH; Mass spectrometer sampling position at the off-gas pipe
- Fig. 18: QUENCH; Hydrogen measurement with the CALDOS analyzer
- Fig. 19: QUENCH-08 test conduct
- Fig. 20: QUENCH-08; Total electric power vs. time, top, and heating rates evaluated from the readings of TIT A/13 together with test phase indication, bottom.
- Fig. 21: QUENCH-08; test conduct compared to that of QUENCH-07 (rod cladding temperature data of level 950 mm, top, shroud temperature data of level 950 mm, center, and electric bundle power history, bottom).
- Fig. 22: QUENCH-08; Temperature response of cladding thermocouples before and during the cooling phase.
- Fig. 23: QUENCH-08; Influence of the “hot zone effect” on the TFS thermocouple readings.
- Fig. 24: QUENCH-08; Temperature response of the shroud thermocouples before and during the cooling phase.

- Fig. 25: Comparison of average bundle temperatures at elevations 12, 16, 17, top, and shroud temperatures at elevations 12, 13, bottom, together with the bundle power history, during the transient and cooldown phases of QUENCH-07 (thick lines) and QUENCH-08 (thin lines).
- Fig. 26: QUENCH-08; Coolant inlet and outlet temperatures, bundle fluid temperatures, and off-gas temperature T 601.
- Fig. 27: QUENCH-08; Overview of the TCI (inner cooling jacket) temperatures.
- Fig. 28: QUENCH-08; Cooling water outlet temperature of the off-gas pipe (T 003) together with electric power history.
- Fig. 29: QUENCH-08; Shroud failure indicated by the shroud insulation pressure (P 406) together with the system pressure P 512, top, and argon coolant pressure in the cooling jacket (P 403), bottom.
- Fig. 30: QUENCH-08; Rod cladding failure indicated by the rod internal pressure (P 411) together with the system pressure P 512, top, and by the krypton release measured by MS GAM 300, bottom.
- Fig. 31: QUENCH-08; Steam flow rate based on flow meters F 205 (before cooldown) and F 204 (during cooldown) compared to the steam flow rate measured by MS GAM 300.
- Fig. 32: QUENCH-08; Hydrogen generation rate vs. time measured by the mass spectrometer (MS GAM 300) and by the CALDOS analyzer.
- Fig. 33: QUENCH-08; Hydrogen generation rate measured by the mass spectrometer (MS GAM 300) together with selected temperatures vs. time, top, and accumulated H₂ measured by the MS GAM 300 and by the CALDOS analyzer, bottom.
- Fig. 34: QUENCH-08; Comparison of the hydrogen generation rate vs. time measured by the MS GAM 300 for the QUENCH-07 and -08 experiments. (Note: Time scale of QUENCH-07 shifted to the left for 105 s to obtain identical starting point for transient).
- Fig. 35: Synopsis of power input, rod temperature, cooldown steam injection, and hydrogen generation for experiments QUENCH-07, top, and QUENCH-08, bottom.
- Fig. 36: Hydrogen production during specific test phases of QUENCH-08 compared to QUENCH-07 and QUENCH-09 (MS data).
- Fig. 37: Appearance of the bundle QUENCH-08: axial segments at the angular position 200°.
- Fig. 38: Appearance of the bundle QUENCH-08: between elevations 845 mm and 1070 mm.
- Fig. 39: QUENCH-08; Posttest appearance of the bundle and shroud at orientations 0° (left photos) and 90° (right photos).
- Fig. 40: QUENCH-08; Posttest appearance of the bundle and shroud at orientations 180° (left photos) and 270° (right photos).
- Fig. 41: Posttest appearance of the hot regions of test bundles QUENCH-08, -07, and -09.
- Fig. 42: QUENCH-08; Rod cladding breach shown at rod 5 by a posttest photograph taken with an endoscope from the position of corner rod B (viewed toward the bottom of the bundle).

- Fig. 43: Sectioning of the QUENCH-08 test bundle.
- Fig. 44: QUENCH-08; Cross sections at 60 mm, 73 mm, 537 mm, and 550 mm.
- Fig. 45: QUENCH-08; Cross sections at 737 mm, 750 mm, 842 mm, and 860 mm.
- Fig. 46: QUENCH-08; Cross sections at 864 mm, 900 mm, 937 mm, and 950 mm.
- Fig. 47: QUENCH-08; Cross sections at 986 mm, 1000 mm, 1050 mm, and 1065 mm.
- Fig. 48: QUENCH-08; Cross sections at 1135 mm, 1150 mm, 1307 mm, and 1320 mm.
- Fig. 49: QUENCH-08; Cross sections at 1410 mm, 1425 mm, 1465 mm, and 1480 mm.
- Fig. 50: QUENCH-08; Axial oxide layer profiles measured at the end of the preoxidation phases of experiments QUENCH-07 (square symbols) and -08 (full circles).
- Fig. 51: Cross section at 73 mm bundle elevation (QUE-08-1); overview from top, reference elevation.
- Fig. 52: Cross section at 550 mm bundle elevation (QUE-08-2); overview from top.
- Fig. 53: Cross section at 750 mm bundle elevation (QUE-08-4); overview from top.
- Fig. 54: Cross section at 860 mm bundle elevation (QUE-08-8); overview from top.
- Fig. 55: Cross section at 860 mm elevation (QUE-08-8); macrographs of separate rods, showing cladding fragmentation and interaction at pellet contact positions.
- Fig. 56: Cross section at 860 mm elevation (QUE-08-8); macrograph of rod 7 and oxidation at a position without pellet contact.
- Fig. 57: Cross section at 860 mm elevation (QUE-08-8); macrograph of rod 2, and details of external cladding oxidation and internal pellet interaction.
- Fig. 58: Cross section at 860 mm elevation (QUE-08-8); microstructures of melt in contact with rod 2.
- Fig. 59: Cross section at 860 mm elevation (QUE-08-8); non-oxidized melt in contact with rods 14 (left) and 15 (right).
- Fig. 60: Cross section at 900 mm bundle elevation (QUE-08-9); overview from top.
- Fig. 61: Cross section at 900 mm elevation (QUE-08-9); cladding oxidation and pellet interaction towards north-west in the bundle.
- Fig. 62: Cross section at 900 mm elevation (QUE-08-9); almost complete cladding oxidation towards south in the bundle, versus occurrence of melt.
- Fig. 63: Cross section at 900 mm elevation (QUE-08-9); details of melt towards south-east in the bundle and within corner rod A; note also empty scale residues.
- Fig. 64: Cross section at 950 mm bundle elevation (QUE-08-6); overview from top.
- Fig. 65: Cross section at 950 mm elevation (QUE-08-6); rods and melt accumulation towards south-west.
- Fig. 66: Cross section at 950 mm elevation (QUE-08-6); fuel rod simulators, partly covered by porous melt.

- Fig. 67: Cross section at 950 mm elevation (QUE-08-6); fuel rod simulators, showing cladding/pellet gap or gap closure by oxidized interaction layer.
- Fig. 68: Cross section at 950 mm elevation (QUE-08-6); central rod, showing filling of the annular pellet by cladding melt, and formation of an interaction layer.
- Fig. 69: Cross section at 1000 mm bundle elevation (QUE-08-10); overview from top.
- Fig. 70: Cross section at 1065 mm bundle elevation (QUE-08-11); overview from top.
- Fig. 71: Cross section at 1150 mm bundle elevation (QUE-08-12); overview from top.
- Fig. 72: Cross sections at 1150 and 1135 mm (QUE-08-12); central rod and areas around, in comparison of top (left) and bottom (right) elevations.
- Fig. 73: Cross section at 1150 mm (QUE-08-12); neck formation between central rod and rod 8, and state of cladding and molybdenum electrode of rod 8.
- Fig. 74: Cross section at 1150 mm (QUE-08-12); state of cladding / molybdenum electrode interaction for different rods.
- Fig. 75: Cross section at 1135 mm (QUE-08-12, slab bottom); melt pool in contact to central rod, and details of trend towards dissolution of embedded scale.
- Fig. 76: Cross section at 1320 mm bundle elevation (QUE-08-14); overview from top.
- Fig. 77: Cross section at 1320 mm (QUE-08-14); rods at bundle periphery, showing strongest oxidation and melting of cladding towards bundle center, indicating remarkable temperature history variations.
- Fig. 78: Cross section at 1320 mm (QUE-08-14); rods of the inner ring, showing cladding melt redistribution and relocation. Mo electrodes not attacked during cooldown-initiated temperature escalation.
- Fig. 79: Cross section at 1425 mm bundle elevation (QUE-08-15); overview from top.
- Fig. 80: Cross section at 1480 mm bundle elevation (QUE-08-16); overview from top.
- Fig. 81: QUENCH-08; Axial distribution of the oxide scale, top, and comparison of the mean data with experiment QUENCH-07, bottom.
- Fig. 82: Axial oxide scale profiles of experiments QUENCH-07, QUENCH-08, and QUENCH-09.
- Fig. 83: QUENCH-08; Oxide layer thicknesses at bundle elevation 550 mm (Cross section QUE-08-2).
- Fig. 84: QUENCH-08; Oxide layer thicknesses at bundle elevation 750 mm (Cross section QUE-08-4).
- Fig. 85: QUENCH-08; Oxide layer thicknesses at bundle elevation 860 mm (Cross section QUE-08-8).
- Fig. 86: QUENCH-08; Oxide layer thicknesses at bundle elevation 900 mm (Cross section QUE-08-9).
- Fig. 87: QUENCH-08; Oxide layer thicknesses at bundle elevation 950 mm (Cross section QUE-08-6).

- Fig. 88: QUENCH-08; Oxide layer thicknesses at bundle elevation 1000 mm (Cross section QUE-08-10).
- Fig. 89: QUENCH-08; Oxide layer thicknesses at bundle elevation 1065 mm (Cross section QUE-08-11).
- Fig. 90: QUENCH-08; Oxide layer thicknesses at bundle elevation 1135 mm (Cross section QUE-08-12).
- Fig. 91: QUENCH-08; Oxide layer thicknesses at bundle elevation 1320 mm (Cross section QUE-08-14).
- Fig. 92: QUENCH-08; Oxide layer thicknesses at bundle elevation 1480 mm (Cross section QUE-08-16).
- Fig. 93: QUENCH-08; Hydrogen absorbed by the remaining Zr(O) metal phases.
- Fig. 94: Evolution of rod and shroud temperatures of QUENCH-08 at different axial locations, CALUMOqx-calculated data in comparison with experimental values.
- Fig. 95: Evolution of rod and shroud temperatures of QUENCH-08 at different axial locations, CALUMOqx-calculated data in comparison with experimental values.
- Fig. 96: Axial distribution of the oxide scale thickness for the drawn corner rod (top, left), at the end of QUENCH-08 for the shroud (top, right) and all rods (bottom).
- Fig. 97: Evolution of the hydrogen production rate and the overall produced hydrogen for QUENCH-08 calculated with CALUMOqx.
- Fig. 98: QUENCH-08 bundle temperature evolution at the elevation 1350 mm measured by thermocouples TFS 2/17 (red), TFS 5/17 (blue) and averaged temperature used in the calculations (black).
- Fig. 99: QUENCH-08 bundle temperature evolution at the 1350 mm elevation during transient and cooling phases (3700-4200 s) measured by thermocouples TFS 2/17 (red), TFS 5/17 (blue) and averaged temperature used in the calculations (black).
- Fig. 100: QUENCH-08 bundle temperature evolution at the elevation 1250 mm measured by thermocouples TFS 3/16 (red), TFS 5/16 (blue) and averaged temperature used in the calculations (black).
- Fig. 101: QUENCH-08 bundle temperature evolution at the elevation 1250 mm during transient and cooling phases (3700-4200 s) measured by thermocouples TFS 3/16 (red), TFS 5/16 (blue) and averaged temperature used in the calculations (black).
- Fig. 102: QUENCH-08 bundle temperature evolution at the elevation 1150 mm measured by thermocouples TFS 2/15 (red), TFS 5/15 (blue) and averaged temperature used in the calculations (black).
- Fig. 103: QUENCH-08 bundle temperature evolution at the elevation 1150 mm during transient and cooling phases (3500-4200 s) measured by thermocouples TFS 2/15 (red), TFS 5/15 (blue) shroud and averaged temperature used in the calculations (black).
- Fig. 104: QUENCH-08 bundle temperature evolution at the elevation 1050 mm measured by thermocouples TFS 3/14 (red), TFS 5/14 (blue), shroud thermocouples TSH 14/90 I (black), TSH 14/270 I (green).

- Fig. 105: QUENCH-08 bundle temperature evolution at the elevation 1050 mm during transient and cooling phases (3500-4200 s) measured by thermocouples TFS 5/14 (blue), shroud thermocouples TSH 14/90 I (black), TSH 14/270 I (green).
- Fig. 106: Shroud temperature evolution at the elevations 950, 1050 and 1150 mm measured by thermocouples TSH14/90 I (black), TSH14/270 I (grey), TSH15/0 I (red), TSH15/180 I (blue) and TSH13/270 I (green) for the time period 3500-4200 s of QUENCH-08.
- Fig. 107: Shroud temperature evolution at the elevations 950 and 1150 mm during pre-oxidation, transient, and cooling phases of QUENCH-08 (3500-4200 s) measured by thermocouples TSH13/270 I (grey), TSH15/0 I (red) and TSH15/180 I (blue) and the estimated basis for the shroud temperature at 1050 mm TSH 14b.
- Fig. 108: Estimated basis for the shroud temperature evolution at the elevation 1050 mm during QUENCH-08 with TSH_14b (blue), TSH_14_1 (red) plotted up to 3816.4 s, and TSH 14 (black) reconstructed after 3816 s.
- Fig. 109: Averaged QUENCH-08 bundle temperature evolution at the elevation 1050 mm during pre-oxidation, transient and cooling phases (3000-4200 s): TFS 14_1 measured up to 3544 s (red), TSH 14 reconstructed (blue), and TFS 14 averaged temperature used in the calculations (black).
- Fig. 110: QUENCH-08 bundle temperature evolution at the elevation 950 mm measured by thermocouples TFS 2/13 (red), TFS 3/13 (blue), TFS 4/13 (grey), TFS 5/13 (light red), central rod thermocouple TCRC 13 (light blue), corner rod thermocouple TIT A/13 (violet) and averaged temperature used in the calculations (black).
- Fig. 111: QUENCH-08 bundle temperature evolution at the elevation 950 mm during pre-oxidation, transient, and cooling phases (3500-4200 s) measured by central rod thermocouple TCRC 13 (blue), corner rod thermocouple TIT A/13 (violet) and averaged temperature used in the calculations (black).
- Fig. 112: QUENCH-08 bundle temperature evolution at the elevation 850 mm measured by thermocouples TFS 2/12B (red), TFS 3/13B (blue), TFS 5/12 (grey), TIT D/12 (violet) and averaged temperature used in the calculations (black).
- Fig. 113: QUENCH-08 bundle temperature evolution at the elevation 850 mm during pre-oxidation, transient and cooling phases (3000-4200 s) measured by thermocouples TFS 2/12B (red), TFS 3/13B (blue), TFS 5/12 (grey), TIT D/12 (violet) and averaged temperature used in the calculations (black).
- Fig. 114: QUENCH-08 bundle temperature evolution at the elevation 750 mm measured by thermocouples TFS 2/11B (red), TFS 4/11 (blue), TFS 5/11 (grey) and averaged temperature used in the calculations (black).
- Fig. 115: QUENCH-08 bundle temperature evolution at the elevation 750 mm during pre-oxidation, transient and cooling phases (2500-4200 s) measured by thermocouples TFS 2/11B (red), TFS 4/11 (blue), TFS 5/11 (grey) and averaged temperature used in the calculations (black).
- Fig. 116: Averaged and smoothed curves representing the temperature evolution of the QUENCH-08 bundle at the elevations from -250 to 1350 mm.
- Fig. 117: Averaged and smoothed curves representing temperature evolution during pre-oxidation, transient, and cooling phases (3500-4100 s) of the QUENCH-08 bundle at the elevations from 1050 to 1350 mm.

- Fig. 118: Averaged and smoothed curves representing temperature evolution of the QUENCH-08 bundle during pre-oxidation, transient, and cooling phases (3500-4100 s) at the elevations from 250 to 950 mm.
- Fig. 119: QUENCH-08 steam flow rate at the bundle inlet measured by F 204/F 205 flow meters (red) and at the bundle outlet (MS GAM.300 data; blue).
- Fig. 120: QUENCH-08 system pressure evolution at bundle inlet measured by P 511 (blue), at bundle outlet measured by P 512 (black), and at the annulus shroud/cooling jacket measured by P 406 (red).
- Fig. 121: QUENCH-08 system pressure evolution during the time period 3760-3800 s at bundle inlet measured by P 511 (blue), at bundle outlet measured by P 512 (black), and at annulus shroud/cooling jacket P 406 (red).
- Fig. 122: The averaged TFS curves of QUENCH-08 at the elevations 1350, 1250, and 1150 mm together with TSH thermocouple curves at 1250, 1150, 1050 and 950 mm.
- Fig. 123: Derivatives dT/dt of the averaged temperatures of QUENCH-08 at different elevations, K/s (upper elevations: lines with symbols, lower elevations: thin lines).
- Fig. 124: Oxide layer thickness axial profile of corner rod B (withdrawn from the QUENCH-08 bundle at 3181 s) compared to the calculated one of the central rod for the same time.
- Fig. 125: QUENCH-08 measured oxide layer thickness profiles of the heated rods (average) and of the central rod (both at final state), compared to the calculated oxide layer thickness profiles of the central rod at 3776 s (initiation of cooldown) and of the central rod (final state).
- Fig. 126: QUENCH-08 hydrogen production rate calculated by the S/Q code (red) and compared to the experimental data of MS GAM 300.
- Fig. 127: Axial profiles of channel wall and gas temperature at 3775 s (1 s before QUENCH-08 cooldown initiation).
- Fig. 128: Axial profiles of channel wall and gas temperature at 3780 s (4 s after QUENCH-08 cooldown initiation).
- Fig. 129: Axial profiles of channel wall and gas temperature at 3785 s (9 s after QUENCH-08 cooldown initiation).
- Fig. 130: Calculated CO_2 , CO , and H_2 mass flow rates of experiment QUENCH-08.
- Fig. 131: Calculated B_2O_3 , HBO_2 , H_3BO_3 and $\text{H}_3\text{B}_3\text{O}_6$ mass flow rates of experiment QUENCH-08.
- Fig. 132: Calculated C mass flow rate (CO_2 , CO , CH_4) for the QUENCH-07 and QUENCH-08 tests. Time scale of the QUENCH-07 data was shifted by 212 s to match cooldown initiation (3564 s in Q-07 and 3776 s in Q-08).
- Fig. A-1 Comparison of the quench initiation for experiments QUENCH-07, top, and QUENCH-08, bottom.
- Fig. A-2 Comparison of steam and hydrogen responses during the quenching phases of experiments QUENCH-07, top, and QUENCH-08, bottom.

Introduction

The most important accident management measure to terminate a severe accident transient in a Light Water Reactor (LWR) is the injection of water to cool the uncovered degraded core. Analysis of the TMI-2 [1] accident and the results of integral out-of-pile (CORA [2, 3]) and in-pile experiments (LOFT [4], PHEBUS [5]) have shown that before the water succeeds in cooling the fuel pins there can be an enhanced oxidation of the Zircaloy cladding that in turn causes a sharp increase in temperature, hydrogen production and fission product release.

Besides, quenching is considered a worst-case accident scenario regarding hydrogen release to the containment. For in- and ex-vessel safety analyses one has to prove that the hydrogen release rate and total amount do not exceed limits for the considered power plant. The hydrogen generation rate must be known to design appropriately accident mitigation measures for the following reasons.

- Passive autocatalytic recombiners require a minimum hydrogen concentration to start. Moreover, they work slowly, and their surface area and their position in the containment have to be quantified carefully.
- The air-steam-hydrogen mixture in the containment may be combustible for only a short time before detonation limits are reached. This limits the time period during which ignitors can be used.

The physical and chemical phenomena of the hydrogen release are, however, not sufficiently well understood (see e.g. [6], [7]). The increased hydrogen production during quenching cannot be determined on the basis of the available Zircaloy/steam oxidation correlations. Presently it is assumed that the following phenomena lead to an enhanced oxidation and hydrogen generation [8]:

- Melt oxidation,
- Steam starvation conditions,
- Crack surfaces oxidation.

In most of the code systems describing severe fuel damage, these phenomena are either not considered or only modeled in a simplified empirical manner.

In addition, no models are yet available to predict correctly the thermal-hydraulic or the clad behavior of the quenching processes in the CORA and LOFT LP-FP-2 tests. An extensive experimental database is therefore needed as a basis for model development and code improvement.

The Forschungszentrum Karlsruhe is therefore running the QUENCH program on the investigation of coolability and determination of the hydrogen source term. The main objectives of this program are:

- The provision of an extensive experimental database for the development of detailed mechanistic fragmentation models,

- The examination of the physico-chemical behavior of overheated fuel elements under different flooding conditions,
- The provision of an improved understanding of the effects of water injection at different stages of a degraded core,
- The determination of cladding failure criteria, cracking of oxide layers, exposure of new metallic surfaces to steam
- The investigation of the oxide layer degradation under steam starvation conditions and influence of this phenomenon on subsequent flooding,
- The investigation of the melt oxidation process,
- The determination of the hydrogen source term.

The experimental part of the QUENCH program began with small-scale experiments using short Zircaloy fuel rod segments [9-11]. On the basis of these results well-instrumented large-scale bundle experiments with fuel rod simulators under nearly adiabatic conditions are performed in the QUENCH facility of the Forschungszentrum Karlsruhe. The large-scale bundle experiments are more representative of prototypic reactor accident conditions than are the single-rod experiments. Important parameters of the bundle test program (see [Table 1](#)) are: quench medium, i.e. water or steam, fluid injection rate, cladding oxide layer thickness, temperature at onset of flooding, the presence of control rod, and possible steam starvation conditions before reflood.

The QUENCH-08 test (without B₄C absorber), performed at the Karlsruhe Research Center on July 24, 2003, was set up as a reference test to be compared to the QUENCH-07 experiment (with B₄C absorber) [14]. So, the major objective of the test was to confirm the impact of B₄C absorber on oxidation and H₂ generation, respectively, and bundle degradation. The second experiment with B₄C absorber, i.e. QUENCH-09 [15], is also linked to QUENCH-07 and -08.

This report describes the test facility and the test bundle, and the main results of the QUENCH-08 experiment including the posttest examination. Analytical support for the test preparation and evaluation is here included, but also published elsewhere [12,13]. An appendix is added as an erratum of the report on test QUENCH-07, i.e. it describes a correction of time offsets for QUENCH-07 test. During the analysis of test QUENCH-08 the QUENCH-07 data set showed that there is some temporary inconsistency between the bundle characteristic data (temperature, pressure, flow rate etc.) and the mass spectrometer data.

1 Description of the Test Facility

The QUENCH test facility consists of the following component systems:

- the test section with 21 fuel rod simulators,
- the electric power supply for the test bundle heating,
- the water and steam supply system,
- the argon gas supply system,
- the hydrogen measurement devices,
- temperature, pressure, mass flow measurement devices,
- the process control system,
- the data acquisition system.

A simplified flow diagram of the QUENCH test facility is given in [Fig. 1](#), a three-dimensional schematic of the components in [Fig. 2](#). The main component of the facility is the test section with the test bundle ([Figs. 3 and 4](#)). The superheated steam from the steam generator and superheater together with argon as the carrier gas for the hydrogen detection systems enter the test bundle at the bottom end. The steam that is not consumed, the argon, and the hydrogen produced in the zirconium-steam reaction flow from the bundle outlet through a water-cooled off-gas pipe to the condenser ([Figs. 1 and 2](#)). Here the steam is separated from the non-condensable gases argon and hydrogen. The quenching (water) or cooling (saturated steam) phase is initiated by turning off the superheated steam of 3 g/s whereas the argon flow rate remains unchanged. At the same time quench water or – as in QUENCH-08 – saturated steam is injected at the bottom of the test section.

The design characteristics of the test bundle are given in [Table 2](#). The test bundle is made up of 21 fuel rod simulators, each with a length of approximately 2.5 m, and of four corner rods (see cross section in [Fig. 5](#)). The fuel rod simulators ([Fig. 6](#)) are held in their positions by five grid spacers, four of Zircaloy, and one of Inconel in the lower bundle zone. The cladding of the fuel rod simulators is identical to that used in PWRs with respect to material and dimensions, i.e. Zircaloy-4, 10.75 mm outside diameter, 0.725 mm wall thickness. The rods are kept at a pressure of 0.22 MPa with a mixture of 95 % argon and 5 % krypton, i.e. a pressure slightly above the system pressure (0.2 MPa). The gas filling of all rods is realized by a channel-like connection system inside the lower sealing plate. The krypton additive allows to detect fuel rod failure during the experiment with help of the mass spectrometer.

Twenty fuel rod simulators are heated electrically over a length of 1024 mm, the unheated fuel rod simulator is located in the center of the test bundle. The unheated fuel rod simulator ([Fig. 7](#)) is filled with ZrO₂ pellets (bore size 2.5 mm ID). For the heated rods ([Fig. 6](#)) 6 mm diameter tungsten heating elements are installed in the center of the rods and are surrounded by annular ZrO₂ pellets. The tungsten heaters are connected to electrodes made of molybdenum and copper at each end of the heater. The molybdenum and copper electrodes are joined by high-frequency/high-temperature brazing under vacuum using an AuNi 18 powder (particle size < 105 µm). For electrical insulation the surfaces of both types of electrodes are plasma-coated with 0.2 mm ZrO₂. To protect the copper electrodes and the

O-ring-sealed wall penetrations against excessive heat they are water-cooled (lower and upper cooling chambers filled with demineralized water). The copper electrodes are connected to the DC electric power supply by means of special sliding contacts at the top and bottom. The total heating power available is 70 kW, distributed among two groups of heated rods with 35 kW each. The first group consists of the inner eight rods (rod numbers 2–9), the second group consists of the outer twelve rods (rod numbers 10–21). The rod designation can be taken from [Fig. 8](#).

The four corner positions of the bundle are occupied either by solid Zircaloy (Zry) rods with a diameter of 6 mm or by solid rods (upper part) / Zry tubes (lower part) of $\varnothing 6 \times 0.9$ mm for thermocouple instrumentation at the inside ([Fig. 8](#)). The positioning of the four corner rods avoids an atypically large flow cross section at the outer positions and hence helps to obtain a rather uniform radial temperature profile. A solid Zry rod (typically rod B) can be pulled out of the bundle to determine the axial oxide layer thickness at that time.

The lower boundary for the lower cooling chamber is a sealing plate made of stainless steel with plastic inlays for electrical insulation, sealed to the system by O-shaped rings. The upper boundary of the lower cooling chamber is a sealing plate of stainless steel. An insulation plate made of plastic (PEEK) forms the top of the upper cooling chamber, and a sealing plate of Al_2O_3 , functioning as a heat-protection shield, is the lower boundary of the upper cooling chamber (see [Fig. 6](#)).

In the region below the upper Al_2O_3 plate the copper electrode is connected firmly to the cladding. This is done by hammering the cladding onto the electrode with a sleeve of boron nitride put between electrode and cladding for electrical insulation. The axial position of the fuel rod simulator in the test bundle is fixed by a groove and a locking ring in the top Cu electrodes. Referred to the test bundle the fixing of the fuel rod simulators is located directly above the upper edge of the upper insulation plate. So, during operation the fuel rod simulators are allowed to expand downwards. Clearance for expansion of the test rods is provided in the region of the lower sealing plate. Also in this region relative movement between cladding and internal heater/electrode can take place.

The test bundle is surrounded by a 2.38 mm thick shroud (80 mm ID) made of Zircaloy with a 37 mm thick ZrO_2 fiber insulation and an annular cooling jacket made of inconel (inner tube) and stainless steel (outer tube; see [Fig 5](#)). The annulus between shroud and cooling jacket is filled with stagnant argon (0.22 MPa) whereas the 6.7 mm annulus of the cooling jacket is cooled by an argon flow. Above the heated zone, i.e. above the 1024 mm elevation there is no ZrO_2 fiber insulation to allow for higher radial heat losses. This region of the cooling jacket is cooled by a water flow ([Figs. 3 and 4](#)). Both the lack of ZrO_2 insulation above the heated region and the water cooling force the axial temperature maximum downward.

2 Test Bundle Assembly

The test section consists of three subassemblies pre-assembled separately. One subassembly comprises the cooling jacket with the bundle head casing; the second subassembly includes the instrumented shroud with the bundle foot; and the third

subassembly is composed of the instrumented test bundle with the bundle head. The test bundle and the shroud, including the respective thermocouples, must be replaced for each experiment. The instrumentation of the bundle head and the foot as well as that of the cooling jacket, however, remains unchanged.

3 Test Bundle Instrumentation

The test bundle was instrumented with sheathed thermocouples (TC) attached to the rod claddings at 17 different elevations between -250 mm and 1350 mm and at different orientations according to [Figs. 8 and 9](#). The elevations of the surface-mounted shroud thermocouples are from -250 mm to 1250 mm. In the lower bundle region, i.e. up to the 550 mm elevation, NiCr/Ni thermocouples (1 mm diameter, stainless steel sheath 1.4541, MgO insulation) are used for temperature measurement of rod cladding and shroud as is illustrated in [Fig. 9](#). The thermocouples of the hot zone are high-temperature thermocouples with W-5Re/W-26Re wires, HfO₂ insulation, and a duplex sheath of tantalum (internal)/Zirconium with an outside diameter of 2.1 mm ([Fig. 10](#)).

The thermocouple attachment technique for the surface-mounted high-temperature TCs is illustrated in [Fig. 11](#). The TC tip is held in place by two clamps of zirconium (0.25 mm thick). As these clamps are prone to oxidation and embrittlement in a steam environment an Ir-Rh wire of 0.25 mm diameter is additionally used in the experiments with pre-oxidation as was the case in test bundle QUENCH-08.

The **designations** of the surface-mounted cladding and shroud thermocouples are “TFS” and “TSH”, respectively. The unheated fuel rod simulator of the QUENCH-08 bundle was especially instrumented to provide information on the accuracy of the temperature measurement with externally mounted thermocouples, particularly during cooldown. Therefore, three thermocouples were inserted in the center of the central rod, i.e. TCRC 7 (at 350 mm, NiCr/Ni, Ø 0.5 mm, routed to bottom), TCRC 9 (at 550 mm, NiCr/Ni, Ø 0.5 mm, routed to bottom), and TCRC 13 (at 950 mm, W/Re, Ø 2.1 mm, routed to top), two thermocouples at the rod cladding inner surface, i.e. TCRI 7 (at 350 mm, NiCr/Ni, Ø 0.5 mm, routed to bottom), and TCRI 9 (at 550 mm, NiCr/Ni, Ø 0.5 mm, routed to bottom), and three thermocouples at the rod cladding outer surface i.e. TCR 7 (at 350 mm, NiCr/Ni, Ø 1 mm, routed to bottom), TCR 9 (at 550 mm, NiCr/Ni, Ø 1 mm, routed to bottom), and TCR 13 (at 950 mm, W/Re, Ø 2.1 mm, routed to top). For the instrumentation of the central rod see also [Figs. 12 and 13](#).

The wall of the inner tube of the cooling jacket is instrumented between -250 mm and 1150 mm with NiCr/Ni thermocouples (designation “TCI”). The thermocouples that are fixed at the outer surface of the outer tube of the cooling jacket (designation “TCO”) are also of the NiCr/Ni type. The designation of the thermocouples inside the Zircaloy corner rods is “TIT”. According to [Fig. 14](#) three of the four corner rods of the QUENCH-08 test bundle were instrumented as follows:

- Rod A: W/Re, 2.1 mm diameter, Zr/Ta duplex sheath, 950 mm elevation (TIT A/13)
- Rod C: NiCr/Ni, 1 mm diameter, stainless steel sheath, 550 mm elevation (TIT C/9)

- Rod D: W/Re, 2.1 mm diameter, Zr/Ta duplex sheath, 850 mm elevation (TIT D/12).

The leads of the thermocouples from the –250 mm to the 650 mm level leave the test section at the bottom whereas the TCs above 650 mm are routed to the top. Based on the results of the previous experiment, QUENCH-09, it was avoided to route the TC cables through the hot zone. Depending on their axial position, they exit the test section either to the top or the bottom. Therefore the following thermocouples of upper levels, i.e. 750 and 850 mm, were routed to the bottom: TFS 2/11 B, TFS 2/12 B, and TFS 3/12 B. Nevertheless, the hot-zone effect was disregarded for two thermocouples during the assembly of the QUENCH-08 bundle: TFS 4/11 and 5/11 resulting in incorrect temperature readings from a certain time on. This is because those TC cables passed the hot zone which is located above the measurement locations of 750 mm in contrast to e.g. TFS 2/11 B (routed to the bottom) which provides correct temperature data (see [Fig. 23](#)). The problem with thermocouples passing hot zones of the QUENCH test section are described in detail in [13, Appendix II]. [Fig. 15](#) demonstrates how the cables of shroud thermocouples TSH xx/x “I” were routed to outside the shroud insulation to avoid heat transfer into the TC cable apart from the TC junction.

A list of the instruments for experiment QUENCH-08 installed in the test section and at the test loop are given in [Table 3](#). The thermocouples that failed prior or during the test are listed in [Table 4](#).

4 Hydrogen Measurement Devices

The hydrogen is analyzed by two different measurement systems: (1) a Balzers mass spectrometer (MS) “GAM 300” ([Fig. 16](#)) located at the off-gas pipe, approx. 2.7 m downstream from the test section outlet, and (2) a hydrogen detection system “Caldos 7 G” ([Fig. 18](#)) located in a bypass to the off-gas line downstream the condenser. Due to their different locations in the facility the mass spectrometer “GAM 300” responds almost immediately (less than 5 s) to a change in the gas composition whereas the Caldos device has a delay time of about 20-30 s. The time delay of the off-gas analyzing systems has been determined with several bundle flows and gas injections at the 700 mm level of a dummy test section particularly installed for calibration purposes. A first series was performed at room pressure and temperature with 3 and 6 g/s argon flow in the bundle and hydrogen as injection gas. A second series was performed at 1000 K maximum rod surface temperature with a mixture of 3 g/s argon and 3 and 50 g/s steam flow in the bundle at a system pressure of 0.2 MPa and with helium as injection gas. Besides the time delay, the signal shapes are different for the CALDOS H₂ analyzer, i.e. resulting in a broader peak due to the diffusion of the hydrogen in the fluid.

The mass spectrometer “BALZERS GAM 300” used is a completely computer-controlled quadrupole MS with an 8 mm rod system which allows quantitative measurement of gas concentrations down to about 10 ppm. For the MS measurement a sampling tube is inserted in the off-gas pipe ([Fig. 17](#)). It has several holes at different elevations to guarantee that the sampling of the gas to be analyzed is representative. To avoid steam condensation in the gas pipes between the sampling position and the MS the temperature of the gas at the MS

inlet is controlled by a heat exchanger to be between 110 °C and 150 °C (the upper operating temperature of the MS inlet valves). This allows the MS to analyze the steam production rate. Besides, the concentrations of the following species were continuously measured by the mass spectrometer during all test phases: argon, hydrogen, steam, nitrogen, oxygen, and krypton. As the fuel rod simulators are filled with krypton as a tracer gas in addition to the argon, i.e. a mixture of argon and 5 % krypton, the measurement of krypton can be used as an indicator for a cladding failure. Additionally, the MS is used to control the atmosphere in the facility, e.g., to monitor the gas composition at the beginning of the test.

The temperature and pressure of the analyzed gas are measured near the inlet valve of the MS. The MS is calibrated for hydrogen with well-defined argon/hydrogen mixtures and for steam with mixtures of argon and steam supplied by a Bronkhorst controlled evaporator mixing (CEM) device. The MS off-gas is released into the atmosphere because the amount of hydrogen taken out of the system is negligible. For the first time, a heated measuring gas pump was used to ensure the continuous flow of the steam-gas-mixture from the off-gas pipe to the mass spectrometer.

The principle of measurement of the Caldos system is based on the different heat conductivities of different gases. The Caldos device is calibrated for the hydrogen-argon gas mixture. To avoid any moisture in the analyzed gas a gas cooler, which is controlled at 296 K, is connected to the gas analyzer (Fig. 18). The response time of the gas analyzer is documented by the manufacturer to be 2 s, i.e. a time in which 90 % of the final value should be reached. In contrast to the mass spectrometer the Caldos device only measures the hydrogen content. Gases other than H₂ cannot be analyzed by this system.

For the Caldos device as well as for the MS the hydrogen mass flow rate is calculated by referring the measured H₂ concentration to the known argon mass flow rate according to equation (1):

$$\dot{m}_{H_2} = \frac{M_{H_2}}{M_{Ar}} \cdot \frac{C_{H_2}}{C_{Ar}} \cdot \dot{m}_{Ar} \quad (1)$$

with M representing the molecular masses, C the concentrations in vol-% and \dot{m} the mass flow rates of the corresponding gases.

With an argon-hydrogen (two-component) mixture that in fact exists at the location of the Caldos analyzer equation (1) can be written as follows

$$\dot{m}_{H_2} = \frac{M_{H_2}}{M_{Ar}} \cdot \frac{C_{H_2}}{100 - C_{H_2}} \cdot \dot{m}_{Ar} \quad (2)$$

5 Data Acquisition and Process Control

A computer control and data acquisition system based on the LabVIEW programming system is used in the QUENCH facility. Data acquisition, data storage, online visualization as well as process control, control engineering and system protection are accomplished by four computer systems that are linked in a network.

The data acquisition system allows recording of about 200 measurement channels at a maximum frequency of 25 Hz per channel. The experimental data and the date and time of the data acquisition are stored as raw data in binary format at the measurement computer. After the experiment the raw data are converted into SI units and stored as ASCII data.

For process control, a system flow chart with the most important actual measurement values is displayed on the control computer screen. Furthermore, the operating mode of the active components (pumps, steam generator, superheater, DC power system, valves) is indicated. Blocking systems and limit switches ensure safe plant operation. Operating test phases, e.g. heating or quenching phases, are pre-programmed and can be started on demand during the experiment. The parameter settings of the control circuits and devices can be modified online.

Online visualization (two PCs) allows to observe and to document the current values of selected measurement positions in the form of tables or plots. Eight diagrams with six curves each can be displayed as graphs. This means that altogether 48 measurement channels can be selected and displayed online during the course of the experiment.

The data of the main data acquisition system and of the mass spectrometers were stored on different computers. Both computers were synchronized by radio-controlled clocks.

The data of the main acquisition system were stored at different frequencies according to the test phases as shown below:

| | |
|--------|------|
| 0 s | 1 Hz |
| 3761 s | 5 Hz |
| 4034.8 | 1 Hz |

The mass spectrometer data were recorded at a frequency of 0.4 Hz during the entire test.

6 Test Conduct and Pertinent Results

The conduct of the QUENCH-08 test (see [Figs. 19 and 20](#) and [Table 5](#)) was planned and conducted as closely as possible to that of QUENCH-07 with the following test phases.

- Phase I Heatup to ~873 K. Facility checks at the ~873 K level.
- Phase II Heatup with ~0.3-0.6 K/s to ~1700 K.

- Phase III **Pre-oxidation** of the test bundle in a flow of 3 g/s of superheated steam and 3 g/s argon for ~16 min at relatively constant temperature of ~1700-1740 K.
- Phase IV **Transient** heatup from ~1740 K to temperatures exceeding 2200 K with an initial heating rate of ~0.2 K/s.
- Phase V **Cooldown** of the bundle by a flow of 15 g/s of saturated steam.

A comparison between the experiments QUENCH-08 and QUENCH-07 for temperatures of the 950 mm level and the electric power input are given in [Fig. 21](#). A direct comparison between the shroud thermocouples at upper elevations, i.e. above 850 mm, is not possible due to hot zone effects in test QUENCH-07. The QUENCH-08 temperatures before and during the quenching phase are given in [Fig. 22](#) (cladding surface and corner rod centerline), [Fig. 24](#) (shroud), and [Fig. 25](#) (fluid). In [Fig. 26](#) average temperatures of different elevations are compared (QUENCH-07, thick lines, and QUENCH-08, thin lines) during the transient and cooldown phases. The temperature histories of the thermocouples of the cooling jacket inner tube (TCI) are depicted in [Fig. 27](#) and those of the cooling water outlet of the off-gas pipe in [Fig. 28](#).

In common with the previous QUENCH experiments, the bundle was heated by a series of stepwise increases of electrical power up to about 4 kW from room temperature to ~873 K. The atmosphere consisted of 3 g/s flowing argon and 3 g/s superheated steam. At the end of this stabilization period the power was ramped smoothly to 13.2 kW, corresponding to a maximum temperature of 1313 K, and then kept constant until the temperature of ~1700 K was reached at 2277 s. At that time, the power was decreased to 8 kW and then controlled to maintain the temperature at that level for a period of ~16 minutes. This period was longer than in test QUENCH-07. Although the electrical power input was the same in both tests, the bundle temperatures were lower in QUENCH-08, probably due to higher heat losses. Therefore, the pre-oxidation phase was extended to reach a similar oxide layer thickness as in test QUENCH-07. Similarly to QUENCH-07, at the end of the temperature plateau one of the corner rods was removed from the test bundle to check the extent of oxidation. The results of the corner rod oxidation are provided in [Table 10](#) and [Fig. 50](#) (maximum ZrO₂ scale thickness of 274 μm, metallographically determined at the 950 mm level).

The second transient started at 3240 s and ~1750 K by ramping the power at 6 W/s. This was continued until the predefined cooling criteria as of QUENCH-07 were reached. Towards the end of this phase there were indications of shroud failure. According to a drop at P 406 (pressure between shroud and cooling jacket), a shroud failure occurred at 3765 s as can be seen in [Fig. 29](#). Shortly after this time, i.e. at 3770 s, krypton was detected by the mass spectrometer, indicating failure of at least one of the fuel rod simulators (see [Fig. 30](#)).

Cooldown was initiated at 3776 s by injecting steam of saturation temperature at a rate of 15 g/s (see flow meter measurement F 204 in [Fig. 31](#)). The maximum bundle temperature at cooling initiation was measured to 2090 K at 950 mm elevation (see [Table 6](#) and TIT A/13 in [Fig. 22](#)). The power ramp was continued for ~40 s and then the electrical power was reduced

from 17.8 to ~4 kW in 16 s and kept constant for ~190 s. It was then shut off, but steam injection continued until a bundle temperature of ~473 K had been reached.

During the transient and at the beginning of the cooling phase it is noted that several thermocouples failed ([Table 4](#)). Within the heated zone all the observations indicated immediate cooling. Several locations toward the top of and above the heated zone, however, experienced a strong escalation with a maximum temperature at the beginning of cooling of ~2300 K at the 1150 mm level (see [Table 6](#) and TFS 2/15 in [Fig. 22](#)). An escalation to ~2175 K of the shroud temperature was observed somewhat later at the 950 mm and higher elevations (see [Table 7](#) and TSH 13/270 I in [Fig. 24](#)). Associated with this escalation an increased release of hydrogen was observed during the cooling phase for a period of about 2 minutes (see second spike in the hydrogen generation rate presented in [Fig. 32](#) and [Fig. 33 top](#)). The first H₂ spike measured by the mass spectrometer coincides with cooling initiation and is considered as a response to enhanced steam flow and consequently an axial heat transfer from the hot zone to the upmost region. The H₂ data of the Caldos analyzer ([Fig. 32](#)) reflect this transient behavior, only much less pronounced because of peak broadening due to its location and the measurement principle (steady-state instrument). [Fig. 33 bottom](#) compares the total H₂ generation measurements by mass spectrometer and Caldos analyzer during the entire QUENCH-08 experiment. The total release of hydrogen measured by the mass spectrometer amounts to ~46 g of total hydrogen generation up to the end of the transient phase and ~38 g of hydrogen release during the cooling phase, hence about 84 g of H₂ in total compared to ~180 g, the total of H₂ during test QUENCH-07.

[Figs. 34 and 35](#) compare hydrogen generation rates of experiments QUENCH-07 and QUENCH-08. The data are comparable in the pre-oxidation phase but different in the transient and cooling phases. The larger peak values of QUENCH-07 could be attributed to the higher temperatures during the transient compared to QUENCH-08 and to the presence of boron carbide which is responsible of early-melt formations.

The evaluation of the total release of hydrogen for specific phases of experiment QUENCH-08 (no B₄C) compared to QUENCH-07 (similar to QUENCH-08, with B₄C) is depicted in [Fig. 36 top](#) and including QUENCH-09 (also with B₄C) is given in [Fig. 36 bottom](#), and in [Table 8](#). As can be seen, the total releases for the test phases up to quenching initiation are quite similar for QUENCH-07 and QUENCH-09 but somewhat lower for QUENCH-08 due to lower temperatures. During quenching (up to the point of electric power decrease and also from there to the very end of quenching) are significantly different: QUENCH-08 gives lowest and QUENCH-09 highest release rates. Also during quenching the QUENCH-08 temperatures were lower than those of test QUENCH-07 as can be seen in [Fig. 26](#). (In addition to the presence of B₄C absorber material in QUENCH-09, this bundle experienced a phase of steam starvation prior to the cooling phase and as well a higher flooding rate, i.e. 50 g/s, compared to QUENCH-07 and QUENCH-08 [13]).

7 Posttest Examination

7.1 QUENCH-08 Posttest Appearance Prior to Bundle Sectioning

In the region from ~850 mm elevation upward the shroud appears severely damaged. As in QUENCH-07, the shroud was formed to a shape of a “bubble”, between ~880 and 1020 mm (see [Figs. 37 and 38](#)). In this region the shroud exhibits different large cracks. Also as in QUENCH-07, there is an intensive interaction between the shroud and the fiber insulation between 900 mm and 1024 mm. The outer shroud surface and bundle are severely oxidized in this region. The zone above 1020 mm shows large regions of shroud melting, at orientations between 270° and 0° (see [Figs. 39 and 40](#)). Below the 750 mm elevation the shroud is intact and the oxidation of the outer shroud surface is negligible.

[Fig. 41](#) shows in a comparison that the posttest appearance of the QUENCH-08 bundle and shroud is similar to that of QUENCH-07 and QUENCH-09 though with less degradation and melt formation of the QUENCH-08 bundle.

The photographs in [Fig. 42](#) which were taken by a videoscope system exhibit an example of a circumferential crack (here of rod 5 at elevation 800 mm). Such cracks could develop during cooling when hot rods are not allowed to freely shrink in the axial direction.

7.2 Sectioning of the Test Bundle

The encapsulation of the test bundle was performed in three steps. First, a cap was placed over the bottom of the copper electrodes and a low-melting metal alloy (containing Pb, Bi, Sn, and In; density of ~10 kg/dm³; melting point of 331 K) was used to seal the bottom of the bundle. Secondly, a small amount of the same resin to be used for the encapsulation of the bundle was placed on top of the metal to generate an interface of around 0.2 m that prevents the metal from being liquefied after starting to epoxy the bundle together with its shroud. The epoxying process generally shows a little heating due to the exothermal heat that develops during the curing stage. The mould for filling the bundle with epoxy resin surrounds the shroud over the entire bundle length and is set up vertically. It is evacuated before charging with the resin to allow filling of pores and cracks. So, the bundle is filled from the bottom with approx. 20 kg of resin and hardener. The epoxy system Rütapox 0273 with the hardener designated LC (manufactured by Bakelite GmbH, Iserlohn) was chosen based on the experience with the CORA test bundles. The shrinkage effect is small. After epoxying the bundle the resin is allowed to harden for one week. To obtain the cross sections a saw with a 2.0 mm-thick diamond blade (mean diamond size 138 µm) of 350 mm OD is used to cut the slabs at 1300 rpm. As an overview the sectioning map is given for test bundle QUENCH-08 in [Fig. 43](#). The exact elevations are listed in [Table 9](#). The top surface cross sections that were polished for metallographic examination can also be taken from Table 9.

The complete series of prepared cross sections is depicted in [Figs. 44 to 49](#), in which slab number, bottom or top side, and bundle elevations are given. Generally, the top sides have been prepared for more detailed examinations.

7.3 Metallographic Examination

7.3.1 Investigation Procedures

As already mentioned, corner rod B was withdrawn from the QUENCH-08 bundle during the experiment, at the end of the pre-oxidation phase. Its extent of oxidation as function of the elevation in the bundle was determined by a non-destructive technique based on the eddy current principle of scale thickness measurement, as well as the scale measurement for polished cross sections of the rod.

The post-test examination of the whole bundle is based on the metallographic preparation of cross section slabs on one side (generally the top one) by carefully grinding and polishing, the visual inspection, and a comprehensive photo documentation. In the evaluation, a selection of the available macrographs and micrographs is given for orientation and used for illustration. The interpretation of the bundle behavior with respect to different aspects is demonstrated by composed, thematic figures. The final bundle state is thus described as far as possible, and the mechanisms of the physical-chemical interaction of the components and of their oxidation are deduced. The bundle will be described from bottom to top, because the extent of interaction increases with the temperature and thus with increasing elevation. The state at lower elevations can be helpful to deduce intermediate states at higher positions.

Special attention was paid to the cladding oxidation and phenomena, related to cooling in steam. The basic degradation behavior, in which no interference of interaction products with low melting temperatures took place, was studied in detail. This is important for the comparison with QUENCH-07 and -09, the bundles containing a control rod arrangement of B₄C type.

The scale thickness on simulator rod and corner rod surfaces as well as inner and outer shroud surfaces was measured. This was done, if possible, in four directions around rods and shroud, and for all prepared cross sections. The results are illustrated in lateral scale thickness profiles and in axial profiles, given for the different components and in comparison to QUENCH-07 and -09.

7.3.2 Axial Oxidation Profile of Corner Rod B

Table 10 summarizes the results of the metallographic and the eddy current method of scale thickness measurement for the given elevations. The comparison of both methods shows consistently some overestimation of thicker scale compared to the more time consuming, but more representative metallographic determination. In Fig. 50 this profile for QUENCH-08 is compared to that of the respective corner rod of the experiment QUENCH-07, which is quite similar. This has been already mentioned in section 6 as argument for the similarity of both test conducts.

7.3.3 Bundle Documentation and Microstructure Interpretation

Cross section QUE-08-01, bundle elevation 73 mm

The cross section overview of bundle, shroud and spacer grid is depicted in Fig. 51. This figure can serve as reference for the non-damaged bundle arrangement since no change

due to the test is detected. It is to be noted that only four rods are seen in complete preservation, whereas all other pellet and heater rod stubs were lost during cutting. This is due to the absence of any epoxy resin to hold them in place, whereas the cladding tubes were fixed by the cured resin. The bottom of slab QUE-08-01 at cross section elevation 60 mm is shown as smaller insert to the right of the figure. Note that this picture has been mirror-inverted (converted to top view) in order to facilitate the comparison. No rubble relocation to both elevations took place. The missing corner rod B (SW position) had been removed towards the end of the transient test phase.

Cross section QUE-08-2, bundle elevation 550 mm

At the elevation of the central spacer grid (550 mm, top of the slab) and slightly below (slab bottom, 537 mm) the bundle arrangement is depicted in [Fig. 52](#). Again, most of the interior rod components are missing, only due to the already explained preparation artifact. Abstracting from this, the bundle arrangement is still perfect, so that only a few fallen rubble fragments can be mentioned, which have been collected at the spacer periphery in SW direction. The unimportant cladding oxidation is treated later, and no detailed illustration is given here.

Cross section QUE-08-04, bundle elevation 750 mm

The more distorted rod positions at this cross section slab elevation are easily explained by some rod bending between spacer grid levels ([Fig. 53](#)). Much stronger cladding oxidation compared to the previous level will be considered later. Solid state interaction between cladding and pellets is understood to have intensified in parallel, so that some contact forces have helped to preserve most pellets from loss during slab preparation. All thermocouples are intact as well as the fixture (spot-welded Zr band) of those, reading at the given elevation. Corner rod C (NW position) is seen as massive rod.

Cross section QUE-08-8, bundle elevation 860 mm

110 mm higher, the bundle shows some damage, worthwhile to be reported ([Fig. 54](#)): The cross section slab was chosen for preparation, to illustrate the lower limit of melt relocation from the hotter zones located above. At top level, melt relocated within the instrumented corner rods A and D is found to have filled those tubes completely; at 842 mm bottom level the thermocouple of corner rod A is only wetted, the TC of corner rod D fully embedded. Melt within the bundle flow channel has obviously reached the slab top surface but not the bottom level. Details of the relocated melt and the interference with the rods are given within the following more detailed description.

Beginning with isolated rods, [Fig. 55](#) depicts a selection of them, including the central rod. It is mentioned in advance that cladding through-wall cracks and loss of cladding due to spalling indicate strong oxidation-related cladding brittleness. The partial cladding loss of the central rod is thus plausible, but it could have occurred during quenching or during bundle handling. The chosen rods vary with respect to presence or extent of internal pellet/cladding interaction according to the solid state contact of those components. [Fig. 56](#) gives details of external cladding oxidation for the example of rod No. 7 at a position where no pellet contact was provided. The duplex (tetragonal/cubic) scale at the external side of the cladding, composed of a double-layered outer and a decomposed inner part indicates a peak temperature clearly above 1800 K; the intact contour of the inner surface indicates absence of melt formation for the metallic matrix and thus a peak temperature below ca. 2100 K. The

example of a pellet/cladding contact situation is depicted in [Fig. 57](#), in which rod No. 2 developed a similar external scale compared to the previous figure, and in addition an internal interaction layer, formed during oxygen transfer from the ZrO₂ simulator pellet. Shape and distribution of the ZrO₂ phase, precipitated from the remaining metallic matrix, do not indicate matrix melting at the peak temperature.

Leading over to details of distributed melt, [Fig. 58](#) shows for a directly adjacent position of rod No. 2 the melt lump in contact and the microstructures of the melt, its scale, and the embedded scale of the rod. The rounded or dendritic shapes of the ZrO₂ phase precipitates confirm the previous molten state. At the contact area the melt coverage has resulted in a clearly visible reductive attack on the previously formed scale of the rod. In turn, the melt lump surface itself is covered by a scale of comparable thickness. The lump is separated by a similar scale from another lump, which covers rods No. 11 and 12 partially, and completes the bridge to rod No. 2. The meltdown occurred obviously in separate flows and was stopped due to violent oxidation and heat loss to less hot structures. An empty “bubble” of scale, attached to rod No. 4, cannot be confirmed as candling residue without information on the vertical elongation of this structure.

In contrast to the above reported melt relocation, quite different relocations are depicted in [Fig. 59](#). Melt between rod No. 14 and the thermocouple, finally found partly detached from the rod, has not developed any visible scale. A quite similar melt is found in contact to rod No. 15, which exerted no visible reduction to the covered cladding scale, and which did not develop an own external scale. Common for both relocation events is some melt porosity. Presently no interpretation can be given, but it seems plausible to assume a rather late relocation of the metallic melt during the quench phase to explain the missing oxidation.

Cross section QUE-08-9, bundle elevation 900 mm

The cross section slab overviews given in [Fig. 60](#) contribute to the reconstruction of the previously described melt relocation. At the slab bottom (864 mm) rods 2, 11, and 12 are contacted as below, whereas the melt path contacts rods No. 2, 12, and 3 at top cross section. Small remnants of scale are attached to melt and corner rod A. Most obvious is the melt agglomeration, southward at the external surface of the shroud, at top but not at bottom, the reason for preparation of the slab.

Macrographs of three different bundle regions serve for orientation in the following illustrations of the typical bundle state ([Figs. 61 to 63](#)). Towards NW to N direction, the fuel rod simulator claddings are typically almost converted to scale and pellet interaction zone. Some confined matrix melting may have occurred, not illustrated in [Fig. 61](#). Southward in the bundle, where the melt agglomeration on the shroud might indicate the relatively highest temperatures, indeed the cladding of most rods is completely converted to the ceramic state ([Fig. 62](#)). Some very limited cladding matrix melt relocation could be deduced from the form of the respective gap for rod No. 14. Finally, [Fig. 63](#) includes some details of the already treated melt relocation and the melt-filled corner rod A.

Cross section QUE-08-6, bundle elevation 950 mm

Within the hottest bundle zone, [Fig. 64](#) illustrates the overview of the maximum of the observed damage: Initiated by shroud matrix melting during the transient, the internal and external shroud fractions separate under scale growth stress and can open wide gaps, or allow their filling during melt agglomeration. The external shroud fraction is at that time

already stabilized by some oxygen pick-up from the ZrO_2 fiber insulation package. The distance of penetration into this package is variable according to local conditions and the temperature evolution. Filling of such a shroud bulge is seen for the bottom elevation towards SE. Continued shroud oxidation during a phase of already completed rod cladding oxidation causes a somewhat unwanted experimentation condition, which has to be taken into consideration. A similar disadvantage of the massive sections of instrumented corner rods is their internal melting during continuing oxidative self-heating. Clearly visible in Fig. 64, shroud and corner rod behavior is able to interfere in the case of neck formation at contact of both structures. This occurred at SE involving corner rod A, and at NW, involving corner rod C and rod No. 19 at the bottom slab elevation. Failure of the common scale of the respective structures may give rise to melt relocation into and within the bundle. The above described melt relocation to the final position between rods of the SW bundle corner is interpreted in this way: Shroud melting has been the event of source formation, and the passage of the melt into the bundle went via corner rod A.

This bundle region is further illustrated by [Fig. 65](#), in which rod No. 12 together with the empty scale of corner rod A and adjacent melt is depicted (bottom, left), together with rod No. 13 and the shroud close by (top, right). The above explained melt transfer from shroud to bundle are not to be seen, however. This is why it is mentioned here, that visual inspection of respective bundle sections has allowed to identify this melt transfer directly within the translucent epoxy resin.

Some rods show the presence of oxidized melt covers on part of their circumference, into which empty bubbles are embedded ([Fig. 66](#)). This appearance is assumed to be related to rather late relocation of highly superheated metallic melt. Low viscosity combined with not too poor wetting might give rise to partial coverage of scale structures. A certain oxygen content of this melt has to be assumed to explain the fair wetting of ceramics. The relocation might well have occurred during quenching, but long distances of relocation were surely not possible due to extremely fast oxidative re-solidification.

Going back to the state of separate rods, which are not influenced by melt, [Fig. 67](#) illustrates the complete conversion of rod cladding due to external steam oxidation and internal pellet contact. The rods are examples, chosen to show the variation range from open gaps to closed contact and oxidized interaction layer.

[Fig. 68](#) illustrates the central rod and details of the pellet bore hole, filled by a metallic melt of (Zr,O) type, which has formed a very regular interaction layer of ceramic character in contact with the pellet. The thermocouple TCRC 13, a TC of W/Re type and insertion from above, should have been installed for measurement just at this elevation according to the bundle instrumentation plan. It seems that it was fixed a bit higher, so that it is not visible here, but only at higher bundle levels, which will be described later. This TC has served reliably during almost the whole experiment, according to the temperature reading. It is possible that melting of the outer part of the duplex TC sheath at some higher elevation was the source of the observed melt relocation and bore hole filling without damage to the TC function. An alternative explanation depends on the fact that rod cladding matrix melting took place around 1000 mm elevation. Such melt could have penetrated between consecutive pellets of the stack into the central channel, driven by local pressure build-up, and capillary forces might have supported the filling and downward relocation along the TC within the central channel.

Cross section QUE-08-10, bundle elevation 1000 mm

The elevation range of this cross section slab, depicted in [Fig. 69](#), can be seen as source region for melt, relocated towards the previously described lower region. For this aspect, the figure should be compared to [Fig. 64](#) and details in [Fig. 65](#). As already interpreted, melt relocation was mainly observed for the thick metallic structures, massive corner rods and the shroud. The resulting shroud structures are stabilized due to the advanced oxidative conversion to the ceramic state. Other missing ones are lost due to brittle fracturing or removal in the post-test dismantling, in which they were taken off, sticking together with the fiber insulation package. No more details are mentioned or depicted.

Cross section QUE-08-11, bundle elevation 1065 mm

At this elevation, the electrode zone of the rods is reached, and the spacer grid elevation ([Fig. 70](#)). Partial melting of the shroud is noticed as well as some melt agglomeration at spacer grid structures in the SE bundle corner. The consequence of partial spacer bands melting is their splitting after double-sided oxidation; some fragment rubble relocation took place as well. The rod claddings have still fulfilled their function.

Cross section QUE-08-12, elevations 1150 mm and 1135 mm (slab top and bottom)

The reason for including both slab sides into the description is the correspondence of the different information contained in them ([Fig. 71](#)). Both show advanced damage mainly at the SE bundle periphery. At the bundle center, melt agglomeration is seen to connect the central rod with rod No. 2 at bottom. Towards source direction, at top elevation, the central rod is seen to form bridges to rods No. 2 and 8. [Fig. 72](#) compares those details for both elevations. The neck between central rod and rod No. 8 is illustrated in [Fig. 73](#): At the top slab elevation, the common scale which forms the neck, is just closed for the exchange of interaction products of cladding and pellet (central rod) or Mo electrode (rod No. 8), respectively. Obviously, the plasma coating of the molybdenum electrode by a zirconia protection layer has failed here under the dilutive attack of cladding melt. The resulting irregular electrode interaction zone is also seen in [Fig. 72](#) and depicted for some other rods, chosen for documentation of their state ([Fig. 74](#)). At the slab bottom elevation, [Fig. 75](#) concerns the local melt pool. The common external scale around two different melt flows is shown, as well as the dissolution tendency of a fully embedded scale segment, and of the scale of the central rod. According to the microstructure, the melt type is (Zr,O) without detectable contamination.

Cross section QUE-08-14, bundle elevation 1320 mm

Far higher within the electrode zone, the overview shown in [Fig. 76](#) is to be understood as the result of fast temperature transition during the cooldown phase. The melting of slightly oxidized cladding occurred thus already around 2050 K, however, in competition with the fast melting temperature increase during the phase of continuing oxidation. The pronounced differences between retained cladding and melt relocation explain themselves by quite remarkable temperature history variations. Rods of the outer ring, depicted in [Fig. 77](#) show melt loss towards the bundle center and stronger oxidation in the respective directions. The same trend is obvious for the inner ring rods, as depicted in [Fig. 78](#). It is mentioned further, that the central rod pellet and the electrode of rod No. 4 are bare, and that some scale fragments can be attributed to them.

Cross section QUE-08-15, bundle elevation 1425 mm

Even at this elevation, the passage of hot steam has supported the oxidation of the components. [Fig. 79](#) shows the rods in regular arrangement, as fixed by the spacer. Melt, kept in the grid, as well as indications of melt movement are obvious. Peak temperatures of at least 2030 K can be deduced without deeper inspection.

Cross section QUE-08-16, bundle elevation 1480 mm

The view is just given as upper reference for the almost undamaged bundle end state below the alumina thermal shield, positioned at 1500 to 1530 mm ([Fig. 80](#)).

7.3.4 Lateral and Axial Oxide Scale Thickness Distribution

At the 550 mm elevation, the ZrO_2 scale thickness of up to a few tens of μm , measured for the bundle components, indicates minor oxidation with quite large and unsystematic relative scatter ([Fig. 81](#)). At 750 mm elevation, rather flat temperature profile across the bundle and much smaller scatter are indicated by far higher absolute values of 100 to 140 μm ([Fig. 82](#)). At the 860 mm level, the local peak ZrO_2 scale thickness is 600 μm , and for the cladding / pellet interaction zone, worth to be measured as well, "internal oxide" layers up of to 150 μm were measured, as included in [Fig. 83](#). The inner shroud surface gives lower and more scattered values (200 to 340 μm); minor and only local outer shroud surface oxidation is registered.

At 900 mm elevation ([Fig. 84](#)), a coarsely doubled cladding oxidation extent compared to the previous elevation is measured. A much less steep increase follows to the 950 mm elevation ([Fig. 85](#)), for which the cladding oxidation is complete for almost all rods. Consequently, it would not make much sense to try to distinguish between external and internal oxidation, which are both influenced by local conditions. The same arguments hold for the 1000 mm elevation ([Fig. 86](#)). The presented profiles support the dominance of oxidation in competition with rod cladding melting, which has been illustrated in the previous section.

The decreased extent of oxidation at the 1065 mm elevation is obvious from the data given in the lateral profile [Fig. 87](#). For the next evaluated level of the electrode zone, the bottom slab elevation 1135 mm ([Fig. 88](#)), the data indicate a still flat lateral oxidation profile. In contrast, far higher at 1320 mm, the less high peak temperatures reached at bundle periphery are indicated by the much lower scale thickness values, compared to the much higher ones in the center ([Fig. 89](#)). This lateral profile seems to persist at 1480 mm, where the absolute scale thickness values are much lower ([Fig. 90](#)). Since the electrode zone was superheated mainly during the bundle cooldown phase, the profiles, presented in this section, indicate clearly the axial spread of superheating and the preference of the central volume of the electrode array by the steam flow.

The essence of the lateral oxidation distribution data and their statistical evaluation is collected in [Table 11](#). Illustrations are given in [Fig. 91](#). At top of the figure axial profiles are shown for the different bundle components. In comparison between them, most items are reasonable consequences of the heat release profile of the tungsten heater rods. The peak value of shroud scale thickness at 1000 mm, found above the profile maximum of heated rods, is seen in relation to the terminated rod oxidation and the continued oxidation-driven heat release within the thicker shroud. The advanced central rod oxidation within the heated zone is not sufficiently explained by radiation heat transfer from the inner rod ring, combined

with some heat loss from the rods of the outer ring to the shroud. The temperature history of the upper electrode zone together with preferred central steam flow during the cooldown phase, as already mentioned, should be the reason for the second peak in the central rod oxidation profile. The graph at bottom of [Fig 91](#) depicts statistics and large local scatter of the rod oxidation data, and for comparison, the profile for Quench-07 is included. Finally, [Fig. 92](#) compares the average rod oxidation profile of QUENCH-08 with the respective results for QUENCH-07 and QUENCH-09. The latter bundles, which included the control rod of B₄C type at central position, had shown broader profiles, corresponding to early melt relocation and more violent response to the cooldown. The especially broad zone of complete oxidation for QUENCH-09 is seen mainly in relation to the intensive components interaction during the steam starvation phase of that experiment, which differed from QUENCH-08 also in the steam flow rate during final cooling.

7.3.5 Summary and Conclusions

The results of the comprehensive metallographic post-test examination of the QUENCH-08 bundle were condensed into the above given description, illustration, and interpretation. This allows insights into the coupled degradation phenomena, to be expected for a fuel rod configuration under the conditions, simulated in the bundle experiment.

The rod arrangement in the bundle remains quite regular up to ca. 850 mm elevation. The extent of damage increases within this range, corresponding to the axial profile of increasing oxidation. In parallel, the observed oxidative pellet interaction, taking place with the cladding at positions of contact, corresponds to the axial temperature profile, as well.

The 860 mm bundle level was inspected as lower limit of melt relocation within the bundle, the 900 mm level as lower limit of external shroud relocation. The obtained information is combined with observations at the 950 mm peak temperature level, and includes visual inspection of the slabs, embedded in the translucent epoxy. Within this elevation range, the rod cladding reaches the full conversion to the ceramic state, in the course of external steam oxidation and internal oxygen transfer from the ZrO₂ pellet. Local cladding matrix melting and internal melt re-distribution take place just at the peak temperature level, and with only negligible influence. In contrast, long range melt relocation from different sources is interpreted as follows: External shroud melting and neck formation between shroud and corner rods take place; at south-west, (Zr,O) melt transfer into the bundle occurs, and continuing meltdown in form of candling events. Those are distinguished by growth of ZrO₂ scale, dissolution of embedded scale, and empty scale remnants. The occurrence is not fully typical for the bundle state itself, since more massive metallic structures (shroud and corner rod) are involved. (Zr,O) melt, formed by cladding matrix melting above the described zone, relocates within the annular pellets of the central rod. The observation is to be transcribed to real and non-instrumented fuel rods. Relocation of superheated (Zr,O) type melt from the near upper vicinity has formed thin partial covers on several rods, characterized by the content of bubbles and the completed oxidation; the given interpretation relies on considering viscosity and wetting arguments. Finally, relocation of almost non-oxidized melt by candling is deduced to have taken place during the cooldown phase, and thus without noticeable oxidation response.

The 1000 mm elevation and the electrode zone levels above, studied for analysis of the strong interim superheating during the cooldown phase, are indeed to be seen as source

region for melt relocation to the described lower elevations. Also shorter range relocation within the considered zone took place. This melt movement was supported by neck formation between rods, and shows, consequently, quite similar candling features. Within the rods, cladding melting, attack of the zirconia coated molybdenum electrodes by melt, and some Mo exposure to steam took place. But even in the hottest section the electrode response can be neglected. Apart from the relocation related aspects, the brittle fragmentation of thin ceramic structures is mentioned.

Compared to the bundles QUENCH-07 and QUENCH-09, for which the control rod of B₄C type has influenced the degradation behavior essentially, QUENCH-08 shows a much less spectacular test history. However, the intentions, to evaluate this test as base case, have been fully reached. Valuable in addition is the availability of the results for comparison with the experiments QUENCH-04 / QUENCH-05 (steam cooling) and QUENCH-06 (water quenching). Comparison within the experiments of the QUENCH series is an ongoing task, dedicated to a condensation of the complex information to a mechanistic data base for model verification purposes.

7.4 Hydrogen Absorption by Zircaloy

The hydrogen absorbed in the remaining Zircaloy-4 metal was analyzed by hot extraction in the so-called LAVA facility, which is an inductively heated furnace coupled to a mass spectrometer. Specimens were taken from bundle slabs especially prepared for destructive analytical purposes from three elevations: 550, 750, and 1150 mm (see also Table 9). They were heated for 20 min to some 1800 K under a well defined argon flow. The hydrogen extracted was measured by the mass spectrometer. Results are given in [Table 12](#) and [Fig. 93](#).

The single data show a large scatter. The amount of hydrogen absorbed increases with the axial bundle level with the maximum H concentration in the remaining metal phase of around 9 at% at 1150 mm. This value is smaller than the maximum one measured after test QUENCH-07 (approx. 20 at%) but larger than that of the QUENCH-09 (approx. 3 at%) where an extended region of the bundle was completely oxidized.

It is difficult to give an integral value of H₂ absorbed due to limited data. A rough estimate based on a mean H absorption of 2 at% assumed for the entire bundle length would result in a total of 2 g of hydrogen absorbed by both bundle and shroud. No statement on hydrogen absorption and release during the test can be made by this posttest analysis.

8 Analytical support

8.1 Analytical Support Using the FZK/IRS Version of the SCDAP/RELAP5 Code

Because of the similarities between QUENCH-08 and the two previous tests, reproducibility of the test conduct during early test phases, the limit of stable operation during pre-oxidation, and time margins for operator intervention could be derived from experimental data of those

two tests. The work for test preparation resulted in recommendations for the conduct of the first transient, in particular for its transition into the pre-oxidation phase. Because of the early temperature escalations in QUENCH-09, an alternative test conduct in case of difficulties was proposed. It was agreed that in such a case the test should be continued similarly to QUENCH-09. However, the bundle status should be “frozen”, i.e. the bundle was to be cooled down as fast as possible.

Pre-test calculations for the cool-down phase in QUENCH-08 with SCDAP/RELAP5 (S/R5), as used for previous tests, demonstrated that modelling of the facility is adequate for cool-down calculations: Not only calculated temperature histories during that phase, but also temperature decrease rates compare quite well with experimental values for QUENCH-07 and QUENCH-09. Deviations are mainly due to differences at the beginning of cool-down and decrease quite rapidly with time.

The pre-test calculations gave the following results. When the steam mass flow rate is 0.4 g/s as in the test phase before and argon mass flow rate is increased from 3 to 6 g/s, the maximum value that can be maintained for a longer time, oxidation is predicted to continue markedly and to keep temperature at a high level for about half an hour. This is in contrast to the aim of the cool-down phase. Cool-down with pure argon is much faster, but still slower than desired. As expected because of the different atomic weights, a much faster cool-down can be achieved, when 6 g/s helium are used instead of argon. Because of constraints of S/R5, helium is assumed as a carrier gas during the whole test instead of argon, the mass flow rate being chosen to give a similar axial temperature profile before cool-down initiation as for the previous calculations. Evaluation and comparison of experimental data is meanwhile extended substantially and documented in [12], computational work in [13].

A first post-test calculation showed similar agreement with experimental data as those for QUENCH-07 and QUENCH-09.

8.2 Calculations of the QUENCH-08 test with the FZK Bundle Code CALUMO

The calculations for the triplet QUENCH-07 [14], QUENCH-08 and QUENCH-09 [15] were done with the most advanced code version CALUMOqx. In this version of the code we have balance equations for the outer ring of 12 heated fuel rods (+ 4 corner rods), balance equations for the inner cluster of 8 heated fuel rods, and balance equations for the central rod or absorber rod with its guide tube, and, of course, balance equations for the shroud and the coolant. In case of QUENCH-07 and QUENCH-09 an absorber rod with a Zry guide tube is in the central position of the bundle. For QUENCH-08 the absorber rod is replaced by an unheated fuel rod of the normal bundle design.

It should be noted that in the following figures the average temperature in the outer ring of fuel rod simulators is denoted as “tsurz”, that of the inner cluster of 8 fuel rod simulators “tcenz”, that of the absorber rod with its guide tube or that of the central rod “trcz”, and the average shroud temperature “tshrz”. They are compared to the available thermocouple readings. In the same way “dox” denotes the oxide scales of the inner cluster of 9 heated fuel

rods, “doxc” that of the guide tube of the absorber rod or the oxide scale on the unheated central rod, “doxa” that of the outer ring of 12 heated fuel rods, and “doxsh” the oxide scale of the shroud.

Results of code calculations in comparison to the respective data of the test instrumentation are to be found in Figs. 94 to 97. These are the temperature evolutions between 150 and 1250 mm (Figs. 94 and 95), the axial profiles of oxide scale thickness for the fuel rod simulators and the shroud in Fig. 96, and in Fig. 97 the results on hydrogen production (rates and overall production). It should be noted that the calculation starts at about 160 s into the test with the increase of the electrical power and ends at about 4100 s.

The temperature evolution in the in the lower part of the heated zone ($z \leq 450$ mm) in the bundle and the shroud is rather well simulated by the code. Most of the features of the temperature evolution are relatively well reproduced in this axial zone. The temperature rise to steady-state conditions, the pre-oxidation phase, the temperature transient, and the cool-down phase are to a good extent well matched. As the temperature evolution in this part of the test section is mainly determined by the electrical heating, one can be rather confident that this effect is correctly simulated by the code.

Between 650 and 950 mm the agreement is not so good. The code overestimates the temperatures in the bundle and shroud during the transient phase considerably, especially at level 12. This leads then to some overestimation of the oxidation and as well of the hydrogen production in this axial region of the test section. It should be noted that the information on the temperature evolution is mainly based on shroud thermocouple readings.

Due to the recently implemented natural convection model the situation in the upper part of the test section (1000-1400 mm) looks now relatively good. This axial zone seems to be rather important for the outcome of QUENCH-08. A considerable part of the hydrogen produced during the cool-down phase originates from oxidation in the upper part of the test section.

Assuming in the CALUMO code outside shroud oxidation between 1000 and 1200 mm starting at the onset of cooldown but no clad cracking caused by distension and split opening as was the case in QUENCH-09, a somewhat satisfying simulation of the experimental conditions in the upper part of the test section could be achieved, with strong but rather short temperature escalations starting shortly after onset of cooldown.

There is some clad distension to be seen in the macrographs of QUENCH-08, especially between 1400 and 1450 mm, but the effects are much less important than in QUENCH-07. Therefore the simulation of the real experimental conditions could, of course, still be improved. The hydrogen signal, for example, indicates a double peak escalation, which is not reproduced by the code. The second peak might be due to effects of relocation of molten material, which is not yet modelled in the code.

The calculated axial profiles of the oxide scale thickness at the time, when the corner rod was withdrawn and when the calculation was stopped are plotted in Fig. 96 together with experimental values from post test examinations.

The oxidation features are in the overall rather well met by the code, although the calculated profiles are a bit shifted from the experimental ones. PTE has provided the maximum the mean, the minimum values of the oxide scale thickness for all the fuel rod simulators and the mean values for the inner and outer rods. There is a big difference between minimum and maximum oxide scale values determined by ceramography, the reason for this effect is not yet clear. It may be that some of the subchannels were better cooled than the remaining part of the bundle, or that there has been partial spalling of the oxide scales.

The calculated profiles show a minimum at about 1000 mm and two maxima, the lower one shifted by about 100 mm compared to the experimental data. The upper maximum is due to the temperature escalation during the cooling phase.

A comparison of measured and calculated hydrogen values (production rate and time integrated values) is to be seen in Fig. 97. The agreement is to some extent satisfactory with an overestimation of the hydrogen production rate in the late pre-oxidation and the early transient phase. At the time of onset of cooldown, the calculated overall hydrogen production is about 56 g compared to a measured value of 46 g. During the cool-down phase an additional 35 g of produced hydrogen is calculated not far from the experimental value of 37 g.

The measured hydrogen production rate shows a high double peak with a maximum value of about 0.5 g/s about 100 s after the onset of cool-down, which corresponds to a temporary steam consumption of about 4.5 g/s. The CALUMO code calculates a single peak with a maximum hydrogen production rate of about 0.65 g/s a few seconds after the onset of cool-down.

The test phases in QUENCH-08 were very similar to that of QUENCH-07 and this is also true for the thermocouple readings. Nevertheless, there is a big difference in hydrogen production, especially during the cooling phase. The direct effect of the control rod in QUENCH-07 can be estimated to an additional amount of hydrogen of about 15 to 20 g. This alone cannot account for the big difference in hydrogen production. The main oxidation phenomena during the cool-down phase occurred in both tests in the upper part of the test section mainly due to the failure of the shroud and eventually due to relocation of molten material. In this aspect, the effects in QUENCH-07 are much more pronounced than in QUENCH-08. The additional heat production of the control rod and the appearance of eutectic melt must have led to somewhat higher temperatures in the upper part of the test section. It appears that relatively small differences can lead to severe consequences.

In the tests QUENCH-02, QUENCH-03, QUENCH-07, and QUENCH-09 the consequences of the temperature escalation were much more severe than in the other steam-cooled QUENCH tests like QUENCH-04 and QUENCH-05 with considerable hydrogen production and damage in the bundles and the structures. Test QUENCH-08 seems to lie in between these two groups of QUENCH experiments.

A possible mechanism for the trigger of the severe effects in the cool-down phase might be clad distension, cracking, and split opening in the upper unheated part of the test section, leading to an enhancement of the oxidation rate due to the increase of the surface area of

the claddings and eventually due to important internal oxidation of the claddings. A rough estimate of the inner clad oxidation yielded that this effect could contribute up to 1 g/s and even more to the hydrogen production rates for some time period. Evidence for clad distension effects in the upper non-heated part of the test section has been found in PTE of QUENCH-02, QUENCH-03 [17], QUENCH-07 [14]. The effect is viewed to be due to loss of strength in the claddings with the attainment of high temperatures, the oxide scale thickness still being relatively small. With thick oxide scales, no clad distension would probably occur, as the oxide scale itself seems to have sufficient strength. The bounds on temperature, temperature increase rate, and oxide scale thickness, where clad distension may occur cannot be determined from integral tests alone, as one does not know all the parameters with sufficient accuracy. But it may be that relevant out-of-pile mechanical tests with Zry claddings under steam atmosphere have been done in the past. The results of these tests could then eventually be used as a guideline. Clad distension in QUENCH tests is presumably not due to an overpressure in the fuel rod simulators, as the rods have failed prior to cool-down. But the effect is presumably caused by growth stresses in the cladding. Under bi-axial oxidation strain one could obtain compressive stresses in the oxide scale and tensile stresses in the metallic substrate.

Clad distension is considered to be a very important phenomenon in QUENCH tests. It is viewed to have led to overheating and severe destructions in the upper part of the test section in some tests. Most probably it should also occur under reactor conditions. There are some indications of clad distension effects also found in the upper part of QUENCH-08. But the effects are much less pronounced than in the tests with a larger degradation. Also there is much less hydrogen production in the cool-down phase than for example in QUENCH-07, although both tests were very similar in their test conditions. It can be surmised, that when a certain threshold in the temperature in the upper part is passed the test evolves in a violent way. This would mean that in QUENCH-08 we were presumably just on the brink of conditions leading to a prolonged violent temperature escalation in the upper part of the test section and consequently massive destruction.

8.3 Application of the SVECHA/QUENCH Code to the Simulation of the QUENCH Bundle Test QUENCH-08

8.3.1 Introduction

In the present work the QUENCH bundle test QUENCH-08 was simulated using the “effective channel” approach developed earlier [18, 19]. Within the framework of this approach the thermal boundary conditions for the central rod are predetermined by specifying the temperatures of the “effective channel” inner wall on the basis of experimentally measured temperatures of the heated rods. The inner surface of the effective channel represents the surfaces of the heated rods surrounding the central rod.

The heat exchange between the central rod and the effective channel is affected via radiation and convective heat transfer to the gas mixture (argon/steam/hydrogen). The thermal-hydraulic characteristics of the effective channel (cross-section, hydraulic diameter) are determined on the basis of geometrical parameters of the bundle (total cross-section, number of rods and their diameters).

The experimentally measured temperatures at all the elevations (TFS and TSH thermocouples data) were analyzed and smoothed. At high elevations the TFS data were used as the basis for the averaged temperature. At the elevations from 1050 mm to 850 mm the TFS data were used up to the moment of corresponding TC failure, then TSH data were taken as such basis. At lower elevations (below 750 mm) only TFS data were applied.

The calculated 'averaged temperature field' describing the temperature evolution around central rod was used in the S/Q code input files for the simulation of the quench bundle tests QUENCH-08.

The calculated oxide thickness axial profile was compared with the experimentally measured one. Due to the fact that in the hottest zone (850-1050 mm) all TFS thermocouples failed long before quenching stage, the temperature data are deficient in this region. Such uncertainty led to underestimation of the oxide thickness at the mentioned elevations. After the comparison the 'averaged temperature field' was corrected using the special calculation procedure and the new simulation of QUENCH-08 test central rod was performed giving much better results with respect to oxide thickness axial profile.

The corrected 'averaged temperature field' was used for the simulation of the QUENCH-08 test with a virtual B₄C central rod by the S/Q code. The calculation data concerning gaseous components release were analyzed and compared with QUENCH-07 calculation results [19].

8.3.2 Processing of the QUENCH-08 Bundle Test Temperature Data

During the QUENCH-08 test the temperature was continuously measured at different locations of the bundle. 33 thermocouples were attached to the cladding of the heated rods at 16 different elevations between -250 mm and 1350 mm; 3 thermocouples were inserted in the centers of three corner rods at 550, 850 and 950 mm elevations; 2 thermocouples were located between cladding and pellets inside central rod at 550 and 350 mm; 3 thermocouples were located in the center of the central rod at 950, 550 and 350 mm; 3 thermocouples were attached to the cladding of the central rod at 950, 550 and 350 mm. The TCs data were processed by the FZK experimental team, incorrect data were deleted and now these data are available in the electronic format. [Table 13](#) presents the TCs designations, corresponding rod numbers and elevations.

20 thermocouples were located at the shroud outer surface at 11 different elevations between -250 mm and 1250 mm. Since the TCs were protected by the shroud wall from direct contact with steam, all of them survived throughout the test (with the only exception of TSH 14/270). [Table 14](#) presents designations and elevations of the shroud thermocouples, available in the electronic format.

The above TCs data were used for the simulation of the effective channel internal surface. The numerical procedure of the rod TCs data recalculation includes smoothening, averaging and interpolation. These operations are described below.

In [Figs. 98 and 99](#) the original TC readings of TFS 2/17 and TFS 5/17 thermocouples as well as the calculated averaged temperature (TFS 17) at 1350 mm are presented. The averaged

temperature was calculated as arithmetic mean of the smoothed TFS 2/17 and TFS 5/17 data sets.

In Figs. 100 and 101 the original TC readings of TFS 3/16 and TFS 5/16 thermocouples as well as the calculated averaged temperature (TFS 16) at 1250 mm are presented. Just like the 1350 mm data, the averaged temperature was calculated as arithmetic mean of the smoothed TFS 3/16 and TFS 5/16 data sets.

In Figs. 102 and 103 the original TC readings of TFS 2/15 and TFS 5/15 thermocouples as well as the calculated averaged temperature (TFS 15) at 1150 mm are presented. Up to the moment of TFS 2/15 failure (3785 s) the averaged temperature was calculated as arithmetic mean of the smoothed TFS 2/15 and TFS 5/15 data sets. After this moment only TFS 5/15 data were used as the basis for TFS 15 with the assumption that the difference between TFS 15 and TFS 5/15 is constant and equal to the value of this difference at the moment of TFS 2/15 failure (96.3 K).

In Figs. 104 and 105 the original TC readings of TFS 3/14 and TFS 5/14 thermocouples, TSH 14/90 I and TSH 14/270 I thermocouples at 1050 mm are presented. Here the averaged temperature TFS 14 was calculated as arithmetic mean of the smoothed TFS 3/14 and TFS 5/14 data sets up to the moment of TFS 3/14 failure (2922 s). After this moment up to the failure of TFS 5/14 (3544 s) only TFS 5/14 data were used as the basis for TFS 14 with the assumption that the difference between TFS 14 and TFS 5/14 is constant and equal to the value of this difference at the moment of TFS 3/14 failure (39 K).

Generally, after the failure of both TFS thermocouples one should use TSH data in order to represent the temperature evolution at a given elevation. However, in our case the TC reading of TSH 14/90 I and TSH 14/270 I thermocouples cannot be considered as reliable basis for temperature representation during the whole test. TSH 14/270 I thermocouple failed at 3816 s during temperature escalation (Table 4). As for TSH 14/90 I data, fast cooling starting from 3777.8 s seems to be non-typical for this elevation. Firstly, such fast cooling is in contradiction with TSH 14/270 I data which demonstrate opposite trend. Secondly, as one can see from Fig. 106, where the original TC readings of TSH 14/90 I and TSH 14/270 I together with TSH 15/0 I, TSH 15/180 I (1150 mm) and TSH 13/270 I (950 mm) data are presented, fast cooling of TSH 14/90 I falls outside the tendencies of temperature evolution at upper and lower elevations which are very similar to each other. Thus, TSH 14/90 I data set was recognized as inadequate starting from approximately 3778 s.

Shroud temperature evolution at the 1050 mm elevation TSH 14 was reconstructed in the following way. Up to the moment of 3778 s the averaged temperature was calculated as arithmetic mean of the smoothed TSH 14/90 I and TSH 14/270 I data sets. In the time interval 3778-3816 s (TSH 14/270 I failure) only TSH 14/270 I data were used as the basis for TSH 14 1 with the assumption that the difference between TSH 14 1 and is constant and equal to the value of this difference at the moment of TSH 14/270 I failure ($\Delta T = 73.2$ K).

In the absence of available temperature data at 1050 mm elevation starting from 3813.6 s the data from 1150 mm and 950 mm elevations (TSH) were used. TSH 15/0 I and TSH 15/180 I data sets were smoothed and their arithmetic mean represented the averaged

shroud temperature at 1150 mm (TSH 15). The arithmetic mean of smoothed TSH 13/270 I data set and TSH 15 data set was considered as the basis for the estimated shroud temperature at 1050 mm (TSH 14b, see [Fig. 107](#)). The transition from the TSH 14 1 curve to the TSH 14b one was achieved with the help of $\exp((t_f - t)/A)$ -type factor (here t is time, $t_f = 3816$ s, see [Fig. 108](#)).

Finally, cubic spline interpolation was used in order to match the part of the TFS 14 curve with the shroud one ([Fig. 109](#)).

At the elevation 950 mm ([Figs. 110 and 111](#)) the TFS 2/13, TFS 3/13, TFS 4/13, TFS 5/13 data were used as basis for the average temperature TFS 13 up to 2823 s (for failure of thermocouples see Table 4) in a way similar to 1150 mm elevation. From 2823 s the arithmetic mean of the smoothed TIT A/13 (corner rod thermocouple) and TCRC 13 data sets were considered as such basis.

At the elevation 850 mm ([Figs. 112 and 113](#)) the TFS 2/12 B, TFS 3/12 B and TFS 5/12 data were used as basis for the average temperature TFS 12 up to 3236 s (failure of the last of these thermocouples). After 3236 s the data of corner rod thermocouple TIT D/12 were considered as such basis.

At the elevation 750 mm ([Figs. 114 and 115](#)) the average temperature TFS 11 was determined as arithmetic mean of smoothed TFS 2/11 B, TFS 4/11 and TFS 5/11 data up to the moment 2900 s (failure of TFS 4/11 and TFS 5/11 thermocouples). After 2900 s the data of TFS 2/11 were considered as the basis for TFS 11.

At the elevations from 650 mm to -250 mm all the TFS thermocouples survived throughout the test. That is why the average temperatures at these elevations were determined as arithmetic mean of the corresponding smoothed TFS curves.

The calculated average temperature curves representing temperature evolution of the bundle at 17 elevations from 1350 mm to -250 mm are given in [Figs. 116 and 117](#). These curves were used as the boundary conditions for the effective channel walls in the S/Q code simulation of the QUENCH-08 test described below.

8.3.3 Experimental Data Analysis

As one can see from [Figs. 117 and 118](#), TFS-type thermocouples located at high elevations (above 950 mm) and the ones located below 950 mm show opposite tendencies starting from the cooling phase initiation at 3776 s. Upper thermocouples demonstrate rapid heating, whereas the lower part of the bundle experienced relatively slow cooling.

Possible Steam Starvation

One of the main reasons that could lead to such different behavior is a possible partial steam starvation during some time period just before cooldown initiation. As it was shown in recent works on FZK steam starvation tests simulation by the S/Q code [20], even short-term steam starvation transforms Zr oxide to completely non-stoichiometric one with flat oxygen profile

(oxygen atomic concentration is equal to oxide/metal boundary value). Simulation of a possible steam starvation effect on the bundle behavior performed earlier [21] has demonstrated that under certain conditions (involving oxide thickness and temperature values at a given elevation) this may lead to sharp temperature escalation at the moment of quenching initiation.

Let us suppose that during some time period before cooldown initiation practically all steam injected in the bundle was consumed by oxidizing cladding and shroud in the lower part of the bundle (at the elevations up to 950 mm). Then, during this time period the upper part of the bundle should experience steam starvation.

Before cooldown initiation the heat balance at the elevations below 950 mm was determined by (i) electrical heating and heat release due to oxidation (positive contribution) and (ii) heat flow to the gas mixture (negative contribution). The temperatures at the different elevations increased slowly (Fig. 118). What changed at the elevations below 950 mm after the beginning of cooldown? Since in this part of the bundle there was enough steam before cooldown, nothing had changed with respect to cladding oxidation – the boundary condition at the steam/oxide interface remained the same (stoichiometric). That is why heat release due to oxidation also remained the same. The electric heating has been slowly increasing with 6 W/s (total bundle value).

As for the heat losses, due to increased velocity of gas flow (from 2.5 to 8.5 m/s at the bundle inlet) it appeared at the hot part of the bundle with lower temperature (in comparison with pre-cooldown time period). This led to an increase in heat flow from the bundle components to the steam. So, one can see that the heat balance at the lower part of the bundle (practically the same heat release rate and increased heat losses) is shifted toward cooling. The last conclusion is completely confirmed by experimental results (Fig. 118).

According to our assumption, at the elevations above 950 mm heat release due to oxidation was absent before cooldown initiation and heat balance was determined by electrical heating and heat flow to the gas mixture. What had changed in the upper part of the bundle after the beginning of cooldown? Due to the recovery of steam atmosphere, the oxidation process started with higher reaction rate (in comparison with steady-state oxidation at lower elevations) and, consequently, higher heat release rate. Under some conditions the heat release due to oxidation can exceed heat losses and the upper part of the bundle will heat up. One may think that this is the case in the bundle test under consideration (Fig. 117).

However, the fact that steam starvation took place over some period of time must be confirmed by MS data. As one can see from [Fig. 119](#), the amount of steam consumed by the oxidizing bundle gradually increased during the transient phase up to cooldown initiation, i.e. 3240-3776 s. Nevertheless, this amount did not exceed one half of the total steam injected in the bundle. Thus, the assumption about temporary steam starvation comes into question.

Shroud Failure Effect

One fact seems to be able to improve the situation. At approximately 3765 s, i.e. 11 s before cooldown initiation (3776 s) shroud failure occurred at about 950-1050 mm elevation. As a

result of this failure, some part of the gas mixture (steam/argon) appeared outside the bundle. If the amount of steam emerged from the bundle was sufficiently high, this could lead to steam starvation at the upper elevations (however, rather short-term, ~10 s) before cooldown.

As for the MS readings, one can suppose that such a short-term variation of the gas mixture composition was “eroded” on its way to the GAM 300 location due to possible steam condensation in the off-gas pipe. We should note here that MS response function, which determines the difference of the gas mixture composition at the bundle outlet and at the GAM 300 location, is not known. This response function may be estimated by a special S/Q code calculation in which the gas flow in the off-gas pipe is modelled.

Direct estimation of the amount of the emerged steam is rather complicated due to uncertainties in shroud breach size in the time period of interest, local pressure distribution, presence of ZrO₂ fiber insulation etc. Posttest measurements of the oxide thickness on the *outer* surface of the shroud (up to 720 μm at 950 mm, polar angle 0°; 400-600 μm at 1000 mm, polar angle 270-320°) point to considerable value of steam.¹

On the other hand, the analysis of the system pressure time evolution (Figs. 120 and 121) shows that pressure outside the shroud (measured by P 406 device) was higher than the pressure inside the bundle (devices P 511 and P 512) up to the moment of cooldown initiation. According to these pressure measurements data, one can conclude that during the time period between shroud failure moment and cooldown beginning gas flow was directed into the bundle and thus, steam did not emerged from the bundle and no starvation took place. Conversely, ‘margin of safety’ of such conclusion is very small (the P 406 curve becomes lower than P 511 one in just 1.4 s after cooldown initiation!) and even slight pressure measurement errors (or time shift between curves) can invert the situation.

Heating-up Due to Oxidation of the Outer Shroud Surface

After shroud failure the oxidation of its outer surface began, leading to additional heat release that affected the heat balance at the upper elevations. Since shroud temperature at the location of failure was rather high (for example, 1980 K at 950 mm (TSH 13/270 I data)) and its outer surface was unoxidized, corresponding heat release was considerable. Could it shift the heat balance toward heating and thus ‘triggered’ temperature escalation? In Fig. 24 the averaged TFS curves together with the TSH ones at the elevations 1350, 1250, 1150 and 950 mm are presented. As one can see, shroud thermocouples TSH 16/0 I, TSH 15/0 I, TSH 15/0 I and TSH 14/270 I curves demonstrate a much slower increase in comparison with the rod TCs TFS 17, TFS 16 and TFS 15, without any evidence of sharp escalation at the moment of cooldown initiation. We note here, that the shroud TCs are located at its outer

¹ We note here that when comparing the above oxide thicknesses with the ones inside the bundle, one should remember that the shroud outer surface was oxidized starting from the shroud failure moment, not during the whole test.

surface and should react immediately in the case of intensive oxidation heat release at this surface (However, the shroud insulation could prevent steam influx).

The only exception are TSH 13/270 I data (upper curve in [Fig. 122](#)), depicting a temperature escalation. However, this took place 13 s *before* cooldown initiation, i.e. at 3763 s test time. This escalation may be correlated with the shroud failure which occurred approximately at the same moment (see the above section). Then, one can assume that probably there was some steam flow *from* the bundle through the shroud breach starting from the very moment of shroud failure, in spite of the system pressure data (Figs. 120 and 121). Generally, this assumption counts in favor of steam starvation hypothesis.

As for the temperature escalation caused the oxidation of the shroud outer surface at the upper part of the bundle, the available shroud TC data do not provide enough reason for such a conclusion. A slow heat-up of the shroud detected by TSH thermocouples can change the heat balance and lead to slow increasing of the bundle temperature, but not to the observed temperature escalation.

Heat Transfer by Gas Flow

One more reason that could lead to a different behavior of the upper and the lower parts of the bundle is a possible heat transfer from the bundle hot region to the upper elevations by the gas flow. Heat flow between bundle components and gas is given by the following expression:

$$q = Nu \cdot \lambda \cdot \frac{\Delta T}{D}, \quad (1)$$

where λ is the gas thermal conductivity, ΔT is the temperature difference and D is effective hydraulic diameter. Nusselt number Nu depends on Reynolds Number

$$Re = \frac{\rho U D}{\eta} \quad (2)$$

(ρ is the density, U is velocity, η is the viscosity of the gas). In the case of laminar flow

$$Nu = const \quad (Re < 2000), \quad (3)$$

and in turbulent regime

$$Nu \propto Re^{0.8} \quad (Re > 2000 \div 4000). \quad (4)$$

For the flow in a channel with constant cross-section gas velocity is proportional to the value of gas temperature, $U \propto T$. Density ρ is inversely proportional to the gas temperature, $\rho \propto 1/T$. Thus, their product ρU does not depend on temperature. As for viscosity, it increases with the temperature. So, the higher the temperature of the gas is the lower is the Reynolds number of the gas along the bundle.

Estimations of the Reynolds number based on the available correlations for the case of lengthwise (co-axial) flow in the bundle of cylindrical rods show that at the bundle inlet (where gas temperature is low and correspondingly, Reynolds number has its maximum value) Reynolds number is 600-700 in the pre-oxidation phase and 1600-1700 at the cooldown phase of the test.

As one can see, in the QUENCH-08 test the laminar flow regime was predominant during the whole test. That is why, according to relations (1) and (3), heat flow between bundle components and gas is proportional to the value of the temperature difference ΔT (with small correction for temperature dependence of the thermal conductivity) at all the elevations.

Let us consider Fig. 123 were the time derivatives of the averaged temperatures (from Figs. 20-21) dT/dt are presented. As we see, time derivatives of the upper temperature curves (TFS 17, TFS 16, and TFS 15) have much higher peak values at the cooldown initiation in comparison with the lower ones (up to 5 times!). Since temperature time derivative (absolute value) is proportional to the heat flow (and, consequently, temperature difference),

$$\left| \frac{dT}{dt} \right| \propto q \propto \Delta T ,$$

one could conclude, that temperature difference between gas and rods at higher elevation (where gas was hotter than rods) should be up to 5 times higher than such difference at lower elevations (where gas was colder than rods), in order to provide the observed temperature escalation. This conclusion generally contradicts to numerous results of the QUENCH bundle simulation (and results of the present simulation as well, see below).

In addition, the fact that the derivative curves of the lower TCs look similar to each other (while starting the cooldown from temperatures in the range 1000-1650 K) and quite different to the upper curves indirectly indicates to different mechanisms of temperature evolution at lower and upper parts of the bundle.

Summing up qualitative analysis of the experimental data could lead to the conclusion, that neither steam starvation effect nor shroud outer surface oxidation, nor heat transfer by the gas flow are able to explain the temperature escalation at higher elevations without serious contradictions with other experimental data. However, partial steam starvation hypothesis seems to be the most credible speculation since its possibility is indirectly confirmed by the discussed above correlation between shroud failure and temperature escalation detected by TSH 13/270_I thermocouple.

It should be emphasized that in the absence of direct information about gas mixture composition in the bundle it is not possible to reproduce all the details of the bundle test under consideration neither by a S/Q code "effective channel" approach nor by full-scale simulation with the help of a system code like SCDAP/RELAP.

8.3.4 QUENCH-08 Bundle Test Simulation

Effective Channel Parameter Determination

The parameters of the effective channel in the present calculation were determined in the same way as for the QUENCH-07 test simulation [19].

The following bundle parameters were used for the channel determination:

Shroud inner diameter $D_{sh} = 80.0$ mm;

Rod outside diameter $D_r = 10.75$ mm;

Corner rod diameter $D_t = 6.0$ mm;

Number of rods $N_r = 21$;

Number of corner rods $N_t = 4$.

The total bundle cross-section is given by the expression:

$$A_{tot} = \frac{1}{4} \pi \cdot D_{sh}^2 - N_r \cdot \frac{1}{4} \pi \cdot D_r^2 - N_t \cdot \frac{1}{4} \pi \cdot D_t^2. \quad (5)$$

The value of A_{tot} is equal to 30.07 cm².

The value of the channel cross-section per one rod is equal to

$$A_{eff} = \frac{A_{tot}}{N_r + N_t} = 1.203 \text{ cm}^2. \quad (6)$$

The effective channel inner radius is connected with the value of A_{eff} by:

$$\pi R_{eff}^2 - \frac{1}{4} \pi D_r^2 = A_{eff} \Rightarrow R_{eff} = \sqrt{\frac{A_{eff}}{\pi} + \frac{D_r^2}{4}} = 8.197 \text{ mm}. \quad (7)$$

The effective hydraulic diameter is then given by:

$$h = \frac{A_{eff}}{\pi \cdot D_r} = 3.562 \text{ mm}. \quad (8)$$

Main Assumptions Used for the QUENCH-08 Bundle Test Simulation

The average temperature field around the central rod, determined above was used as boundary conditions for the heat exchange problem.

On the basis of the effective channel parameters specified in the previous section, the argon and steam mass flows at all the test phases were determined. By definition, inlet gas flow in the effective channel is connected with the total inlet gas flow by:

$$J_{eff} = J_{tot} \frac{A_{eff}}{A_{tot}} . \quad (9)$$

The value of the argon total inlet flow rate J_{tot}^{Ar} was specified to be constant and equal to 2.96 g/s (based on F 401 data). Since inlet steam flow rate varied significantly during the test, the readings of F 205 (flow rate steam 10 g/s) from the beginning of the test to the cooldown initiation (3776 s) and F 204 (flow rate steam 50 g/s) from the cooldown initiation to the end of the test were used directly in the S/Q code input file. Also the reading of T 511 (gas temperature at bundle inlet) was used there.

Time step values were:

- 1.0 s up to 3500 s,
- 0.1 s up to 3750 s,
- 0.02 s up to 3900 s,
- 0.1 s up to 3950 s,
- 1.0 s up to the end of the calculation.

The bundle nodalization is characterized by the following values:

Heat conduction module

| | |
|--|-----|
| Number of total nodes in the radial direction: | 35 |
| Number of pellet nodes in the radial direction: | 21 |
| Number of external layer (oxide) nodes: | 7 |
| Number of total nodes in the vertical direction: | 197 |

The vertical grid used in the heat conduction module is adaptive one, with maximum density in the region of the maximum temperature gradients.

The total number of meshes used by oxidation, mechanical deformation and hydrogen absorption modules was 98. The total central rod length considered was 1975 mm – from the upper point 1500 mm (adjacent to the Al₂O₃ plate thermal shield) to the lower point –475 mm (adjacent to the lower SS plate).

Oxide Thickness Axial Profile

As described above, at the elevations 1050 and 950 mm all the TFS thermocouples failed before cooldown initiation and so, TSH thermocouples data were used with certain assumptions concerning interpolation between different temperature curves (especially in the case of 1050 mm, where the TSH thermocouples also failed), averaging procedure, etc. This fact led to unknown uncertainty in the temperature distribution during the hottest period of the test.

The simulation of the QUENCH-08 test with the above described initial and boundary conditions was performed. Similarly to the QUENCH-07 test simulation [19], at first the main attention was paid to the comparison of the calculated oxide layer axial profile with the measured one. The experimental information about the oxide layer thickness is available at 3181 s when the corner rod was withdrawn, and at the end of the experiment.

Quite similar to the other quench bundle tests, the radial temperature distribution inside the bundle was generally close to uniform during the QUENCH-08 test (however, there exists some difference in the oxide thickness axial profiles of the central rod and of the heated rods (final status) pointing to temperature difference, see below). Nevertheless, comparison of the calculated central rod oxide thickness with that of corner rod oxide thickness seems to be quite reasonable.

The calculational results show that the oxide thickness was underestimated at 950 mm elevation (for the time moment 3181 s) where there was the above mentioned lack of reliable temperature information. Similar underestimation, mainly at the 950 and 1050 mm elevations, was obtained for the final status of the central rod.

In order to improve the correspondence between the real temperature around the central rod and the one used in the calculations, the correction of average temperature field in the time interval 1800-3800 s was performed. Basically, the correction procedure was based on the estimation of the dependence of the oxide layer thickness on the average temperature at a given elevation and introduction of proportional corrections to the temperature evolution curves. As in the case of the QUENCH-07 test simulation, the correction procedure was considered as artificial but acceptable, since direct information of the temperature field at some elevations is absent due to thermocouple failures.

The simulation of the QUENCH-08 test with the corrected average temperature field was performed. In [Fig. 124](#) the measured oxide layer thickness of the withdrawn corner rod and the calculated oxide layer thickness of the central rod at 3181 s are presented. In [Fig. 125](#) the measured oxide layer thickness (averaged over the heated rods) and oxide layer thickness of the central rod (final status) as well as the calculated oxide layer thickness of the central rod at 3776 s (initiation of cooldown) and calculated oxide layer thickness of the central rod (final status) are presented. One can see quite good agreement between the calculated oxide thickness and the measured one. Since oxidation kinetics strongly depends on temperature, one may conclude that the temperature regime around the central rod was reproduced adequately (in the average over test duration).

As follows from Fig. 125, practically all the oxide layer at the elevations lower 950 mm has grown before cooldown initiation. On the contrary, major part of the oxide scale at the elevations above 950 mm appeared during cooldown stage. Different oxidation kinetics correlates well with the above discussed different temperature evolution in the upper and lower parts of the bundle at the beginning of cooldown. Cooling of the lower part naturally led to the decreasing of the oxidation rate. One can say that the increased steam flow 'froze' the state of the lower part of the bundle. At the same time, fast heat up of the upper part caused intensification of oxidation and hydrogen production discussed in the following subsection.

Hydrogen Release Analysis

Due to the uniformity of the radial temperature distribution inside the bundle mentioned above, one can say that the central rod behavior represents the average behavior of the 20 heated rods and shroud in the QUENCH-08 test. Using this consideration one can extrapolate the hydrogen production results calculated for the central rod to the whole bundle [18, 19]. The total hydrogen production rate of the whole bundle \dot{m}_{bundle} is connected with calculated central rod production rate \dot{m}_{rod} by the following relation:

$$\dot{m}_{bundle} = \dot{m}_{rod} \left(N_{heated} + 1 + N_{corner} \frac{R_{corner}}{R_{rod}} + \frac{R_{shroud}}{R_{rod}} \right). \quad (10)$$

Here $N_{heated} = 20$ is the number of heated rods, $N_{corner} = 4$ is the number of corner rods, R_{corner} , R_{rod} and R_{shroud} are heated rod, corner rod and shroud radii correspondingly.

In [Fig. 126](#) hydrogen production rate calculated according to relation (10) on the basis of the S/Q code simulation (second approximation) and the experimental data are presented. As one can see, experimental curve has two peaks, one of which occurred at the very beginning of cooldown. This fact directly points to the intensification of oxidation. However, it is not clear what was cause and what effect – oxidation intensification (due to preceding steam starvation) led to temperature escalation or vice versa, upper bundle part heating-up occurred in some way led to more intensive oxidation.

The calculated hydrogen production rate curve does not correlate well with the experimental one at the cooldown phase of the test – as one may think mainly due to the above-mentioned uncertainties. However, according to the calculational results, the total amount of generated hydrogen is 81 g (40.5 g during cooldown). These values practically coincide with the experimental ones (without contribution of spacer grids and thermocouples according to [16]) the corresponding values were 79 g and 38 g.

Gas Axial Temperature Distribution

The results of the S/Q code calculation make it possible to evaluate the heat transfer by gas flow from the hot part of the bundle to the upper elevations. As it was shown above, under the QUENCH-08 test conditions, heat flow between gas and bundle components is

proportional to their temperature differences with approximately the same heat transfer coefficient at all elevations.

In [Figs. 127-129](#) the axial temperature profiles of the effective channel wall (experimental data) and gas (calculated) at the time moments 3775 s (1 s before cooldown initiation), 3780 s and 3785 s (4 and 9 s after cooldown initiation) are presented. As one can expect, after start of the cooldown, due to increased velocity, maximum temperature of the gas mixture decreased (from 2150 to 2060 K) and location of this maximum was somewhat shifted toward upper elevations. Temperature difference between hot gas and channel wall at this elevations (approximately above 1050 mm) increased considerably (compare [Fig. 127](#) and [Fig. 128](#)). Nevertheless, this difference appears to be 2-3 times *smaller* than the difference between hot wall and colder gas at lower elevations.

As it was shown above, the temperature escalation observed in the QUENCH-08 test could be explained by the gas heat transfer if the temperature difference between hot gas and bundle components at the upper elevations would be 3-5 times *higher* than the temperature difference between hot bundle and gas at lower elevations. As one can see from [Figs. 30-32](#), this assumption about temperature differences is in obvious contradiction with the S/Q code calculation results. Thus, temperature escalation in the upper part of the bundle cannot be explained by the gas heat transfer.

8.3.5 QUENCH-08 bundle test simulation with B₄C central rod

With the help of the average temperature field used in the above-described calculation a simulation of imaginary bundle test with the QUENCH-08 temperature history and B₄C central rod was performed. In the calculations, the modified version of B₄C oxidation model was used. In this modified model the presence of the new chemical component – the trimer of metaboric acid (H₃B₃O₆) along with H₃BO₃ and HBO₂ is accounted for. The results of such calculation are presented below².

Calculated CO₂, CO and H₂ mass flow rates from the central rod are given in [Fig. 130](#); calculated B₂O₃, H₃BO₃, HBO₂ and H₃B₃O₆ mass flow rates are shown in [Fig. 131](#). The calculated mass flow rate values correspond to the temperature of the gas mixture at the bundle outlet (gradually varying during the test). Since chemical composition of the gas mixture strongly depends on temperature, direct comparison of the calculated results with the GAM300 experimental data (which is kept at 110-120 °C) is not possible.

However, the total amount of carbide release estimated in accordance with following relation

$$\dot{m}_C = \dot{m}_{CO_2} \frac{M_C}{M_C + 2M_O} + \dot{m}_{CO} \frac{M_C}{M_C + M_O} + \dot{m}_{CH_4} \frac{M_C}{M_C + 4M_H} \quad (11)$$

² The model of B₄C-Zr-SS interactions has not been yet implemented in the S/Q code. Therefore, it was assumed that the cladding was absent and B₄C pellets were exposed to steam flow throughout the whole test. This assumption is not realistic enough and leads to some overestimation of the 'total carbide release'.

does not change whatever chemical reactions involving CO₂, CO and CH₄ take place in the gas mixture under consideration. In [Fig. 132](#) the calculated total carbide release for QUENCH-08 (virtual) and QUENCH-07 [19] are presented. Time scale of the QUENCH-07 data was shifted by 212 s in order to have in line the moments of cooldown initiation (3564 s in QUENCH-07 and 3776 s in QUENCH-08). As one can see, the QUENCH-07 curve lies much higher than the QUENCH-08 one. This can be naturally explained by higher temperatures in QUENCH-07 test.

According to the B₄C oxidation BOX tests results [22], oxidation reaction rate is proportional to steam partial pressure. This fact is accepted as one of the main assumptions of the S/Q code B₄C oxidation model. After start of cooldown partial pressure of steam increases and this results in the intensification of B₄C oxidation. This is well reflected by both QUENCH-07 and QUENCH-08 curves.

In [Table 15](#) the calculated total amount of different components released by oxidation of B₄C during the QUENCH-07 and QUENCH-08 test are presented.

The QUENCH-08 values are generally smaller than the QUENCH-07 ones due to lower temperatures. The ratio of the QUENCH-07/QUENCH-08 values is explained by different temperature histories of the tests. We also notice substantial redistribution of the B-containing components in favor of newly introduced H₃B₃O₆ acid.

The amount of methane is negligibly small in both cases; however according to equiTherm chemical equilibriums database one could expect the increase of this value at lower temperatures.

The amount of released hydrogen is higher than that from the Zr/ZrO₂ central rod (2.53 g), however it is rather small in comparison with total calculated and experimental value (about 80 g).

Release of 5.71 g of carbon means that $5.29/12 = 0.476$ moles of B₄C were oxidized during the test. Total heat release due to B₄C oxidation (at the pellets surface) may be evaluated using the value of 768 kJ/mol for this reaction [23]:

$$Q_{B_4C} = 768 \cdot 0.476 = 365.4 \text{ (kJ)}. \quad (12)$$

The value corresponds to 635.5 kJ in the QUENCH-07 calculation. This value should be compared with the total chemical heat release which may be estimated on the basis of the total hydrogen generation of the QUENCH-08 test. The value of 84 g of released hydrogen means 42 atomic moles of oxygen involved in the bundle oxidation. Assuming that heat effect of bundle oxidation is 300 kJ/mol one has:

$$Q_{total} = 300 \cdot 42 = 12600 \text{ (kJ)}, \quad (13)$$

compared to 27300 kJ in the case of the QUENCH-07 test. I.e. B₄C oxidation contribution is only 2.9 % of the total heat release (2.3 %, QUENCH-07 test).

Thus, one can conclude that like QUENCH-07 test, not with respect to hydrogen production neither concerning heat release did B₄C central rod contribute substantially to heat release and hydrogen production. One may think that the main effect of B₄C central rod on the bundle behavior is connected with liquid B₄C-Zr and B₄C-SS eutectics formation, their early relocation and flow channels blockage.

As the SVECHA/QUENCH code works with a so-called 'effective channel approach' it cannot simulate the above processes for an entire test bundle. An estimation of the integral influence of the B₄C-Zr and B₄C-SS eutectic formation was performed by IRSN Cadarache with the integral ICARE/CATHARE computer code by comparing the QUENCH-07 temperature history with that of a virtual QUENCH-07 bundle without B₄C absorber. The results presented in [24] show an additional hydrogen release of 26 g due to the presence of B₄C absorber in the QUENCH-07 bundle. Seven of the 26 g are caused by the oxidation of the control rod (including the stainless steel cladding and the Zircaloy guide tube), and **19** of the 26 g are due to *indirect* effects such as additional melting due to eutectic formation.

8.3.6 Summary and Conclusions

- The experimentally measured temperatures of the heated rods were processed, smoothed and then used as boundary conditions (average temperature field) for the central rod.
- Different temperature evolutions of the upper and lower parts of the bundle after cooldown initiation were analyzed in terms of heat balance. Slow cooling of the lower part of the bundle correlates well with the qualitative consideration about increased heat flow to the gas mixture at nearly unchanged oxidation heat release.
- Several hypotheses were proposed in order to explain sharp temperature escalation at the upper part of the bundle. Among them: partial steam starvation during some time period just before cooldown initiation, shroud failure effect on the gas mixture composition, additional heat release due to shroud outer surface oxidation, heat transfer by gas flow to the upper elevations.
- None of these hypotheses is able to explain the temperature escalation at higher elevations without serious contradictions with other experimental data or calculational results. However, steam starvation hypothesis seems to be the most credible speculation indirectly confirmed by the correlation between shroud failure and temperature escalation detected by TSH 13/270 I thermocouple pointing to gas flow from the bundle before cooldown initiation.
- The simulation of the QUENCH-08 test using averaged temperature field was performed. Correction of the temperatures performed in order to control the uncertainties introduced by thermocouples failure at 950 and 1050 mm allowed adequate reproduction of the temperature field around the central rod (average over test duration) and satisfactory

agreement of the measured and calculated oxide scale axial profiles at 3181 s (withdrawal of corner rod B) and at the end of the test.

- The total amount of generated hydrogen was evaluated as 81 g (40.5 g during cooldown). These values practically coincide with the experimental ones (79 g and 38 g, correspondingly). However, calculated hydrogen production rate curve does not correlate well with the experimental one at the cooldown stage of the test mainly due to the uncertainties in the nature of temperature escalation of the upper part of the bundle. Such uncertainties lead to a more pronounced difference between SVECHA calculations and experiment in the case of QUENCH-07: calculated total hydrogen production was 115 g [19] and the corresponding experimental value was 152 g (without contribution of Mo electrodes, grid spacers and thermocouples as was documented in [16]).
- The simulation of the imaginary bundle test with the QUENCH-08 temperature history and B₄C central rod was performed. Data concerning release rate of B₄C oxidation products were analyzed and compared with the QUENCH-07 simulation results.
- QUENCH-08 values are generally smaller than QUENCH-07 ones due to lower temperatures. The ratio of the QUENCH-07/QUENCH-08 values is explained by different temperature histories of the tests.
- Like the results of the QUENCH-07 test simulation, the amount of produced hydrogen in the last calculation for the virtual QUENCH-08 test, i.e. 7.46 g from the control rod, is higher than that from the Zr/ZrO₂ central rod (2.53 g). It is, however, rather small in comparison with the experimental value, i.e. 84 g of H₂ in total. The estimated amount of heat released due to B₄C oxidation is also small in comparison with the total chemical heat release (2.9 %). Thus, one could conclude that the main effect of B₄C central rod on the bundle behavior is connected with liquid B₄C-Zr and B₄C-SS eutectics formation, their early relocation and flow channels blockage.

References

- [1] J.M. Broughton, P. Kuan, and D.A. Petti, "A Scenario of the Three Mile Island Unit 2 Accident," *Nuclear Technology*, Vol. 87, p. 34, 1989.
- [2] P. Hofmann, S. Hagen, V. Noack, G. Schanz, L. Sepold, "Chemical-Physical Behavior of Light Water Reactor Core Components Tested under Severe Reactor Accident Conditions in the CORA Facility," *Nuclear Technology*, Vol. 118, p. 200, 1997.
- [3] S. Hagen, P. Hofmann, V. Noack, L. Sepold, G. Schanz, G. Schumacher, "Comparison of the Quench Experiments CORA-12, CORA-13, CORA-17," FZKA 5679, Forschungszentrum Karlsruhe, 1996.
- [4] S.M. Modro and M.L. Carboneau, "The LP-FP-2 Severe Fuel Damage Scenario; Discussion of the Relative Influence of the Transient and Reflood Phase in Affecting the Final Condition of the Bundle," OECD/LOFT Final Event, ISBN 92-64-03339-4, p. 388, 1991.
- [5] B. Clement, N. Hanniet-Girault, G. Repetto, D. Jacquemain, A.V. Jones, M.P. Kissane, P. von der Hardt, "LWR Severe Accident Simulation: Synthesis of the Results and Interpretation of the First Phebus FP Experiment FPT 0," *Nuclear Engineering and Design*, Vol. 226, Issue 1, P. 5-82, 2003
- [6] T.J. Haste, B. Adroguer, U. Brockmeier, P. Hofmann, K. Müller, M. Pezzilli, "In-Vessel Core Degradation in LWR Severe Accidents," Final Report eUR 16695, European Commission, 1996.
- [7] P. Hofmann, "Current Knowledge an Core Degradation Phenomena a Review," *J. Nuclear Materials* 270, pp. 194-211, 1999.
- [8] L. Sepold, A. Miassoedov, G. Schanz, U. Stegmaier, M. Steinbrück, J. Stuckert, C. Homann, "Hydrogen Generation in Reflooding Experiments with LWR-type Rod Bundles (QUENCH Program)," *Journal Nuclear Technology*, Vol. 147, pp. 202-214, 2004.
- [9] P. Hofmann, V. Noack, M.S. Veshchunov, A.V. Berdyshev, L.V. Matweev, A.V. Palagin, V.E. Shestak: „Physico-Chemical Behavior of Zircaloy Fuel Rod Cladding Tubes During LWR Severe Accident Reflood," FZKA 5846, Forschungszentrum Karlsruhe, 1997.
- [10] P. Hofmann, A. Miassoedov, L. Steinbock, M. Steinbrück, M. Veshchunov et al.: "Quench Behavior of Zircaloy Fuel Rod Cladding Tubes. Small-Scale Experiments and Modeling of the Quench Phenomena," FZKA 6208, Forschungszentrum Karlsruhe, 1999.
- [11] J. Stuckert, M. Steinbrück, U. Stegmaier, "Single Rod Quench Tests with Zr-1Nb. Comparison with Zircaloy-4 Cladding Tests and Modelling," FZKA 6604, Forschungszentrum Karlsruhe, 2001.

-
- [12] Ch. Homann, W. Hering, G. Schanz, "Analysis and Comparison of Experimental Data of QUENCH-07 to QUENCH-09 about B₄C Control Rod Behaviour," FZKA 7101, in preparation.
- [13] M. Steinbrück (editor), 9th International QUENCH Workshop at Forschungszentrum Karlsruhe, Oct. 13-15, 2003, CD-ROM, Forschungszentrum Karlsruhe, 2003.
- [14] M. Steinbrück, C. Homann, A. Miassoedov, G. Schanz, L. Sepold, U. Stegmaier, H. Steiner, J. Stuckert, "Results of the B₄C Control Rod Test QUENCH-07," FZKA 6746, Forschungszentrum Karlsruhe, 2004.
- [15] M. Steinbrück, A. Miassoedov, G. Schanz, L. Sepold, U. Stegmaier, H. Steiner, J. Stuckert, "Results of the QUENCH-09 Experiment with a B₄C Control Rod," FZKA 6829, Forschungszentrum Karlsruhe, 2004.
- [16] M. Steinbrück, "Analysis of Hydrogen Production in QUENCH Bundle Tests," FZKA 6968, Forschungszentrum Karlsruhe, 2004.
- [17] P. Hofmann, Ch. Homann, W. Leiling, A. Miassoedov, D. Piel, G. Schanz, L. Schmidt, L. Sepold, M. Steinbrück, "Experimental and Computational Results of the Experiments QUENCH-02 and QUENCH-03," FZKA 6295, Forschungszentrum Karlsruhe, 2000.
- [18] L. Sepold, P. Hofmann, C. Homann, W. Leiling, A. Miassoedov, D. Piel, G. Schanz, L. Schmidt, U. Stegmaier, M. Steinbrück, H. Steiner, A.V. Palagin, A.V. Boldyrev, M.S. Veshchunov, A.V. Berdyshev, V.E. Shestak, "Investigation of an Overheated PWR-Type Fuel Rod Simulator Bundle," FZKA 6412, Forschungszentrum Karlsruhe, 2001.
- [19] M.S. Veshchunov, A.V. Berdyshev, A.V. Boldyrev, A.V. Palagin, V.E. Shestak, M. Steinbrück, J. Stuckert. "Modelling of B₄C oxidation by steam at high temperatures based on separate-effects tests and its application to the bundle experiment QUENCH-07," FZKA 7118, Forschungszentrum Karlsruhe, Juni 2005.
- [20] A.V. Palagin, J. Stuckert, unpublished, 2003.
- [21] M.S. Veshchunov, A.V. Berdyshev, A.V. Boldyrev, A.V. Palagin, V.E. Shestak, unpublished, 2002.
- [22] M. Steinbrück, A. Meier, U. Stegmaier, L. Steinbock, "Experiments on the Oxidation of Boron Carbide at High Temperatures", FZKA 6979, Forschungszentrum Karlsruhe, 2004.
- [23] I. Barin, O. Knacke, "Thermochemical properties of inorganic substances," Springer Verlag, 1973.
- [24] N. Seiler and F. Bertrand, "Analysis of QUENCH Test Including a B₄C Control Rod with the ICARE/CATHARE Code and B₄C Modelling Assessment," The 11th International Topical Meeting on Nuclear Thermal-Hydraulics (NURETH-11), Avignon, France, Oct. 2-6, 2005.

Acknowledgements

At the Karlsruhe Research Center the broad support needed for preparation, execution, and evaluation of the experiment is gratefully acknowledged. In particular, the authors would like to thank Messrs. L. Anselment and S. Horn for the assembly of the heated test rods, Mr. Horn for the preparation of the hydrogen measurement with the "Caldos" analyzer and the various support. The determination of the test conduct was based on numerous pretest calculations with the FZK/IRS version of SCDAP/RELAP5 performed by Drs. Ch. Homann and W. Hering. Furthermore, the authors would like to express their gratitude to Mrs. J. Laier for processing the test data, and to Mrs. M. Heck for elaborately processing the results of the metallographic examination.

Table 1: QUENCH test matrix

| Test | Quench medium | Flooding rate ¹⁾ | Heat-up rate | Temp. at onset of flooding ²⁾ | Max. ZrO ₂ after preoxidation ³⁾ | Max. ZrO ₂ layer thickness ⁴⁾ | H ₂ production before / during cooldown | Remarks, objectives |
|-------------------------------------|---------------|------------------------------|--------------|--|--|---|--|---|
| QUENCH-00 Oct. 9 - 16, 97 | Water | 2.8 cm/s from the bottom | 1.0 K/s | ≈ 1800 K | | ≈ 500 μm | | COBE Project; commissioning tests. |
| QUENCH-01 February 26, 98 | Water | 1.6 cm/s; from the bottom | 0.5 K/s | ≈ 1900 K | 312 μm | ≈ 580 μm | 36 / 3 | COBE Project; partial fragmentation of pre-oxidized cladding. |
| QUENCH-02 July 7, 98 | Water | 1.6 cm/s; from the bottom | 0.5 K/s | > 2400 K | | completely oxidized | 20 / 140 | COBE Project; no additional pre-oxidation; quenching from high temperatures. |
| QUENCH-03 January 20, 99 | Water | 1.4 cm/s from the bottom | 0.6 K/s | > 2400 K | | completely oxidized | 18 / 120 | No additional pre-oxidation, quenching from high temperatures. |
| QUENCH-04 June 30, 99 | Steam | ≈ 50 g/s; from the bottom | 0.5 K/s | ≈ 2300 K | 82 μm | ≈ 170 μm | 10 / 2 | Cool-down behavior of slightly pre-oxidized cladding by cold steam injection. |
| QUENCH-05 March 29, 2000 | Steam | ≈ 50 g/s from the bottom | 0.5 K/s | ≈ 2300 K | 160 μm | ≈ 400 μm | 25 / 2 | Cool-down behavior of pre-oxidized cladding by cold steam injection. |
| QUENCH-06 Dec. 13 2000 | Water | 1.4 cm/s from the bottom | 0.5 K/s | ≈ 2300 K | 207 μm | ≈ 660 μm | 32 / 4 | OECD-ISP 45; prediction of H ₂ source term by different code systems. |
| QUENCH-07 July 25, 2001 | Steam | ≈ 15 g/s from the bottom | 0.5 K/s | > 2300 K | 230 μm | completely oxidized | 66 / 120 | COLOSS Project; impact of B ₄ C absorber rod failure on H ₂ , CO, CO ₂ , and CH ₄ generation. |

| Test | Quench medium | Flooding rate ¹⁾ | Heat-up rate | Temp. at onset of flooding ²⁾ | Max. ZrO ₂ after preoxidation ³⁾ | Max. ZrO ₂ layer thickness ⁴⁾ | H ₂ production before / during cooldown | Remarks, objectives |
|-----------------------------------|---------------|------------------------------|--------------|--|--|---|--|---|
| QUENCH-09 July 3, 2002 | Steam | ≈ 50 g/s; from the bottom | 0.5 K/s | ≈ 2500 K | | completely oxidized | 60 / 400 | As QUENCH-07, steam-starved conditions prior to cooldown. |
| QUENCH-08 July 24, 2003 | Steam | ≈ 15 g/s; from the bottom | 0.5 K/s | > 2100 K | 274 μm | completely oxidized | 46 / 38 | As QUENCH-07, no absorber rod |

¹⁾ Flooding rate for water: rise of the water level at the -250 mm bundle elevation (single-phase flow).

²⁾ Maximum measured or estimated temperature in test section.

³⁾ Measured at the withdrawn corner rod

⁴⁾ Measured posttest at the bundle elevation of max. temperature.

Revised: July, 2005

Table 2: Design characteristics of the QUENCH-08 test bundle

| | | |
|------------------------------|--|---|
| Bundle type | | PWR |
| Bundle size | | 21 rods |
| Number of heated rods | | 20 |
| Number of unheated rods | | 1 |
| Pitch | | 14.3 mm |
| Rod outside diameter | | 10.75 mm |
| Cladding material | | Zircaloy-4 |
| Cladding thickness | | 0.725 mm |
| Rod length | heated rod (levels) unheated rod (levels) | 2480 mm (-690 mm to 1790 mm) 2842 mm (-827 mm to 2015 mm, incl. extension piece) |
| Heater material | | Tungsten (W) |
| Heater length | | 1024 mm |
| Heater diameter | | 6 mm |
| Annular pellet | material heated rod unheated rod | ZrO ₂ ;Y ₂ O ₃ -stabilized Ø 9.15/6.15 mm; L=11 mm Ø 9.15/2.5 mm; L=11 mm |
| Pellet stack | heated rod unheated rod | 0 mm to ~ 1020 mm 0 mm to 1553 mm |
| Corner rod | material instrumented solid (rod B) | Zircaloy-4, total length=2440 mm tube Ø 6x0.9 (bottom: -1140 mm) rod Ø 6 mm (top: +1300 mm) |
| Grid spacer | material length location of lower edge | Zircaloy-4, Inconel 718 Zry 42 mm, Inc 38 mm -200 mm Inconel 50 mm Zircaloy-4 550 mm Zircaloy-4 1050 mm Zircaloy-4 1410 mm Zircaloy-4 |
| Shroud | material wall thickness outside diameter length (extension) | Zircaloy-4 2.38 mm 84.76 mm 1600 mm (-300 mm to 1300 mm) |
| Shroud insulation | material insulation thickness elevation | ZrO ₂ fiber ~ 37 mm -300 mm to ~1000 mm |
| Molybdenum-copper electrodes | length of upper electrodes length of lower electrodes diameter of electrodes: - prior to coating - after coating with ZrO ₂ | 766 mm (576 Mo, 190 mm Cu) 690 mm (300 Mo, 390 mm Cu) 8.6 mm 9.0 mm |
| Cooling jacket | Material: inner/outer tube inner tube outer tube | Inconel 600 (2.4816)/SS (1.4571) Ø 158.3 / 168.3 mm Ø 181.7 / 193.7 mm |

Table 3: List of instrumentation for the QUENCH-08 Test

| Channel | Designation | Instrument, location | Output in |
|---------|--------------|---|--------------------|
| 0 | TCR 13 | TC (W/Re) central rod, cladding, 950 mm | K |
| 1 | | Reserve | |
| 2 | TFS 2/13 | TC (W/Re) fuel rod simulator 2 (type 2), 950 mm, 225° | K |
| 3 | TFS 2/15 | TC (W/Re) fuel rod simulator 4 (type 2), 1150 mm, 315° | K |
| 4 | TFS 2/17 F | TC (W/Re) fuel rod simulator 6 (type 2), 1350 mm, 45°, fluid temperature | K |
| 5 | TSH 15/180 I | TC (W/Re) shroud outer surface, 1150 mm, 206°, behind shroud insulation | K |
| 6 | TFS 3/10 | TC (W/Re) fuel rod simulator 7 (type 3), 650 mm, 135° | K |
| 7 | | Reserve | |
| 8 | TFS 3/13 | TC (W/Re) fuel rod simulator 3 (type 3), 950 mm, 315° | K |
| 9 | TFS 3/14 | TC (W/Re) fuel rod simulator 5 (type 3), 1050 mm, 45° | K |
| 10 | TFS 4/11 | TC (W/Re) fuel rod simulator 14 (type 4), 750 mm, 45° | K |
| 11 | TFS 4/13 | TC (W/Re) fuel rod simulator 20 (type 4), 950 mm, 135° | K |
| 12 | TFS 5/10 | TC (W/Re) fuel rod simulator 12 (type 5), 650 mm, 225° | |
| 13 | TFS 5/11 | TC (W/Re) fuel rod simulator 13 (type 5), 750 mm, 45° | K |
| 14 | TFS 5/12 | TC (W/Re) fuel rod simulator 15 (type 5), 850 mm, 315° | K |
| 15 | TFS 5/13 | TC (W/Re) fuel rod simulator 16 (type 5), 950 mm, 135° | K |
| 16 | TFS 5/14 | TC (W/Re) fuel rod simulator 18 (type 5), 1050 mm, 45° | K |
| 17 | TSH 16/180 I | TC (W/Re) shroud outer surface, 1250 mm, 206°, behind shroud insulation (defective) | K |
| 18 | | Reserve; TC TSH 13/90 used for long TFS 3/12 B | K |
| 19 | TSH 14/90 I | TC (W/Re) shroud outer surface, 1050 mm, 116°, behind shroud insulation | K |
| 20 | TSH 11/0 I | TC (W/Re) shroud outer surface, 750 mm, 26°, behind shroud insulation | K |
| 21 | | Reserve; TC TSH 12/0 used for long TFS 2/11 B | K |
| 22 | TFS 2/5 | TC (NiCr/Ni) fuel rod simulator 2 (type 2), 150 mm, 225° | K |
| 23 | TFS 2/7 | TC (NiCr/Ni) fuel rod simulator 6 (type 2), 350 mm, 45° | K |
| 24 | F 902 | Off-gas flow rate before Caldos (H ₂) | Nm ³ /h |
| 25 | FM 401 | Argon gas mass flow rate | g/s |
| : | | | |
| 32 | TIT A/13 | TC (W/Re) corner rod A, center, 950 mm | K |
| 33 | TCRC 13 | TC (W/Re) central rod, center, 950 mm | K |

| Chan- nel | Designation | Instrument, location | Output in |
|--------------|-----------------|--|--------------|
| 34 | TFS 2/12 B | TC (W/Re) fuel rod simulator 2 (type 2), 850 mm, 315°, bottom penetration | K |
| 35 | TSH 9/90 | TC (NiCr/Ni) shroud outer surface, 550 mm, 116° | K |
| 36 | TSH 9/270 | TC (NiCr/Ni) shroud outer surface, 550 mm, 296° | K |
| 37 | TFS 3/16 | TC (W/Re) fuel rod simulator 7 (type 3), 1250 mm, 135° | K |
| 38 | TFS 5/9 | TC (NiCr/Ni) fuel rod simulator 10 (type 5), 550 mm, 315° | K |
| 39 | TFS 2/9 | TC (NiCr/Ni) fuel rod simulator 8 (type 2), 550 mm, 135° | K |
| 40 | TIT D/12 | TC (W/Re) corner rod D, center, 850 mm | K |
| : | | Reserve | |
| 42 | TFS 5/8 | TC (NiCr/Ni) fuel rod simulator 21 (type 5), 450 mm, 135° | K |
| 43 | TFS 3/8 | TC (NiCr/Ni) fuel rod simulator 5 (type 3), 450 mm, 45° | K |
| 44 | T003 | Outlet temperature of cooling water for off-gas pipe, measurement location near condenser | K |
| : | | | |
| 46 | TIT C/9 | TC (NiCr/Ni) corner rod C, center, 550 mm | K |
| 47 | TFS 5/15 | TC (W/Re) fuel rod simulator 19 (type 5), 1150 mm, 225° | K |
| 48 | TFS 5/16 | TC (W/Re) fuel rod simulator 21 (type 5), 1250 mm, 135° | K |
| 49 | TFS 5/17 | TC (W/Re) fuel rod simulator 10 (type 5), 1350 mm, 315° | K |
| 50 | TFS 3/12 B | TC (W/Re) fuel rod simulator 9 (type 3), 850 mm nominal, 865 mm real, 225°, bottom penetration | K |
| 51 | TFS 2/11 B | TC (W/Re) fuel rod simulator 8 (type 2), 750 mm nominal, 765 mm real, 135°, bottom penetration | K |
| 52 | TSH 13/270 I | TC (W/Re) shroud outer surface, 950 mm, 296°, behind shroud insulation | K |
| 53 | TSH 14/270 I | TC (W/Re) shroud outer surface, 1050 mm, 270°, behind shroud insulation | K |
| 54 | TSH 11/180 I | TC (W/Re) shroud outer surface, 750 mm, 206°, behind shroud insulation | K |
| 55 | TSH 12/180 I | TC (W/Re) shroud outer surface, 850 mm, 206°, behind shroud insulation | K |
| : | | | |
| 61 | T 206 | Temperature before steam flow instrument location 1 g/s | K |
| 62 | P 206 | Pressure at steam flow instrument location 1 g/s | bar |
| 63 | F 206 | Flow rate steam 1 g/s | g/s |
| 64 | T 402 b | Temperature of the tube surface after gas heater | K |
| : | | | |

| Chan- nel | Designation | Instrument, location | Output in |
|--------------|-------------|--|--------------|
| 66 | TSH 15/0 I | TC (W/Re) shroud outer surface, 1150 mm, 26°, behind shroud insulation | K |
| 67 | TSH 16/0 I | TC (W/Re) shroud outer surface, 1250 mm, 26°, behind shroud insulation | K |
| 68 | T 512 | Gas temperature bundle outlet | K |
| : | | | |
| 71 | Ref. T 01 | Reference temperature 1 | K |
| 72 | TFS 2/1 F | TC (NiCr/Ni) fuel rod simulator 4 (type 2), -250 mm, 315°, fluid temperature | K |
| 73 | TCRC 9 | TC (NiCr/Ni) central rod, center, 550 mm | K |
| 74 | TFS 2/3 | TC (NiCr/Ni) fuel rod simulator 8 (type 2), -50 mm, 135° | K |
| 75 | TCRI 7 | TC (NiCr/Ni) central rod, cladding inner surface, 350 mm | K |
| 76 | TFS 2/6 F | TC (NiCr/Ni) fuel rod simulator 4 (type 2), 250 mm, 315°, fluid temperature | K |
| 77 | TCRI 9 | TC (NiCr/Ni) central rod, cladding inner surface, 550 mm | K |
| 78 | TFS 5/4/0 F | TC (NiCr/Ni) fuel rod simulator 15 (type 5), 50 mm, 315°, fluid temperature | K |
| 79 | TFS 5/4/180 | TC (NiCr/Ni) fuel rod simulator 21 (type 5), 50 mm, 135° | K |
| 80 | TCRC 7 | TC (NiCr/Ni) central rod, center, 350 mm | K |
| 81 | TFS 5/6 | TC (NiCr/Ni) fuel rod simulator 18 (type 5), 250 mm, 45° | K |
| 82 | TFS 5/7 | TC (NiCr/Ni) fuel rod simulator 19 (type 5), 350 mm, 225° | K |
| 83 | TSH 4/270 | TC (NiCr/Ni) shroud outer surface, 50 mm, 296° | K |
| 84 | TSH 3/180 | TC (NiCr/Ni) shroud outer surface, -50 mm, 206° | K |
| 85 | TSH 4/180 | TC (NiCr/Ni) shroud outer surface, 50 mm, 206° | K |
| 86 | TSH 7/180 | TC (NiCr/Ni) shroud outer surface, 350 mm, 206° | K |
| 87 | TSH 4/90 | TC (NiCr/Ni) shroud outer surface, 50 mm, 116° | K |
| 88 | TSH 1/0 | TC (NiCr/Ni) shroud outer surface, -250 mm, 26° | K |
| 89 | TSH 4/0 | TC (NiCr/Ni) shroud outer surface, 50 mm, 26° | K |
| 90 | TSH 7/0 | TC (NiCr/Ni) shroud outer surface, 350 mm, 26° | K |
| 91 | TCI 9/270 | TC (NiCr/Ni) cooling jacket inner tube wall, 550 mm, 270° | K |
| 92 | TCI 10/270 | TC (NiCr/Ni) cooling jacket inner tube wall, 650 mm, 270° | K |
| 93 | TCI 11/270 | TC (NiCr/Ni) cooling jacket inner tube wall, 750 mm, 270° | K |
| 94 | TCI 13/270 | TC (NiCr/Ni) cooling jacket inner tube wall, 950 mm, 270° | K |
| 95 | | Reserve, feed through of TCR 7 (and TFS 2/2) used for TFS 3/12 B | K |
| 96 | TCI 1/180 | TC (NiCr/Ni) cooling jacket inner tube wall, -250 mm, 180° | K |

| Chan- nel | Designation | Instrument, location | Output in |
|--------------|-------------|---|--------------|
| 97 | TCI 4/180 | TC (NiCr/Ni) cooling jacket inner tube wall, 50 mm, 180° | K |
| 98 | TCI 7/180 | TC (NiCr/Ni) cooling jacket inner tube wall, 350 mm, 180° | K |
| 99 | TCI 11/180 | TC (NiCr/Ni) cooling jacket inner tube wall, 750 mm, 180° | K |
| 100 | TCI 12/180 | TC (NiCr/Ni) cooling jacket inner tube wall, 850 mm, 180° | K |
| 101 | TCI 13/180 | TC (NiCr/Ni) cooling jacket inner tube wall, 950 mm, 180° | K |
| 102 | TCI 15/180 | TC (NiCr/Ni) cooling jacket inner tube wall, 1150 mm, 180° | K |
| 103 | T002 | Inlet temperature of cooling water for off-gas pipe, measurement location near test section (defective) | K |
| 104 | TCI 9/90 | TC (NiCr/Ni) cooling jacket inner tube wall, 550 mm, 90° | K |
| 105 | TCI 10/90 | TC (NiCr/Ni) cooling jacket inner tube wall, 650 mm, 90° | K |
| 106 | TCI 11/90 | TC (NiCr/Ni) cooling jacket inner tube wall, 750 mm, 90° | K |
| 107 | TCI 13/90 | TC (NiCr/Ni) cooling jacket inner tube wall, 950 mm, 90° | K |
| : | | | |
| 109 | TCI 1/0 | TC (NiCr/Ni) cooling jacket inner tube wall, -250 mm, 0° | K |
| 110 | TCI 4/0 | TC (NiCr/Ni) cooling jacket inner tube wall, 50 mm, 0° | K |
| 111 | TCI 7/0 | TC (NiCr/Ni) cooling jacket inner tube wall, 350 mm, 0° | K |
| 112 | TCI 11/0 | TC (NiCr/Ni) cooling jacket inner tube wall, 750 mm, 0° | K |
| 113 | TCI 12/0 | TC (NiCr/Ni) cooling jacket inner tube wall, 850 mm, 0° | K |
| 114 | TCI 13/0 | TC (NiCr/Ni) cooling jacket inner tube wall, 950 mm, 0° | K |
| 115 | TCI 15/0 | TC (NiCr/Ni) cooling jacket inner tube wall, 1150 mm, 0° | K |
| : | | | |
| 120 | TCO 1/0 | TC (NiCr/Ni) cooling jacket outer tube surface, -250 mm, 0° | K |
| 121 | TCO 7/0 | TC (NiCr/Ni) cooling jacket outer tube surface, 350 mm, 0° | K |
| 122 | TCO 13/0 | TC (NiCr/Ni) cooling jacket outer tube surface, 950 mm, 0° | K |
| 123 | T 601 | Temperature downstream F 601 (off-gas flow, orifice) | K |
| : | | | |
| 128 | T 104 | Temperature quench water | K |
| 129 | T 201 | Temperature steam generator heating pipe | K |
| 130 | T 204 | Temperature upstream steam flow instrument location 50 g/s | K |
| 131 | T 205 | Temperature upstream steam flow instrument location 10 g/s | K |
| 132 | T 301A | Temperature behind superheater | K |
| 133 | T 302 | Temperature superheater heating pipe | K |
| 134 | T 303 | Temperature upstream total flow instrument (orifice) location | K |
| 135 | T 401 | Temperature upstream gas flow instrument (orifice) location | K |

| Channel | Designation | Instrument, location | Output in |
|---------|-------------|--|------------------|
| 136 | T 403 | Temperature at inlet cooling gas | K |
| 137 | T 404 | Temperature at outlet cooling gas | K |
| 138 | T 501 | Temperature inside the containment, above elevation of bundle head | K |
| 139 | T 502 | Temperature at containment | K |
| 140 | T 503 | Temperature at containment | K |
| 141 | T 504 | Temperature at containment | K |
| 142 | T 505 | Temperature at containment | K |
| 143 | T 506 | Temperature at containment | K |
| 144 | T 507 | Temperature at containment | K |
| 145 | T 508 | Temperature at containment | K |
| 146 | T 509 | Temperature bundle head outside (wall) | K |
| 147 | T 510 | Temperature at containment | K |
| 148 | T 511 | Gas temperature at bundle inlet | K |
| 149 | T 901 | Temperature upstream off-gas flow instrument F 901 | K |
| : | | | |
| 151 | Ref. T 02 | Reference temperature 2 | K |
| 152 | P 201 | Pressure steam generator | bar |
| 153 | P 204 | Pressure at steam flow instrument location 50 g/s | bar |
| 154 | P 205 | Pressure at steam flow instrument location 10 g/s | bar |
| 155 | P 303 | Pressure before total flow instrument (orifice) location | bar |
| 156 | P 401 | Pressure upstream gas flow instrument location | bar |
| 157 | P 511 | Pressure at bundle inlet | bar |
| 158 | P 512 | Pressure at bundle outlet | bar |
| 159 | P 601 | Pressure upstream off-gas flow instrument (orifice) F 601 | bar |
| 160 | P 901 | Pressure upstream off-gas flow instrument F 901 | bar |
| 161 | L 201 | Liquid level steam generator | mm |
| 162 | L 501 | Liquid level quench water | mm |
| 163 | L 701 | Liquid level condensation vessel | mm |
| 164 | Q 901 | H ₂ concentration, off-gas (Caldos) | % H ₂ |
| 165 | P 411 | Pressure Ar-Kr supply | bar |
| 166 | P 403 | Pressure Ar cooling of cooling jacket | bar |
| 167 | P 406 | Pressure insulation shroud/cooling jacket | bar |
| 168 | F 104 | Flow rate quench water | l/h |

| Chan- nel | Designation | Instrument, location | Output in |
|--------------|-------------|---|--------------------|
| 169 | F 204 | Flow rate steam 50 g/s | g/s |
| 170 | F 205 | Flow rate steam 10 g/s | g/s |
| 171 | F 303 | Flow rate at bundle inlet (steam + argon), orifice | mbar |
| 172 | F 401 | Argon gas flow rate | Nm ³ /h |
| 173 | F 403 | Flow rate cooling gas | Nm ³ /h |
| 174 | F 601 | Flow rate off-gas (orifice) | mbar |
| 175 | F 901 | Off-gas flow rate upstream Caldos (H ₂) | m ³ /h |
| 176 | E 201 | Electric current steam generator | A |
| 177 | E 301 | Electric current superheater | A |
| 178 | E 501 | Electric current inner ring of fuel rod simulators | A |
| 179 | E 502 | Electric current outer ring of fuel rod simulators | A |
| 180 | E 503 | Electric voltage inner ring of fuel rod simulators | V |
| 181 | E 504 | Electric voltage outer ring of fuel rod simulators | V |
| 182 | Hub_V302 | Gas supply valve lift | % |
| 183 | Ref. T 03 | Reference temperature 3 | K |
| : | | | |
| 250 | E 505 | Electric power inner ring of fuel rod simulators | W |
| 251 | E 506 | Electric power outer ring of fuel rod simulators | W |
| | | | |

Remarks:

1. Tip of thermocouples TFS 2/1 F, TFS 5/4/0 F, TFS 2/6 F, TFS 2/17 F were bent into flow channel to measure the fluid temperature
2. Feed through of TFS 5/5 (and TCR 9) used for TFS 2/11 B
3. Feed through of TFS 2/2 (and TCR 7) used for TFS 3/12 B
4. Feed through of TCR 9 (and TFS 5/5) used for TFS 2/11 B
5. The cables of shroud thermocouples TSH xx/x "I" were routed to the exterior of the shroud insulation.
6. The cables of rod surface thermocouples TFS xx/x "B" were routed to the bottom (bottom penetration)

Table 4: QUENCH-08; Failure of thermocouples

| Thermocouple | Elevation [mm] | Time at failure [s] | Failure temperature [K] |
|--------------|-------------------------------------|--------------------------------|-------------------------|
| T002 | Cooling water inlet at off-gas pipe | Pretest failure | |
| TSH 16/180 I | 1250 | Pretest failure | |
| TFS 3/13 | 950 | 2607 | 1609 |
| TCR 13 | 950 | 2611 | 1632 |
| TFS 2/13 | 950 | 2674 | 1611 |
| TFS 5/13 | 950 | 2693 | 1633 |
| TFS 4/13 | 950 | 2823 | 1657 |
| TFS 3/14 | 1050 | 2922 | 1636 |
| TFS 3/12 B | 850 | 3116 | 1699 |
| TFS 4/11 | 750 | 3183 2900 (hot zone effect) | 1629 1516 |
| TFS 5/11 | 750 | 3183 2900 (hot zone effect) | 1603 1501 |
| TFS 5/12 | 850 | 3204 | 1656 |
| TFS 2/12 B | 850 | 3236 | 1672 |
| TFS 5/14 | 1050 | 3544 | 1633 |
| TSH 14/270 I | 1050 | 3816 | 2325 |
| TFS 2/15 | 1150 | 3885 | 2240 |
| TCRC 13 | 950 | 3955 | 1771 |

Table 5: QUENCH-08; Sequence of events

| Time [s] | Event |
|-------------|---|
| 0 | Start of data recording, test bundle at 873 K (TIT A/13), data acquisition frequency at 1 Hz. Oxidation steam: 3 g/s @ 783 K |
| 134 | Start of heatup from 871 K (TIT A/13) |
| 1628 | 13 kW electric power reached. TIT A/13: 1282 K |
| 2277 | Temperature of 1700 K (TIT A/13) reached. End of electric power plateau at ~13 kW |
| 3181 | Withdrawal of corner rod B |
| 3240 | Start of the transient phase (TIT A/13: 1749 K) |
| 3761 | Data acquisition frequency at 5 Hz |
| 3765 | Shroud failure according to drop of P 406 (pressure between shroud and cooling jacket) |
| 3770 | First rod failure, based on Kr detection |
| 3776-3799 | First hydrogen peak |
| 3775.5 | Cooling initiation (steam 15 g/s @ 435 K). TIT A/13: 2090 K; TSH 13/270 I: 2099 K |
| 3777 | Start of temperature escalation at elevations 15 - 17 |
| 3814 | Start of electric power reduction from 17.7 kW to 3.9 kW. TIT A/13: 2065 K |
| 3824 | Acceleration of the temperature increase on the inner surface of cooling jacket (TCI 12/0, TCI 13/270) |
| 3830 | Electric power at 3.9 kW (simulation of decay power) |
| 3836...3842 | Maximum of the temperature escalation at elevations 15 - 17 reached. TFS 2/15: 2264 K; TFS 5/16: 2144 K; TSH 16/0 I: 1957 K (TSH 13/270 I: 2175 K). Maximum of the second hydrogen peak |
| 4018 | Start of power shutoff |
| 4021 | Electric power under 0.1 kW |
| 4034.8 | Data acquisition frequency at 1 Hz |
| 4218 | Temperature maximum on cooling jacket (TCI 13/270: 555 K) |
| 4647.8 | End of data recording |

0 s = 10:15:12 h on July 24, 2003

Table 6: QUENCH-08; Maximum measured test bundle temperatures of each elevation

| | Thermocouple | Time [s] | Maximum temperature [K] |
|------|------------------------|----------------|-------------------------|
| - 50 | TFS 2/3 | 3773 | 760 |
| 50 | TFS 5/4/180 | 3773 | 813 |
| 150 | TFS 2/5 | 3775 | 956 |
| 250 | TFS 2/6 | 3770 | 1019 |
| 350 | TFS 2/7 | 3775 | 1137 |
| 450 | TFS 5/8 | 3775 | 1218 |
| 550 | TFS 2/9 | 3775 | 1301 |
| 650 | TFS 3/10 | 3775 | 1436 |
| 750 | (TFS 4/11) | (3173) | (1638) |
| 850 | (TFS 2/12 B) | (3138) | (1725) |
| 950 | (TFS 2/13) TIT A/13 | (2575) 3776 | (1693) 2090 |
| 1050 | TFS 3/14 | 2889 | 1677 |
| 1150 | TFS 5/15 | 3845 | 2317 |
| 1250 | TFS 5/16 | 3837 | 2145 |
| 1350 | TFS 2/17 | 3846 | 2208 |

Note: Temperatures given in parentheses were measured by thermocouples that failed prior to cooling. Without these early failures the thermocouples would have indicated significantly higher temperatures.

Table 7: QUENCH-08; Maximum measured shroud temperatures of each elevation

| Elevation [mm] | Thermocouple | Time [s] | Maximum temperature [K] |
|----------------|--------------|----------|-------------------------|
| - 250 | TSH 1/0 | 3859 | 597 |
| - 50 | TSH 3/180 | 3770 | 667 |
| 50 | TSH 4/90 | 3775 | 735 |
| 350 | TSH 7/180 | 3776 | 1088 |
| 550 | TSH 9/270 | 3776 | 1222 |
| 750 | TSH 11/180 | 3776 | 1556 |
| 850 | TSH 12/180 I | 3777 | 1717 |
| 950 | TSH 13/270 I | 3836 | 2175 |
| 1050 | TSH 14/270 I | 3791 | 1908 |
| 1150 | TSH 15/0 I | 3844 | 1809 |
| 1250 | TSH 16/0 I | 3842 | 1957 |

Table 8: Hydrogen accumulated up to characteristic events of the QUENCH-07, -08, and -09 experiments [g]

| | Up to withdrawal of corner rod | Up to start of transient phase | Up to cooldown initiation | Up to begin of decay power | Total H ₂ |
|------------------|--------------------------------|--------------------------------|---------------------------|----------------------------|-----------------------|
| QUENCH-07 | 25* (t = 3090 s) | 26* (t = 3140 s) | 66* (t = 3557 s) | 131* (t = 3602 s) | 198** (t = 4800 s) |
| QUENCH-08 | 24 (t = 3181 s) | 25 (t = 3240 s) | 46 (t = 3776 s) | 65 (t = 3830 s) | 84 (t = 4650 s) |
| QUENCH-09 | | | 60 (t = 3316 s) | 222 (t = 3356 s) | 468** (t = 4500 s) |

* Corrected data due to time shift between MS recordings and main data acquisition system.

** Mass spectrometer data (Best estimate values are 182 and 460 g of total H₂ for QUENCH-07 and QUENCH-09, respectively [16]).

Table 9: QUENCH-08; Cross sections for the metallographic examination

23.04.2004

| Sample | Sample length (mm) | Axial position | | Remarks |
|-----------|--------------------|----------------|------------|--------------------------------------|
| | | bottom (mm) | top (mm) | |
| QUE-08-a | 78 | -20 | 58 | |
| Cut | 2 | 58 | 60 | |
| QUE-08-1 | 13 | 60 | 73 | Reference, 73 mm polished |
| Cut | 2 | 73 | 75 | |
| QUE-08-b | 356 | 75 | 431 | |
| Cut | 4 | 431 | 435 | |
| QUE-08-c | 100 | 435 | 535 | |
| Cut | 2 | 535 | 537 | |
| QUE-08-2 | 13 | 537 | 550 | TC elevation 9, 550 mm polished |
| Cut | 2 | 550 | 552 | |
| QUE-08-3 | 5 | 552 | 559 | Sample for H ₂ absorption |
| Cut | 2 | 559 | 561 | |
| QUE-08-d | 174 | 561 | 735 | |
| Cut | 2 | 735 | 737 | |
| QUE-08-4 | 13 | 737 | 750 | TC elevation 11, 750 mm polished |
| Cut | 2 | 750 | 752 | |
| QUE-08-5 | 5 | 752 | 759 | Sample for H ₂ absorption |
| Cut | 2 | 759 | 761 | |
| QUE-08-e | 79 | 761 | 840 | |
| Cut | 2 | 840 | 842 | |
| QUE-08-8 | 18 | 842 | 860 | 860 mm polished |
| Cut | 4 | 860 | 864 | |
| QUE-08-9 | 36 | 864 | 900 | 900 mm polished |
| Cut | 2 | 900 | 902 | |
| QUE-08-f | 33 | 902 | 935 | |
| Cut | 2 | 935 | 937 | |
| QUE-08-6 | 13 | 937 | 950 | TC elevation 13, 950 mm polished |
| Cut | 2 | 950 | 952 | |
| QUE-08-g | 32 | 952 | 984 | |
| Cut | 2 | 984 | 986 | |
| QUE-08-10 | 14 | 986 | 1000 | |
| Cut | 3 | 1000 | 1003 | |

| Sample | Sample length (mm) | Axial position | | Remarks |
|-----------|--------------------|----------------|-------------|--------------------------------------|
| | | bottom (mm) | top (mm) | |
| QUE-08-h | 45 | 1003 | 1048 | |
| Cut | 2 | 1048 | 1050 | |
| QUE-08-11 | 15 | 1050 | 1065 | 1065 mm polished |
| Cut | 2 | 1065 | 1067 | |
| QUE-08-i | 66 | 1067 | 1133 | |
| Cut | 2 | 1133 | 1135 | |
| QUE-08-12 | 15 | 1135 | 1150 | 1135 mm and 1150 mm polished |
| Cut | 2 | 1150 | 1152 | |
| QUE-08-13 | 7 | 1152 | 1159 | Sample for H ₂ absorption |
| Cut | 2 | 1159 | 1161 | |
| QUE-08-j | 48 | 1161 | 1209 | |
| Cut | 4 | 1209 | 1213 | |
| QUE-08-k | 92 | 1213 | 1305 | |
| Cut | 2 | 1305 | 1307 | |
| QUE-08-14 | 13 | 1307 | 1320 | 1320 mm polished |
| Cut | 2 | 1320 | 1322 | |
| QUE-08-l | 86 | 1322 | 1408 | |
| Cut | 2 | 1408 | 1410 | |
| QUE-08-15 | 15 | 1410 | 1425 | 1425 mm polished |
| Cut | 2 | 1425 | 1427 | |
| QUE-08-m | 35 | 1427 | 1462 | |
| Cut | 3 | 1462 | 1465 | |
| QUE-08-16 | 15 | 1465 | 1480 | 1480 mm polished |
| Cut | 2 | 1480 | 1482 | |
| QUE-08-n | 68 | 1482 | 1550 | |

**Table 10: QUENCH-08; Oxide scale thickness of corner rod B
(withdrawn from the bundle prior to the transient phase)**

| Bundle elevation [mm] | Oxide scale thickness (metallography) [μm] | Oxide scale thickness (eddy-current) [μm] |
|-----------------------|---|--|
| 550 | 11 | 5 |
| 650 | 32 | 22 |
| 750 | 74 | 66 |
| 800 | 103 | 106 |
| 850 | 145 | 172 |
| 870 | 164 | 203 |
| 950 | 274 | 351 |
| 1020 | 153 | 167 |
| 1050 | 115 | 114 |
| 1100 | 75 | 63 |

Table 11: QUENCH-08; Oxide scale thickness

| Height [mm] | All rods, mean [μm] | All rods, standard deviation | All rods, min [μm] | All rods, max [μm] | Heated rods, mean [μm] | Heated rods, stand. de. | Heated rods, min [μm] | Heated rods, max [μm] | Central rod [μm] | Shroud [μm] | Corner rods [μm] |
|-------------|---------------------|------------------------------|--------------------|--------------------|------------------------|-------------------------|-----------------------|-----------------------|------------------|-------------|------------------|
| 550 | 14,5 | 2,5 | 11 | 20 | 15,2 | 2,5 | 11 | 20 | 14,3 | 23 | |
| 750 | 114 | 10,5 | 100 | 140 | 114 | 10,7 | 100 | 140 | 118 | 104 | 102 |
| 860 | 410 | 101 | 225 | 665 | 409 | 102 | 225 | 665 | 436 | 270 | 367 |
| 900 | 884 | 174 | 500 | 1200 | 877 | 174 | 500 | 1200 | 1033 | 591 | 728 |
| 950 | 1001 | 88 | 830 | 1250 | 1000 | 90 | 830 | 1250 | 1025 | 916 | 933 |
| 1000 | 956 | 113 | 740 | 1270 | 951 | 113 | 740 | 1270 | 1053 | 1125 | 1051 |
| 1065 | 717 | 202 | 240 | 1100 | 716 | 207 | 240 | 1100 | 743 | 232 | 463 |
| 1135 | 641 | 256 | 170 | 1230 | 627 | 259 | 170 | 1230 | 848 | 285 | 491 |
| 1320 | 254 | 161 | 20 | 600 | 252 | 161 | 20 | 600 | 420 | -- | |
| 1480 | 13,8 | 9,7 | 5 | 60 | 11,8 | 4,1 | 5 | 20 | 53 | -- | |

Table 12: QUENCH-08; Hydrogen absorbed by the remaining Zr(O) metal phases

| Sample | Bundle elevation [mm] | File | Oxide Scale Thickness [μm] | Mass of Zry + oxide [g] | Volume of H ₂ [ml] | H ₂ conc.in metal [at %] |
|------------------------|-----------------------|---------|---|-------------------------|-------------------------------|-------------------------------------|
| Quench 08-3 Rod 18 | 552-559 | W40127D | 16,25 | 1,1951 | 0,52 | 0,34 |
| Quench 08-3 Rod 11 | 552-559 | W40128A | 13,35 | 1,0177 | 0,74 | 0,56 |
| Quench 08-3 Rod 6 | 552-559 | W40128B | 17,25 | 1,2046 | 1,43 | 0,91 |
| Quench 08-3 Rod 3 | 552-559 | W40128C | 16,75 | 1,085 | 0,48 | 0,34 |
| Quench 08-3 Rod 1 | 552-559 | W40129A | 10,75 | 1,1873 | 0,63 | 0,41 |
| Quench 08-5 Rod 15 | 752-759 | W40129B | 107,5 | 1,0629 | 5,34 | 4,20 |
| Quench 08-5 Rod 14 | 752-759 | W40129C | 102,5 | 0,9945 | 0,5 | 0,43 |
| Quench 08-5 Rod 5 | 752-759 | W40130A | 115 | 0,9764 | 1,44 | 1,28 |
| Quench 08-5 Rod 4 | 752-759 | W40130B | 122,5 | 0,9605 | 0,45 | 0,40 |
| Quench 08-5 Rod 1 | 752-759 | W40130C | 117,5 | 1,0661 | 0,43 | 0,34 |
| Quench 08-3 Shroud 0° | 552-559 | W40203A | 20 | 3,253 | 4,13 | 0,96 |
| Quench 08-5 Shroud 0° | 752-759 | W40203B | 85 | 2,6123 | 5,33 | 1,57 |
| Quench 08-13 Shroud 0° | 1152-1159 | W40204A | 550 | 2,8634 | 21,5 | 6,55 |
| Quench 08-13 Rod 1 | 1152-1159 | W40204B | 810 | 1,9033 | 10,46 | 9,49 |
| Quench 08-13 Rod 5 | 1152-1159 | W40204C | 773 | 1,3481 | 1,66 | 6,59 |
| Quench 08-13 Rod 8 | 1152-1159 | W40205A | 625 | 1,5045 | 7,63 | 8,60 |
| Quench 08-13 Rod 11 | 1152-1159 | W40205B | 715 | 1,2911 | 0,37 | 0,81 |
| Quench 08-13 Rod 15 | 1152-1159 | W40206A | 683 | 1,5690 | 0,26 | 0,38 |

Table 13: Locations of the TCs used for the temperature measurements of the fuel rod simulators of the QUENCH-08 bundle

| | Channel | TC | Elevation |
|----|---------|-------------|-----------|
| 1 | KAN: 04 | TFS2/17 | 1350 mm |
| 2 | KAN: 49 | TFS5/17 | 1350 mm |
| 3 | KAN: 37 | TFS3/16 | 1250 mm |
| 4 | KAN: 48 | TFS5/16 | 1250 mm |
| 5 | KAN: 03 | TFS2/15 | 1150 mm |
| 6 | KAN: 47 | TFS5/15 | 1150 mm |
| 7 | KAN: 09 | TFS3/14 | 1050 mm |
| 8 | KAN: 16 | TFS5/14 | 1050 mm |
| 9 | KAN: 02 | TFS2/13 | 950 mm |
| 10 | KAN: 08 | TFS3/13 | 950 mm |
| 11 | KAN: 11 | TFS4/13 | 950 mm |
| 12 | KAN: 15 | TFS5/13 | 950 mm |
| 13 | KAN: 34 | TFS2/12 B | 850 mm |
| 14 | KAN: 50 | TFS3/12 B | 850 mm |
| 15 | KAN: 14 | TFS5/12 | 850 mm |
| 16 | KAN: 51 | TFS2/11 B | 750 mm |
| 17 | KAN: 10 | TFS4/11 | 750 mm |
| 18 | KAN: 13 | TFS5/11 | 750 mm |
| 19 | KAN: 06 | TFS3/10 | 650 mm |
| 20 | KAN: 12 | TFS5/10 | 650 mm |
| 21 | KAN: 39 | TFS2/9 | 550 mm |
| 22 | KAN: 38 | TFS5/9 | 550 mm |
| 23 | KAN: 43 | TFS3/8 | 450 mm |
| 24 | KAN: 42 | TFS5/8 | 450 mm |
| 25 | KAN: 23 | TFS2/7 | 350 mm |
| 26 | KAN: 82 | TFS5/7 | 350 mm |
| 27 | KAN: 76 | TFS2/6 F | 250 mm |
| 28 | KAN: 81 | TFS5/6 | 250 mm |
| 29 | KAN: 22 | TFS 2/5 | 150 mm |
| 30 | KAN: 78 | TFS 5/4/0 F | 150 mm |
| 31 | KAN: 79 | TFS 5/4/180 | 50 mm |
| 32 | KAN: 74 | TFS 2/3 | -50 mm |
| 33 | KAN: 72 | TFS 2/1 F | -250 mm |
| 34 | KAN: 32 | TIT A/13 | 950 mm |
| 35 | KAN: 00 | TCR 13 | 950 mm |
| 36 | KAN: 33 | TCRC 13 | 950 mm |
| 37 | KAN: 40 | TIT D/12 | 850 mm |
| 38 | KAN: 46 | TIT C/9 | 550 mm |
| 39 | KAN: 73 | TCRC 9 | 550 mm |
| 40 | KAN: 77 | TCRI 9 | 550 mm |
| 41 | KAN: 75 | TCRI 7 | 350 mm |
| 42 | KAN: 80 | TCRC 7 | 350 mm |

Table 14: Locations of the TCs used for the shroud temperature measurement in the QUENCH-08 bundle test

| | Channel | TC | Elevation |
|----|---------|--------------|-----------|
| 1 | KAN: 67 | TSH 16/0 I | 1250 mm |
| 2 | KAN: 17 | TSH 16/180 I | 1250 mm |
| 3 | KAN: 66 | TSH 15/0 I | 1150 mm |
| 4 | KAN: 05 | TSH 15/180 I | 1150 mm |
| 5 | KAN: 19 | TSH 14/90 I | 1050 mm |
| 6 | KAN: 53 | TSH 14/270 I | 1050 mm |
| 7 | KAN: 52 | TSH 13/270 I | 950 mm |
| 8 | KAN: 55 | TSH 12/180 I | 850 mm |
| 9 | KAN: 20 | TSH 11/0 I | 750 mm |
| 10 | KAN: 54 | TSH 11/180 I | 750 mm |
| 11 | KAN: 35 | TSH 9/90 | 550 mm |
| 12 | KAN: 36 | TSH 9/270 | 550 mm |
| 13 | KAN: 90 | TSH 7/0 | 350 mm |
| 14 | KAN: 86 | TSH 7/180 | 350 mm |
| 15 | KAN: 89 | TSH 4/0 | 50 mm |
| 16 | KAN: 87 | TSH 4/90 | 50 mm |
| 17 | KAN: 85 | TSH 4/180 | 50 mm |
| 18 | KAN: 83 | TSH 4/270 | 50 mm |
| 19 | KAN: 84 | TSH 3/180 | - 50 mm |
| 20 | KAN: 88 | TSH 1/0 | -250 mm |

Table 15: Calculated total amount of different components released from a B₄C absorber rod during tests QUENCH-07 and QUENCH-08 (with virtual absorber)

| Component | Q-07 total release, g | Q-08 total release, g | Q-07/Q-08 ratio |
|--|-----------------------|-----------------------|-----------------|
| H ₂ | 12.51 | 7.46 | 1.68 |
| CO ₂ | 17.93 | 16.16 | 1.11 |
| CO | 11.76 | 3.04 | 3.87 |
| CH ₄ | 2.6·10 ⁻⁴ | 5.11·10 ⁻⁵ | 5.17 |
| B ₂ O ₃ | 1.31 | 0.161 | 8.14 |
| HBO ₂ | 71.5 | 18.74 | 3.82 |
| H ₃ BO ₃ | 57.63 | 7.04 | 8.19 |
| H ₃ B ₃ O ₆ | - | 59.48 | - |
| Total C | 9.94 | 5.71 | 1.74 |

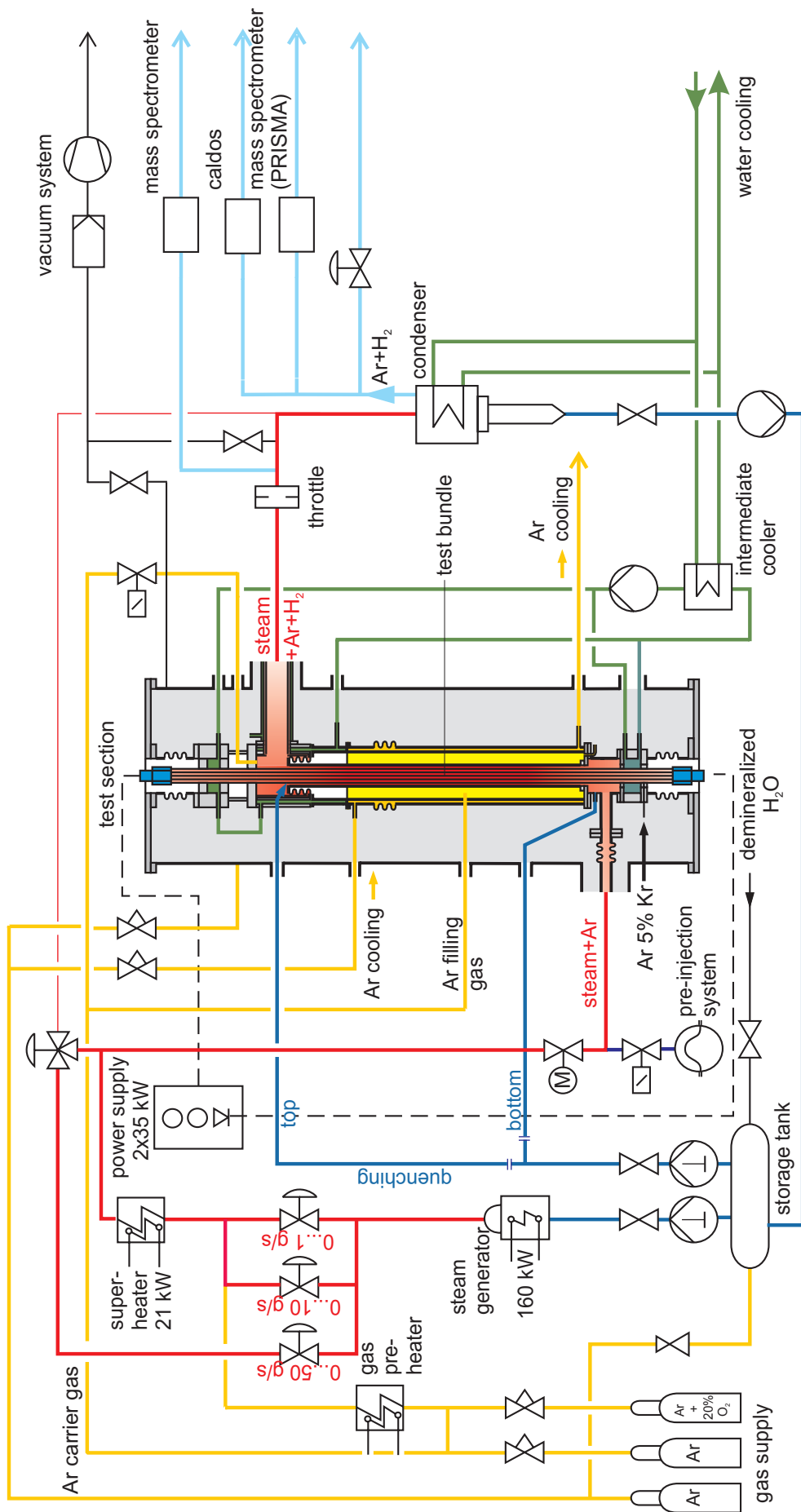


Fig. 1-QUE08-Flow diagram.cdr
18.09.03 - IMF

Fig. 1: Flow diagram of the QUENCH test facility

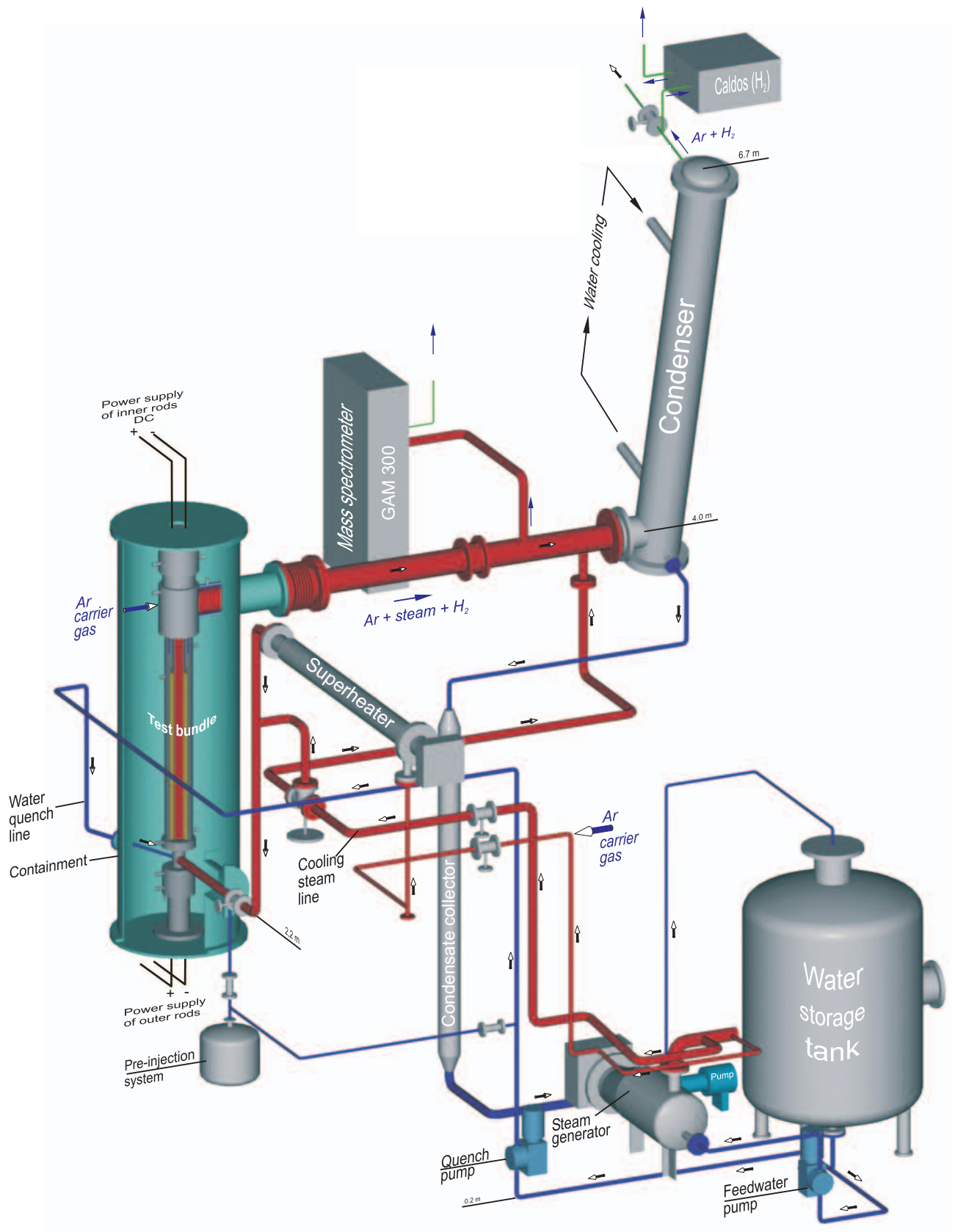


Fig.2-QUE08-Gesamtanlage.cdr
09.12.03 - IMF

Fig. 2: QUENCH Facility - Main components

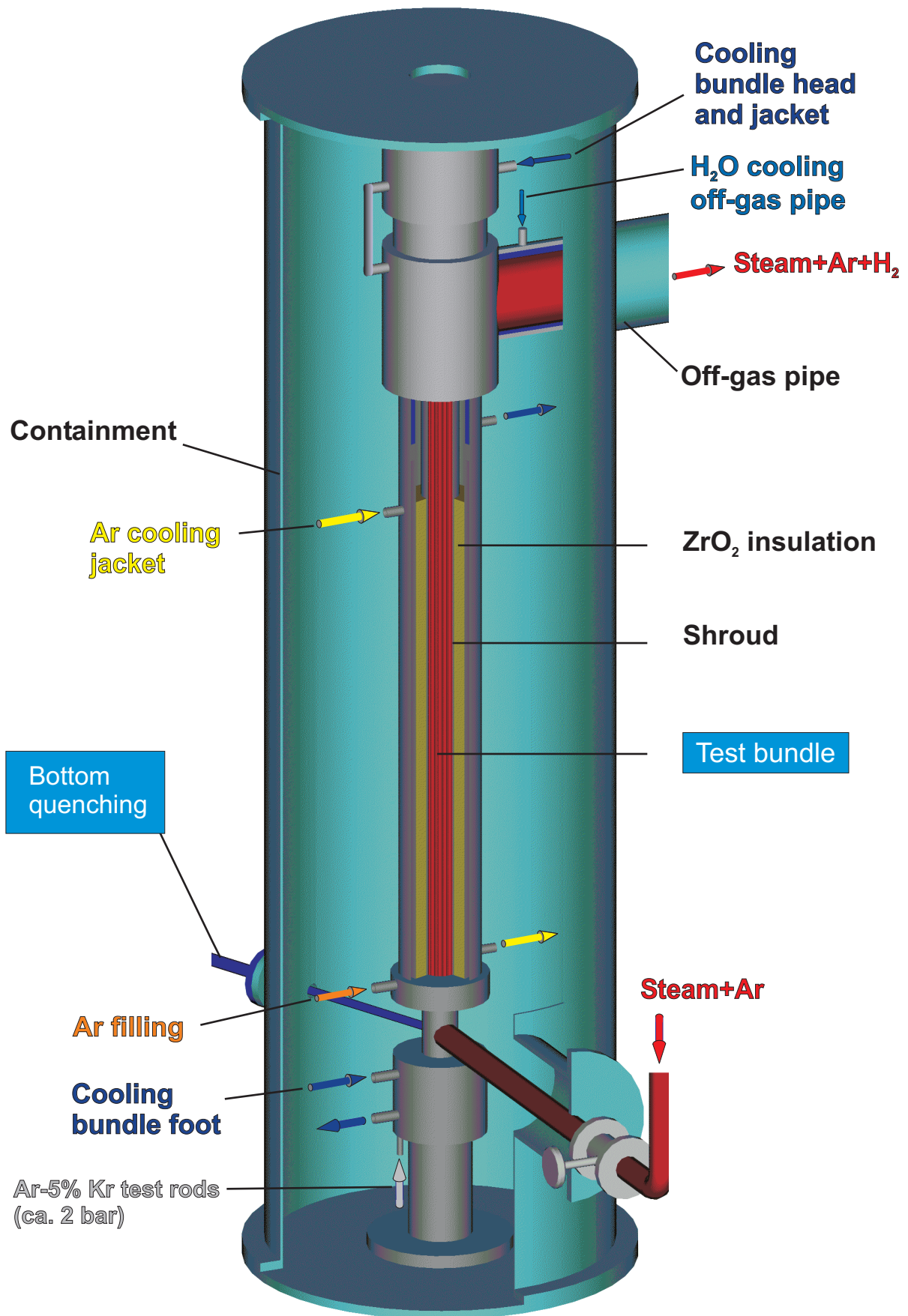


Fig.3-QUE08 Containment 3D.cdr
14.04.05 - IMF

Fig. 3: QUENCH Facility; containment and test section

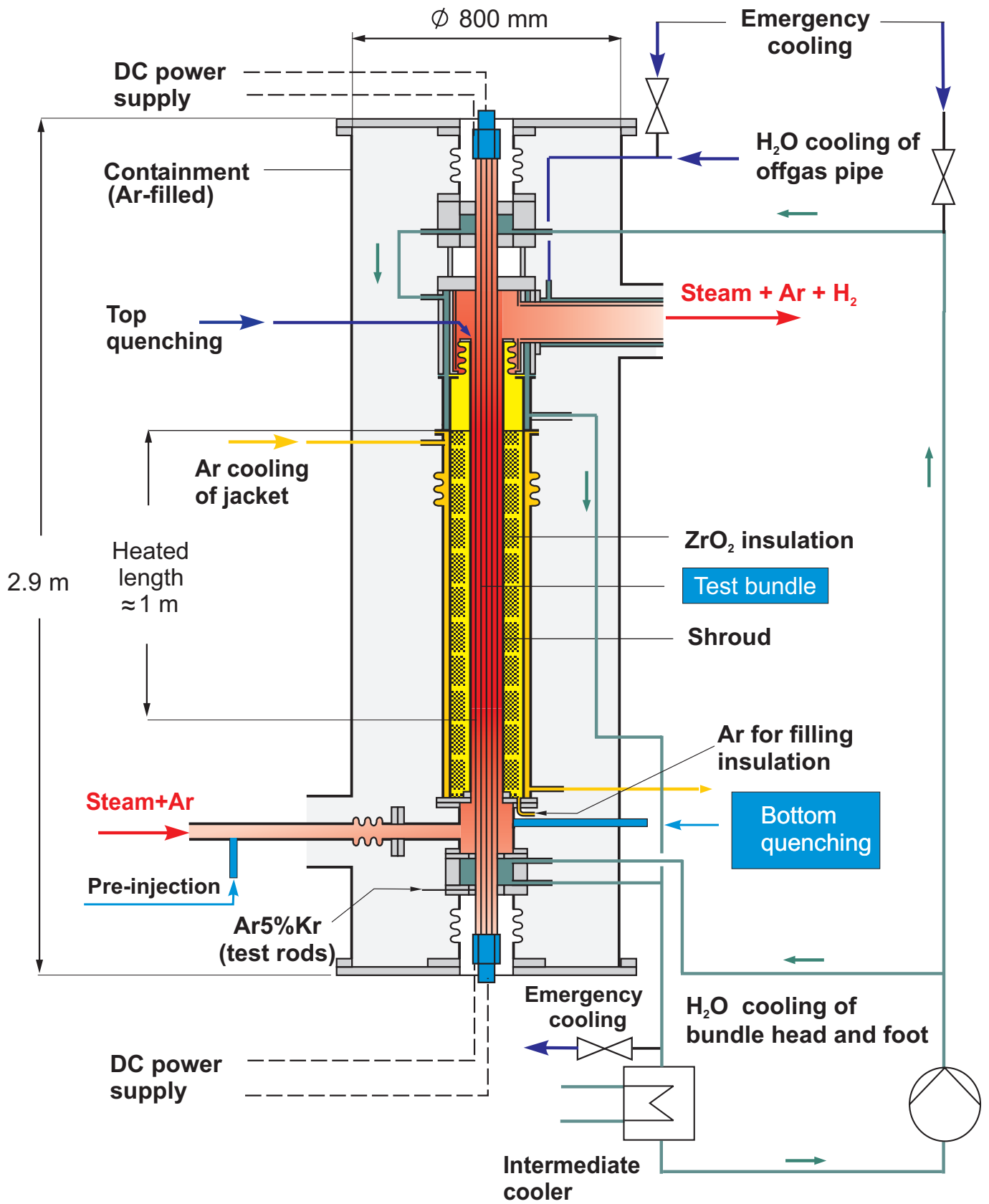


Fig 4-QUE08-Flow lines (ab QUE05).cdr
18.09.03 - IMF

Fig. 4: QUENCH test section; flow lines

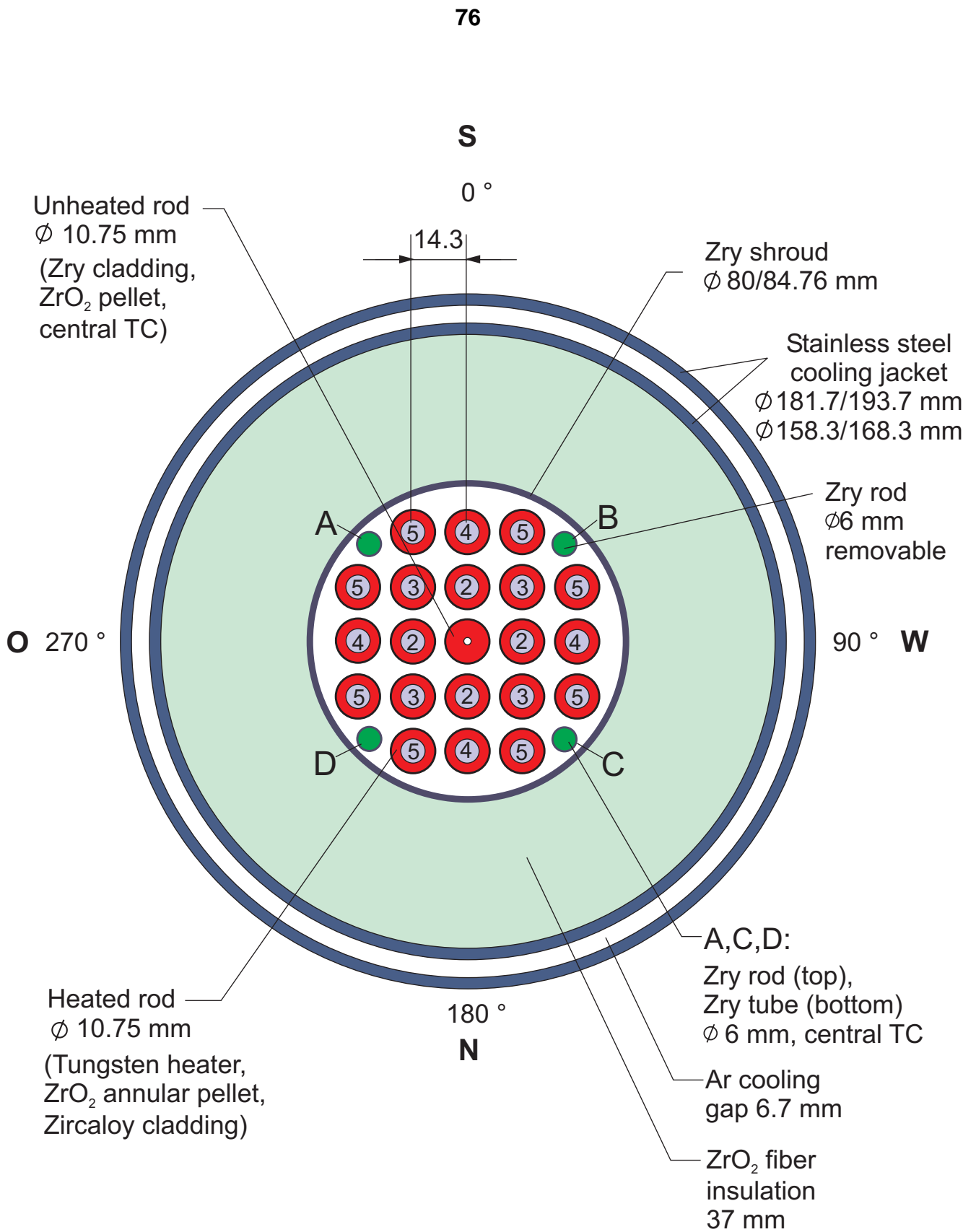


Fig.5-QUE08 Cross section.cdr
 29.06.05 - IMF

Fig. 5: QUENCH-08; Fuel rod simulator bundle (cross section, top view) and rod type designation.

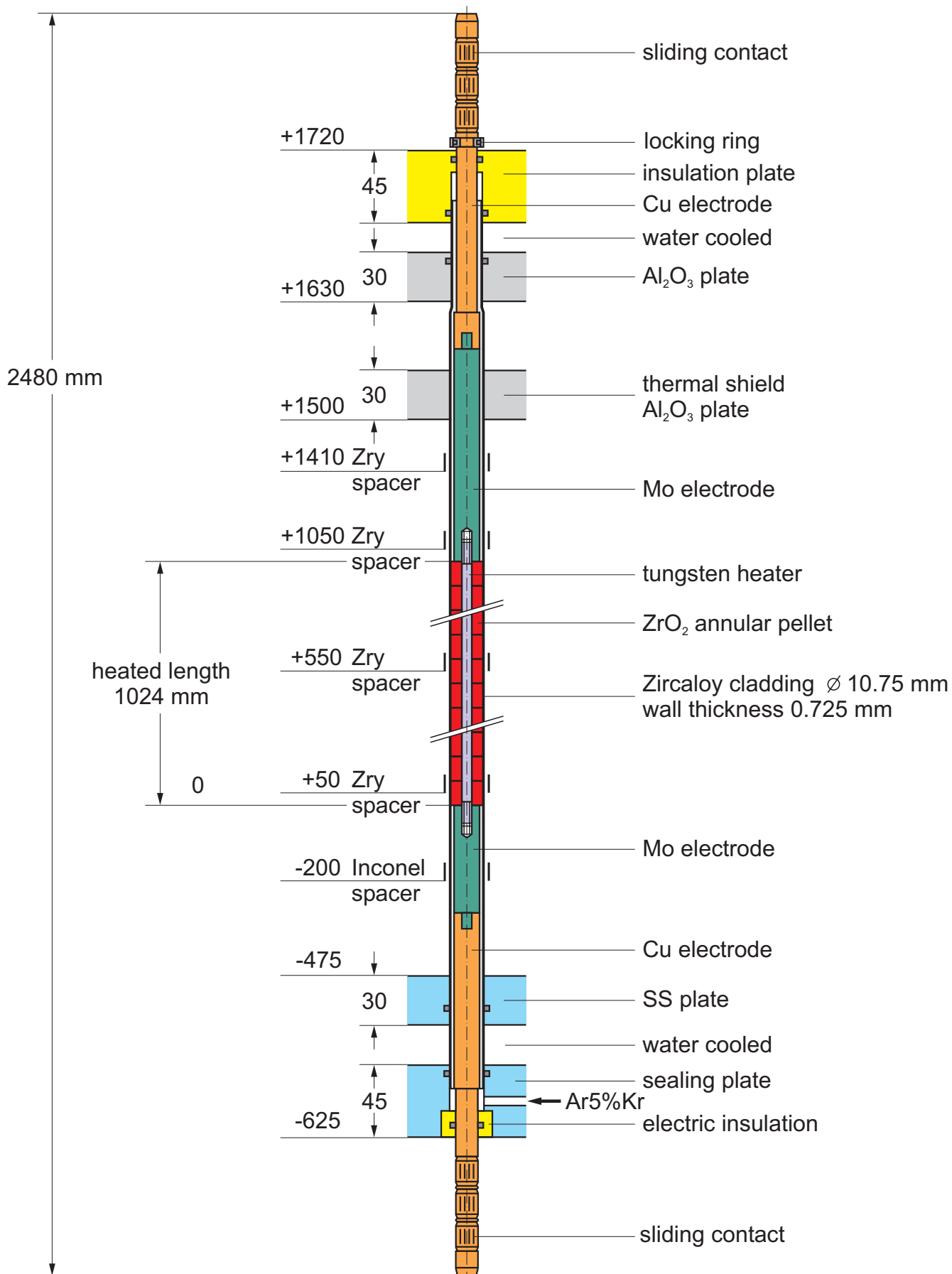


Fig.6-QUE08-Heated fuel rod sim.cdr
18.09.03 - IMF

Fig. 6: Heated fuel rod simulator

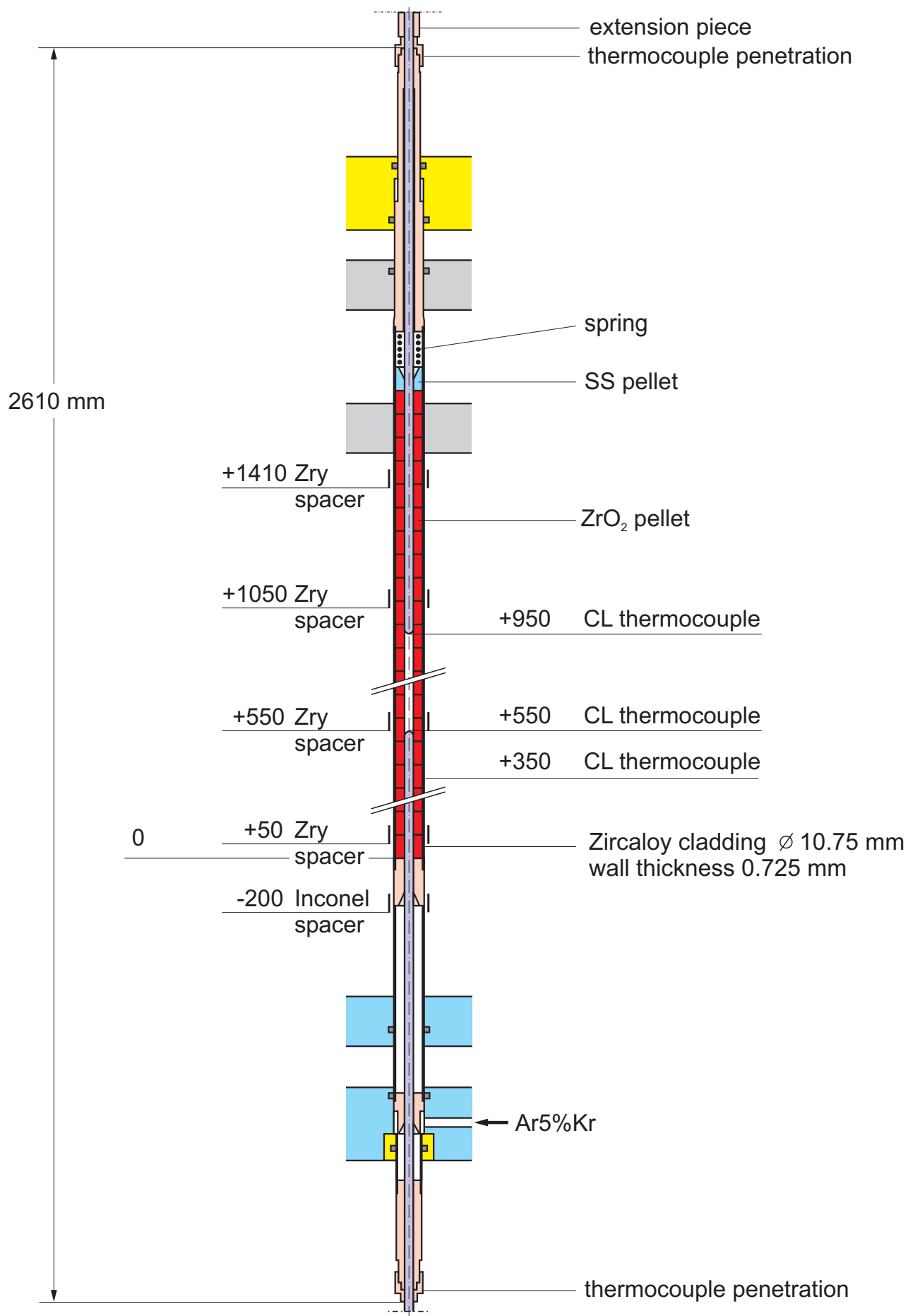


Fig. 7: Unheated fuel rod simulator

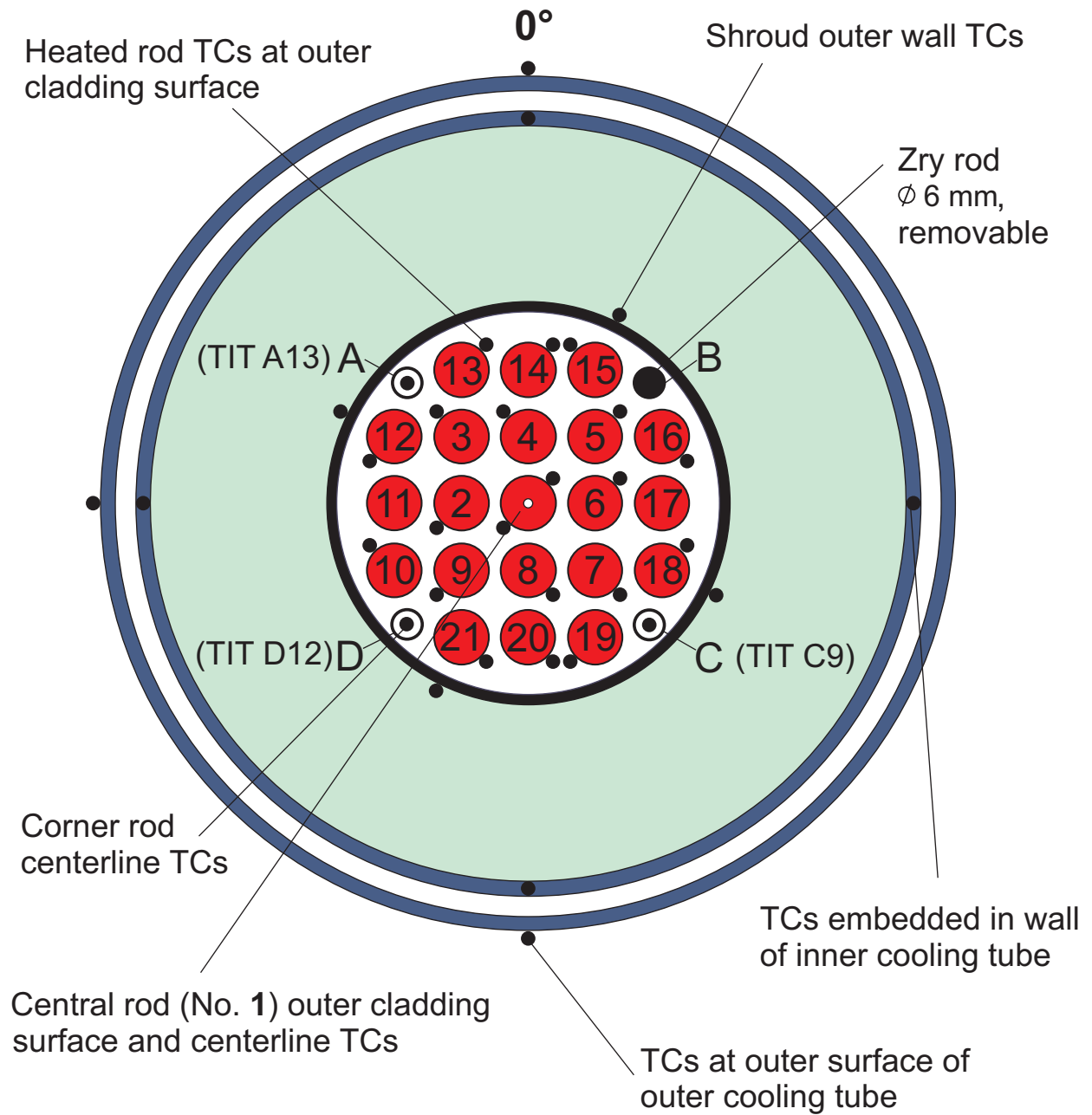
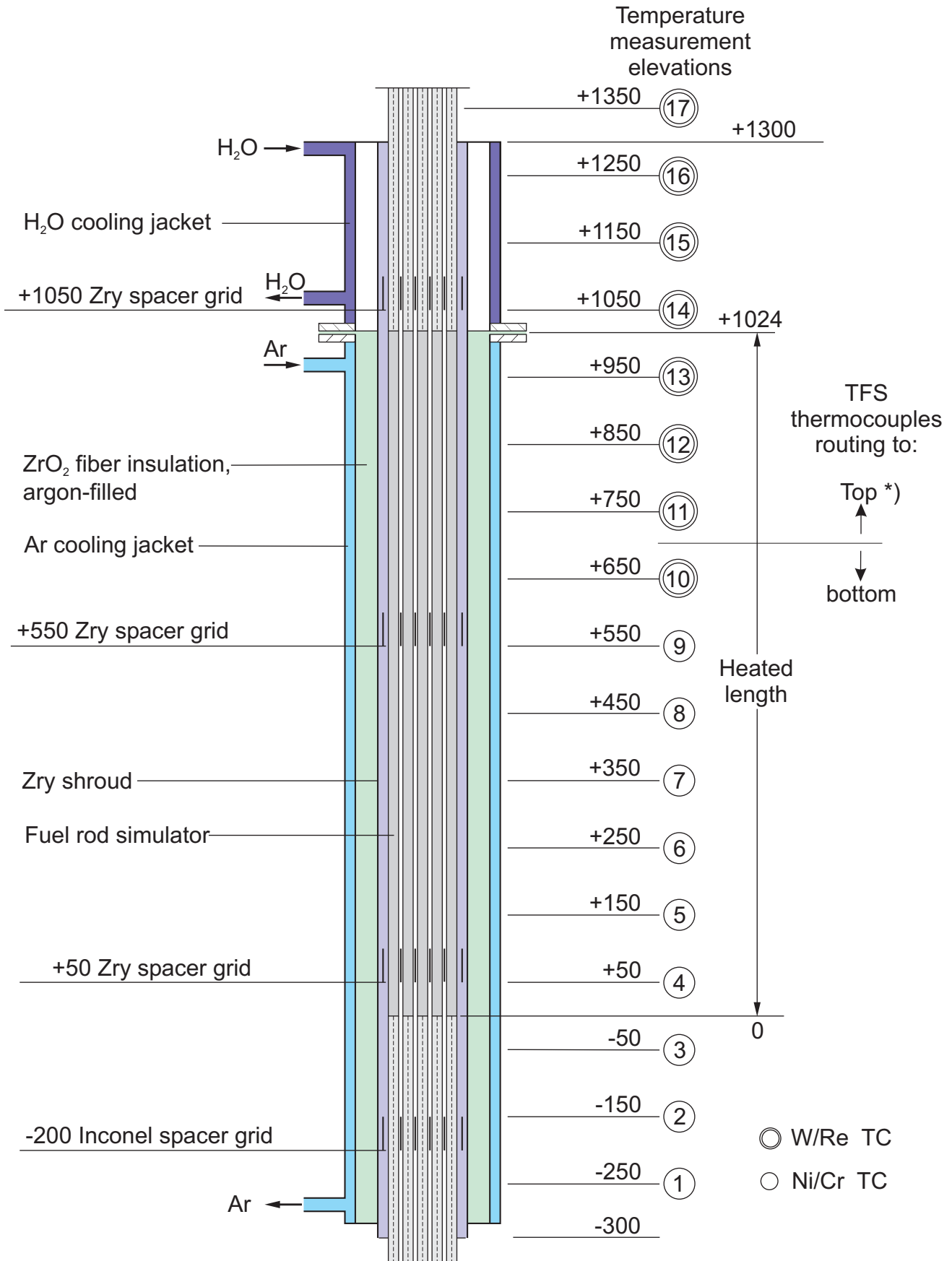


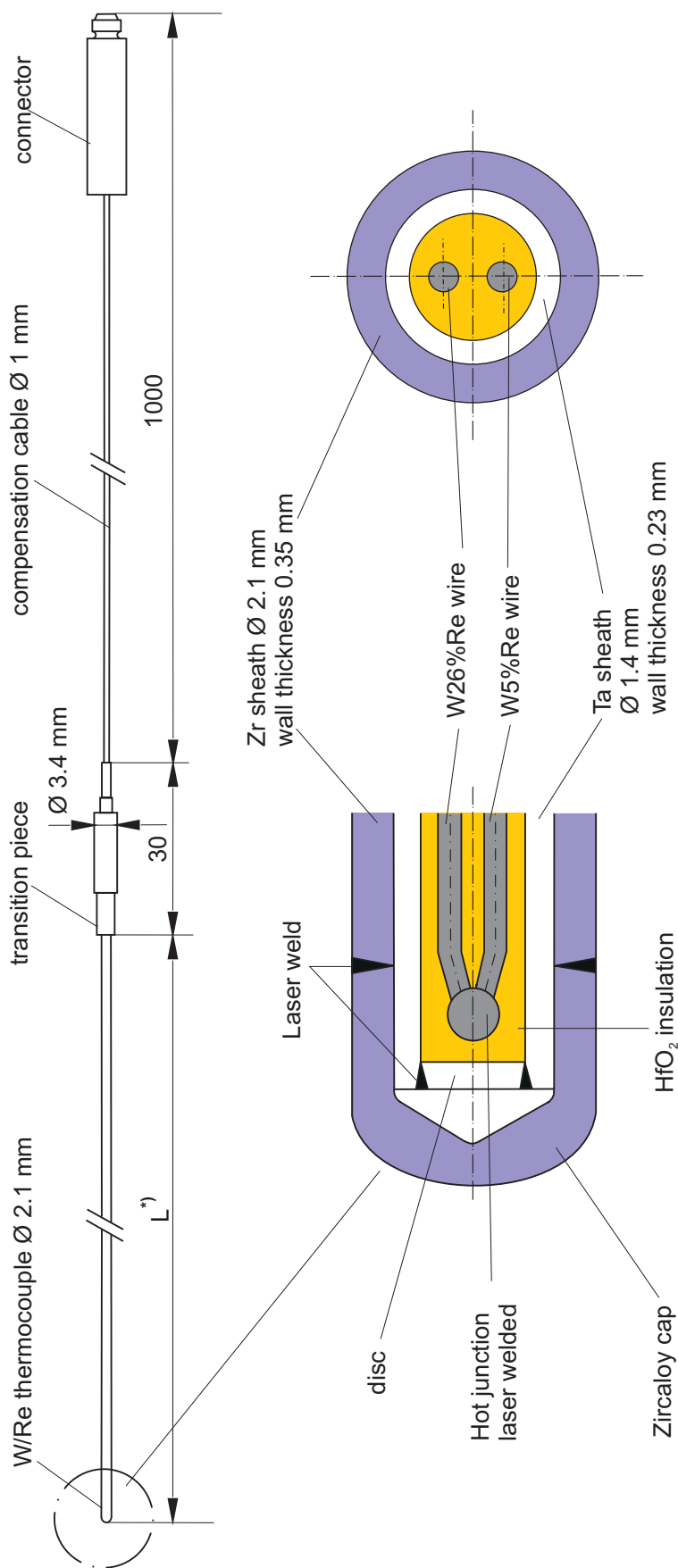
Fig. 8: QUENCH-08; Test bundle, TC instrumentation and rod designation (cross section, top view)



*) Thermocouples TFS 2/11 B, TFS 2/12 B, and TFS 3/12 B are routed to the bottom.

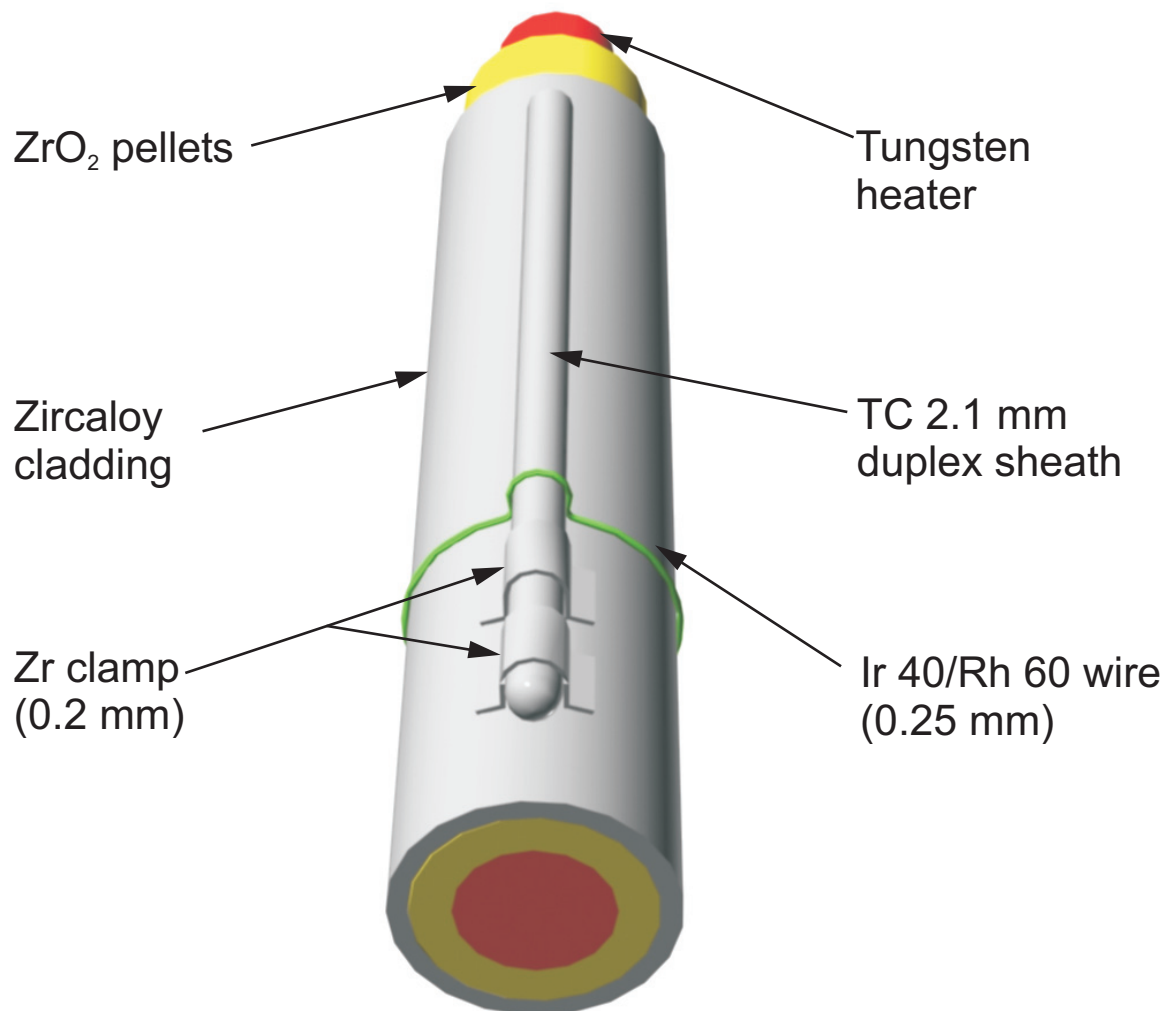
Fig.9-QUE08-TC elevations.cdr
17.03.05 - IMF

Fig. 9: Axial temperature measurement locations in the QUENCH test section.



*) L: high-temperature section length dependent on the TC position in the test bundle, i.e. 500 - 1700 mm

Fig. 10: QUENCH; High-temperature thermocouple



Tests with pre-oxidation: Zr clamp + wire

Tests without pre-oxidation: Zr clamp

Fig. 11: QUENCH; Concept for TC fastening at the test rod

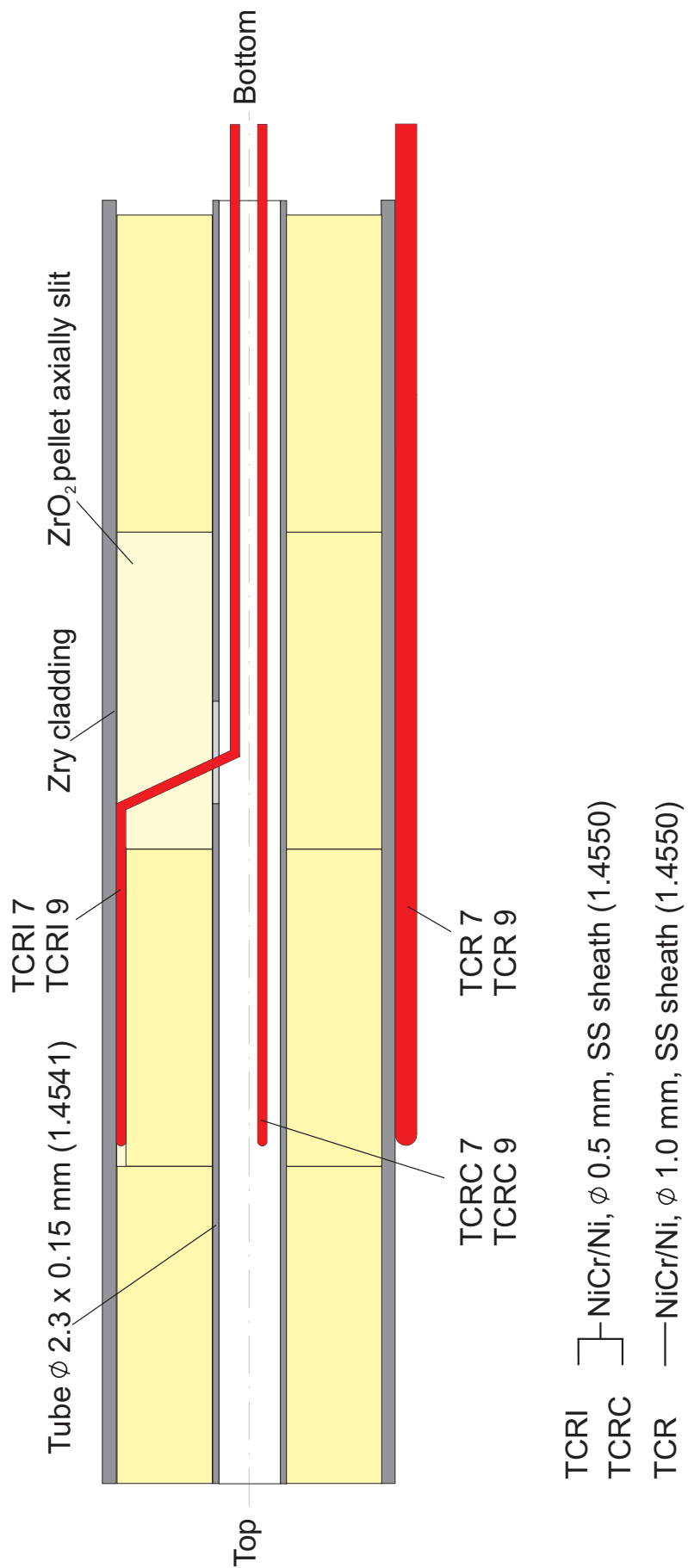


Fig 12 QUE08 Zentralstab.cdr
18.09.03 - IMF

Fig. 12: QUENCH-08; TC instrumentation of the unheated fuel rod simulator at levels 7 (350 mm) and 9 (550 mm)

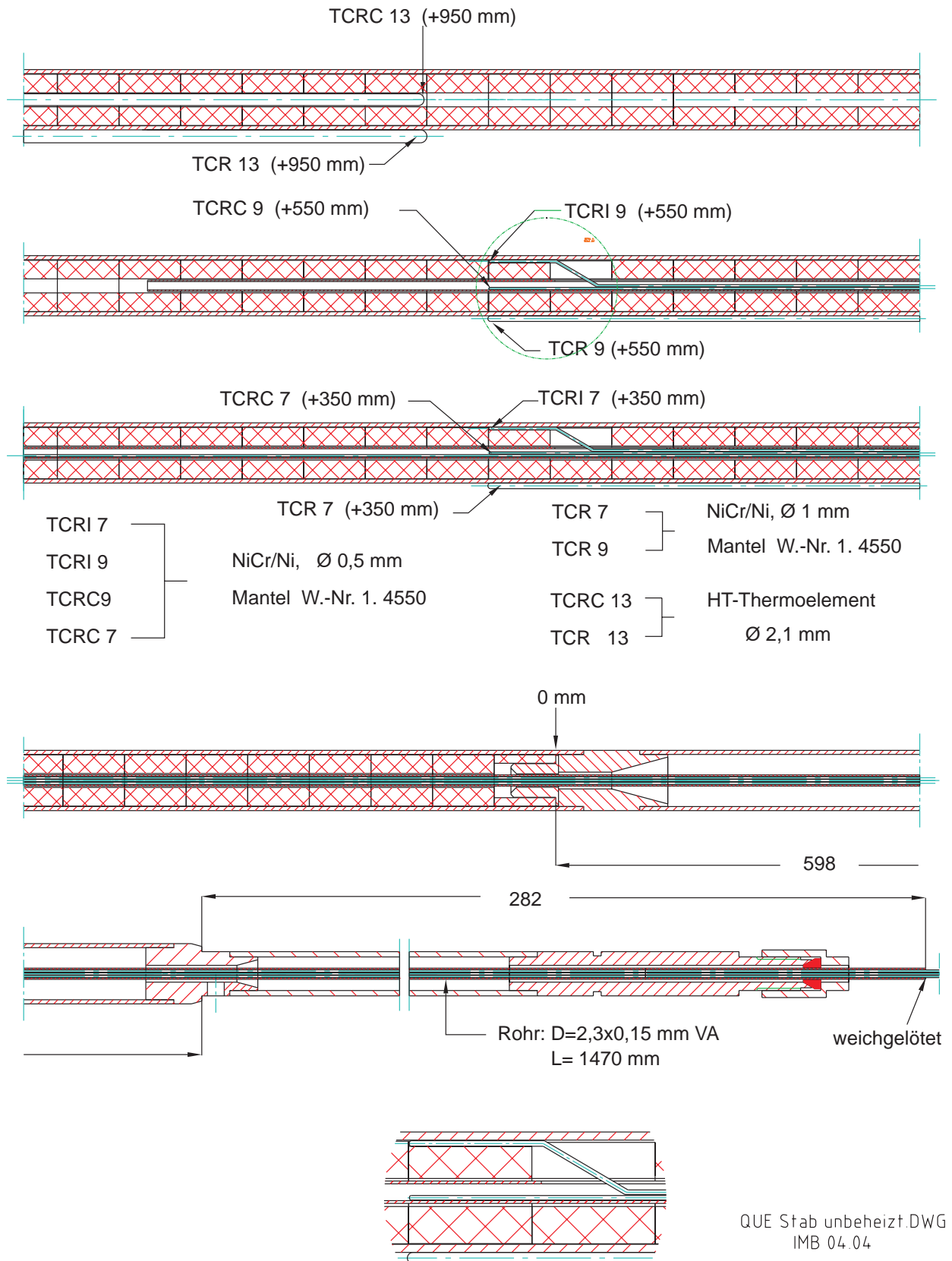
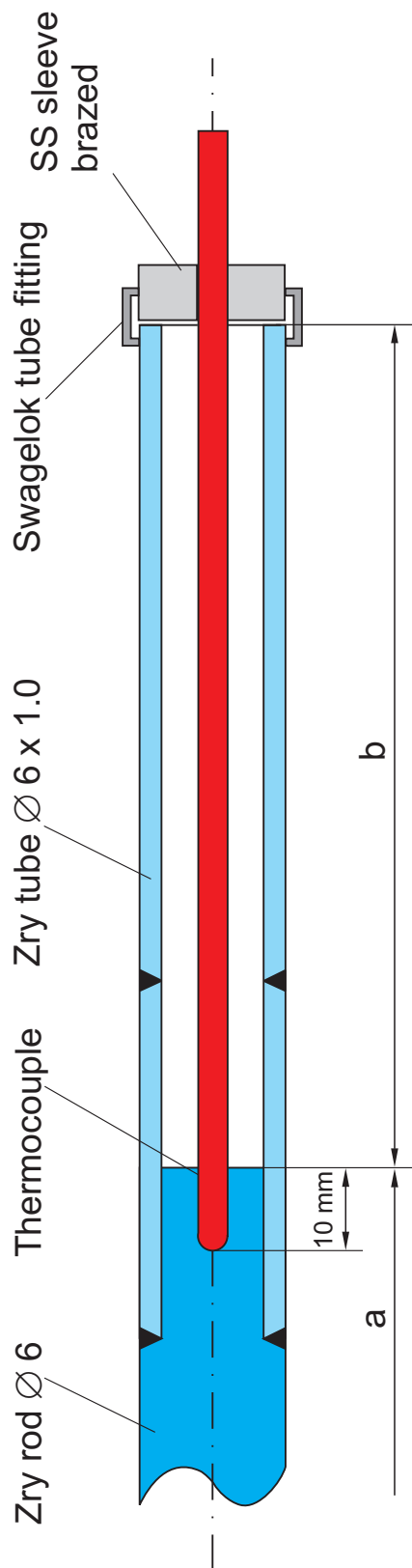


Fig. 13: QUENCH-08; TC instrumentation of the unheated fuel rod simulator at all levels

(TIT A13, TIT D12, TIT C9)



Rod A: TIT A13 (950 mm), W/Re, $\varnothing 2.1$ mm, $a = 360$ mm, $b = 2080$ mm

Rod D: TIT D12 (850 mm), W/Re, $\varnothing 2.1$ mm, $a = 460$ mm, $b = 1980$ mm

Rod C: TIT C 9 (550 mm), NiCr/Ni, $\varnothing 1$ mm, $a = 760$ mm, $b = 1680$ mm

(Rod B: Zry-4 rod, $\varnothing 6$ mm, removable)

Fig. 14: QUENCH-08; Arrangement of the thermocouples inside the corner rods

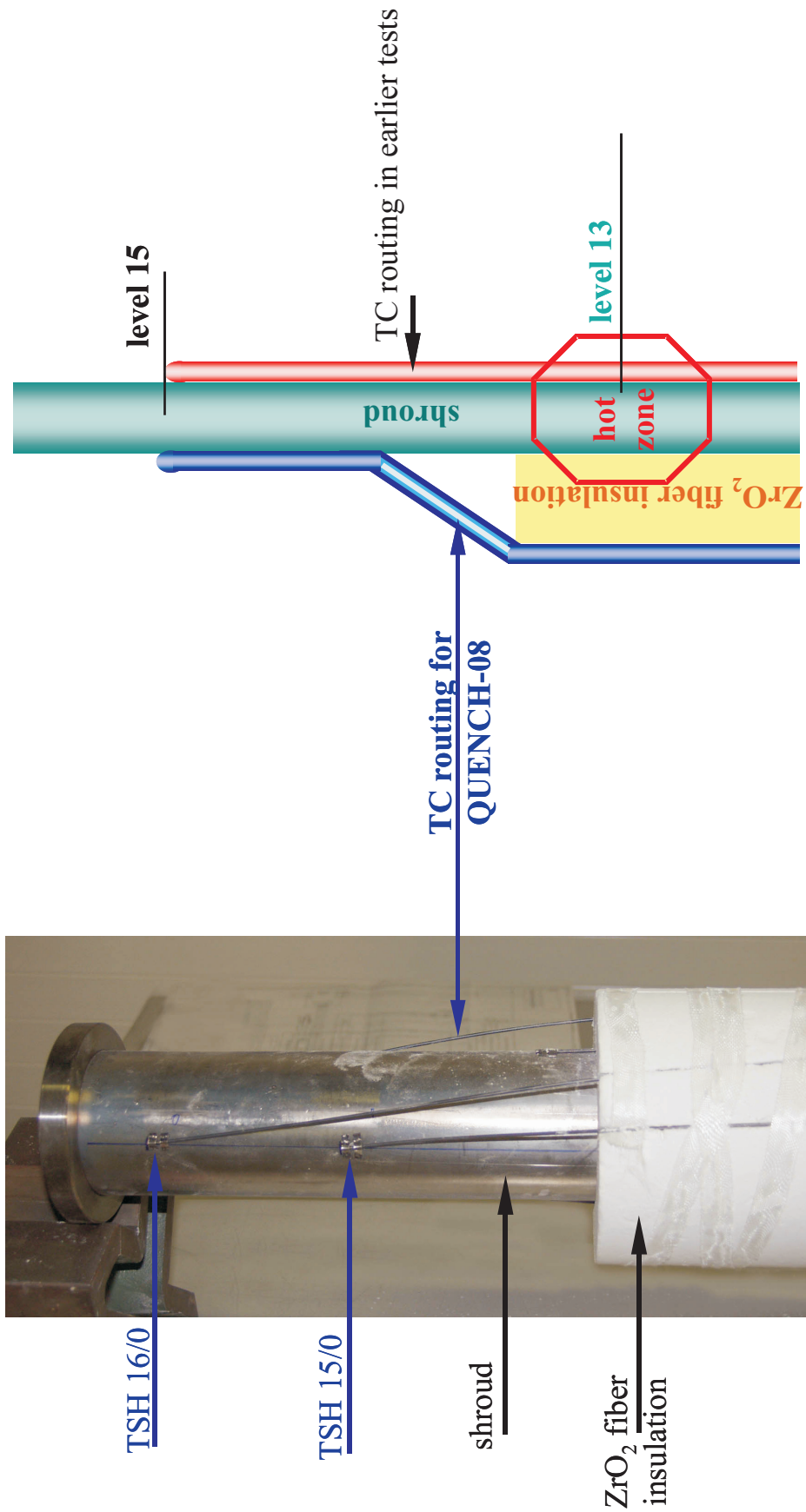


Fig 15-QUE08-routing TSH.cdr
25.01.05 - IMF

Fig. 15: QUENCH-08; Routing of the shroud thermocouples (TSH) towards outside the insulation of the QUENCH-08 test bundle compared to TC routing in earlier tests

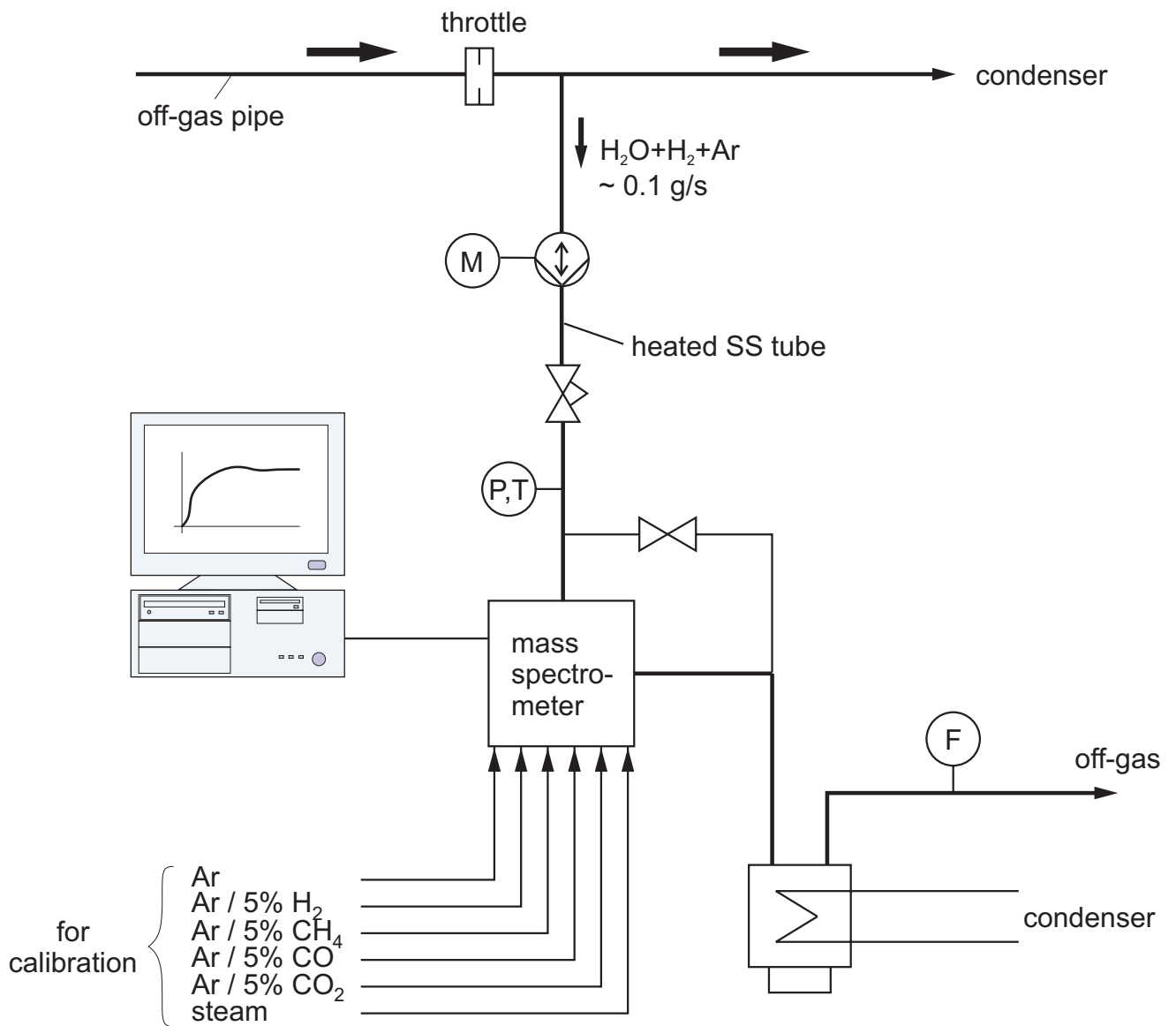


Fig.16-QUE08-MS Quench facility.cdr
14.04.05 - IMF

Fig. 16: QUENCH; H_2 measurement with the GAM 300 mass spectrometer

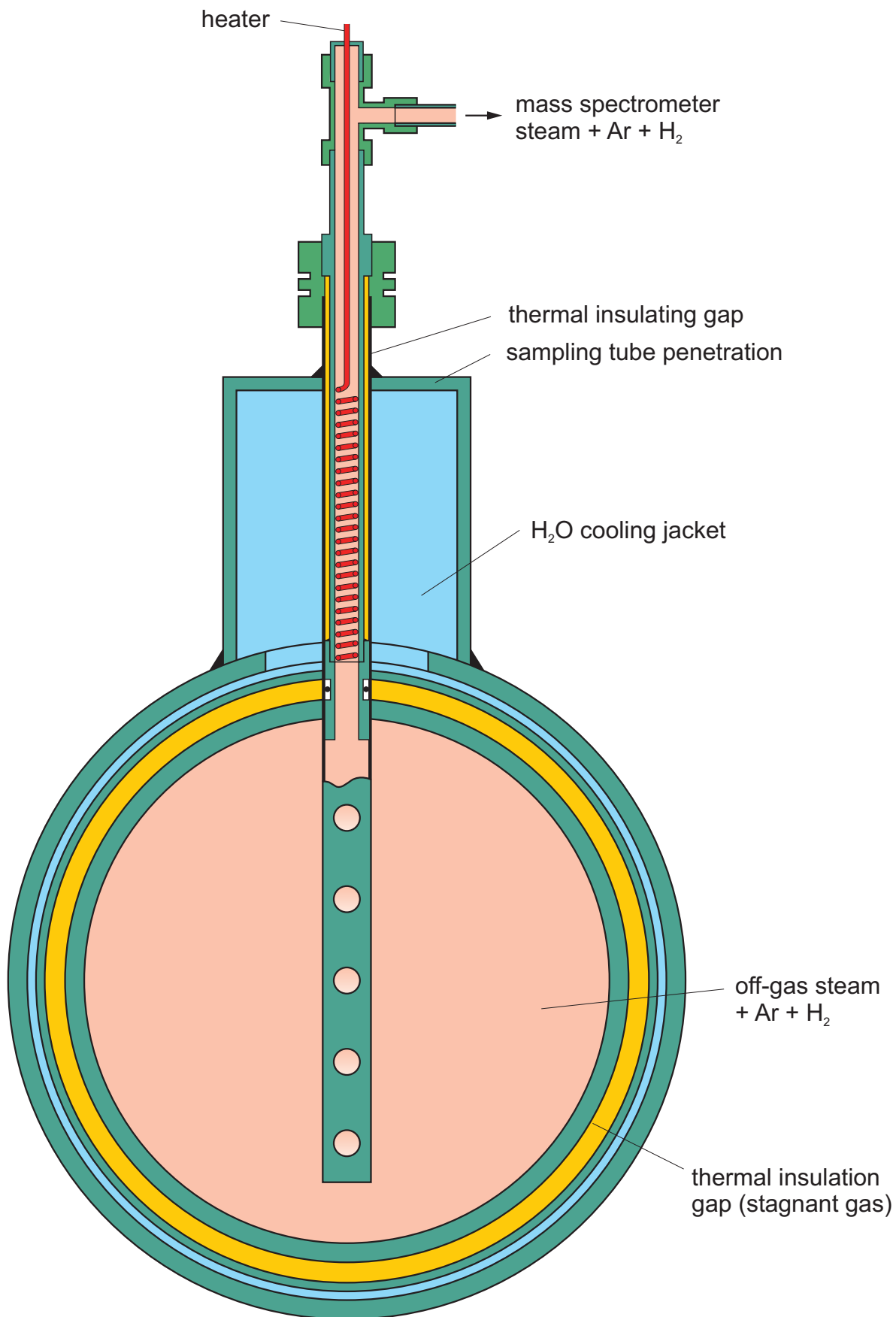


Fig 17-QUE08-MS sampling position new.cdr
17.03.05 - IMF

Fig.17: QUENCH; Mass spectrometer sampling position at the off-gas pipe

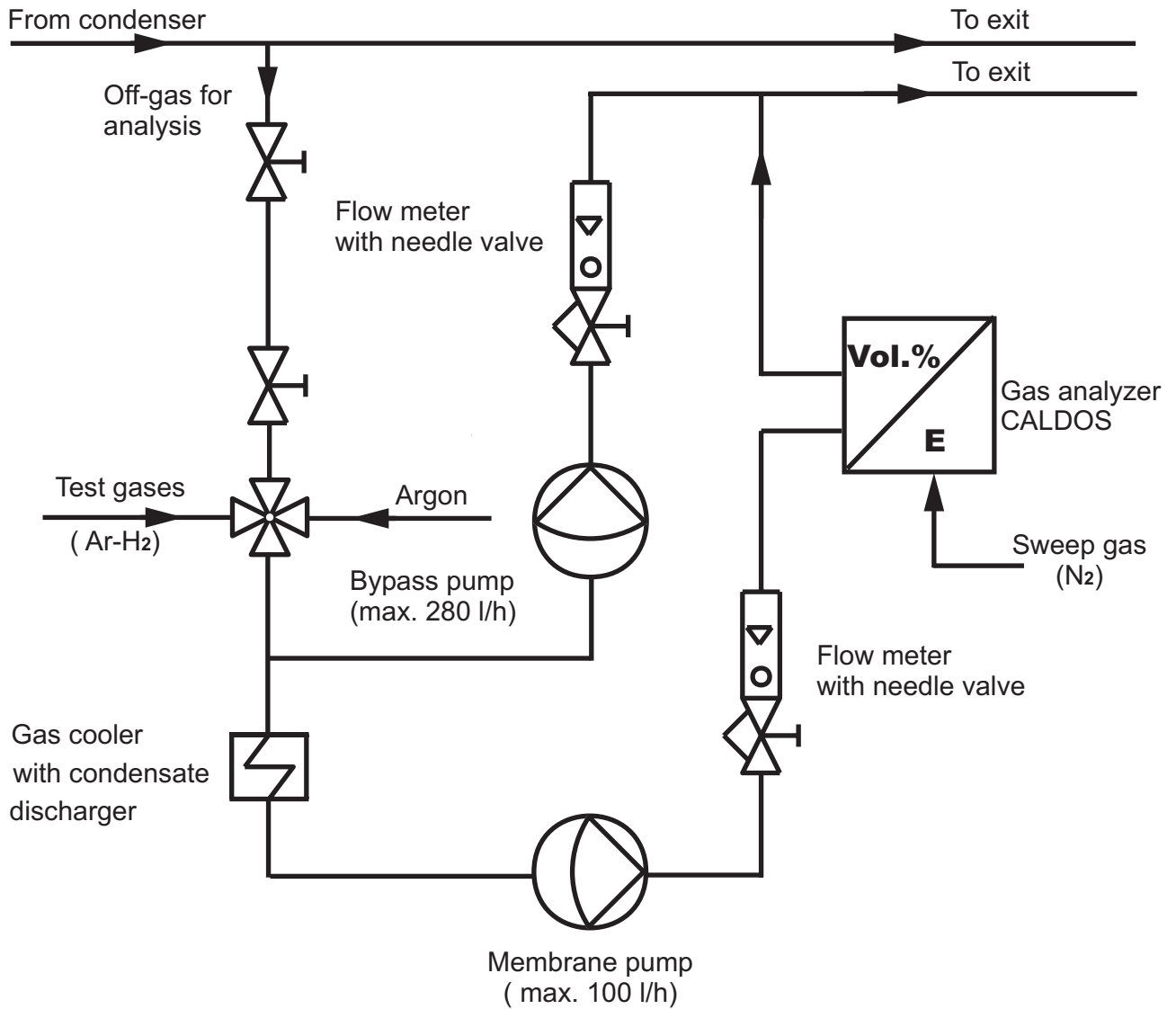


Fig 18-QUE08-Caldos Schema (ab QUE04).cdr
26.01.05 - IMF

Fig.18: QUENCH; Hydrogen measurement with the CALDOS analyzer

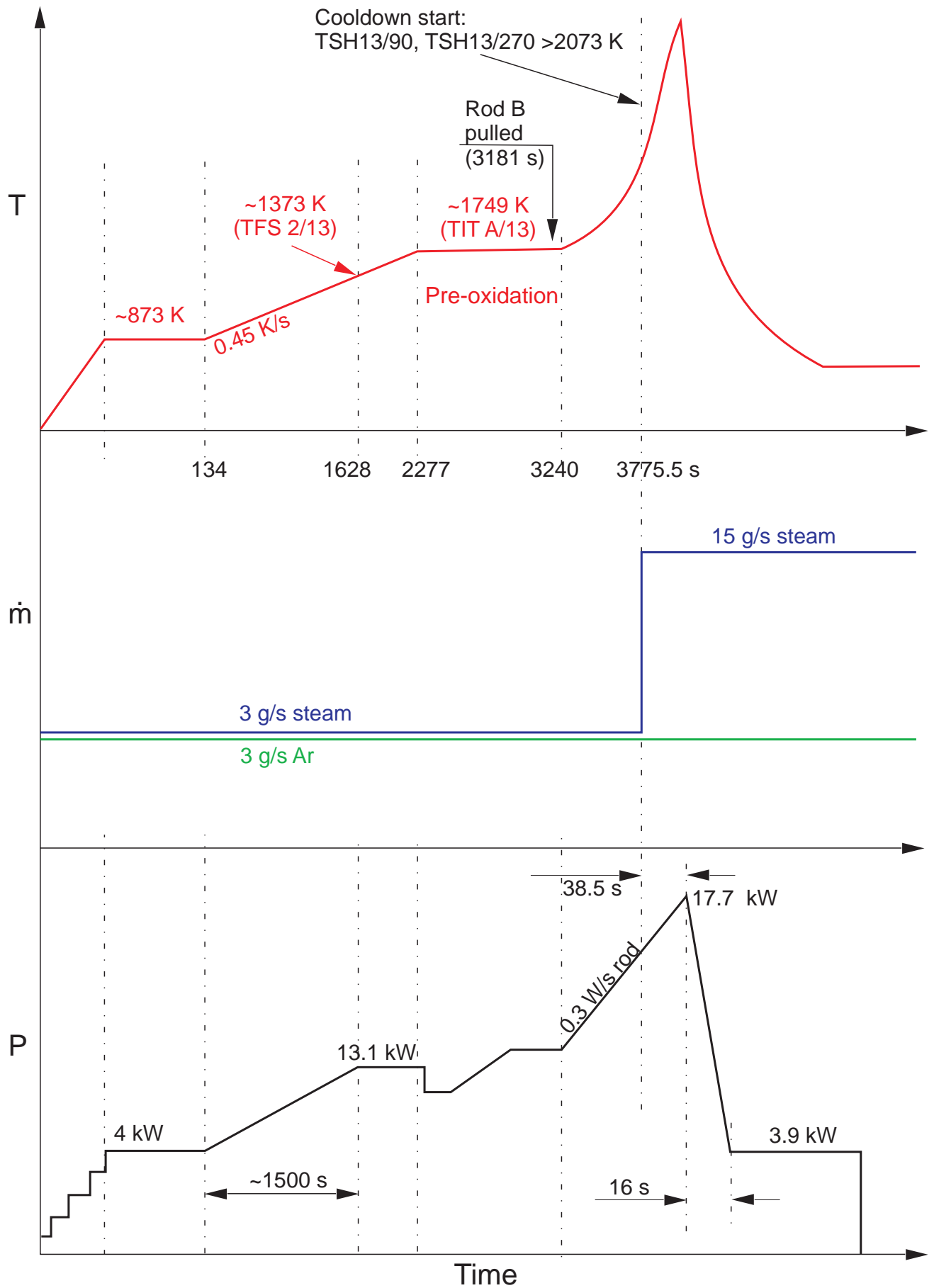


Fig.19 : QUENCH-08 test conduct

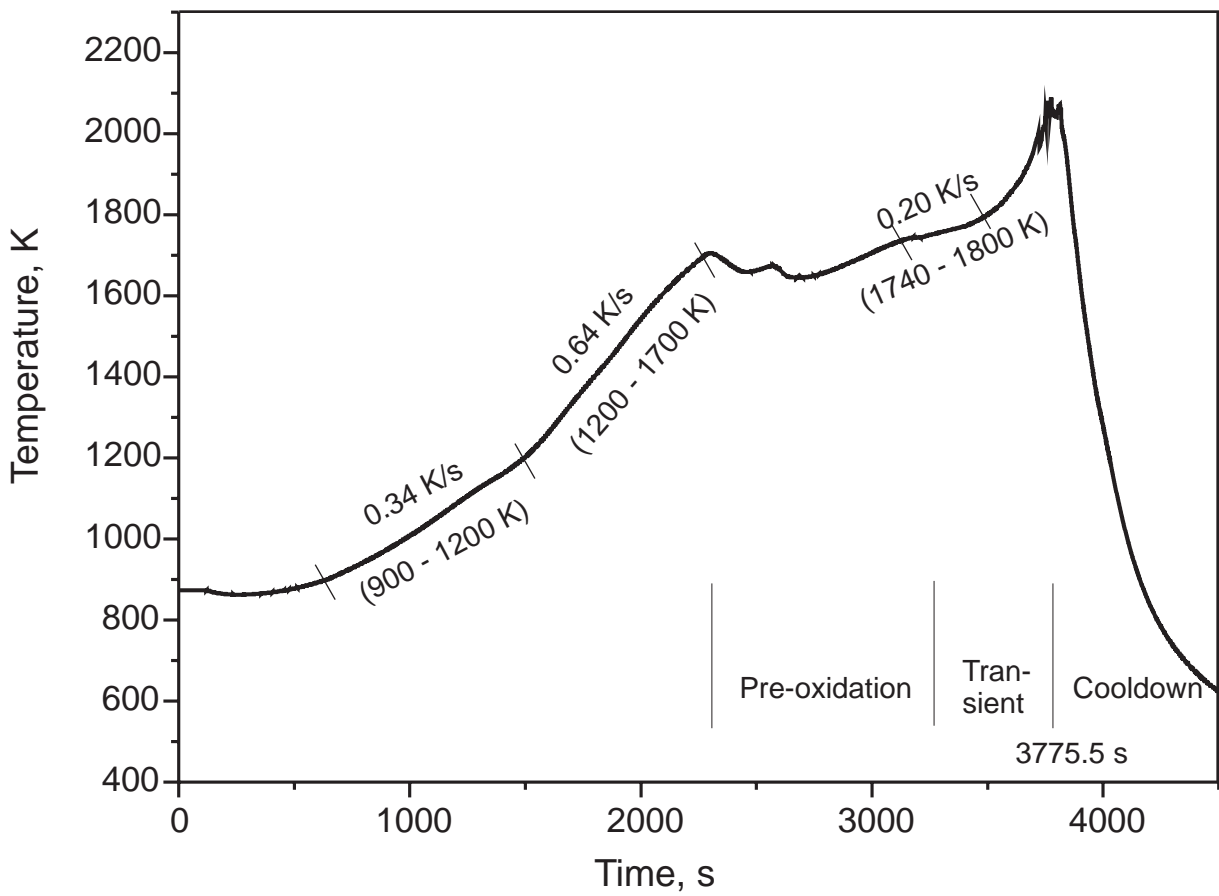
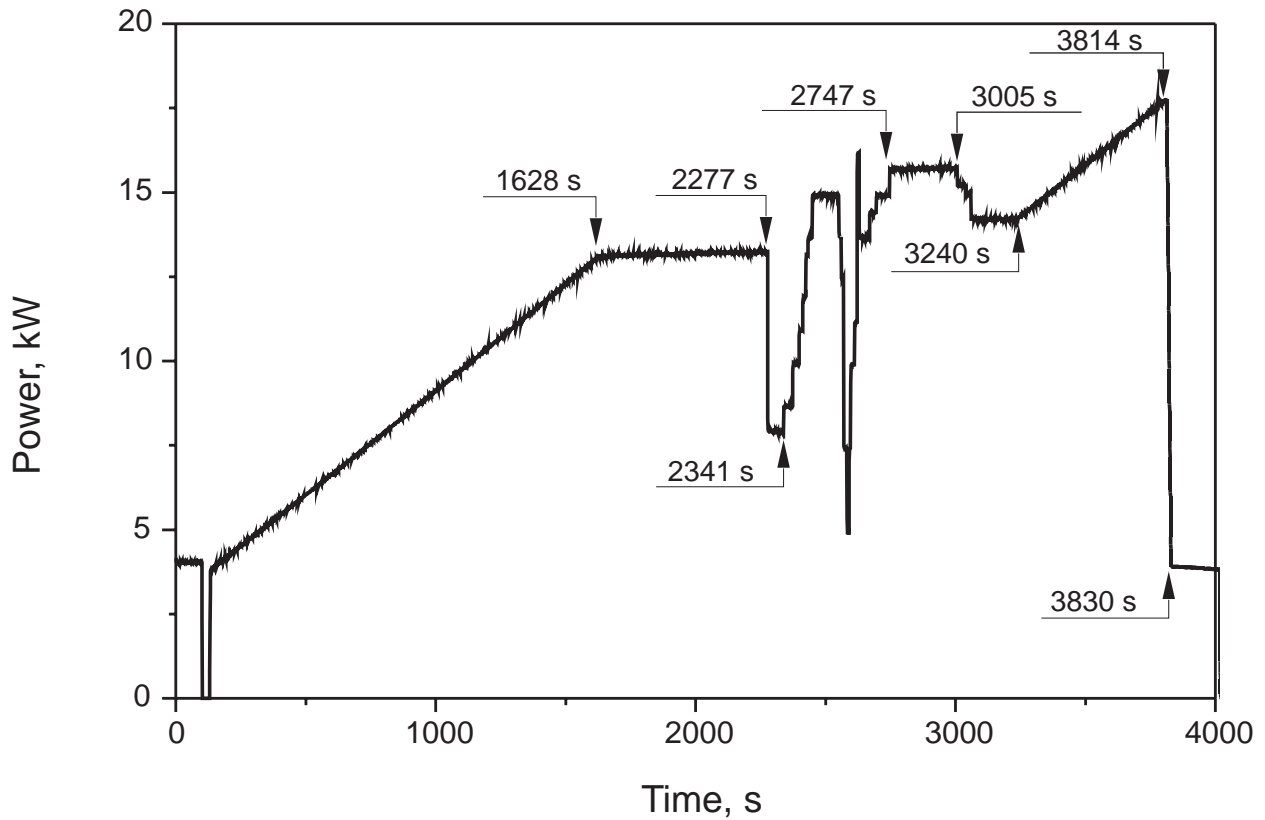


Fig.20-QUE08-Leistung.cdr
28.07.05 - IMF

Fig. 20: QUENCH-08; Total electric power vs. time, top, and heating rates evaluated from the readings of TIT A/13 together with test phase indication, bottom.

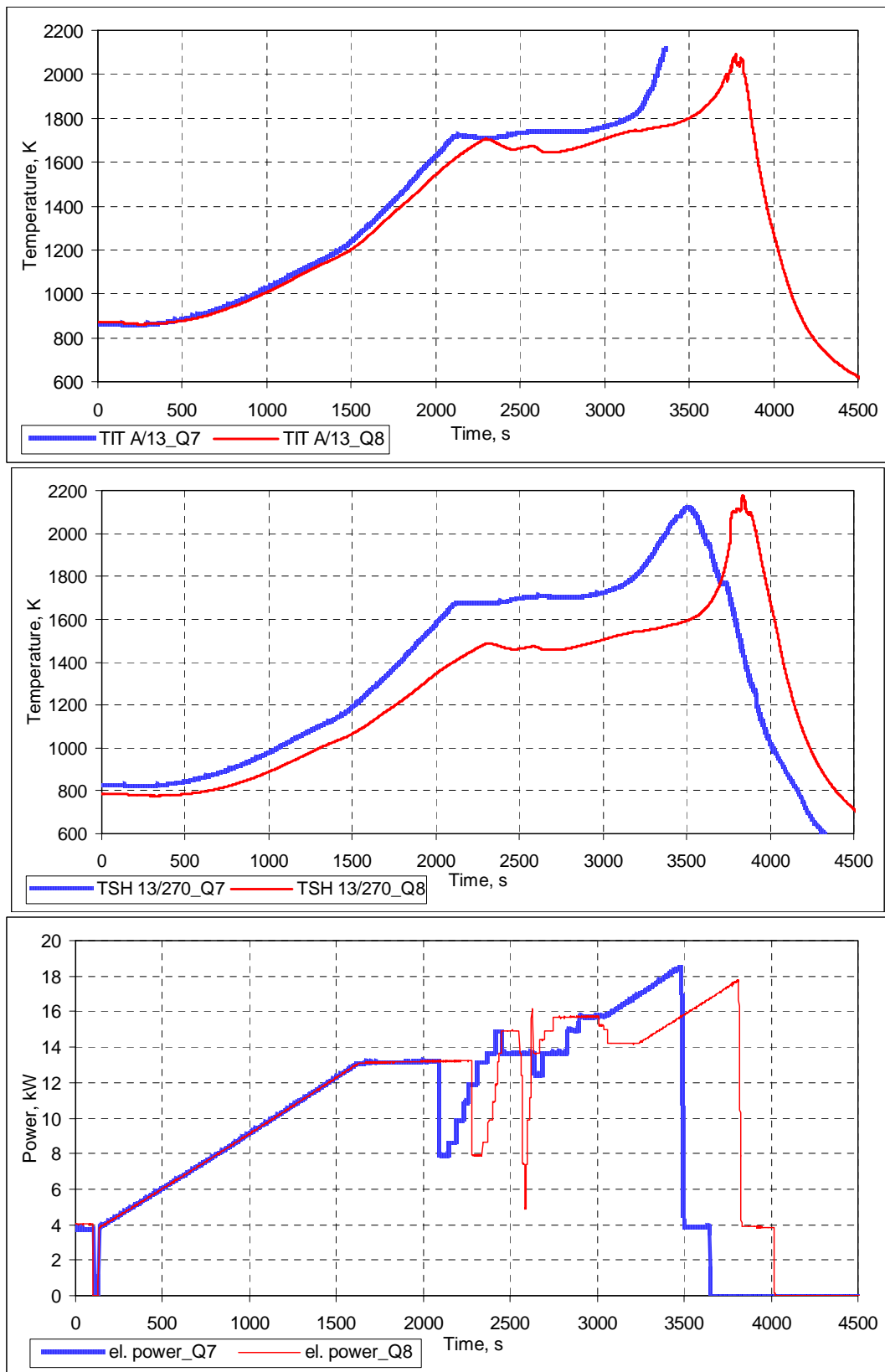


Fig 21-QU08 Stuckert.doc
26.07.05 - IMF

Fig. 21: QUENCH-08 test conduct compared to that of QUENCH-07 (rod cladding temperature data of level 950 mm, top, shroud temperature data of level 950 mm, center, and electric bundle power history, bottom).

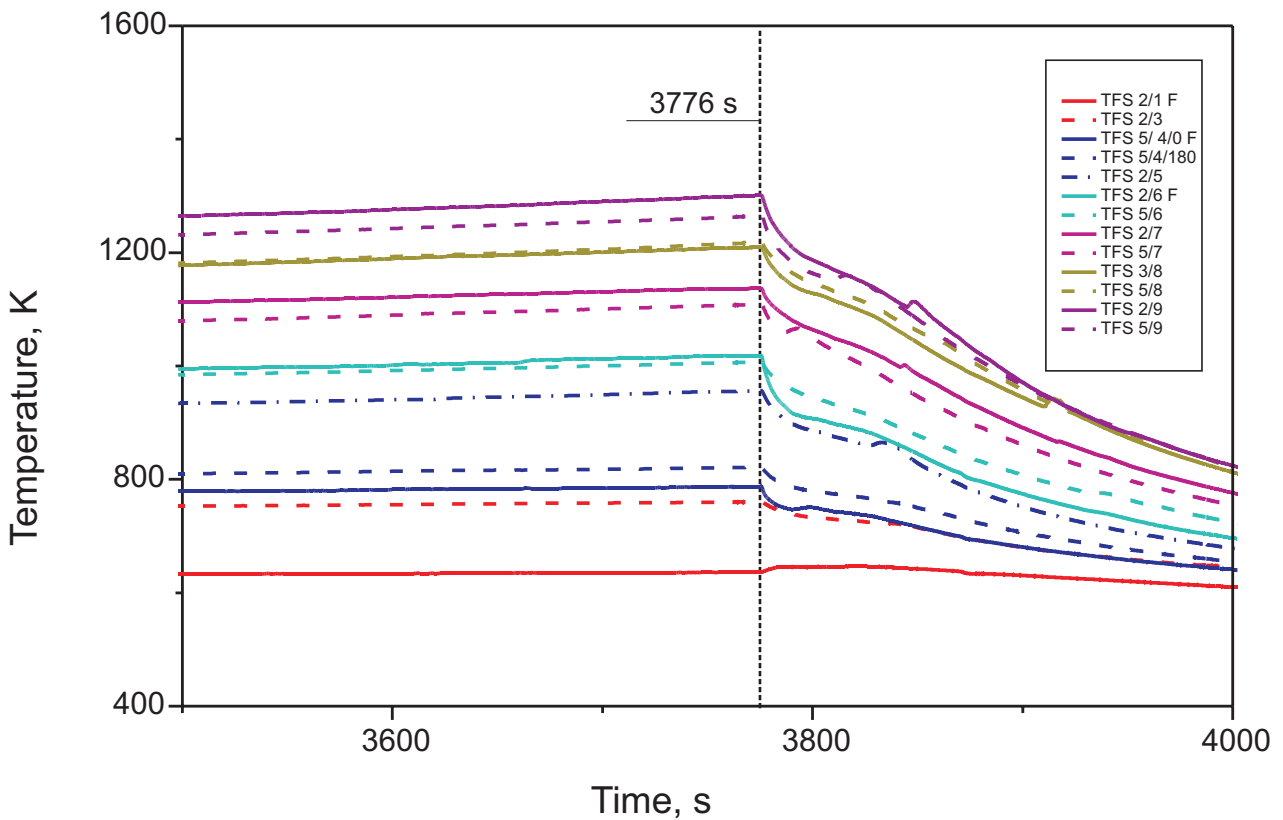
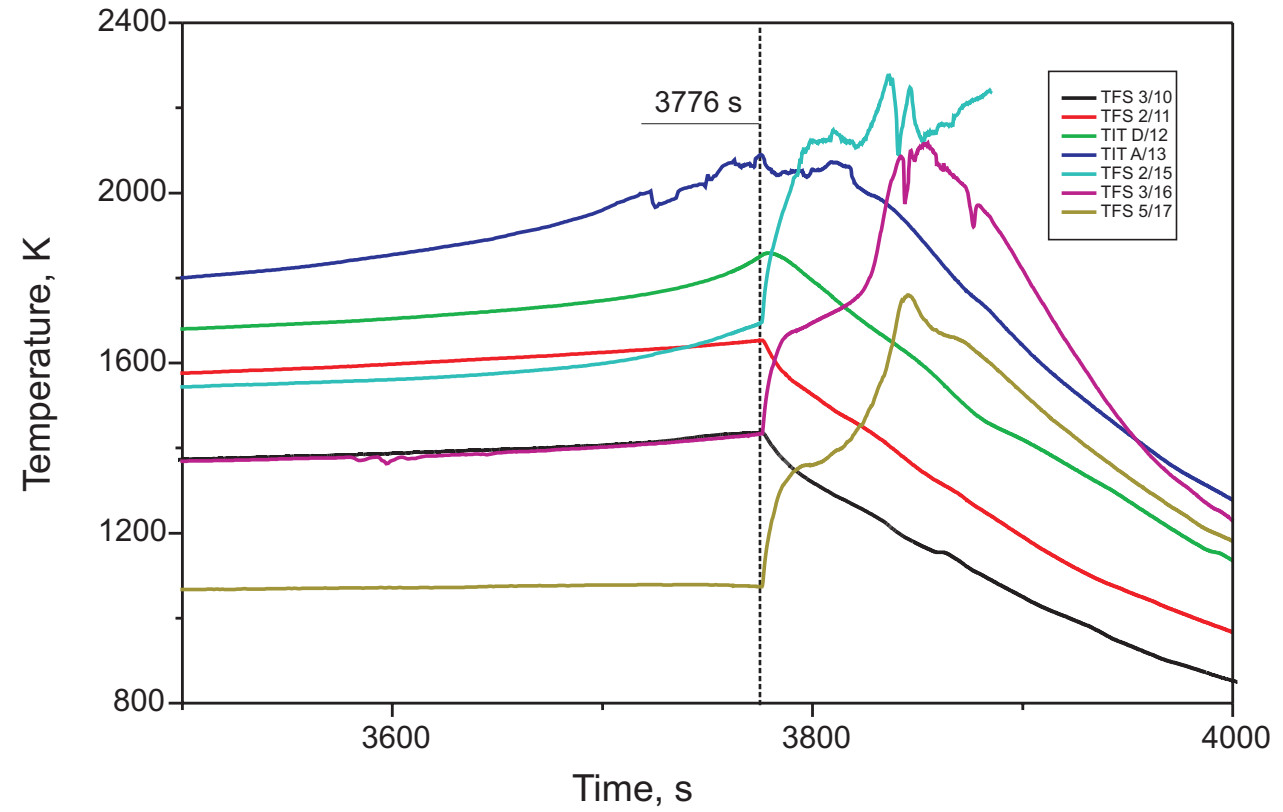


Fig 22-QUE08-alle TFS.cdr
11.07.05 - IMF

Fig. 22: QUENCH-08; Temperature response of cladding thermocouples before and during the quenching phase

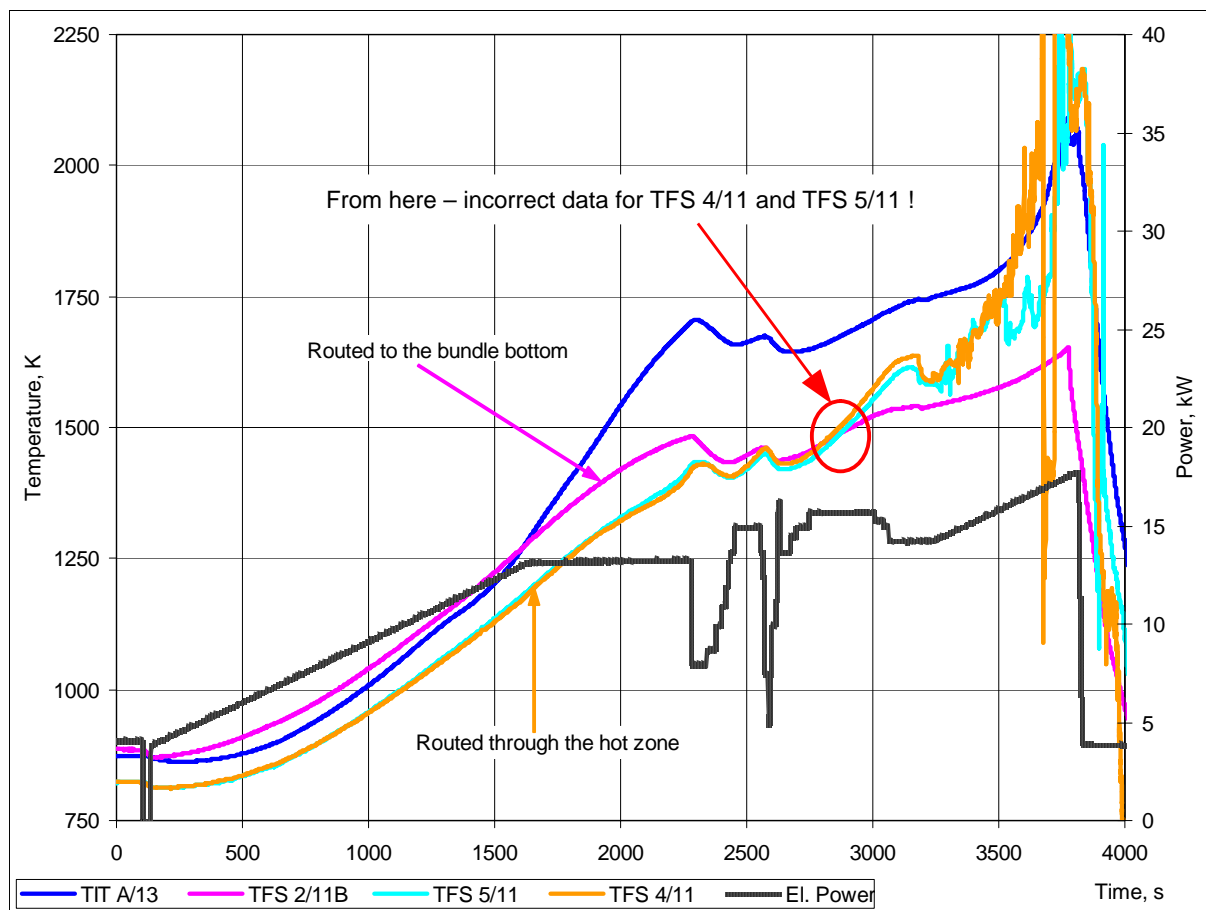


Fig 24-QU08 Stuckert.doc
11.07.05 - IMF

Fig. 23: QUENCH-08; Influence of the “hot zone effect” on the TFS thermocouple readings.

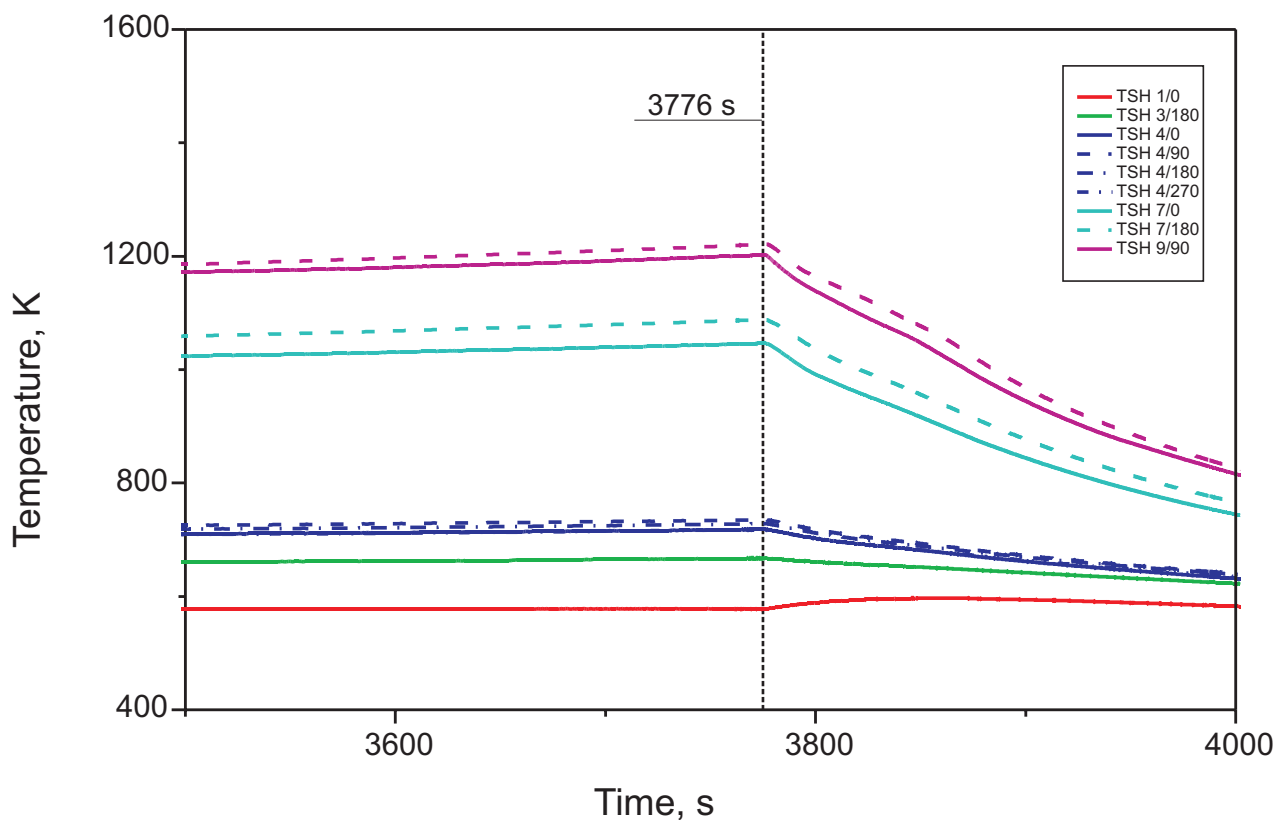
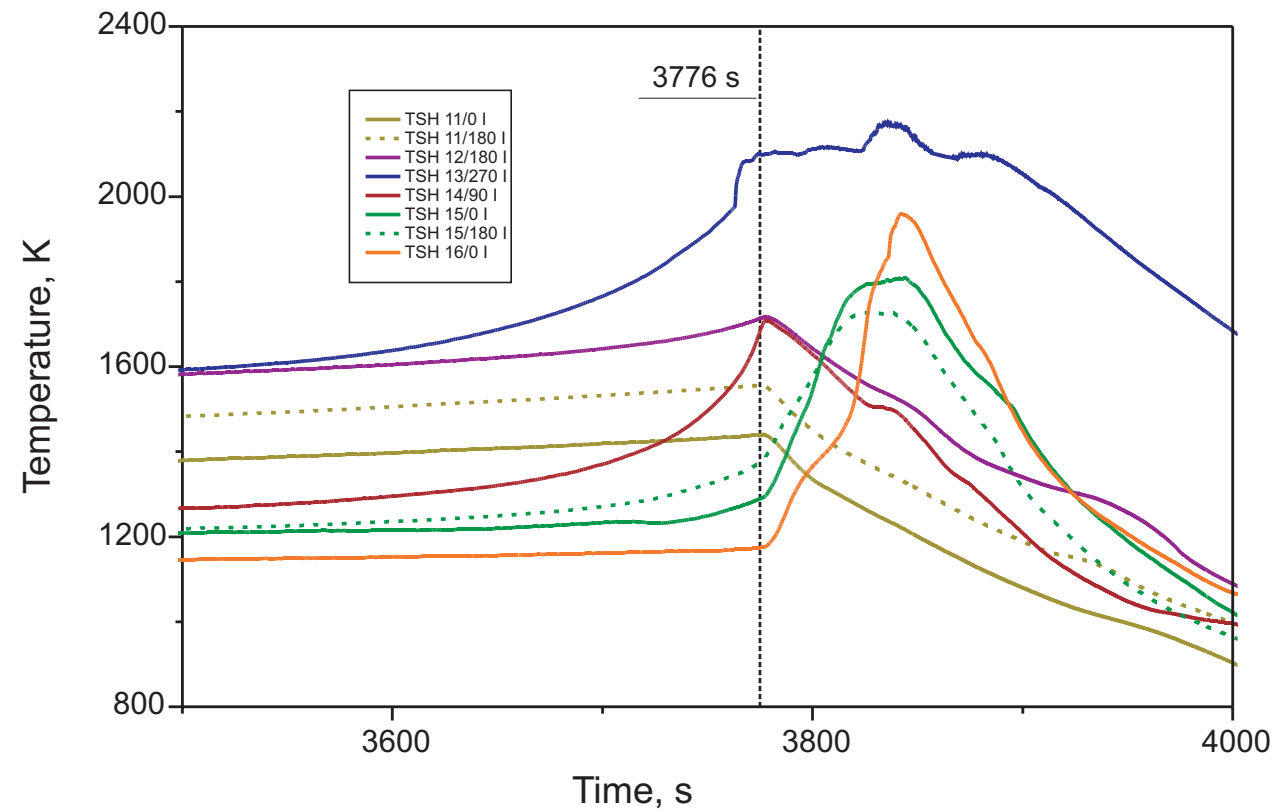


Fig 24-QUE08-alle TSH.cdr
11.07.05 - IMF

Fig. 24: QUENCH-08; Temperature response of the shroud thermocouples before and during the quenching phase

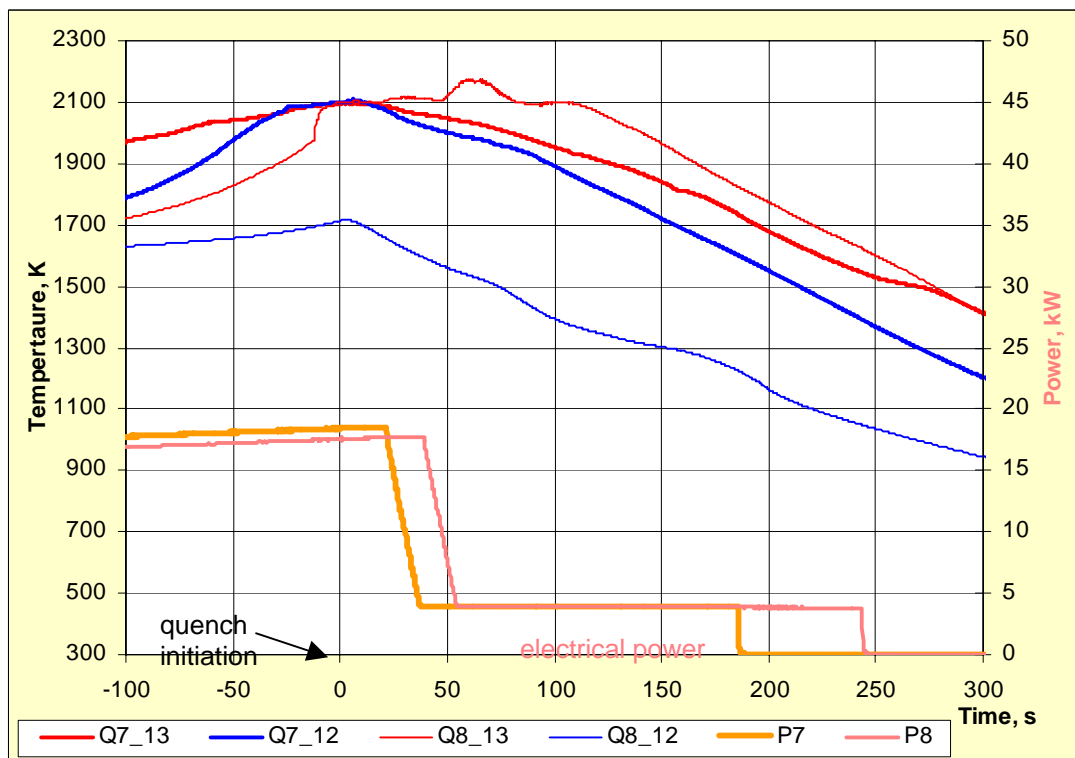
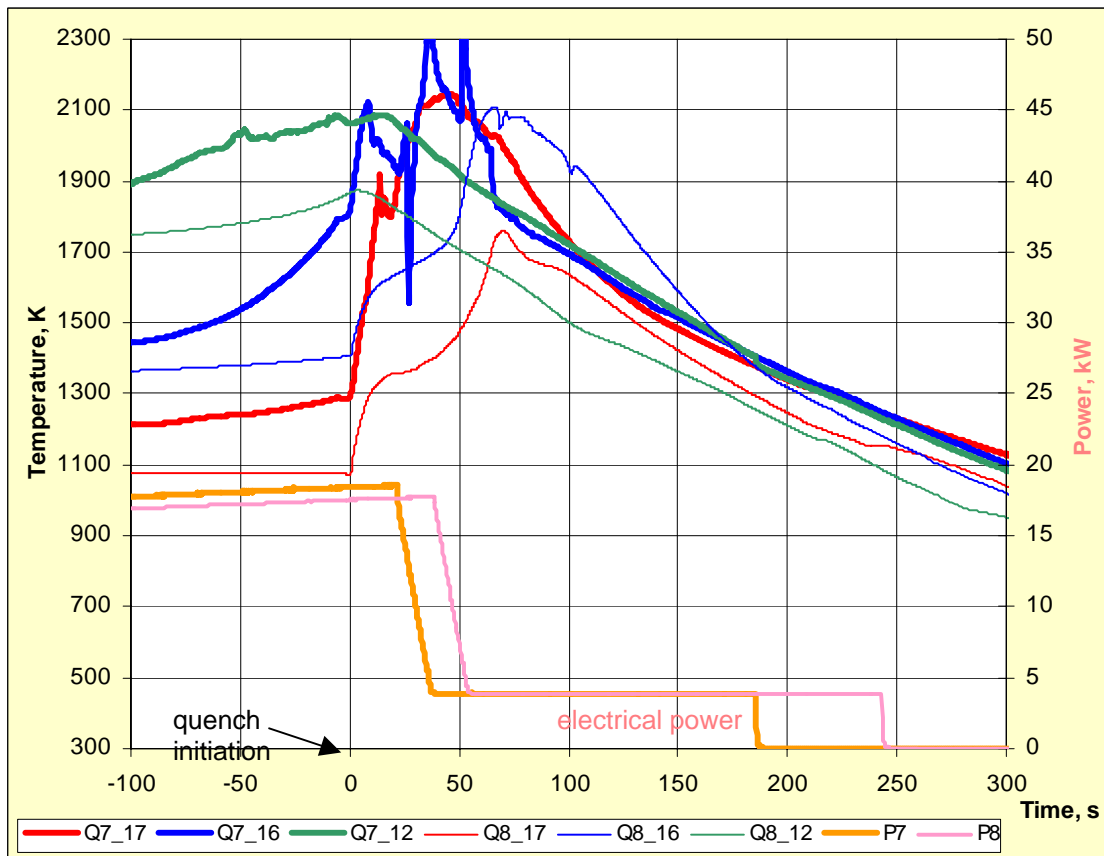


Fig. 25

Comparison of average bundle temperatures at elevations 12, 16, 17, top, and shroud temperatures at elevations 12, 13, bottom, together with the bundle power history, during the transient and cooldown phases of QUENCH-07 (thick lines) and QUENCH-08 (thin lines).

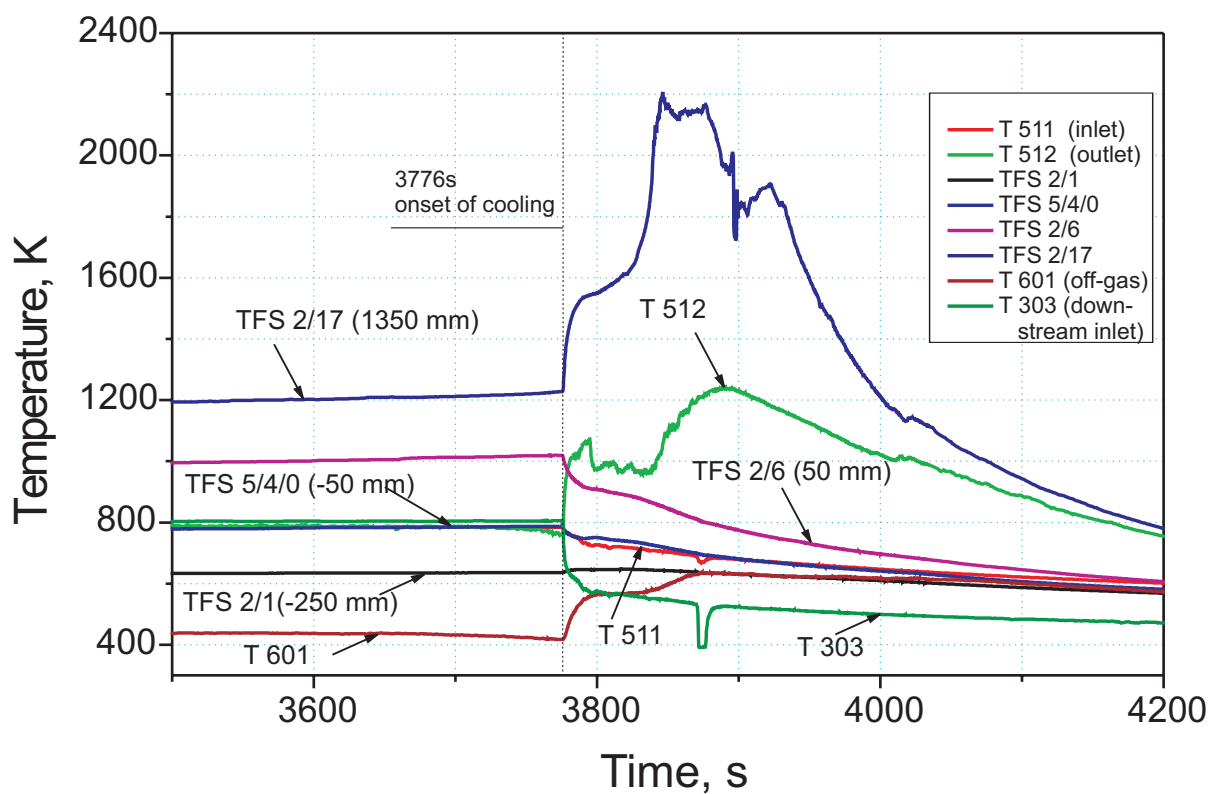


Fig. 26-QUE08-anlage T511
14.04.05 - IMF

Fig. 26: QUENCH-08; Coolant inlet and outlet temperatures, bundle fluid temperatures, and off-gas temperature T 601.

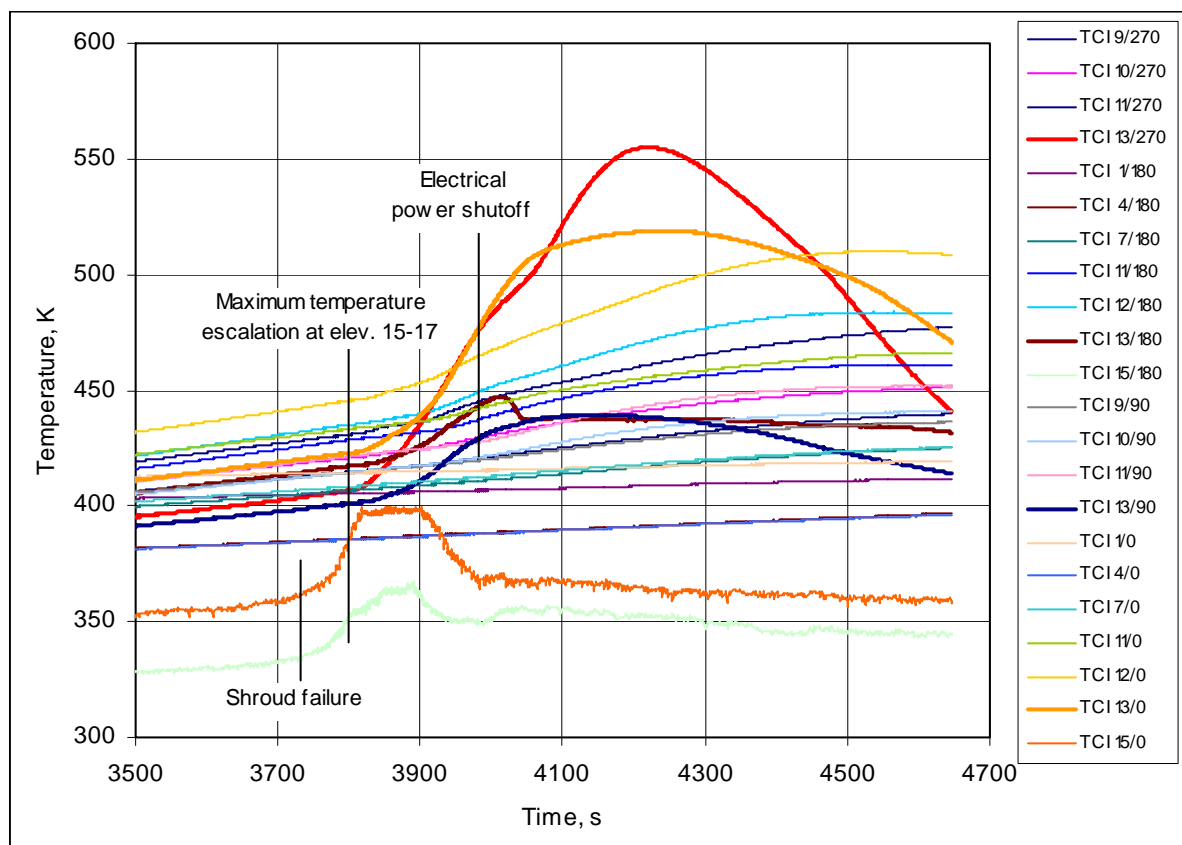
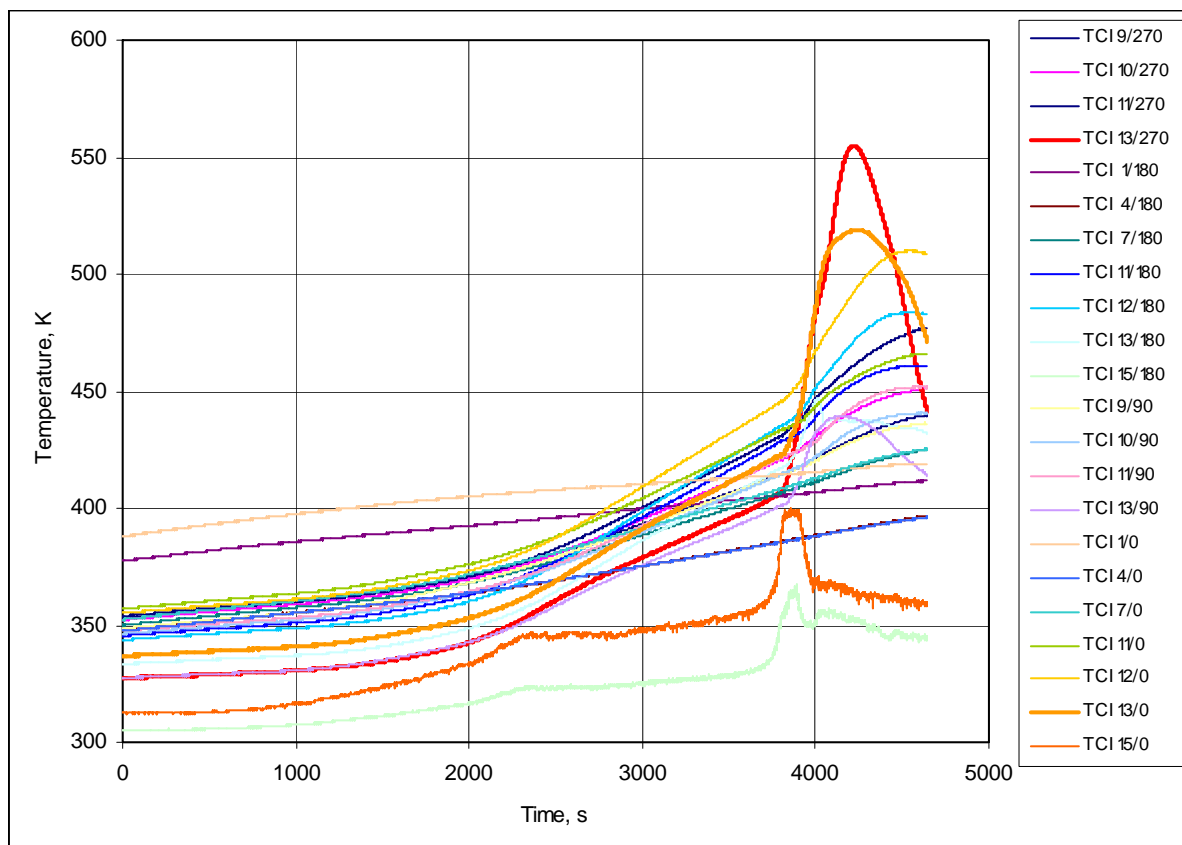


Fig 27-QU08 Stuckert.doc
10.12.03 - IMF

Fig. 27: QUENCH-08; Overview of the TCI (inner cooling jacket) temperatures

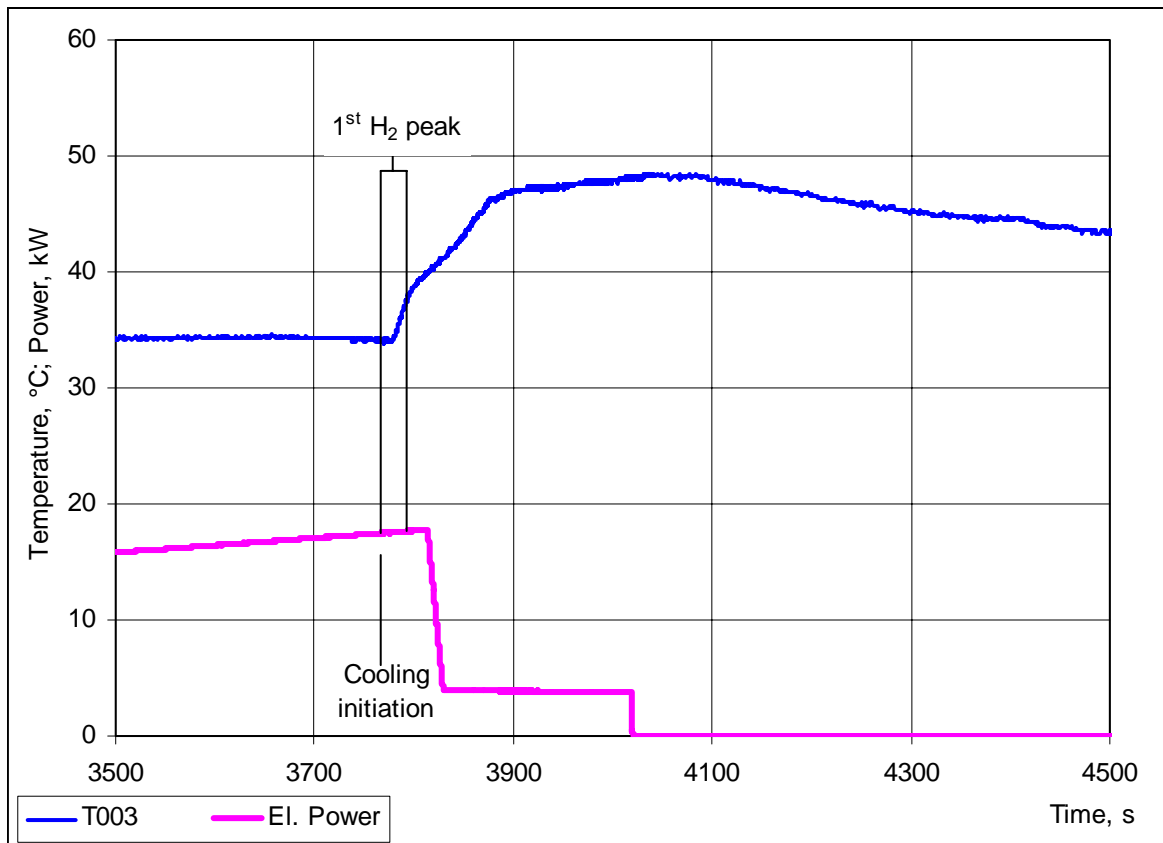
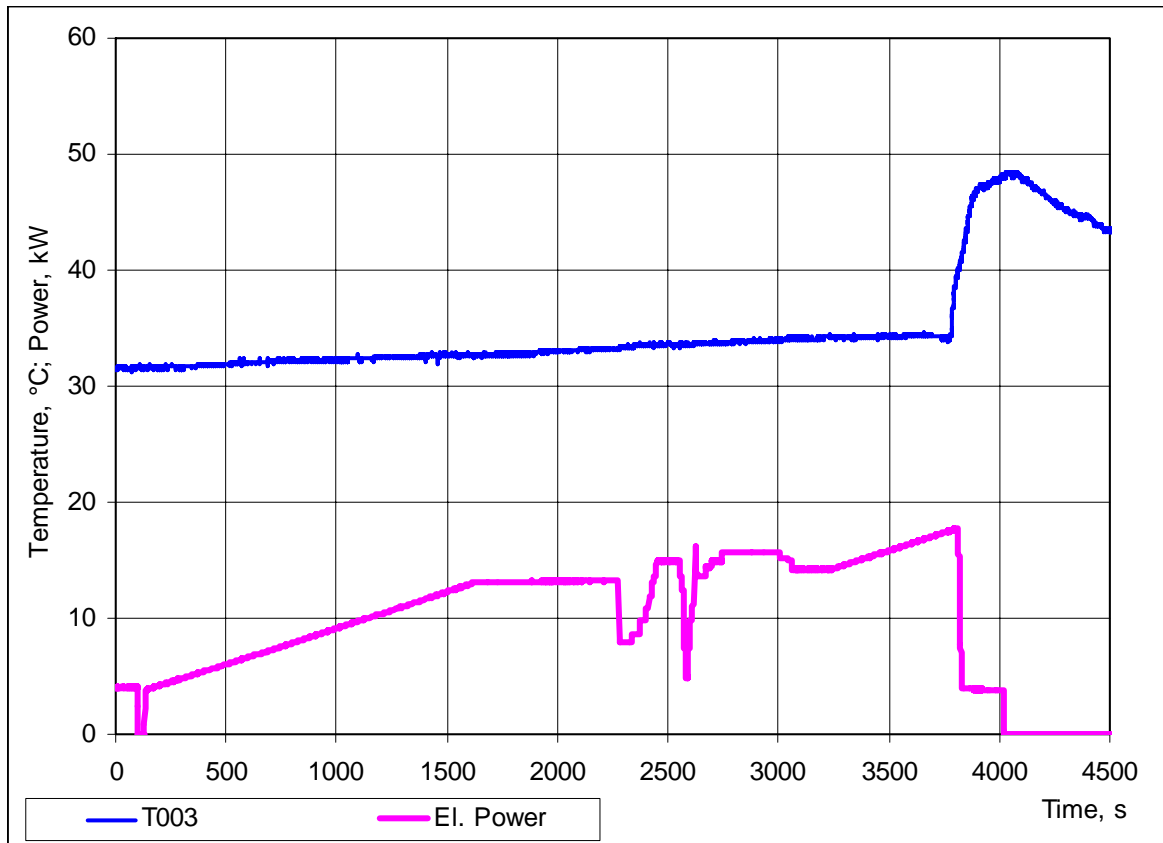


Fig 28-QU08 Stuckert.doc
10.12.03 - IMF

Fig. 28: QUENCH-08; Cooling water outlet temperature of the off-gas pipe (T003) together with electric power history.

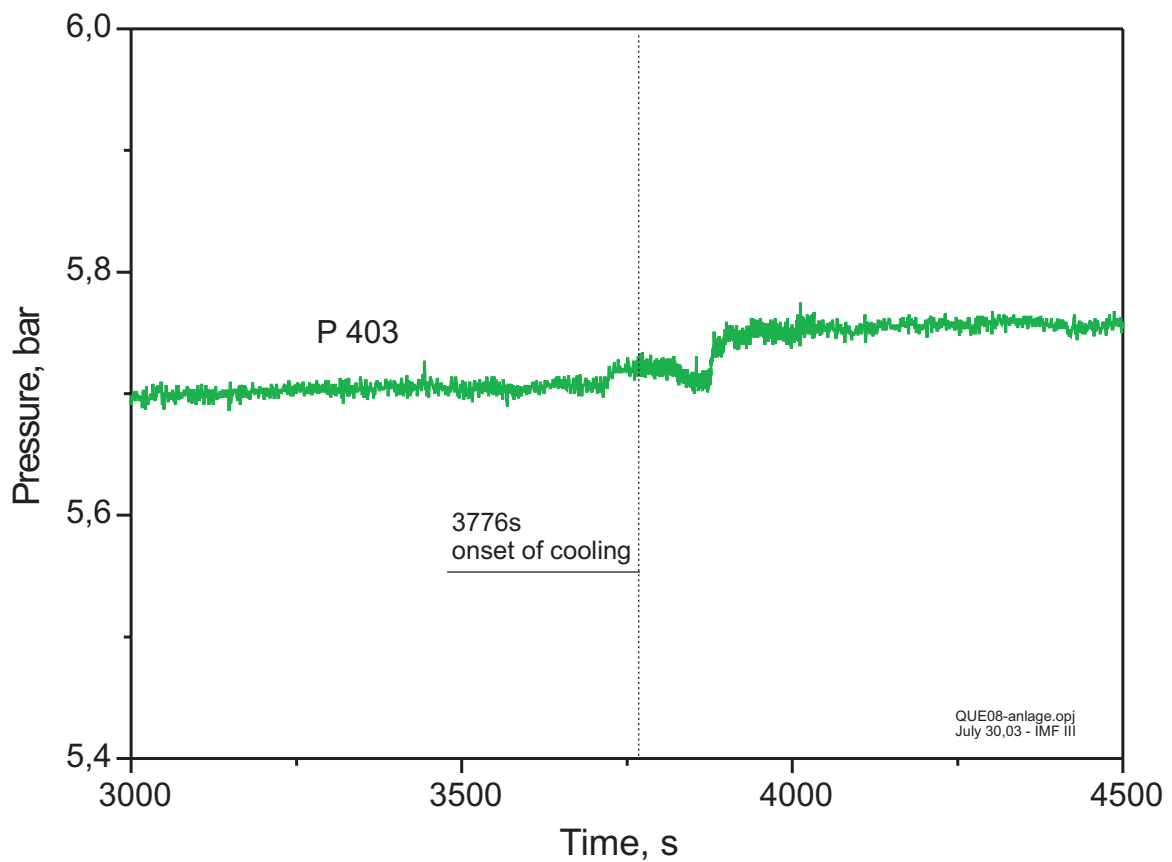
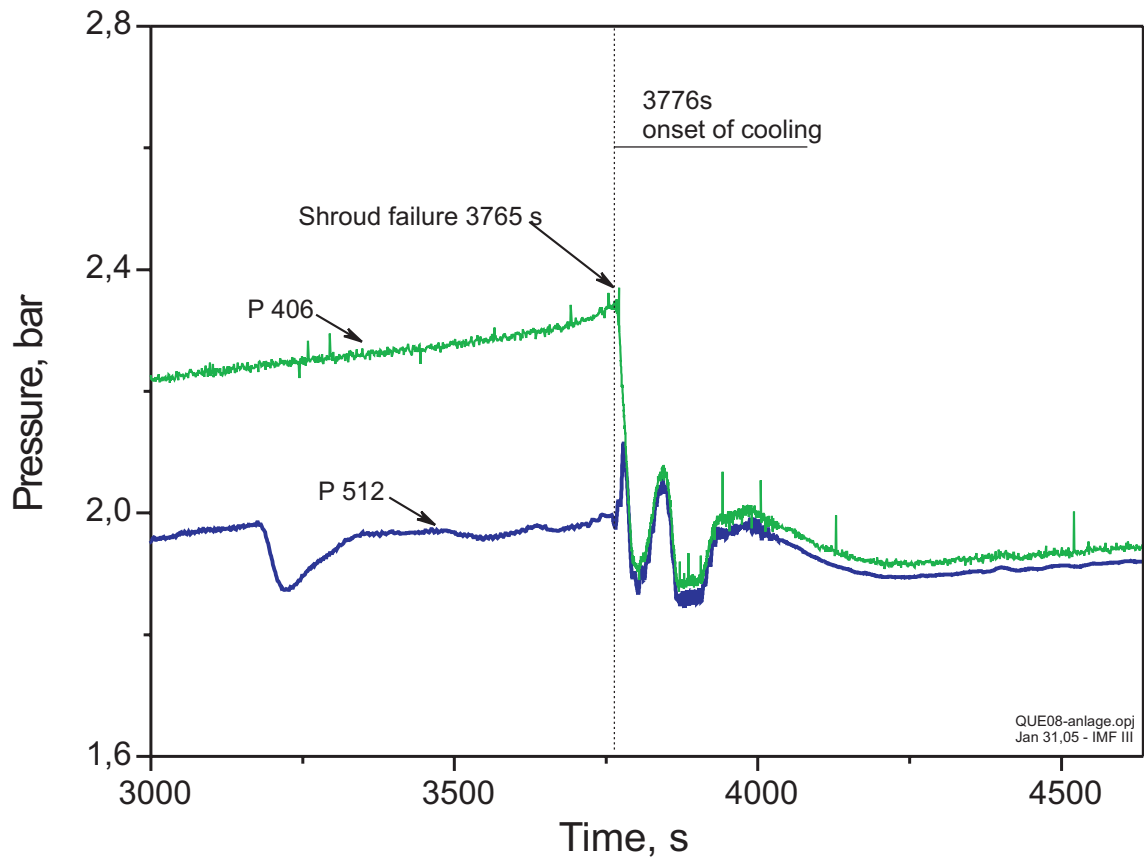


Fig. 29: QUENCH-08; Shroud failure indicated by the shroud insulation pressure (P 406) together with the system pressure P 512, top, and argon coolant pressure in the cooling jacket (P 403), bottom.

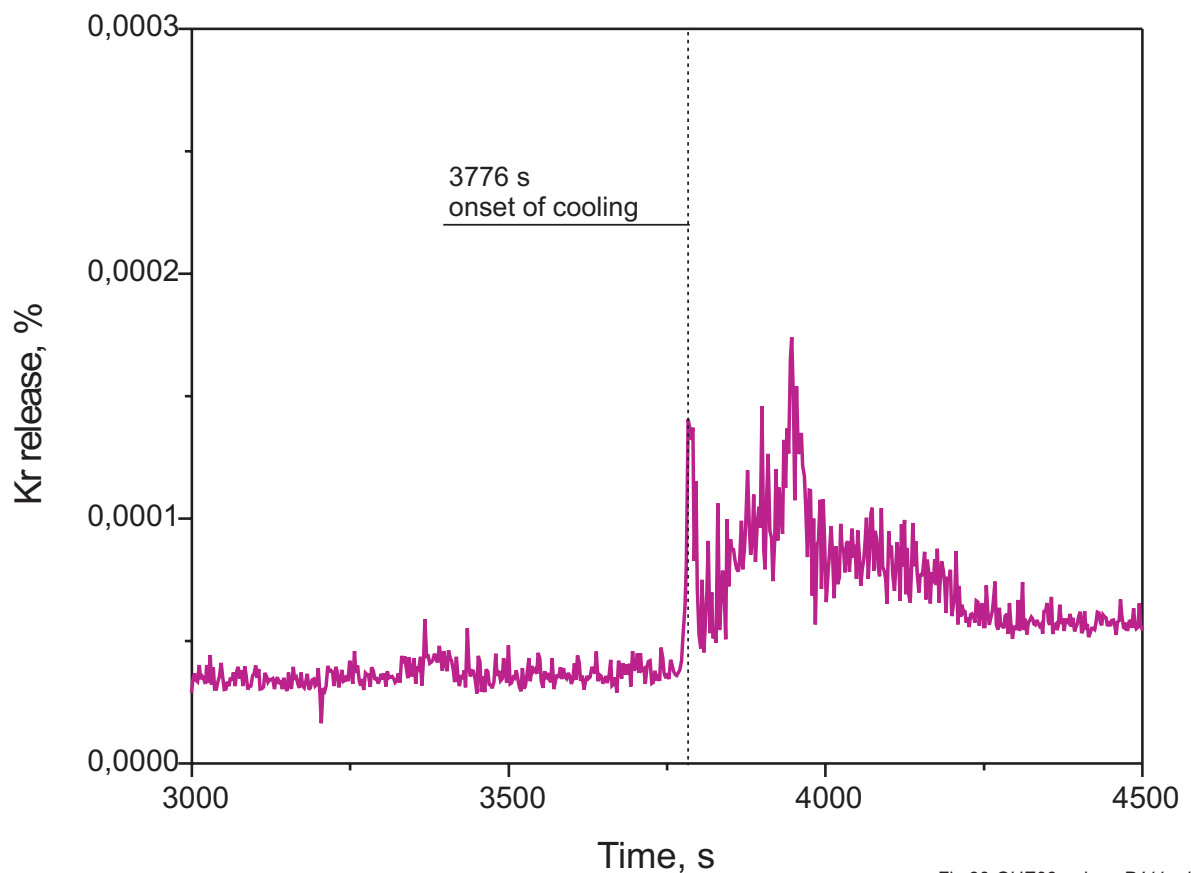
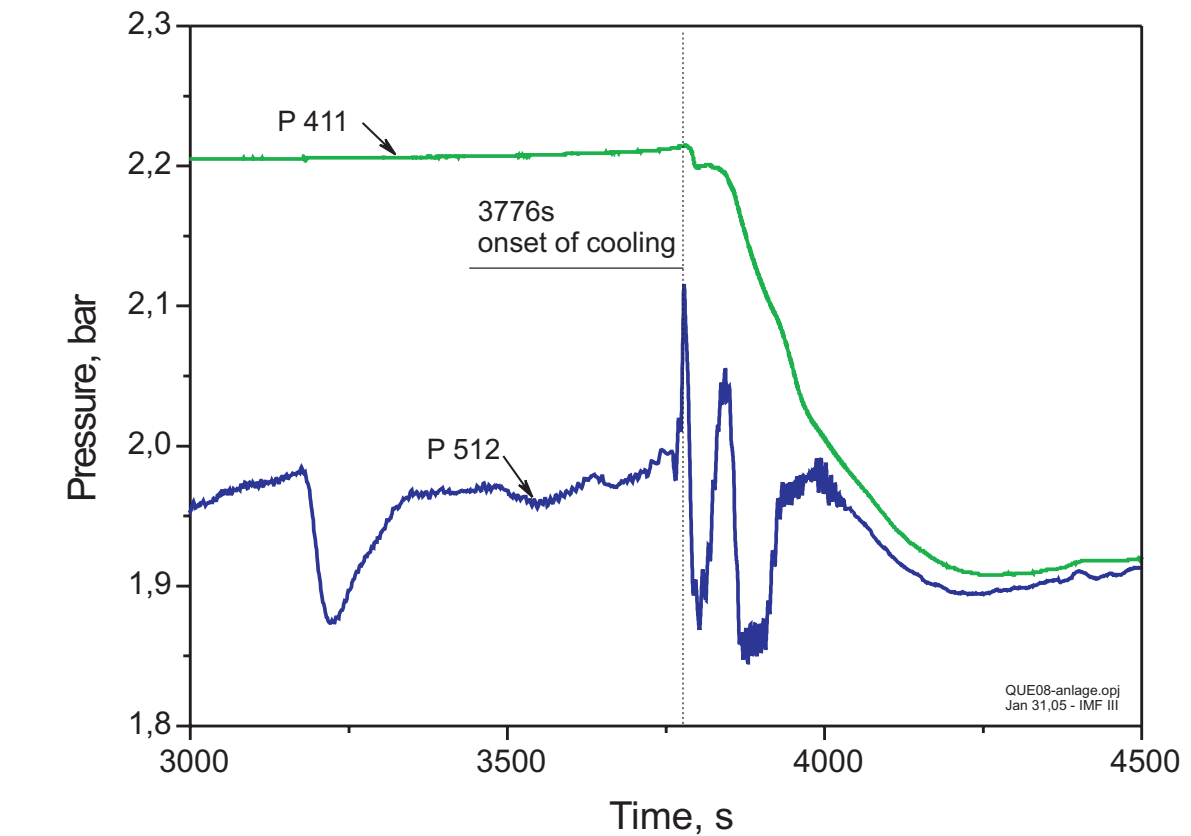


Fig 30-QUE08-anlage P411.cdr
31.01.05 - IMF

Fig. : 30 QUENCH-08; Rod cladding failure indicated by the rod internal pressure (P 411) together with the system pressure P 512, top, and by the krypton release measured by MS GAM 300, bottom.

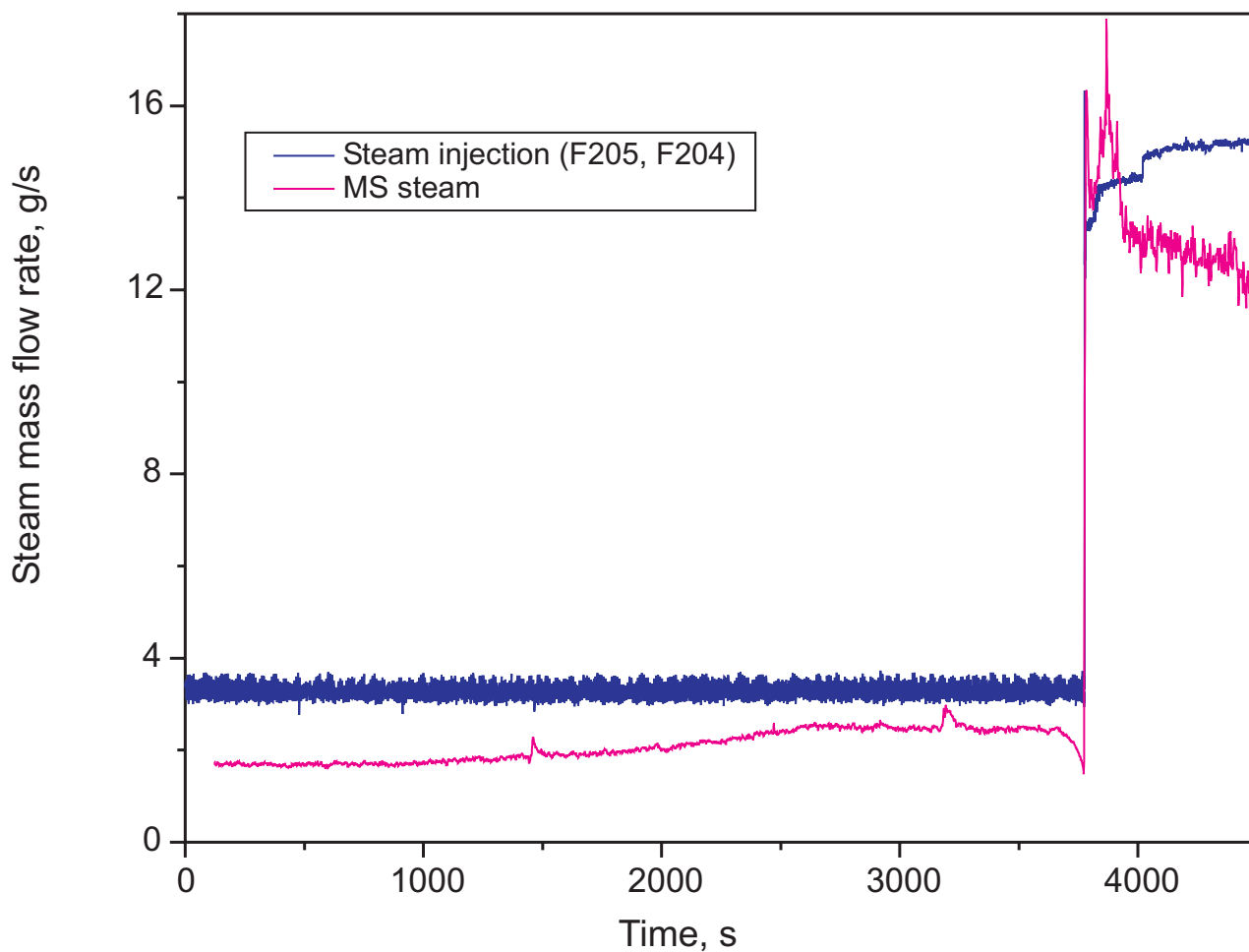


Fig. 31-QUE08-anlage_wasserstoff-gase4.cdr
17.03.05 - IMF

Fig. 31: QUENCH-08; Steam flow rate based on flow meters F 205 (before cooldown) and F 204 (during cooldown) compared to the steam flow rate measured by the MS GAM 300.

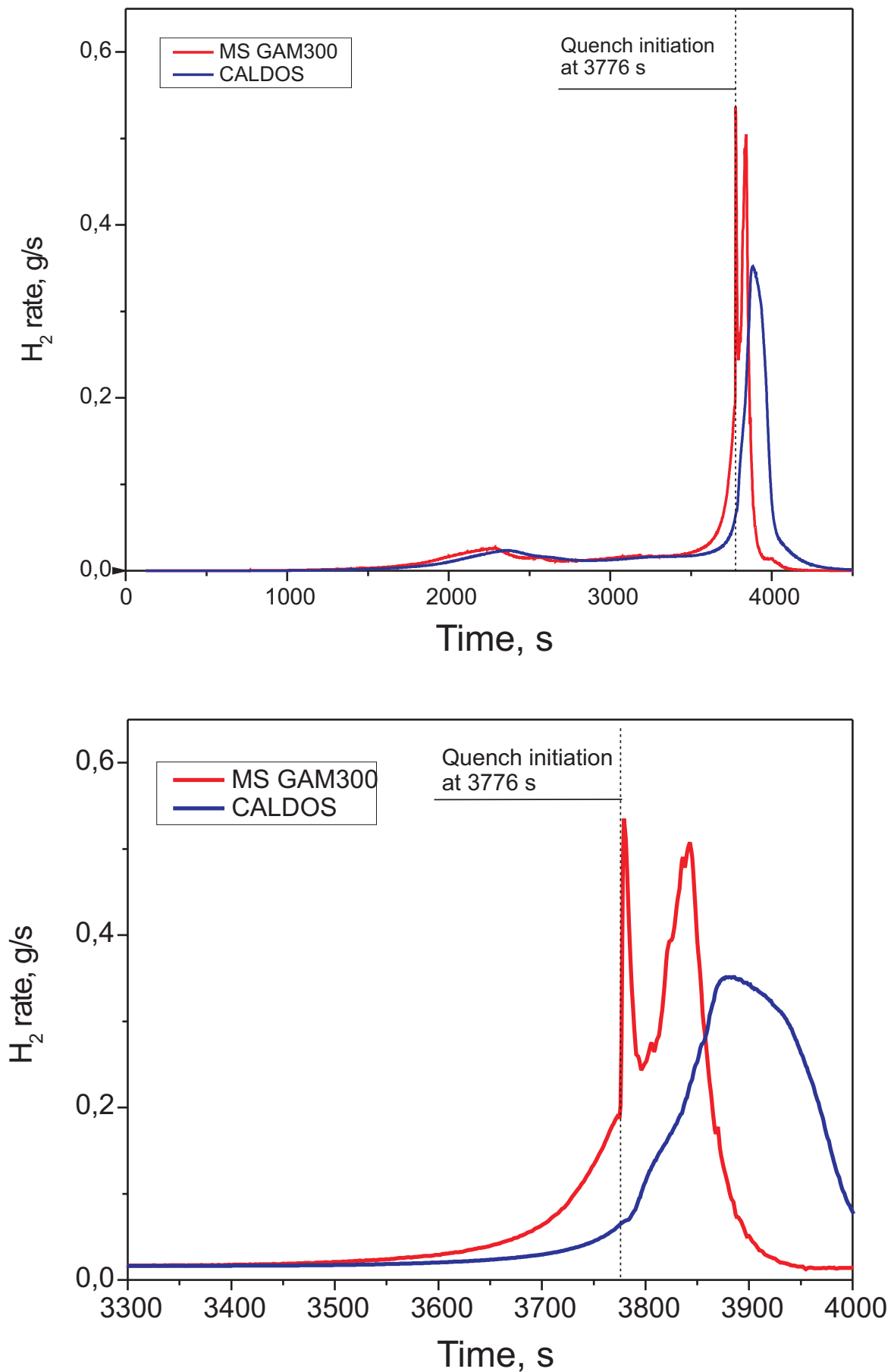


Fig. 32-QUE08-wasserstoff-gase-2+5.cdr
21.04.05 - IMF

Fig. 32: QUENCH-08; Hydrogen generation rate vs. time measured by the mass spectrometer (MS GAM 300) and by the CALDOS analyzer.

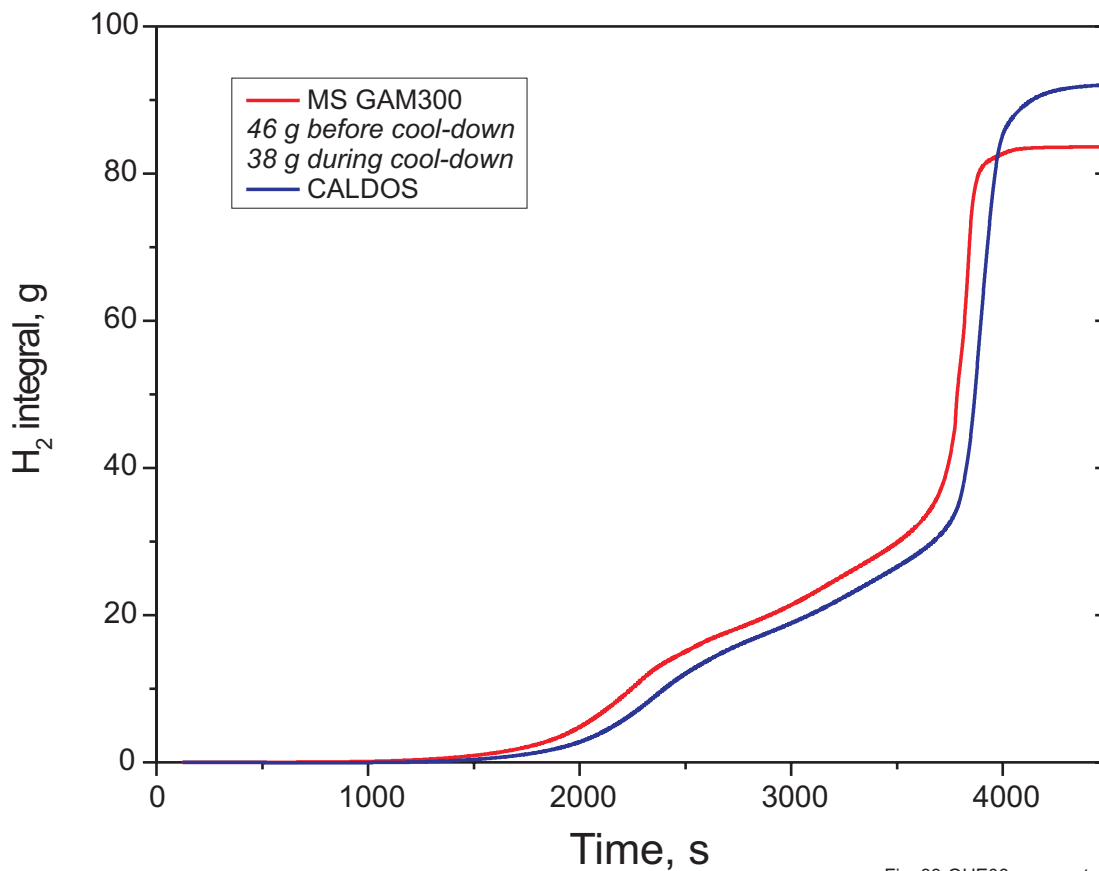
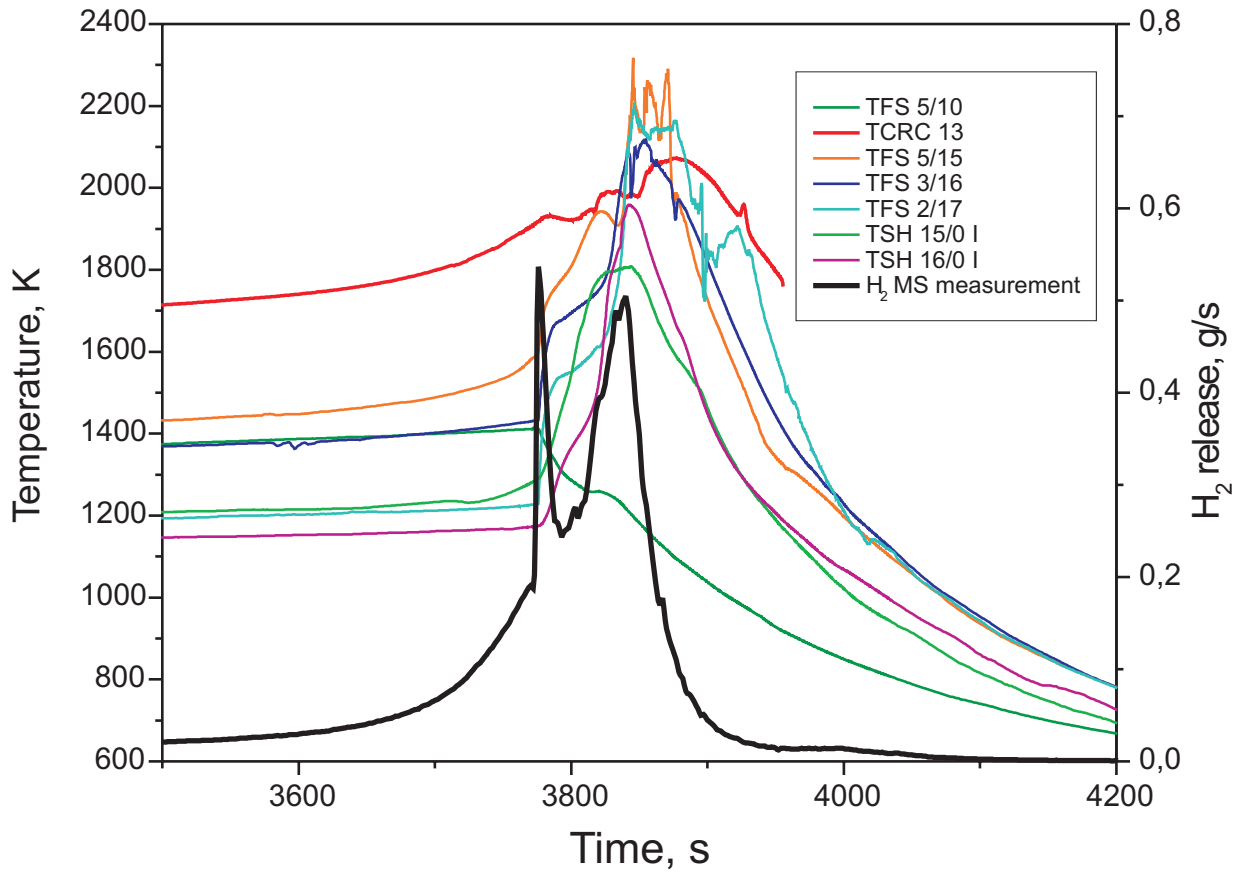


Fig. 33-QUE08-wasserstoff-gase-10+1.cdr
17.03.05 - IMF

Fig. 33: QUENCH-08; Hydrogen generation rate measured by the mass spectrometer (MS GAM 300) together with selected temperatures vs. time, top, and accumulated H₂ measured by the MS GAM 300 and by the CALDOS analyzer, bottom.

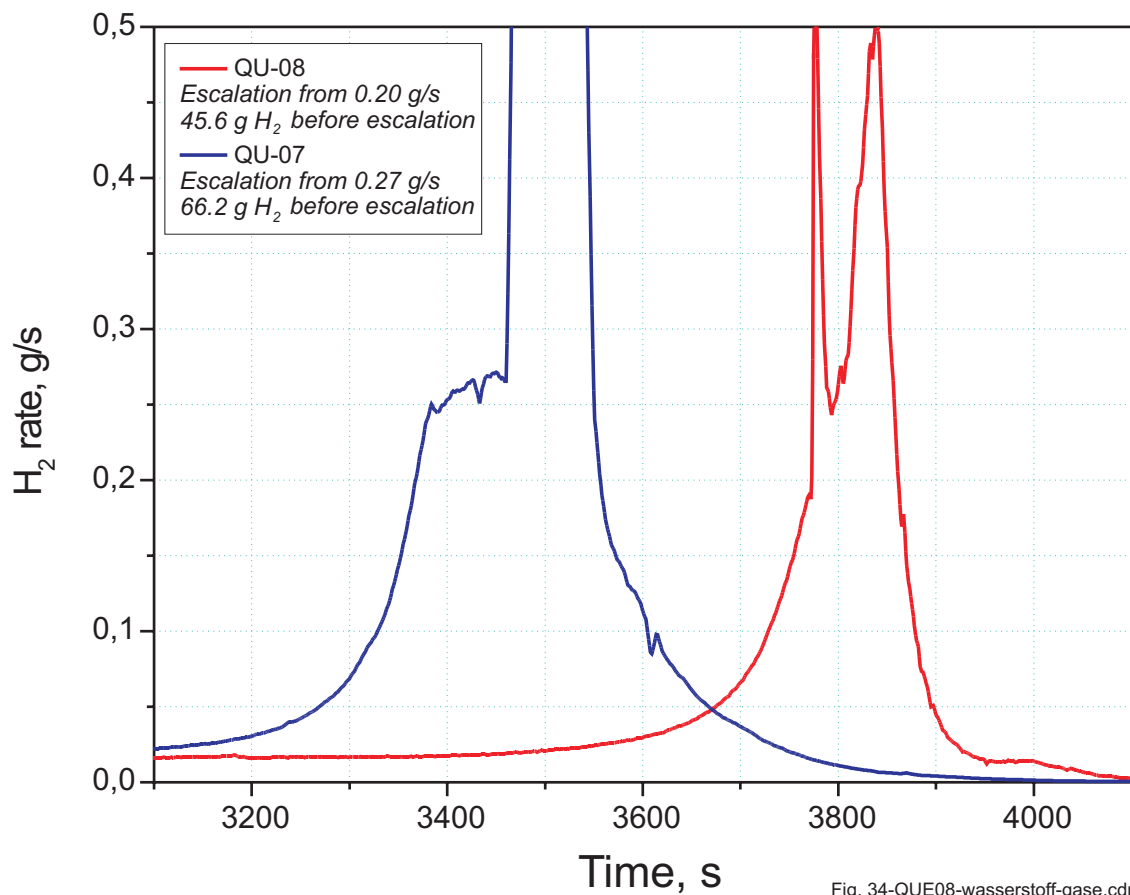
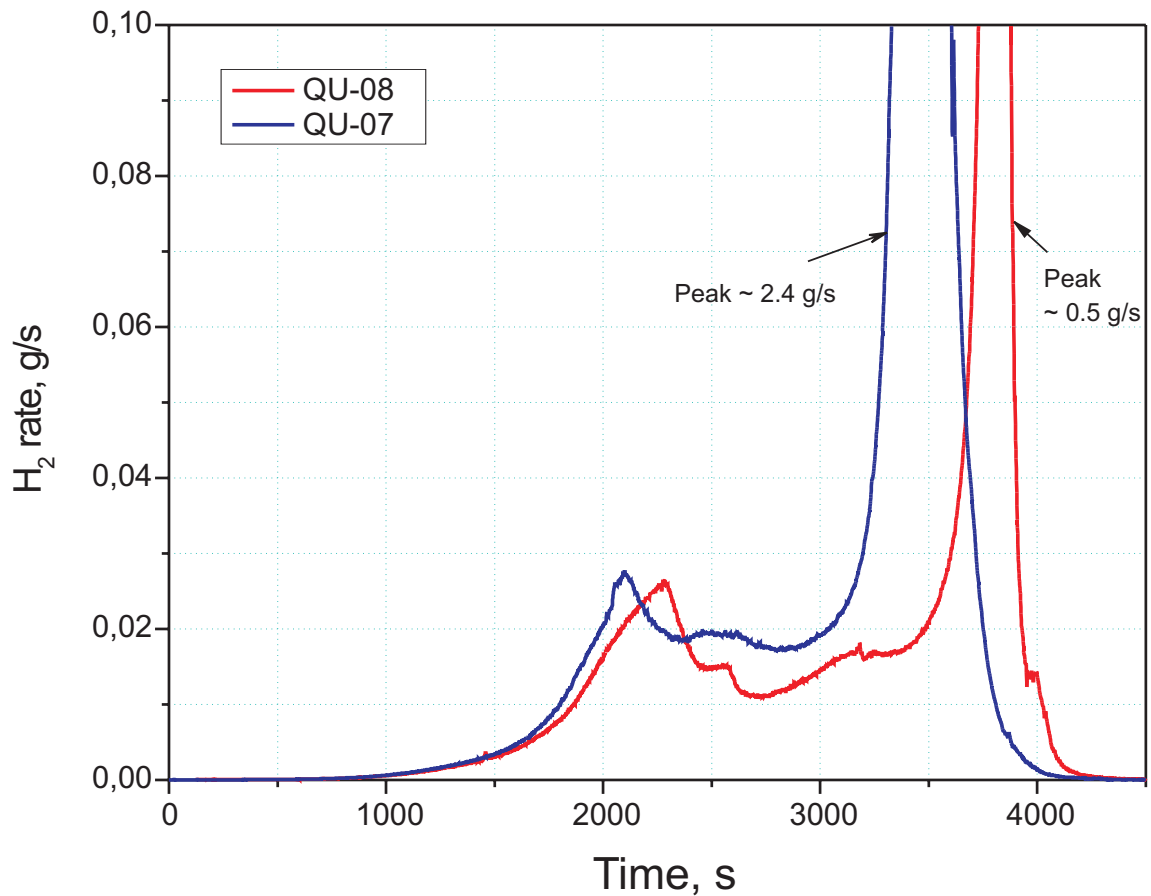


Fig. 34-QUE08-wasserstoff-gase.cdr
17.03.05 - IMF

Fig. 34: Comparison of the hydrogen generation rate vs. time measured by the MS GAM 300 for the QUENCH-07 and -08 experiments. (Note: Time scale of Quench-07 shifted to the left for 105 s to obtain identical starting point for transient).

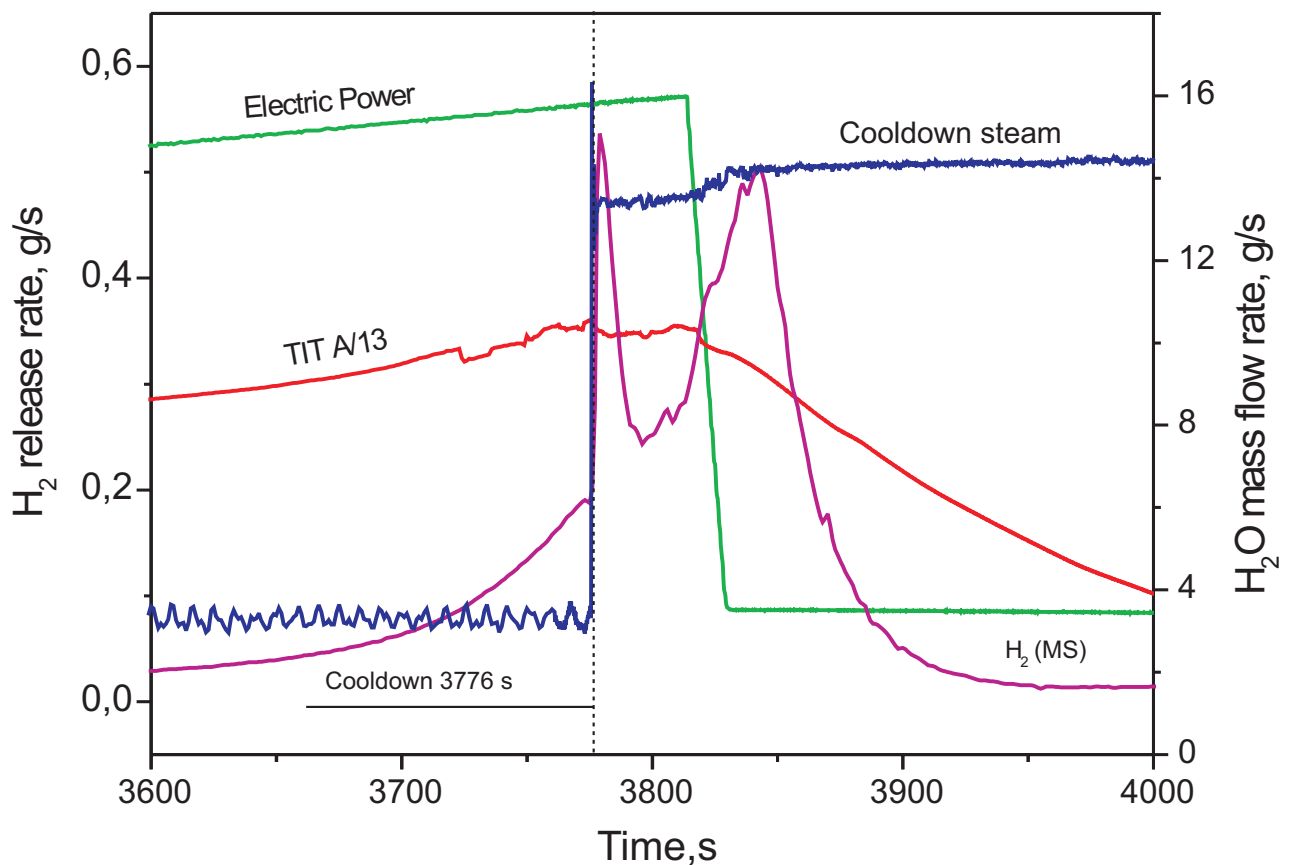
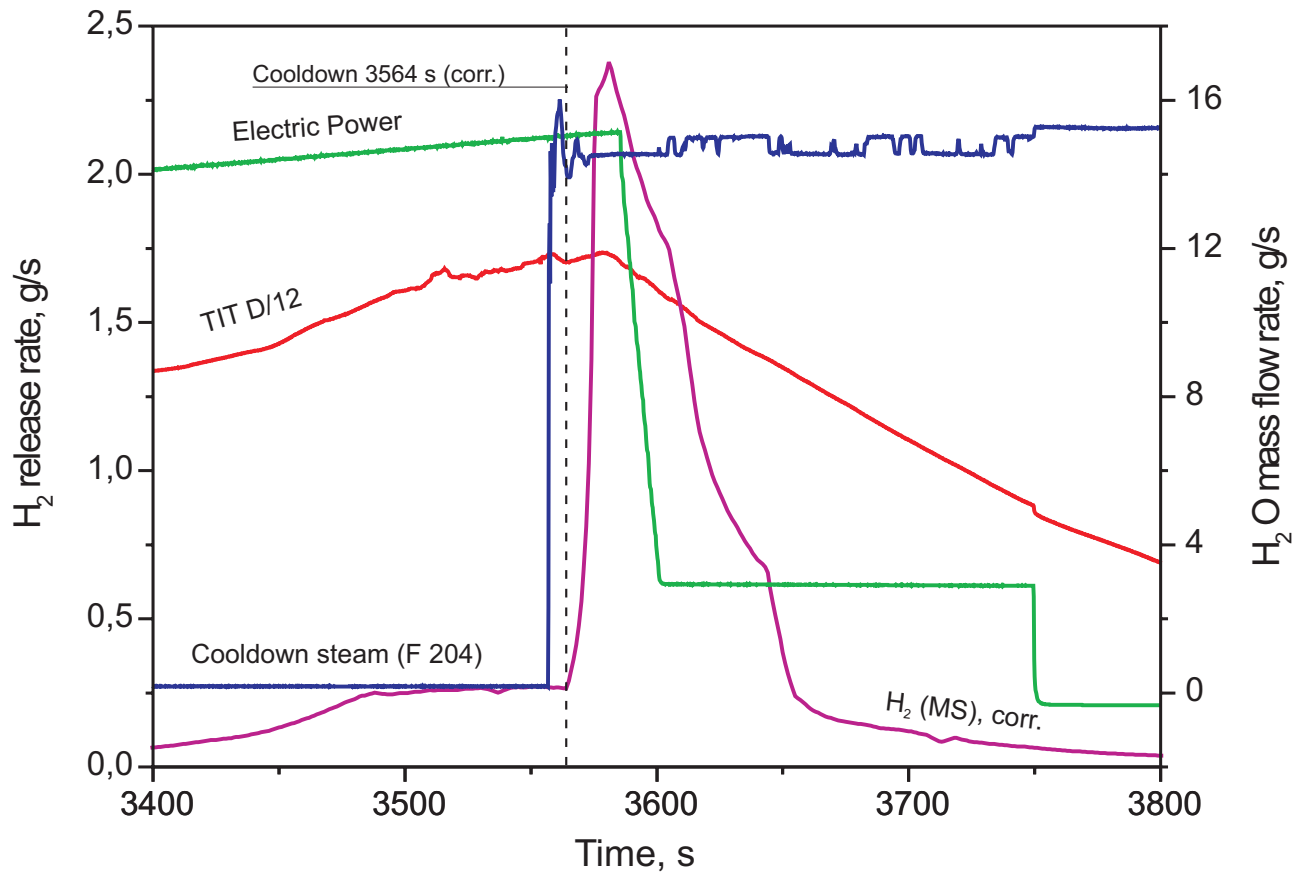


Fig 35-QUE08 Zeitbezug.cdr
21.04.05 - IMF

Fig. 35: Synopsis of power input, rod temperature, cooldown steam injection, and hydrogen generation for experiments QUENCH-07, top, and QUENCH-08, bottom.

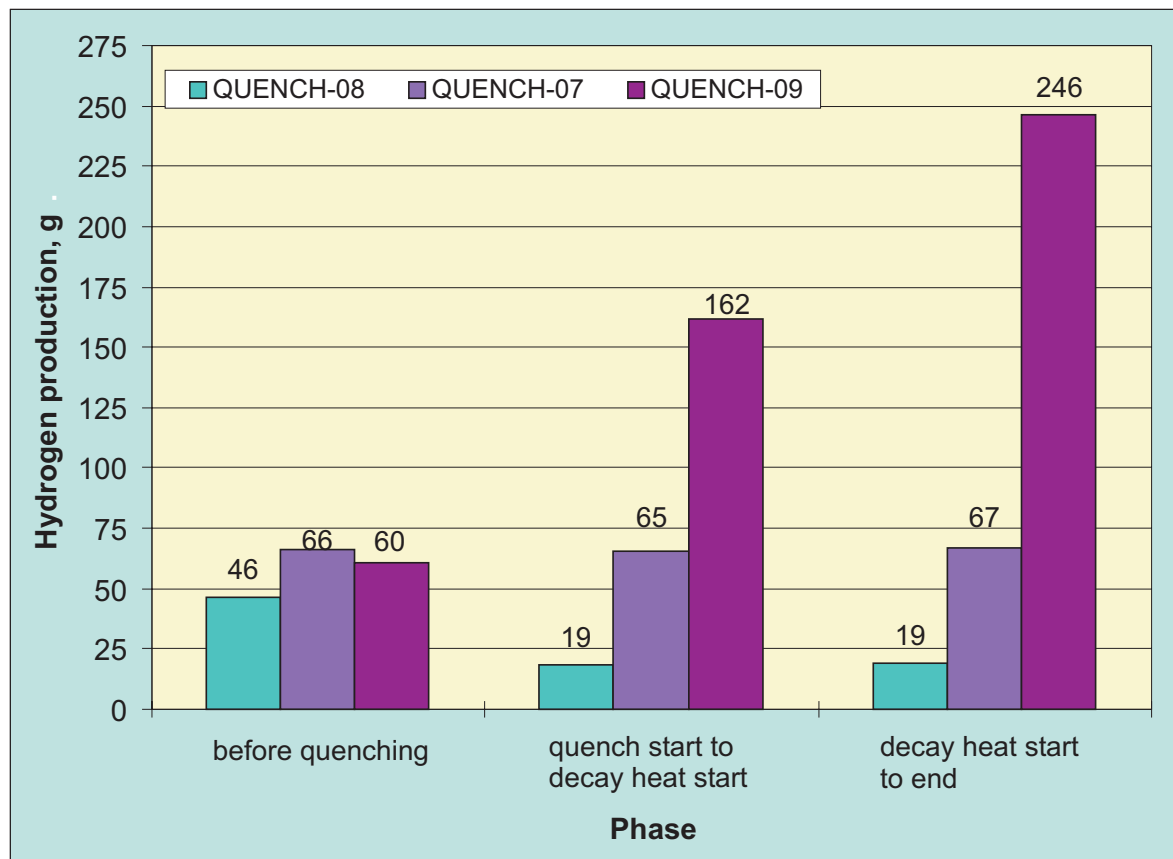
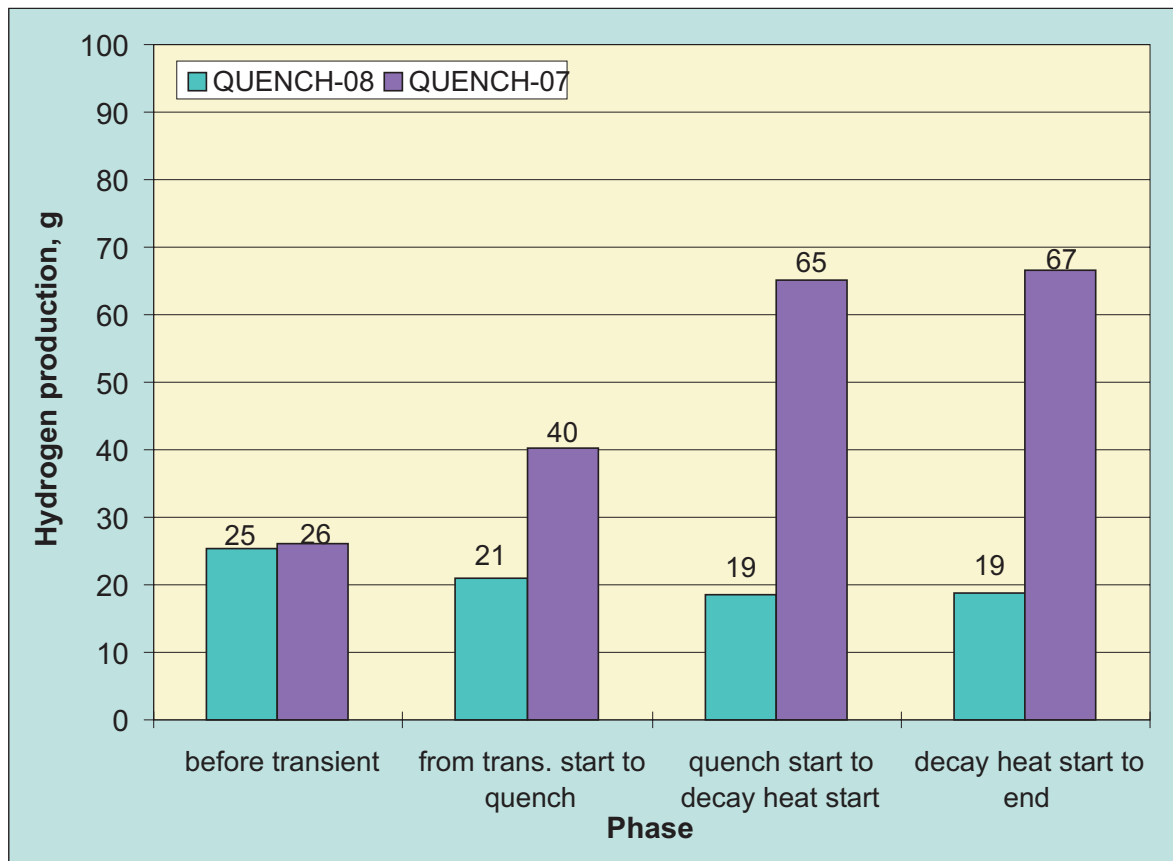


Fig 36-QUE08+07+09 hydrogen production.cdr
10.02.05 - IMF

Fig. 36: Hydrogen production during specific test phases of QUENCH-08 compared to QUENCH-07 and QUENCH-09 (MS data).

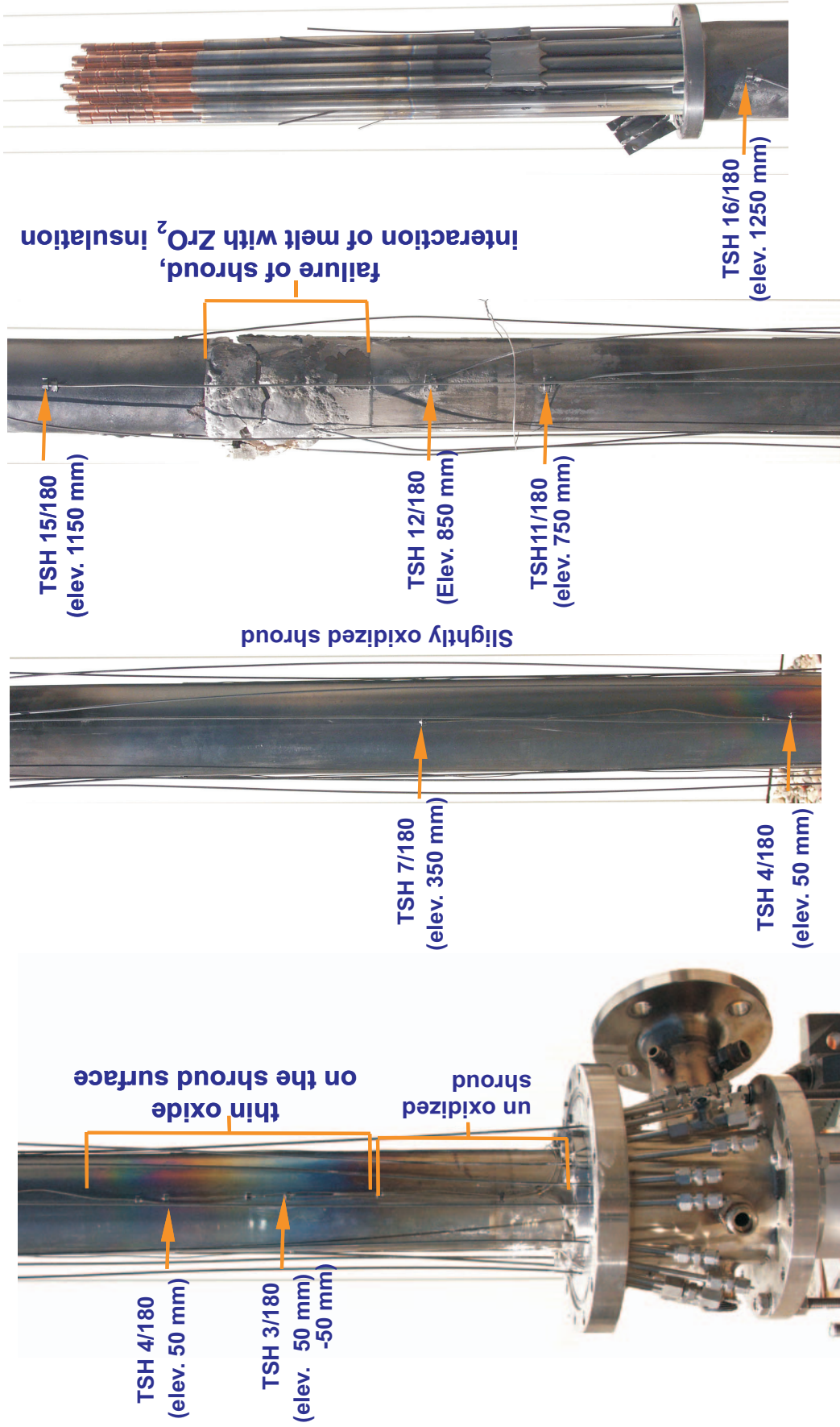


Fig. 37-QUENCH-08-appearance bundle 1.cdr
14.02.05 - IMF

Fig. 37: Appearance of the bundle QUENCH-08: axial segments at the angular position 200°.

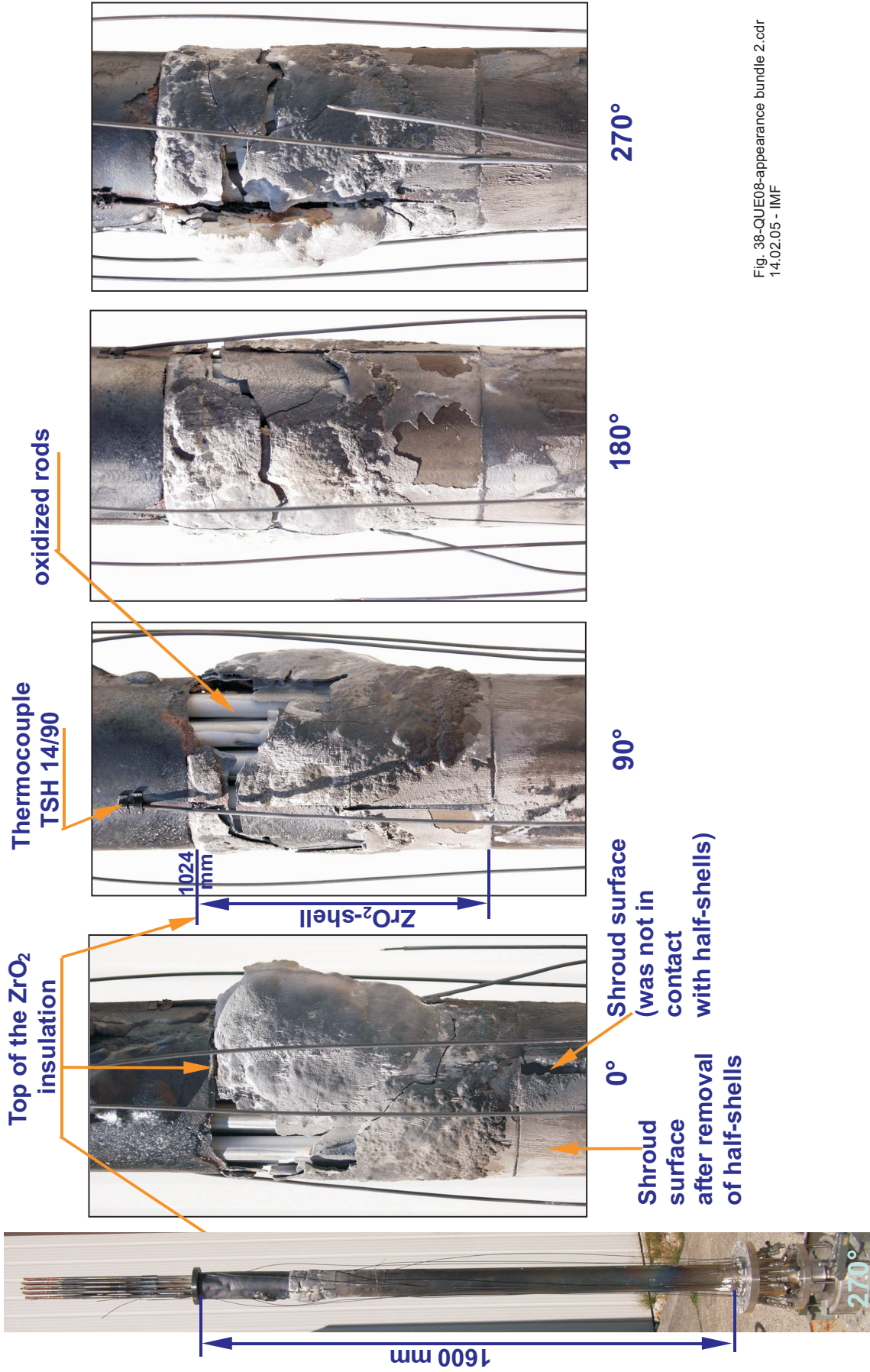


Fig. 38-QUE08-appearance bundle 2.cdr
14.02.05 - IMF

Fig. 38: Appearance of the bundle QUENCH-08 between elevations 845 mm and 1070 mm.

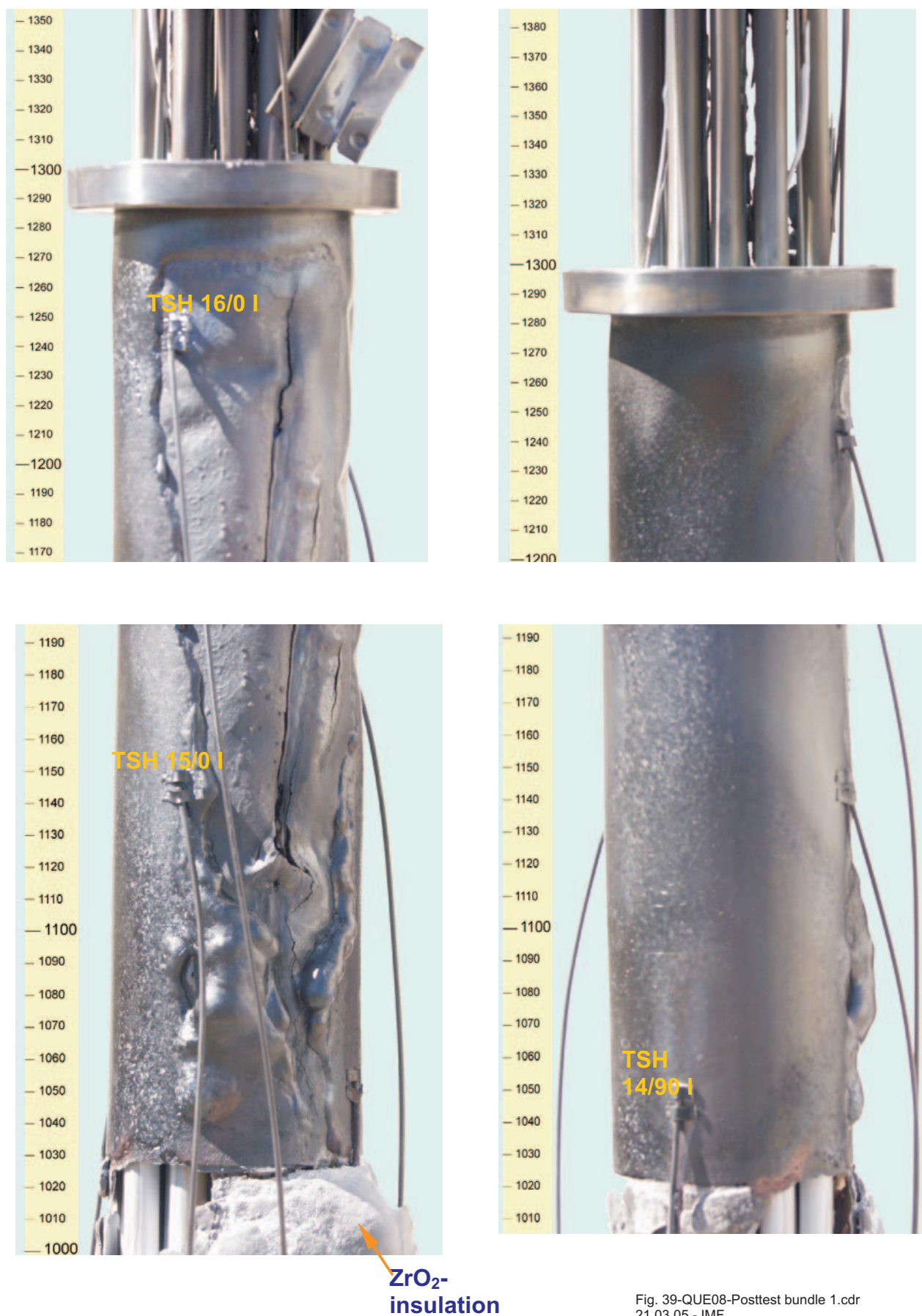


Fig. 39-QUE08-Posttest bundle 1.cdr
21.03.05 - IMF

Fig. 39: QUENCH-08; Posttest appearance of the bundle and shroud at orientations 0° (left photos) and 90° (right photos).

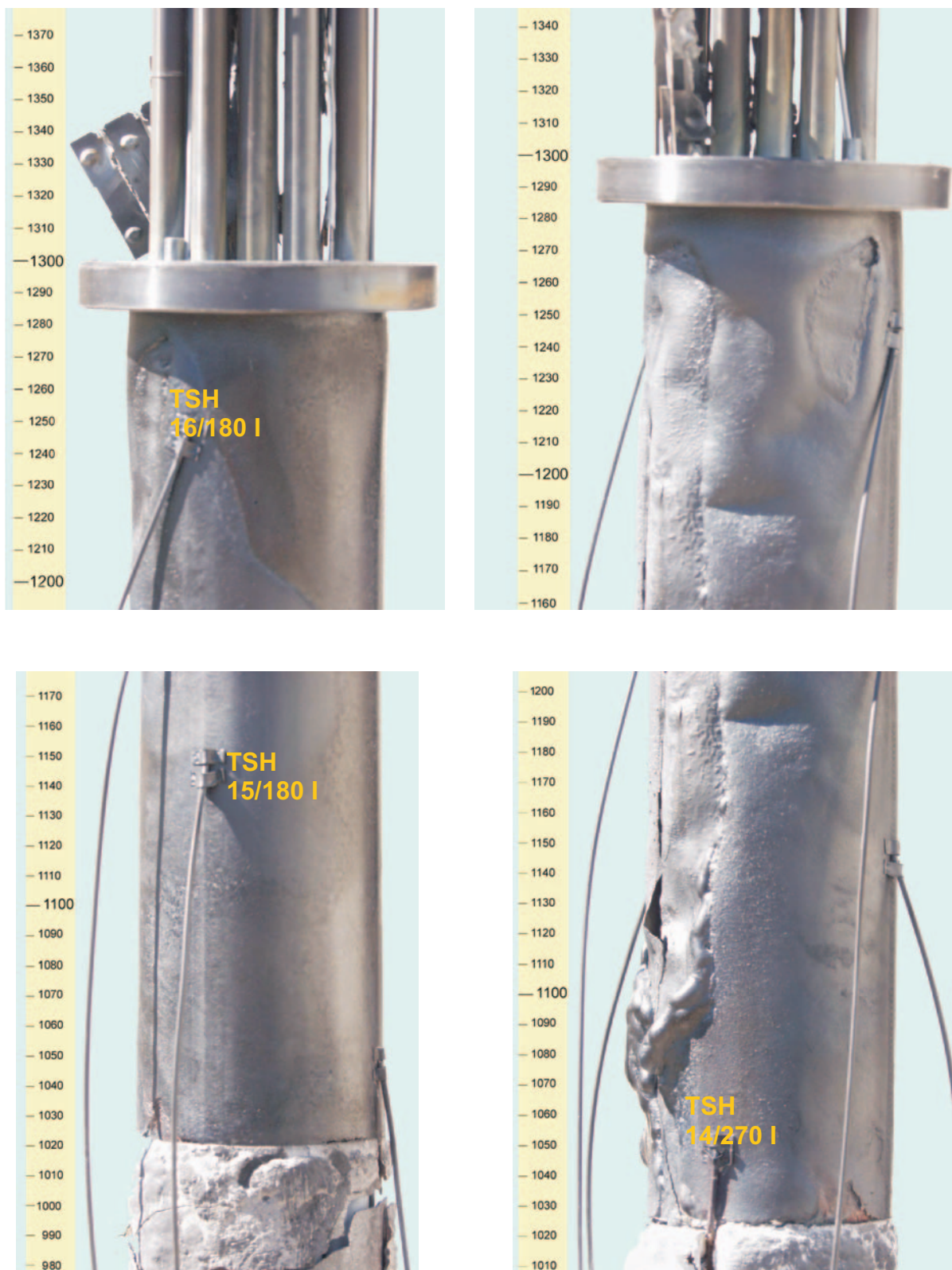


Fig. 40-QUE08-Posttest bundle 1.cdr
21.03.05 - IMF

Fig. 40: QUENCH-08; Posttest appearance of the bundle and shroud at orientations 180° (left photos) and 270° (right photos).

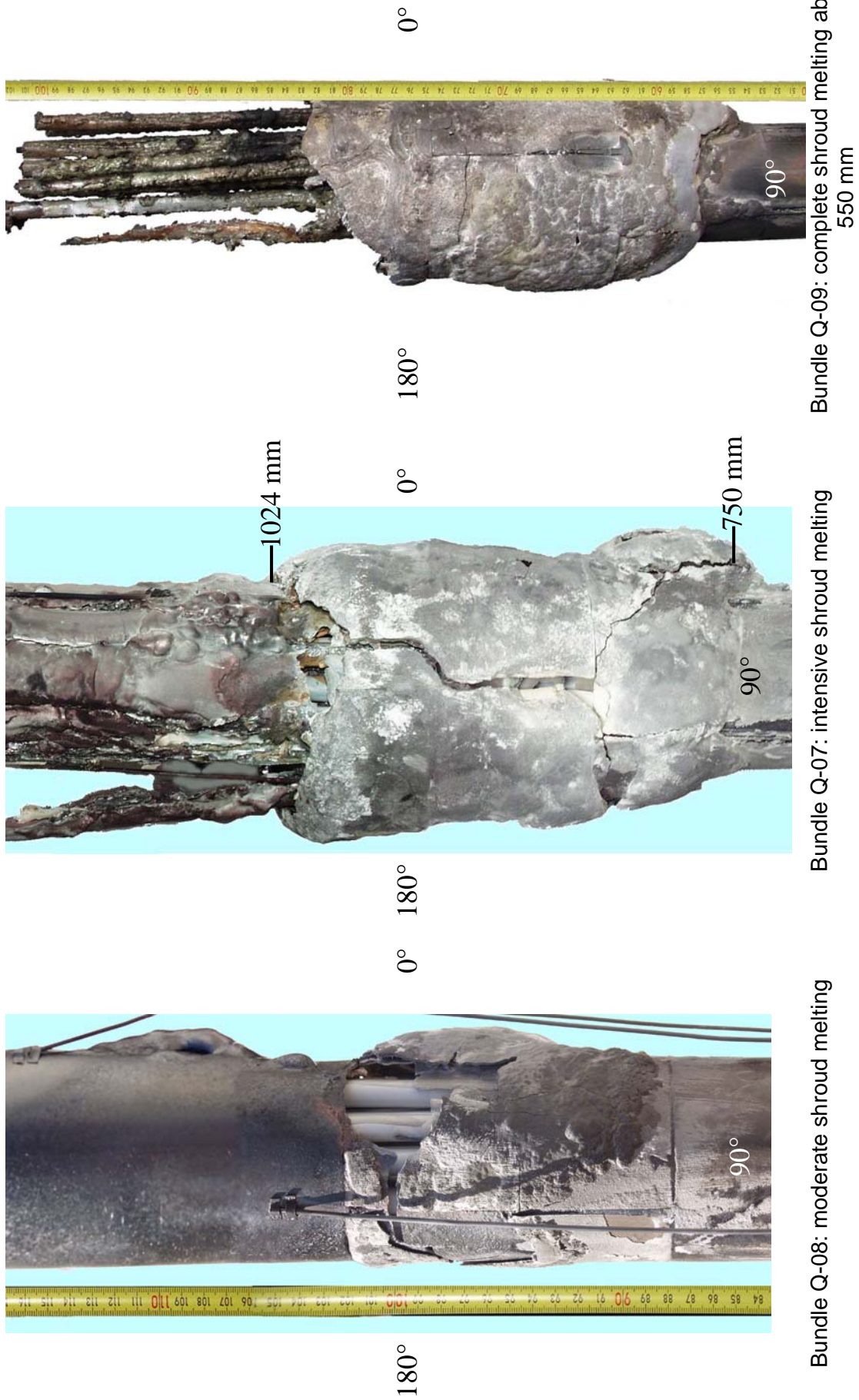


Fig. 41-QUE08 Bundle posttest Q8_7_9.doc
22.03.05 - IMF

Fig. 41: Posttest appearance of the hot regions of test bundles QUENCH-08, -07, and -09.

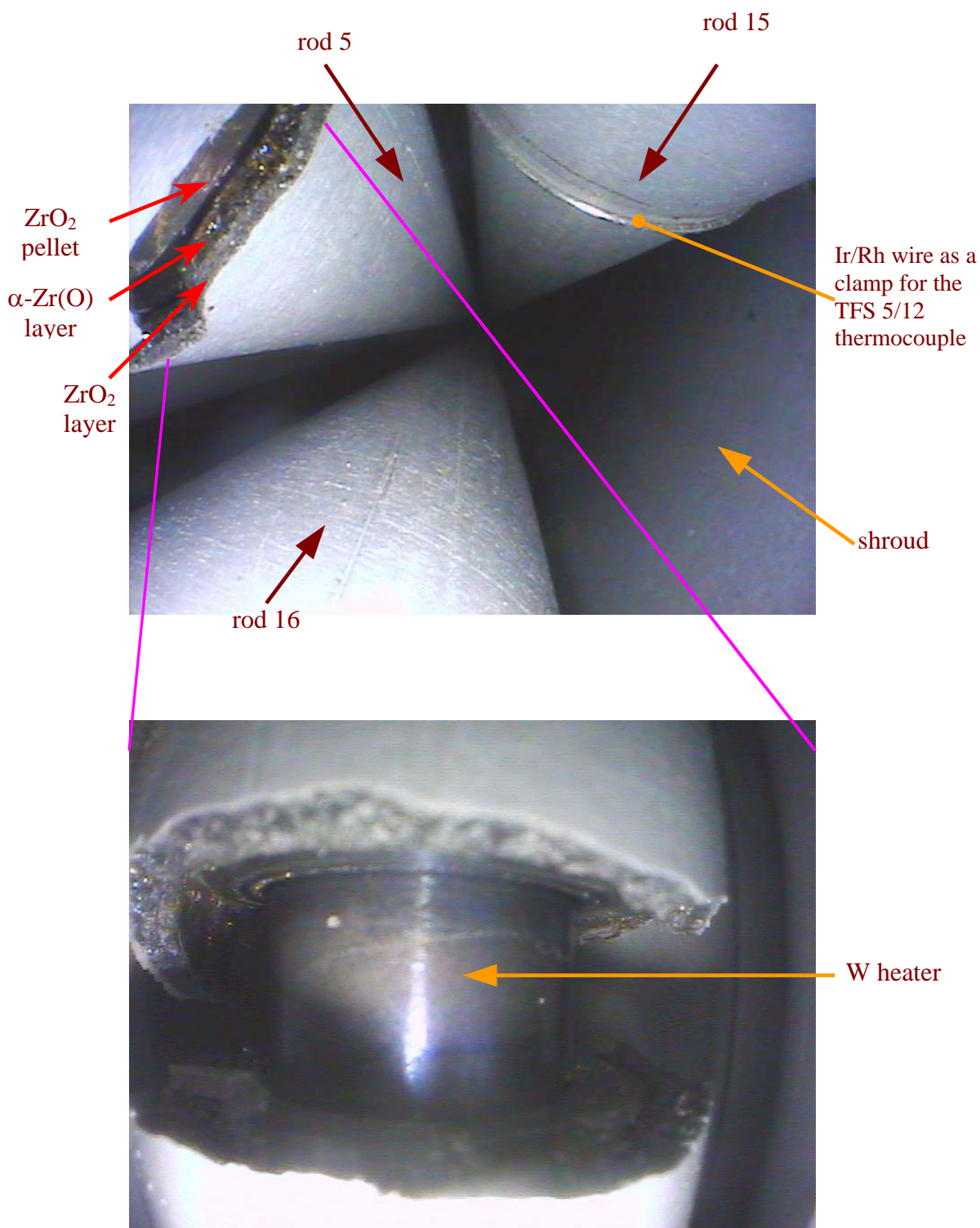


Fig 42-QU08 Stuckert.doc
15.02.05 - IMF

Fig. 42: QUENCH-08; Rod cladding breach shown at rod 5 by a posttest photograph taken with an endoscope from the position of corner rod B (viewed toward the bottom of the bundle).

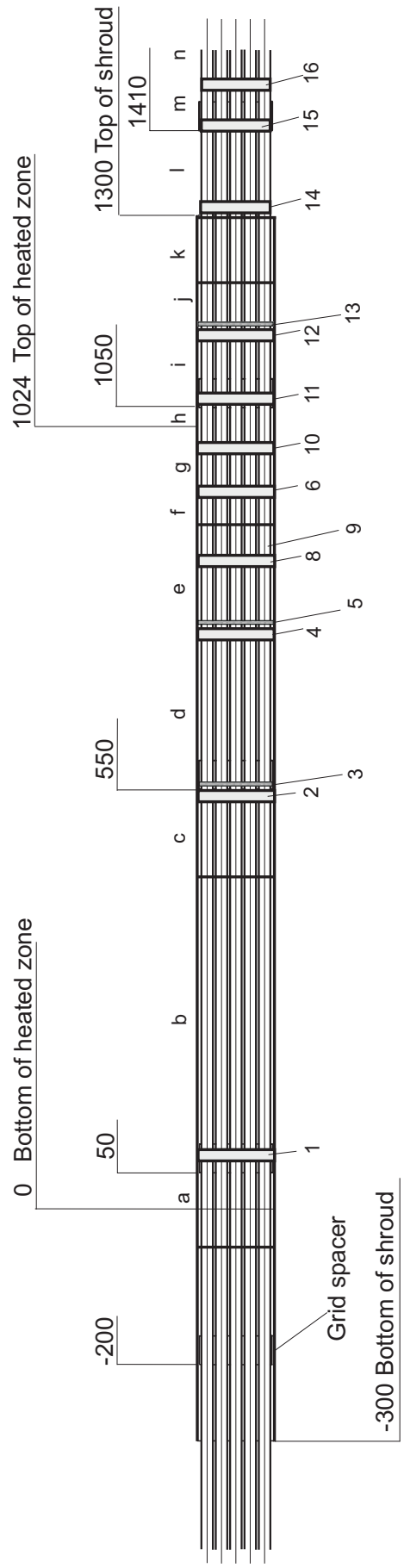


Fig 43-QUE08 Schnittplan.cdr
22.03.05 - IMF

Fig. 43: Sectioning of the QUENCH-08 test bundle.

QUE-08-1
bottom
60 mm



QUE-08-1
top
73 mm



QUE-08-2
bottom
537 mm



QUE-08-2
top
550 mm

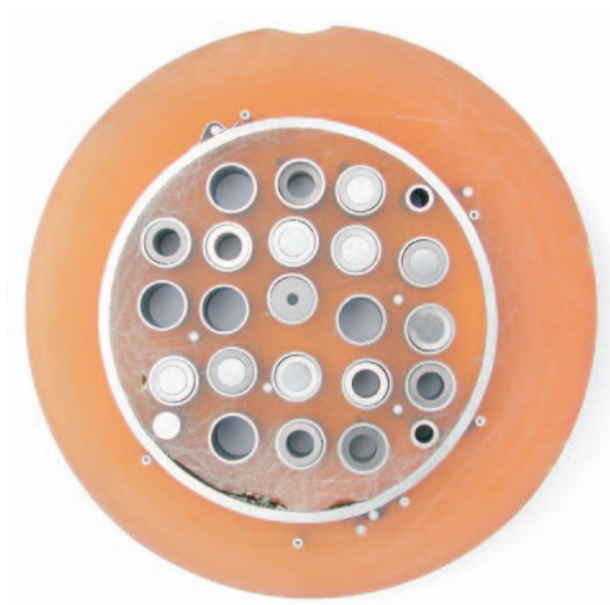


Fig 44 -QUE08 Cross section1+2.cdr
15.02.05 - IMF

Fig. 44: QUENCH-08; Cross sections at 60 mm, 73 mm, 537 mm, and 550 mm.

QUE-08-4
bottom
737 mm

QUE-09-4
top
750 mm



QUE-08-8
bottom
842 mm

QUE-08-8
top
860 mm



Fig 45-QUE08 Cross section 4+8.cdr
15.02.05 - IMF

Fig. 45: QUENCH-08; Cross sections at 737 mm, 750 mm, 842 mm, and 860 mm.

QUE-08-9
bottom
864 mm



QUE-08-9
top
900 mm



QUE-08-6
bottom
937 mm



QUE-08-6
top
950 mm



Fig 46-QUE08 Cross section 9+6.cdr
15.02.05 - IMF

Fig. 46: QUENCH-08; Cross sections at 864 mm, 900 mm, 937 mm, and 950 mm.

QUE-08-10
bottom
986 mm



QUE-08-10
top
1000 mm



QUE-08-11
bottom
1050 mm



QUE-08-11
top
1065 mm



Fig 47-QUE08 Cross section 10+11.cdr
15.02.05 - IMF

Fig. 47: QUENCH-08; Cross sections at 986 mm, 1000 mm, 1050 mm, and 1065 mm.

QUE-08-12
bottom
1135 mm



QUE-08-12
top
1150 mm



QUE-08-11
bottom
1307 mm



QUE-08-11
top
1320 mm



Fig 48-QUE08 Cross section 12+14.cdr
15.02.05 - IMF

Fig. 48: QUENCH-08; Cross sections at 1135 mm, 1150 mm, 1307 mm, and 1320 mm.

QUE-08-15
bottom
1410 mm



QUE-08-15
top
1425 mm



QUE-08-16
bottom
1465 mm



QUE-08-16
top
1480 mm



Fig 49-QUE08 Cross section 15+16.cdr
15.02.05 - IMF

Fig. 49: QUENCH-08; Cross sections at 1410 mm, 1425 mm, 1465 mm, and 1480 mm.

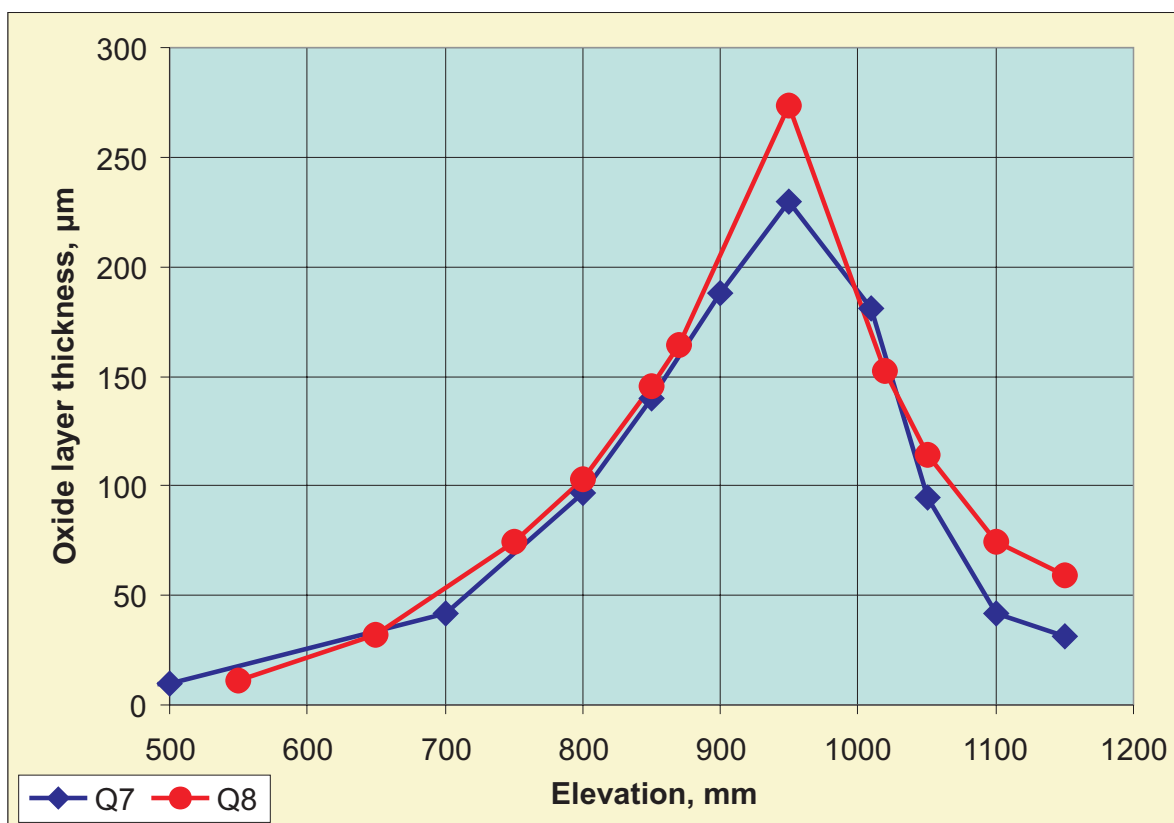


Fig. 50-QUE08-axiale oxide.cdr
22.03.05 - IMF

Fig. 50: QUENCH-08; Axial oxide layer profiles measured at the end of the preoxidation phases of experiments QUENCH-07 (square symbols) and -08 (full circles).

Bottom of cross section slab, 60 mm elevation, inverted to top view

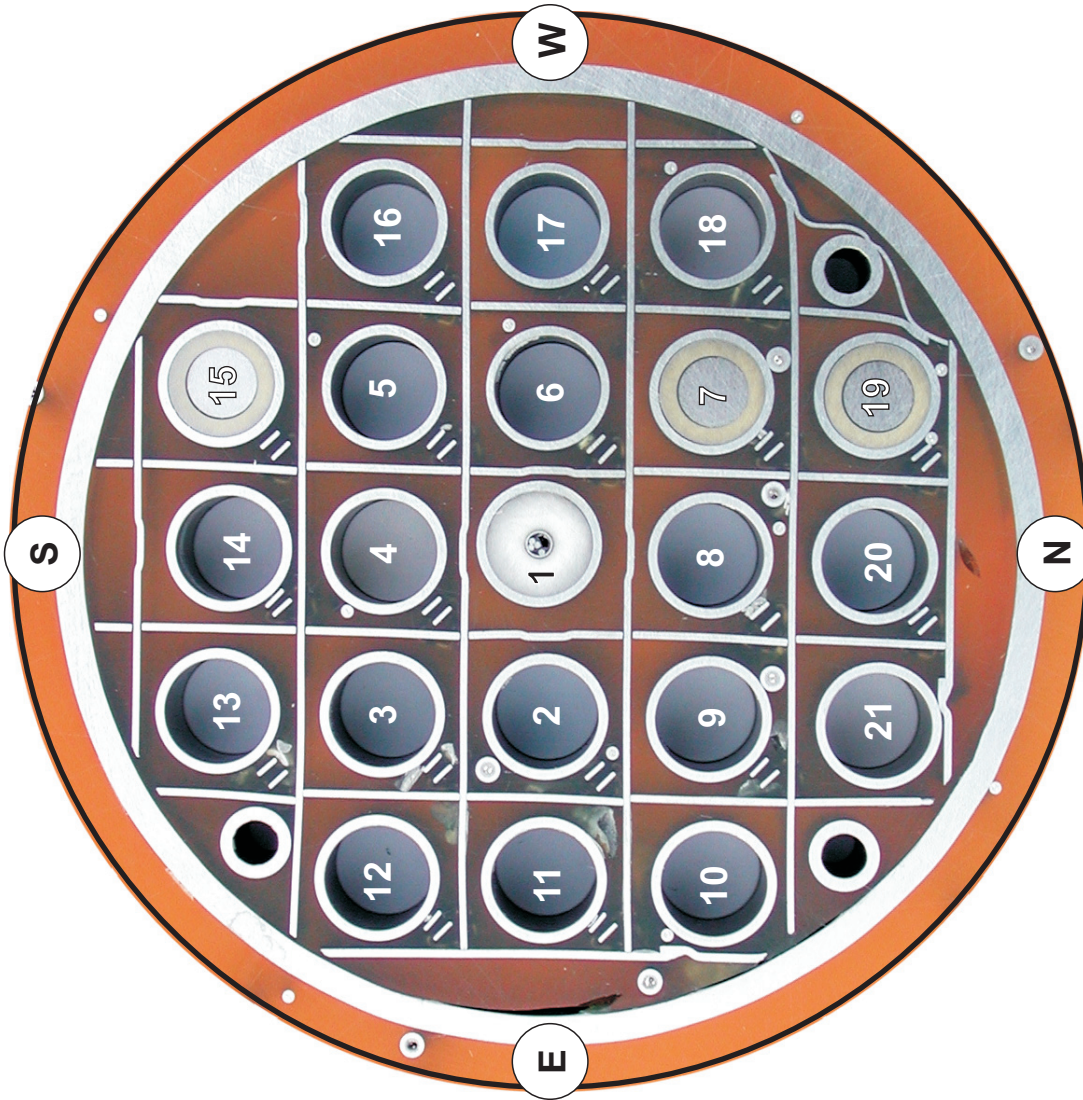


Fig. 51: Cross section at 73 mm bundle elevation (QUE-08-1); overview from top, reference elevation.

Bottom of cross section slab, 537 mm elevation, inverted to top view



Fig. 52: Cross section at 550 mm bundle elevation (QUE-08-2); overview from top.

Bottom of cross section slab, 737 mm elevation, inverted to top view

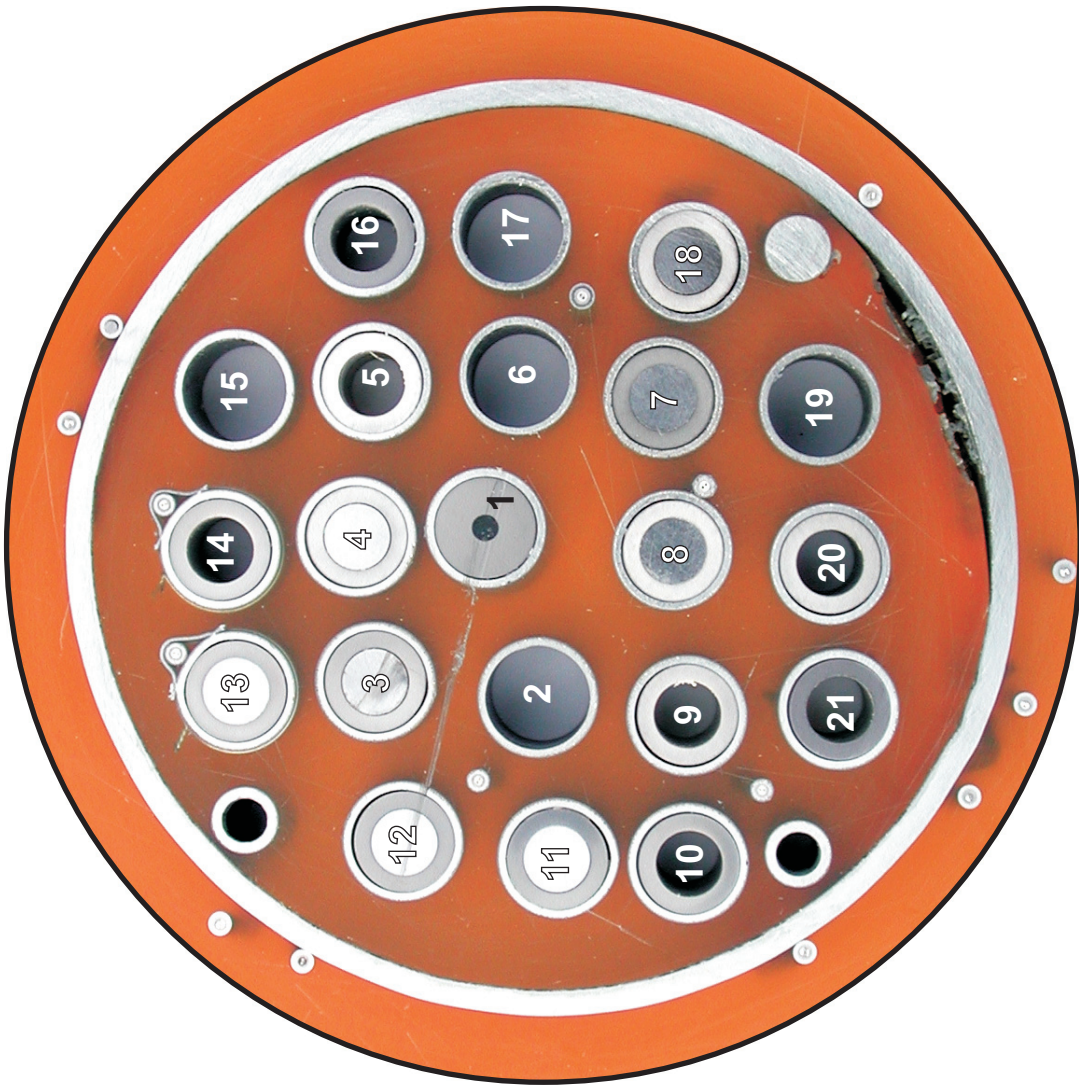
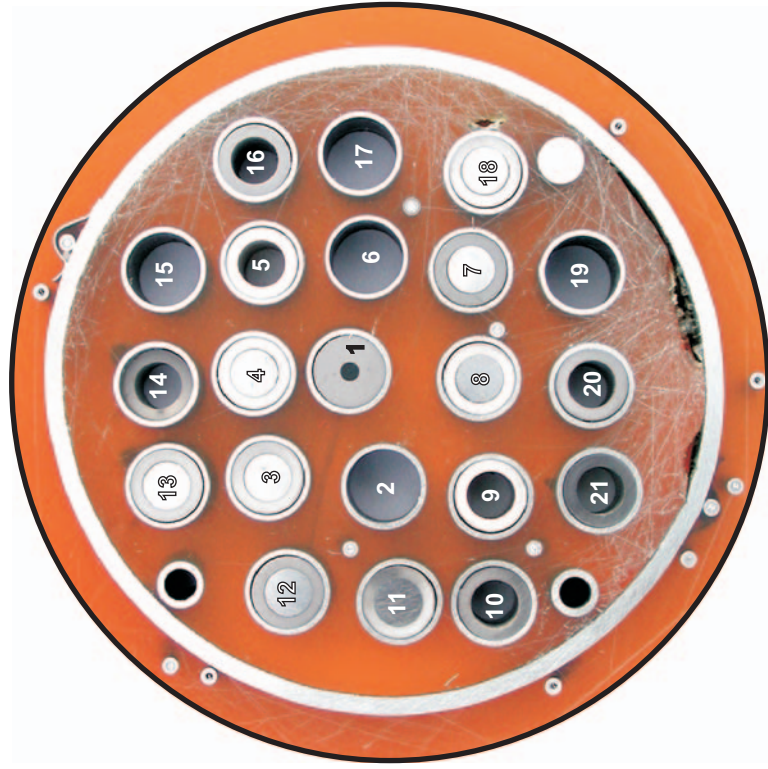


Fig. 53: Cross section at 750 mm bundle elevation (QUE-08-4); overview from top.

Bottom of cross section slab, 842 mm elevation, inverted to top view

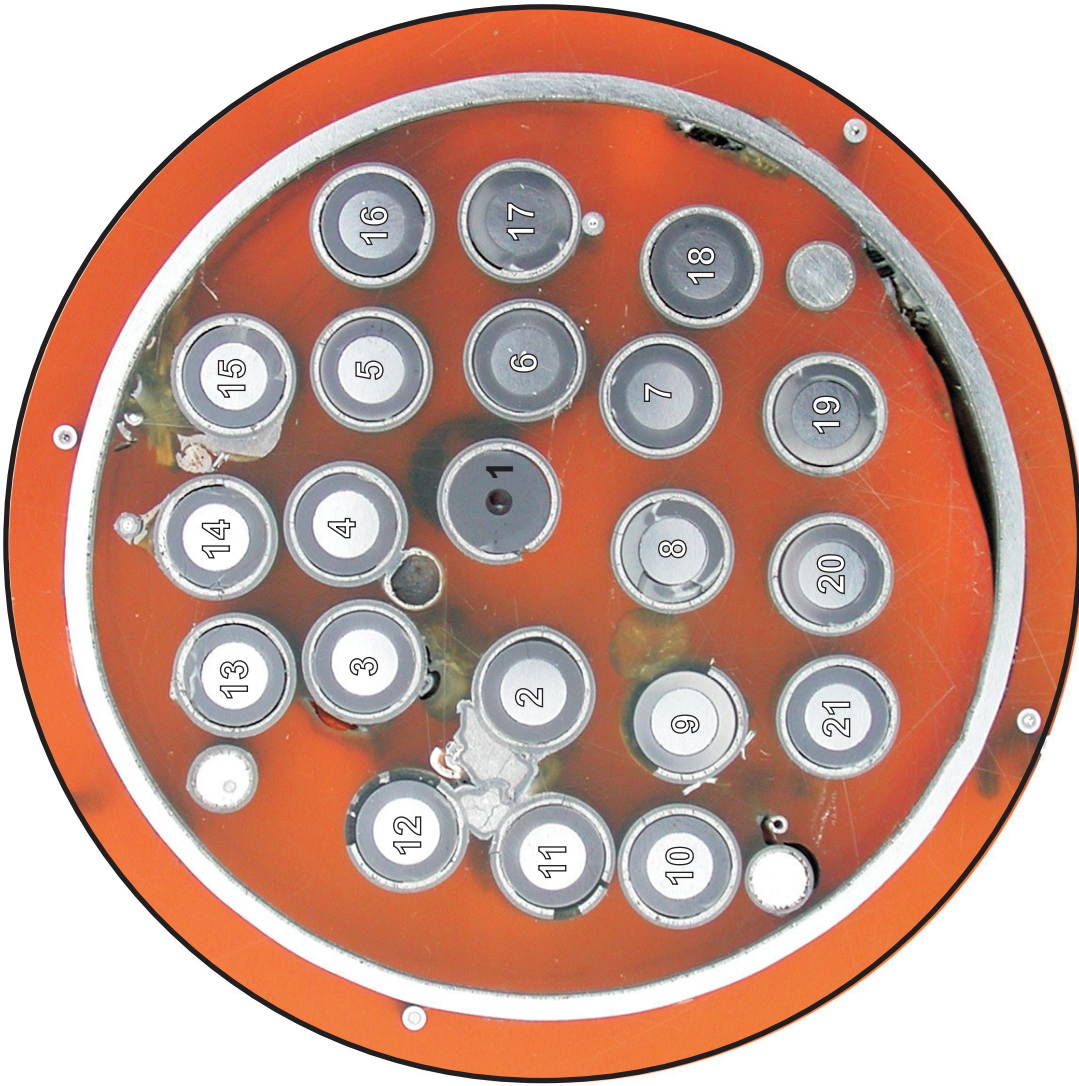
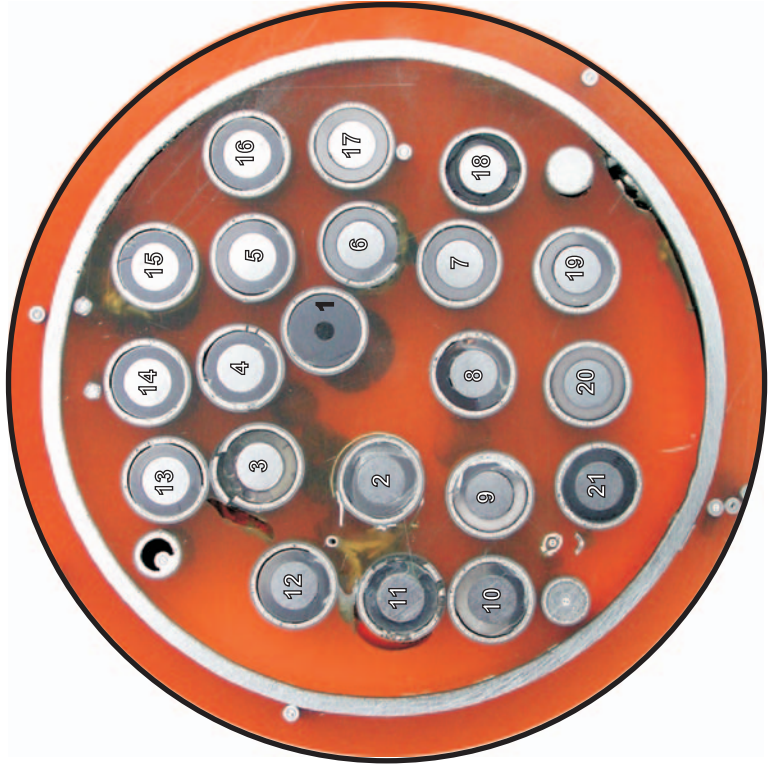


Fig. 54: Cross section at 860 mm bundle elevation (QUE-08-8); overview from top.

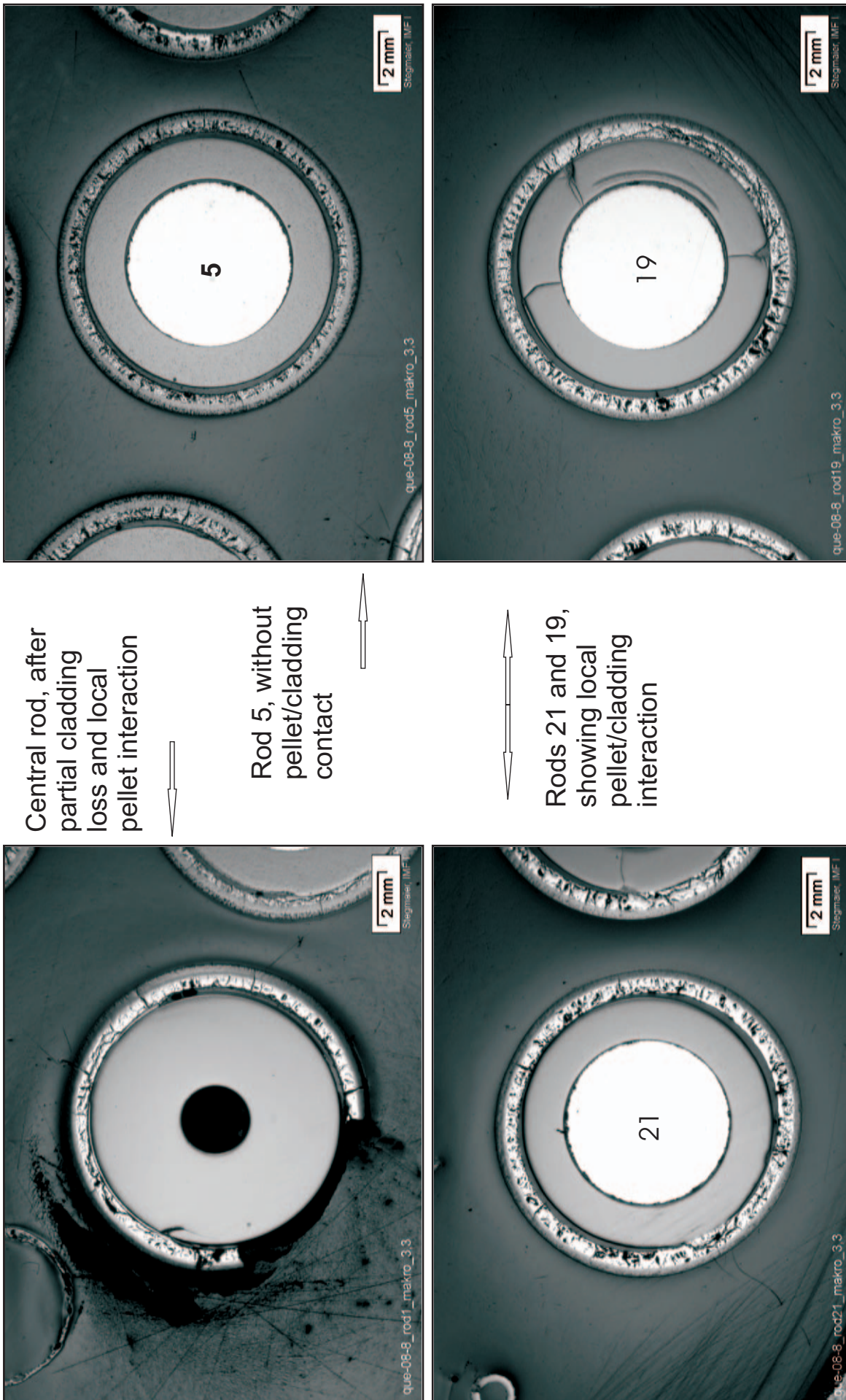


Fig. 55: Cross section at 860 mm elevation (QUE-08-8); macrographs of separate rods, showing cladding fragmentation and interaction at pellet contact positions.

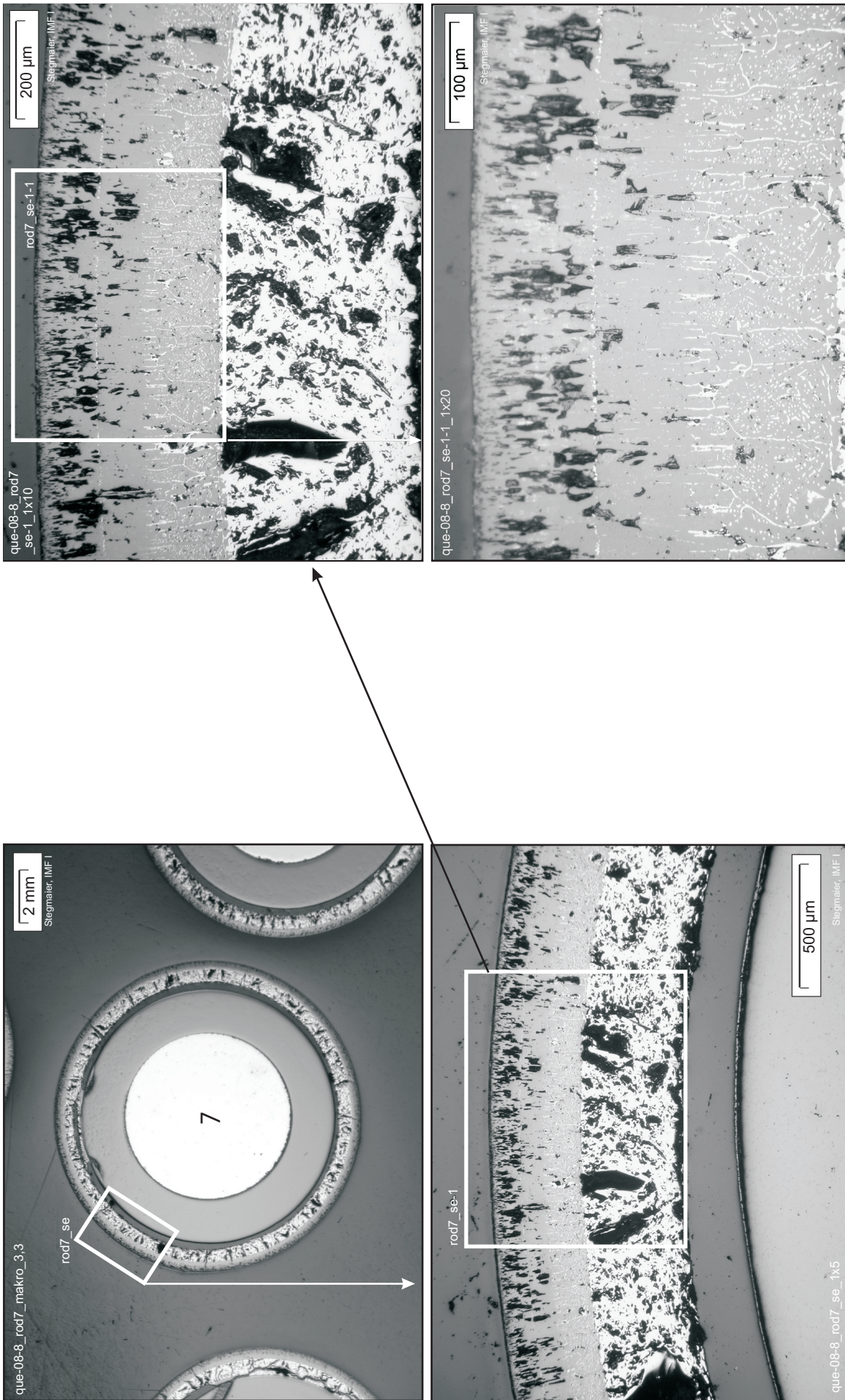


Fig. 56: Cross section at 860 mm elevation (QUE-08-8); macrograph of rod 7 and oxidation at a position without pellet contact.

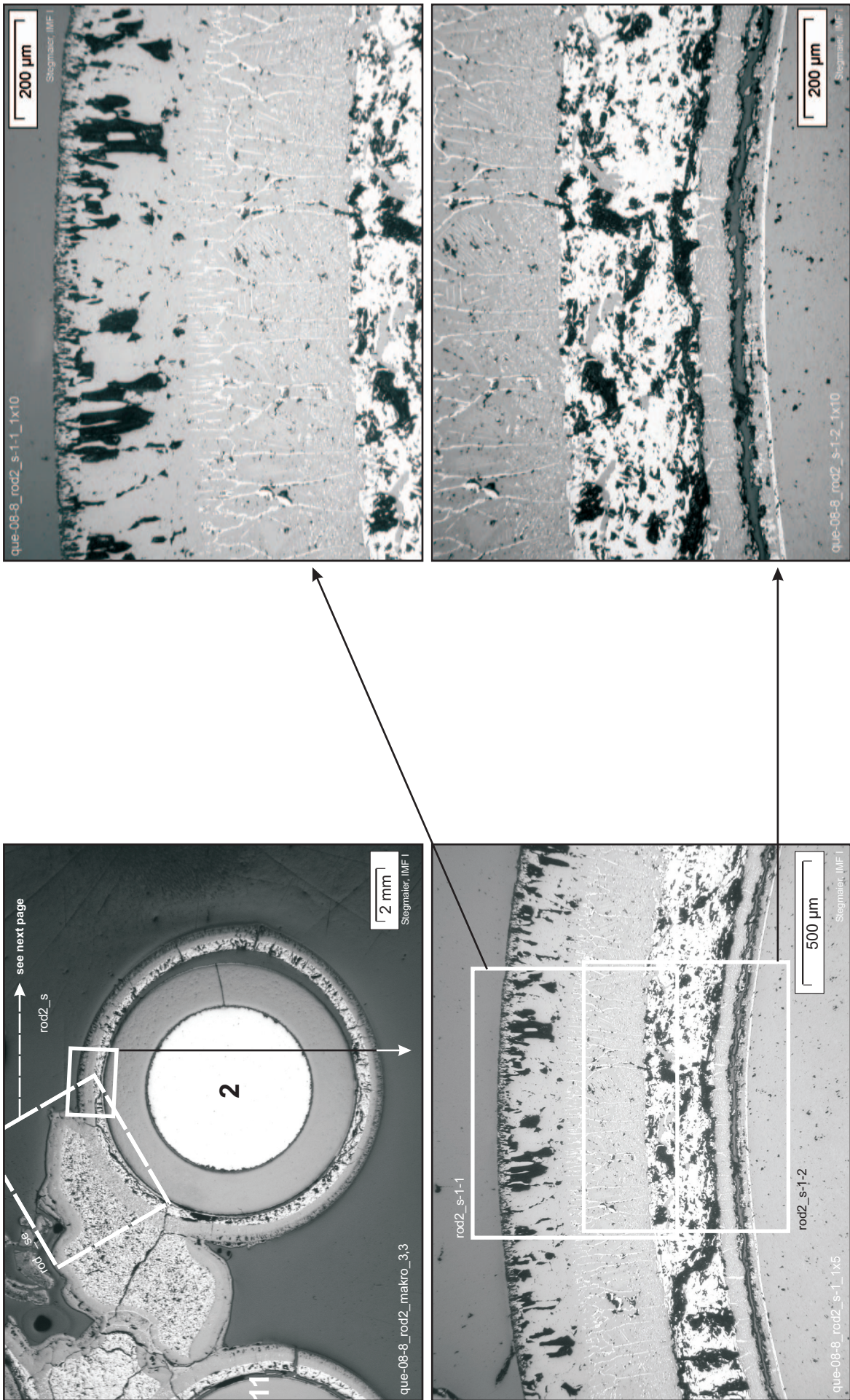
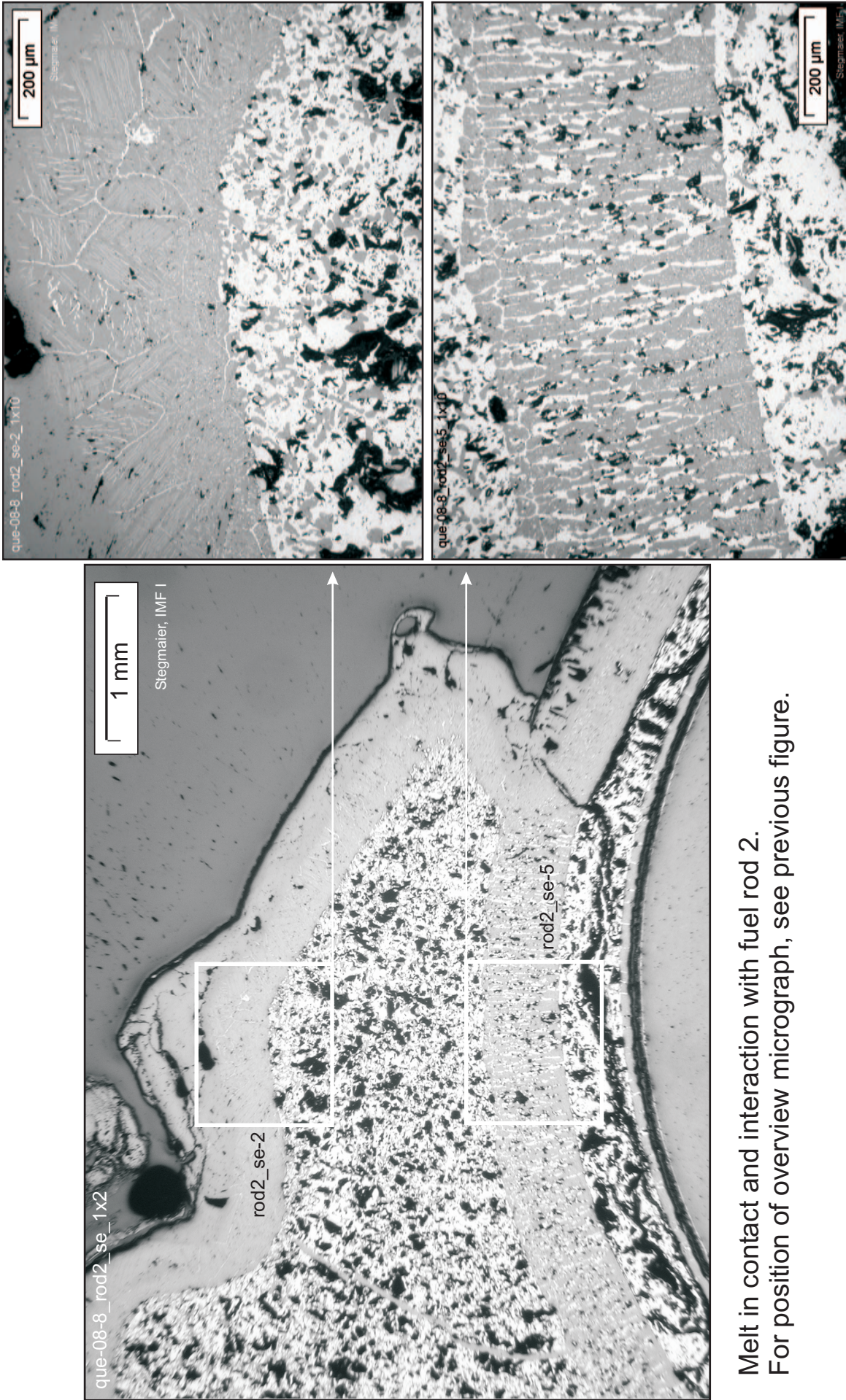


Fig. 57: Cross section at 860 mm elevation (QUE-08-8); macrograph of rod 2, and details of external cladding oxidation and internal pellet interaction.



Melt in contact and interaction with fuel rod 2.
For position of overview micrograph, see previous figure.

Fig. 58: Cross section at 860 mm elevation (QUE-08-8); microstructures of melt in contact with rod 2.

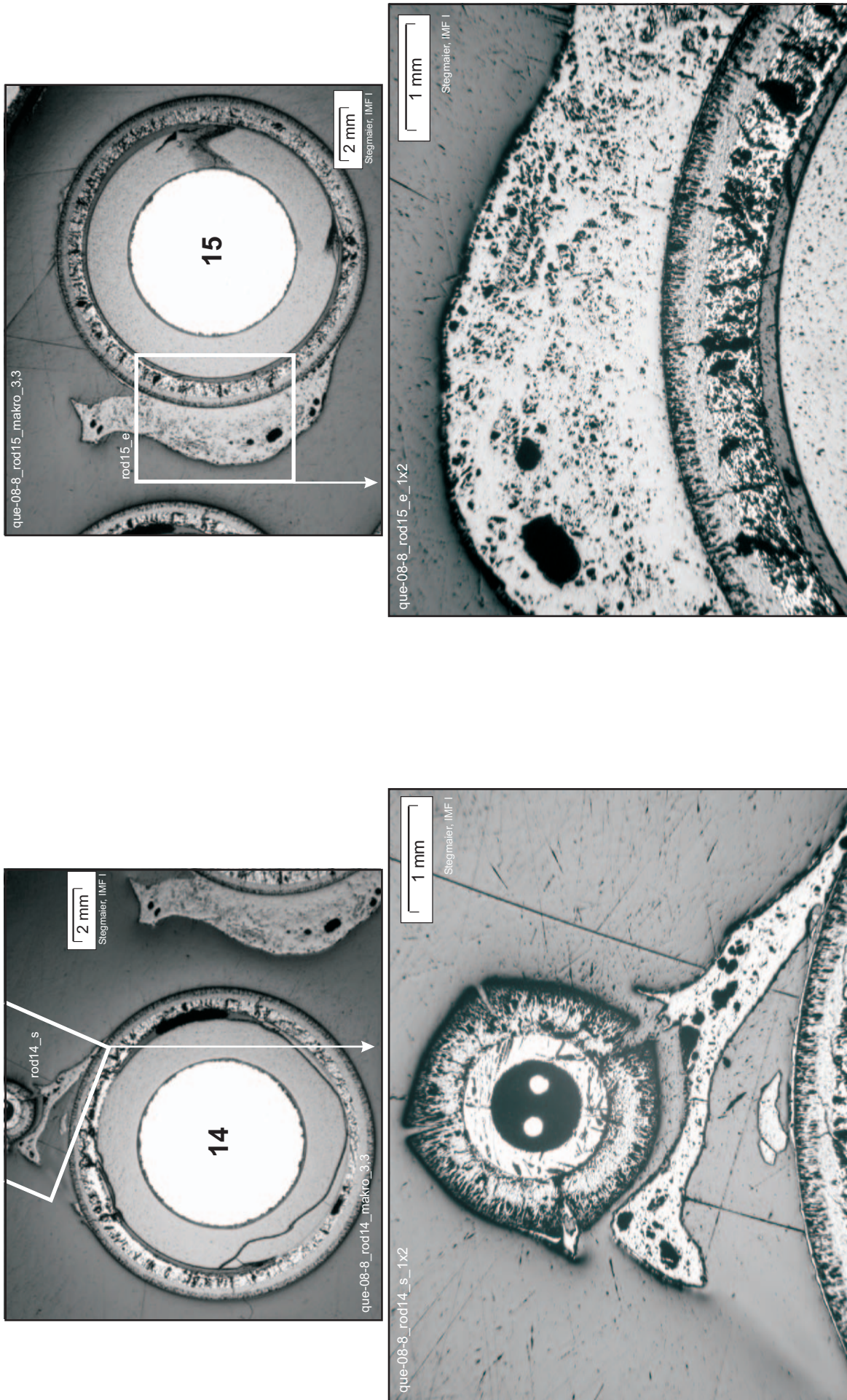


Fig. 59: Cross section at 860 mm elevation (QUE-08-8); non-oxidized melt in contact with rods 14 (left) and 15 (right).

Bottom of cross section slab, 864 mm elevation, inverted to top view

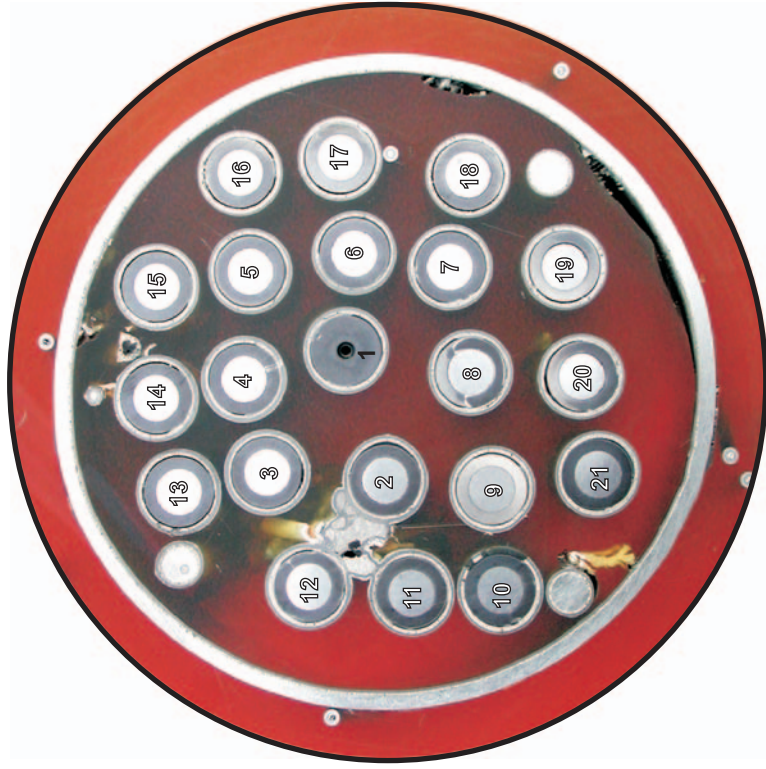
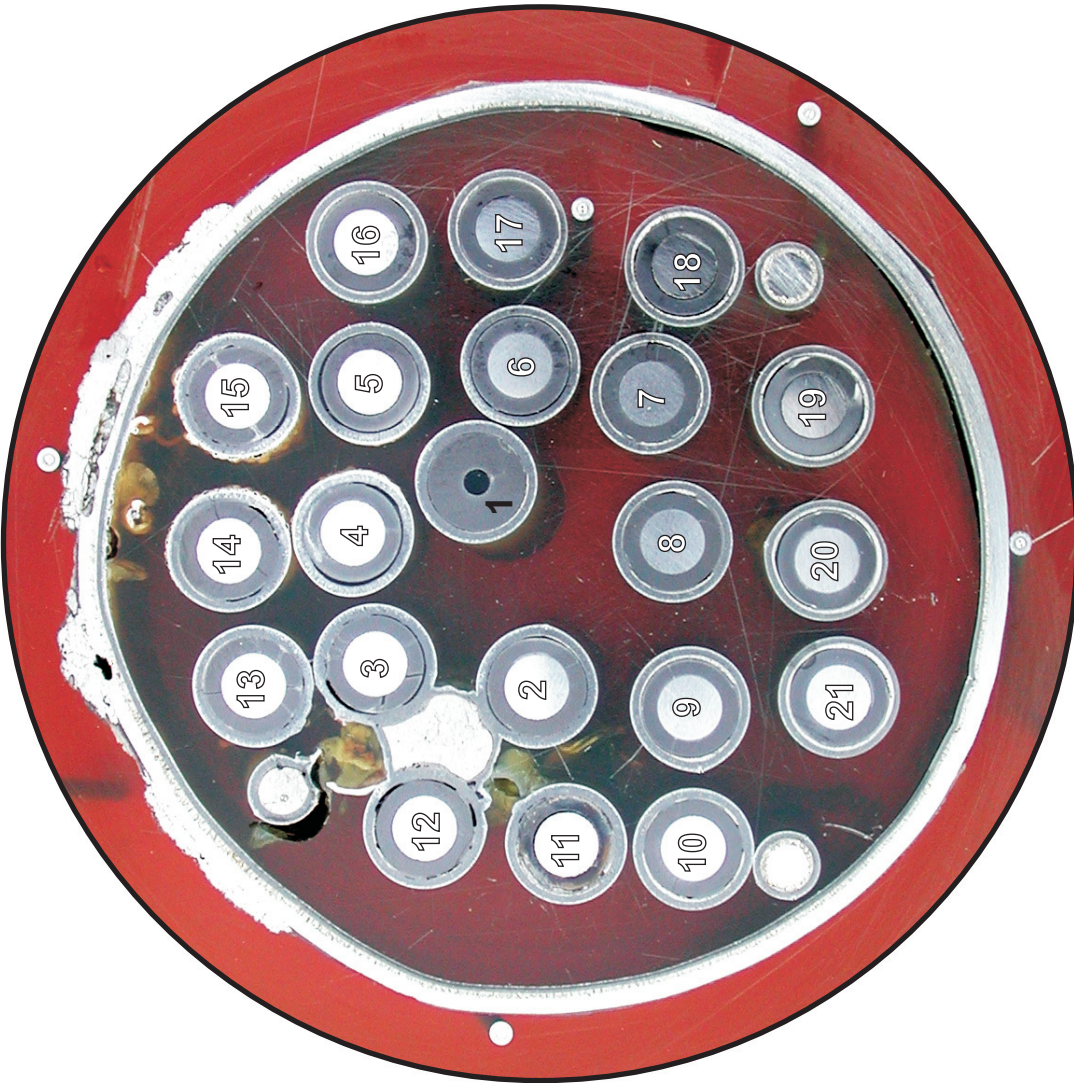


Fig. 60: Cross section at 900 mm bundle elevation (QUE-08-9); overview from top.

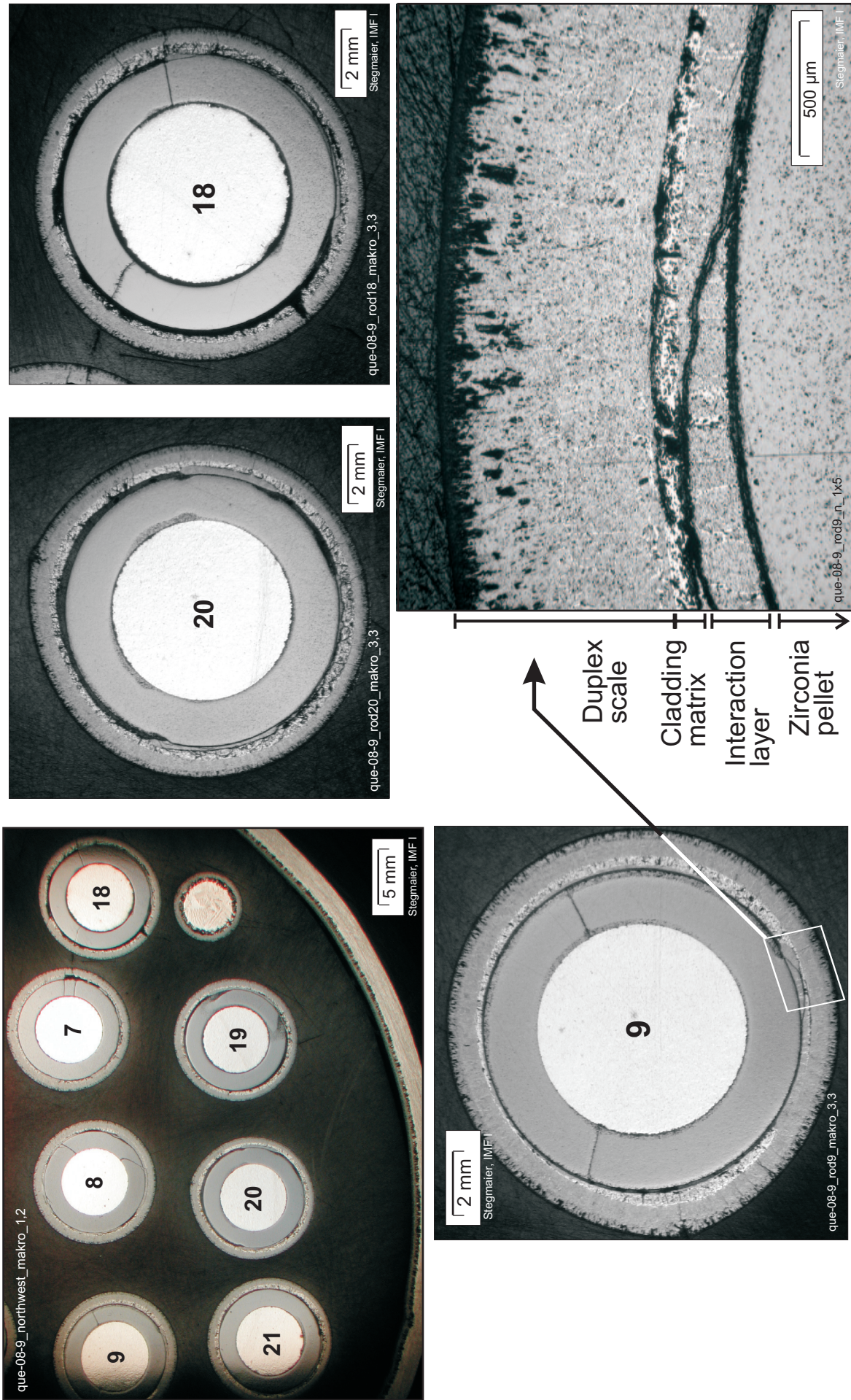


Fig. 61: Cross section at 900 mm elevation (QUE-08-9); cladding oxidation and pellet interaction towards north-west in the bundle.

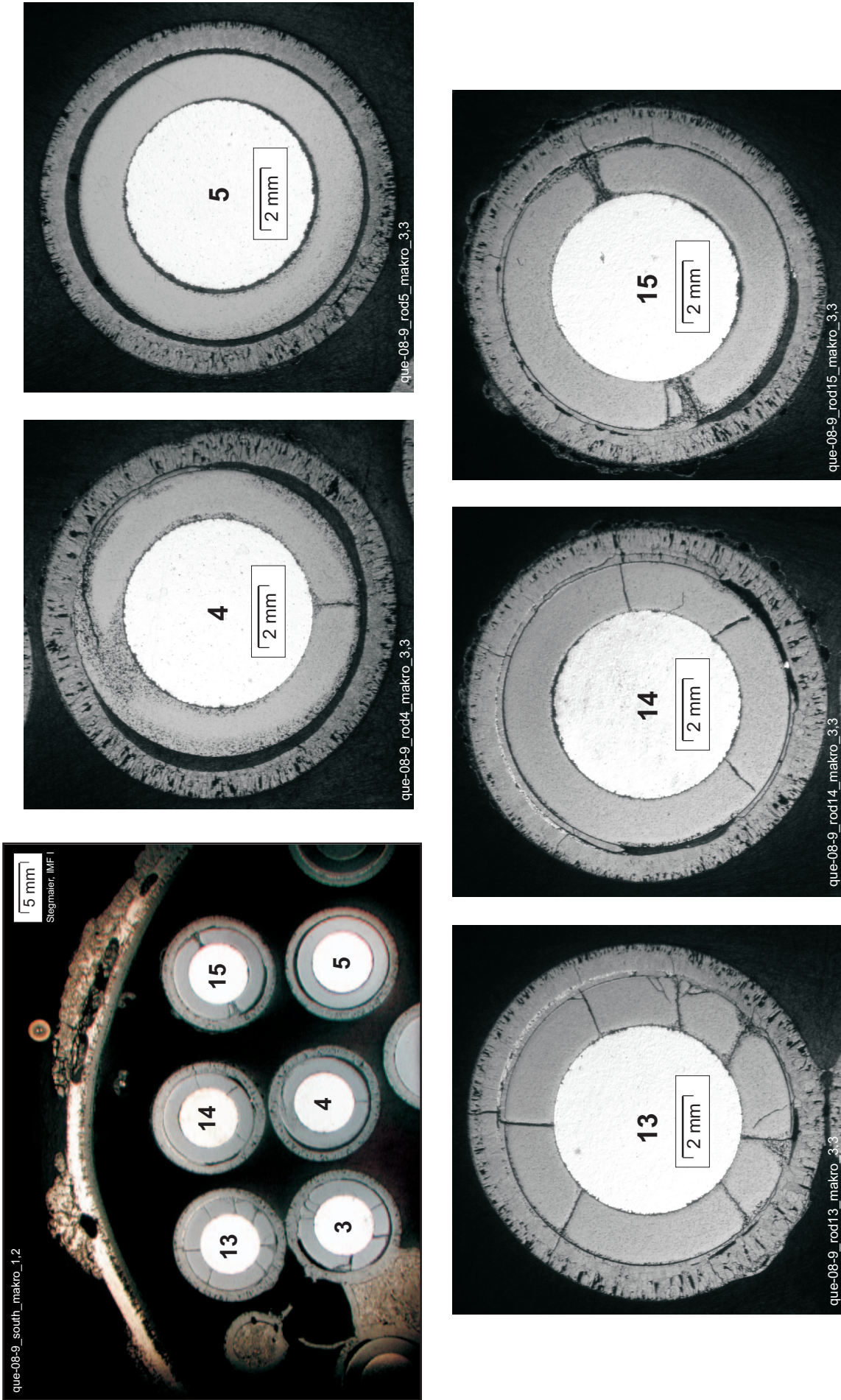


Fig. 62: Cross section at 900 mm elevation (QUE-08-9); almost complete cladding oxidation towards south in the bundle, versus occurrence of melt.

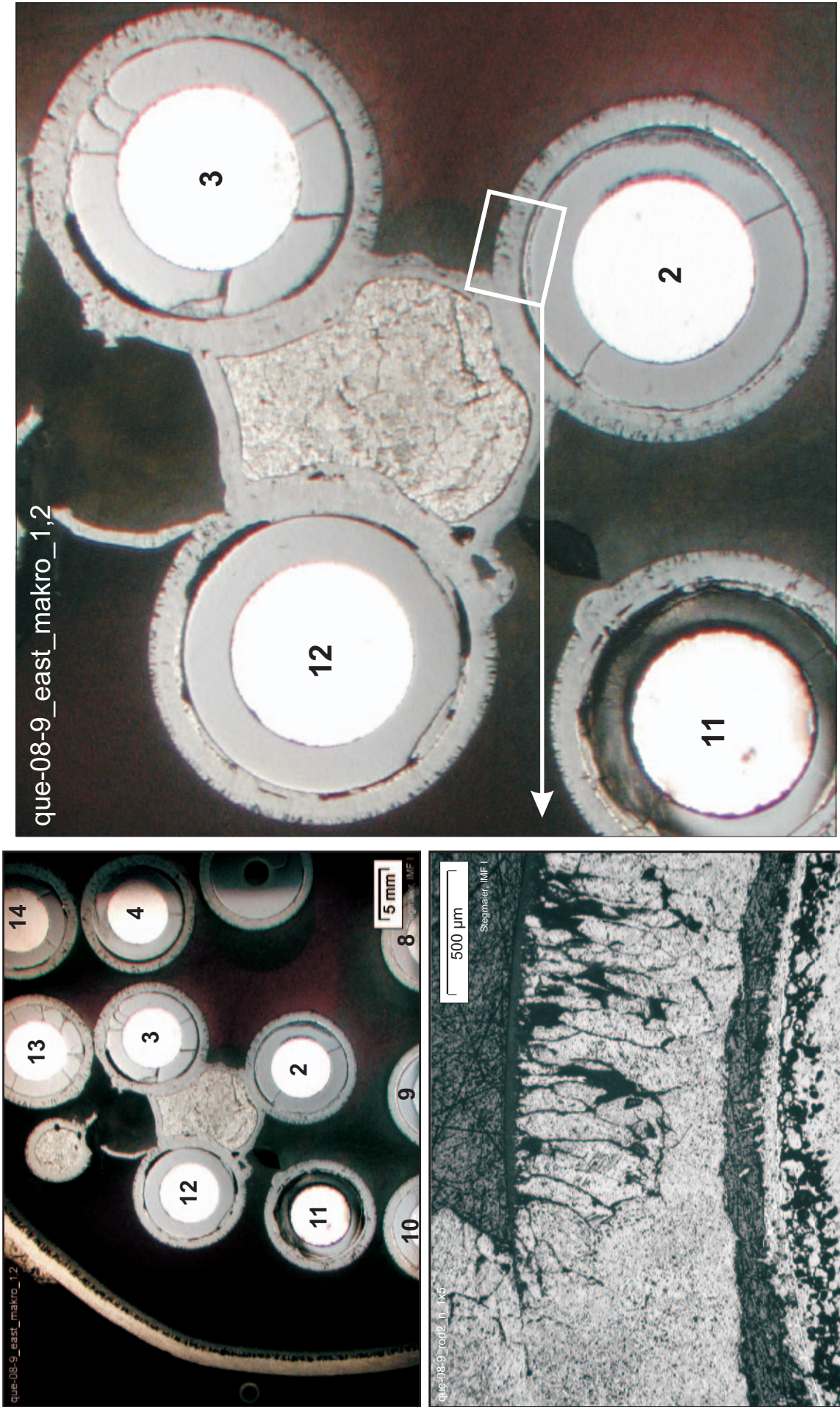


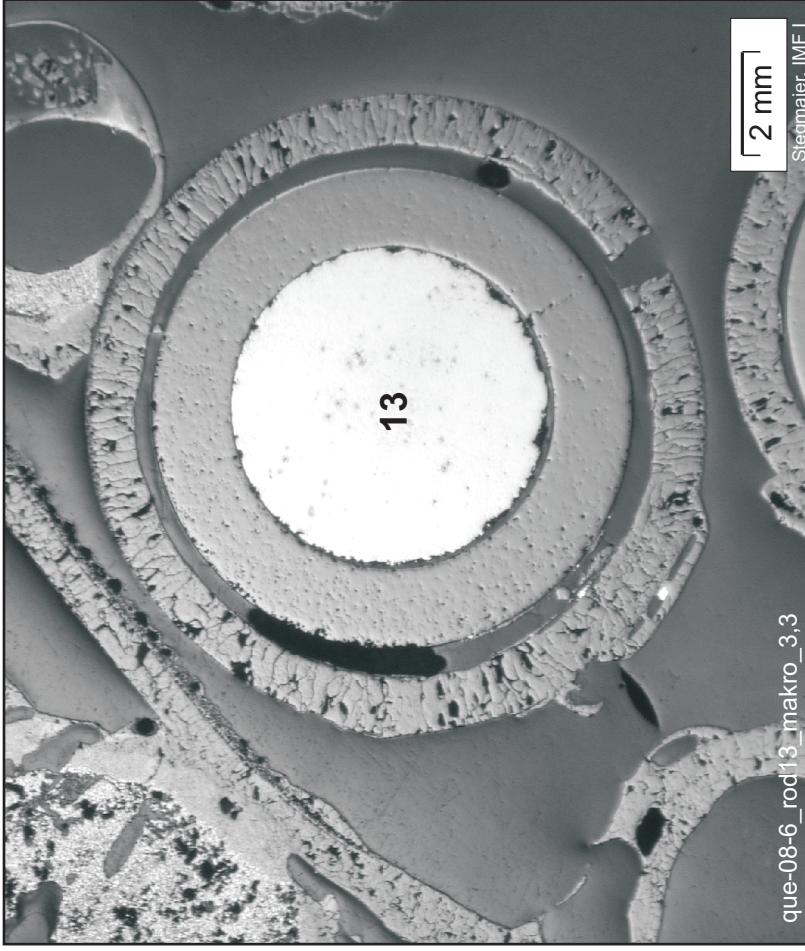
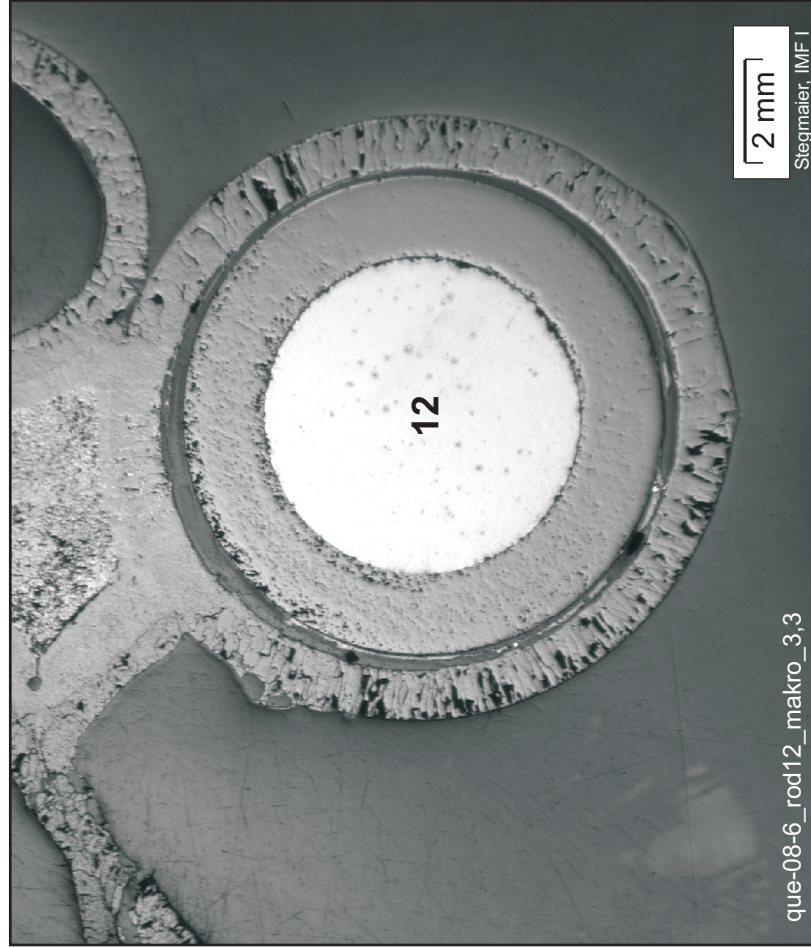
Fig. 63: Cross section at 900 mm elevation (QUE-08-9); details of melt towards south-east in the bundle and within corner rod A; note also empty scale residues.

Bottom of cross section slab, 937 mm elevation, inverted to top view



Fig. 64: Cross section at 950 mm bundle elevation (QUE-08-6); overview from top.

Rod 12, together with adjacent melt, and the empty scale of corner rod A



Rod 13, together with the shroud (top, left)

Fig. 65: Cross section at 950 mm elevation (QUE-08-6); rods and melt accumulation towards south-west.

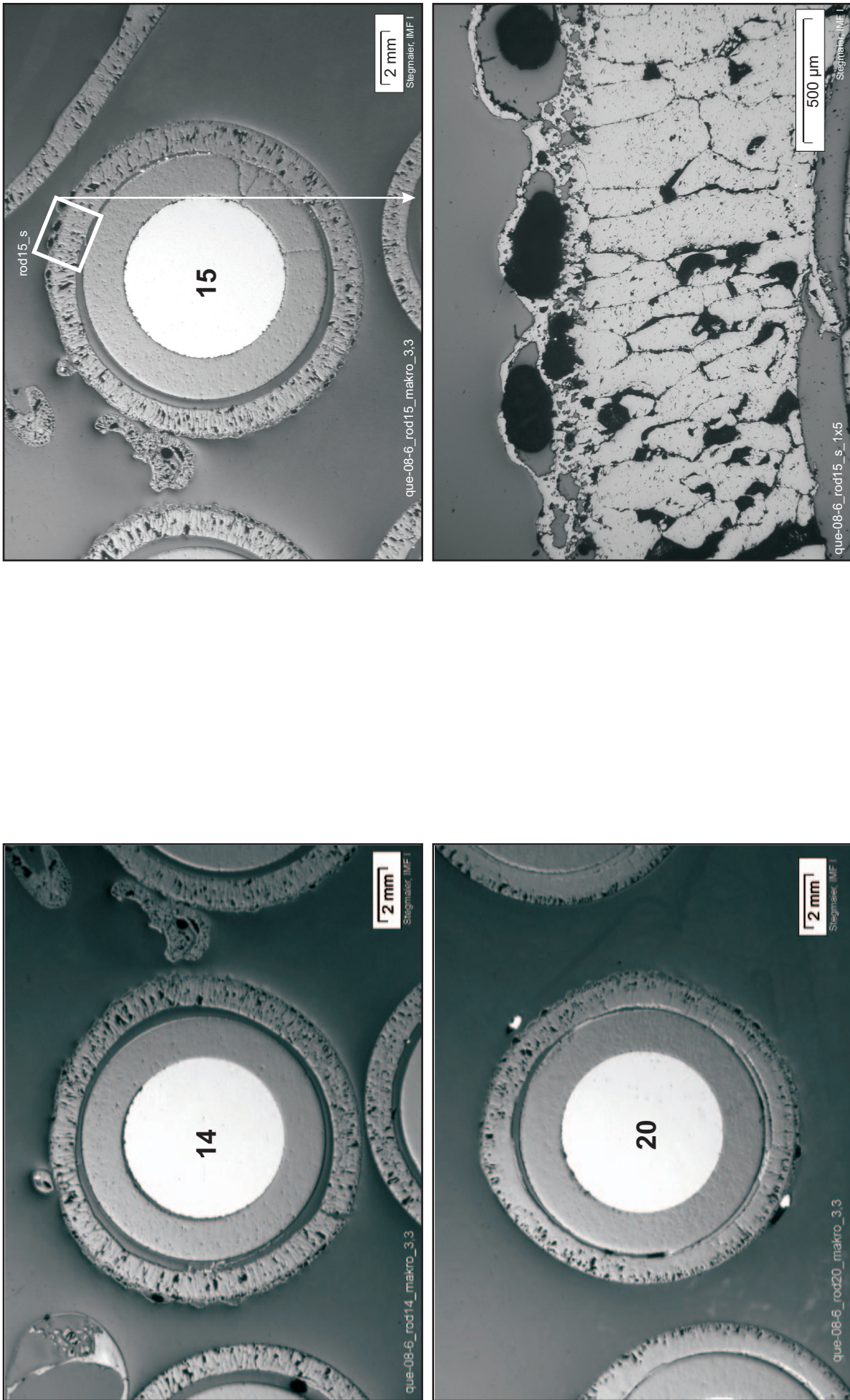


Fig. 66: Cross section at 950 mm elevation (QUE-08-6); fuel rod simulators, partly covered by porous melt.

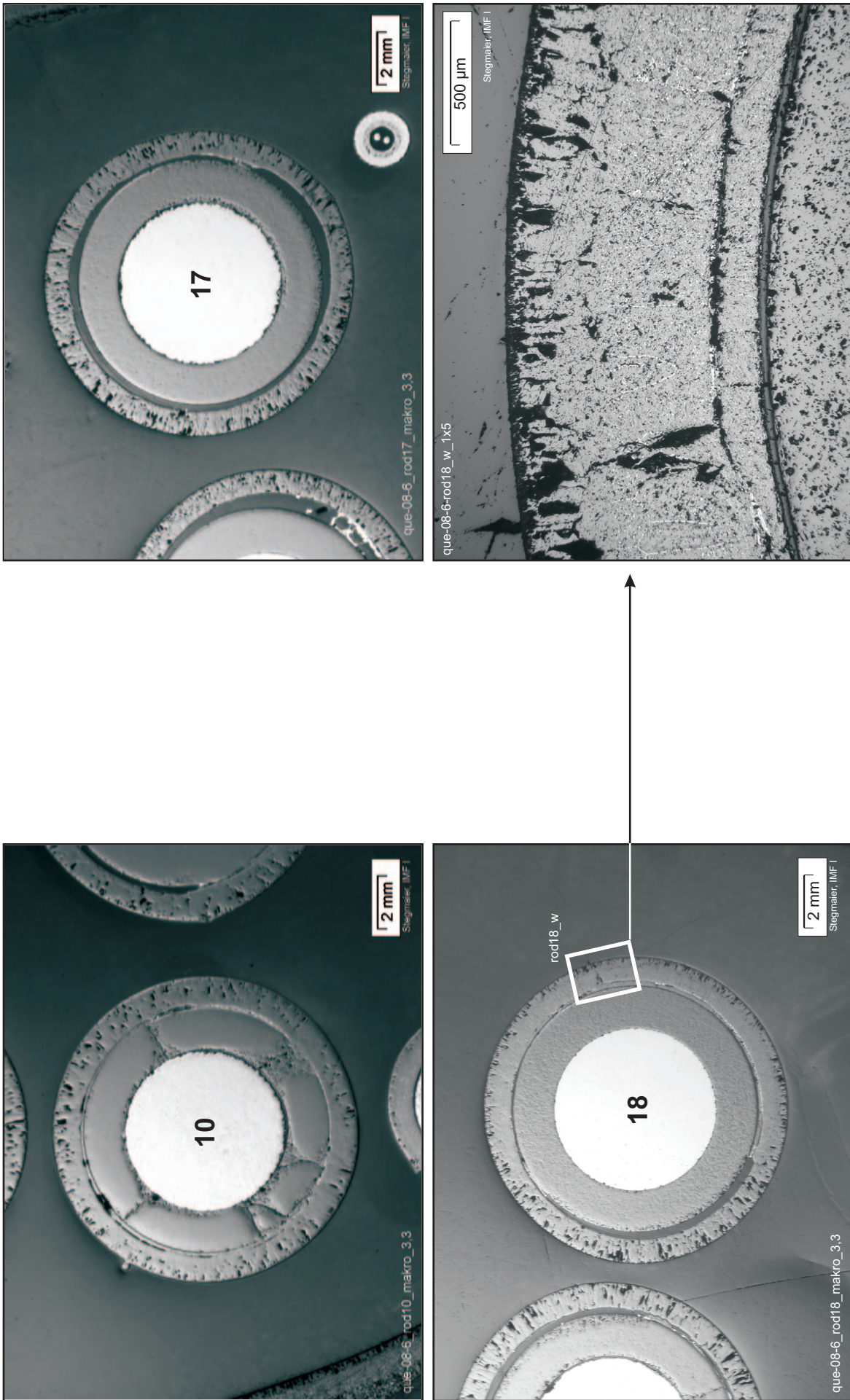


Fig. 67: Cross section at 950 mm elevation (QUE-08-6); fuel rod simulators, showing cladding/pellet gap or gap closure by oxidized interaction layer.

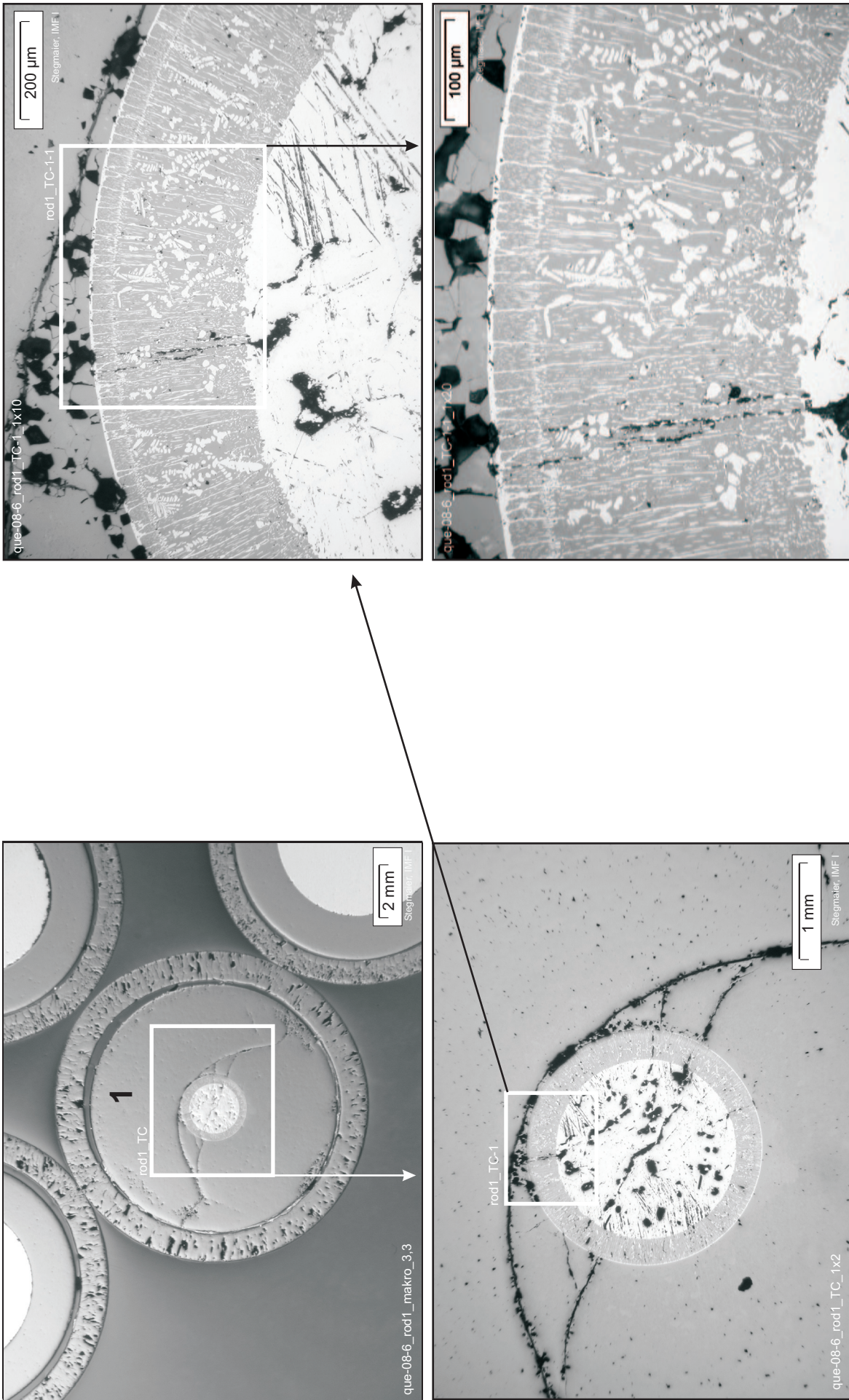


Fig. 68: Cross section at 950 mm elevation (QUE-08-6); central rod, showing filling of the annular pellet by cladding melt, and formation of an interaction layer.

Bottom of cross section slab, 986 mm elevation, inverted to top view

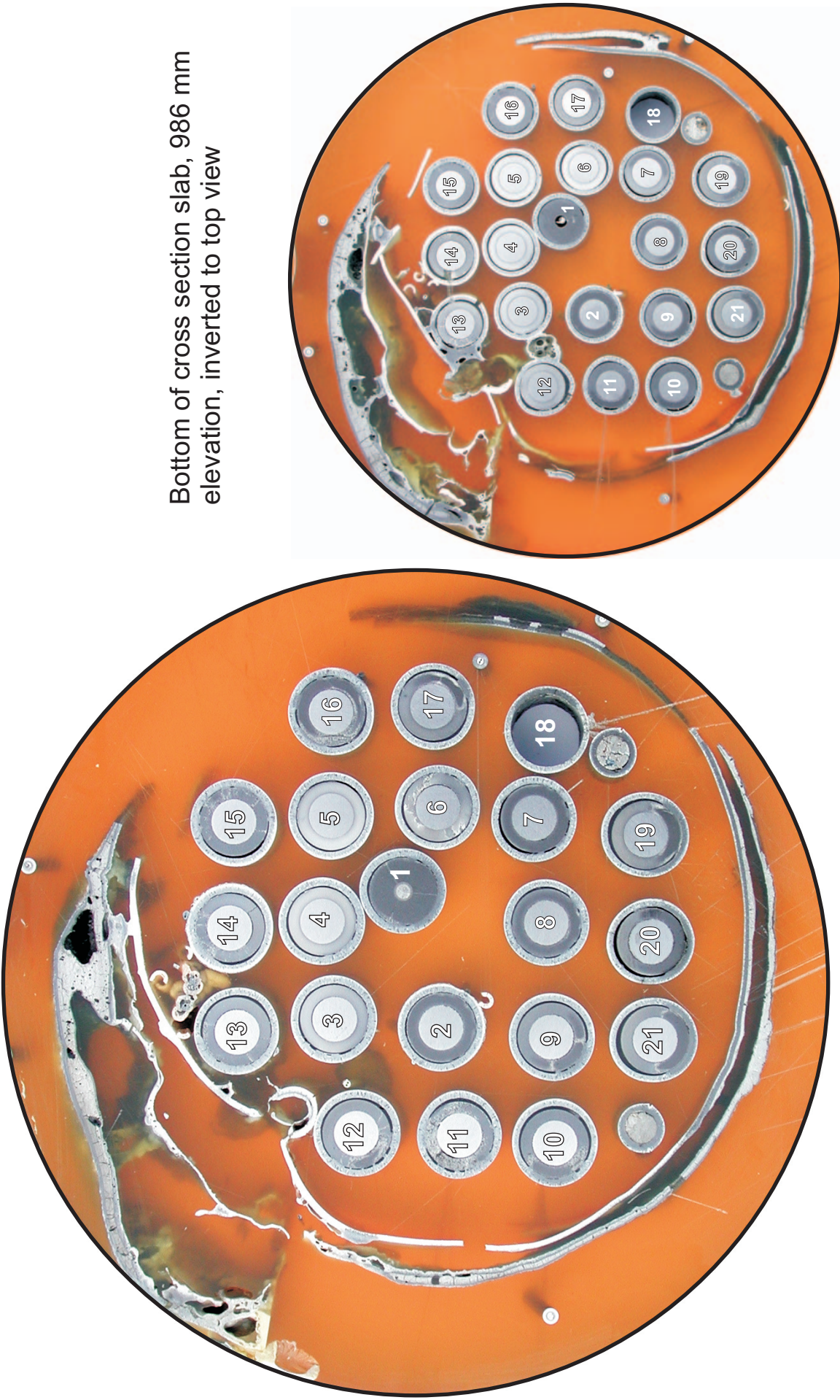


Fig. 69: Cross section at 1000 mm bundle elevation (QUE-08-10); overview from top.

Bottom of cross section slab, 1050 mm elevation, inverted to top view



Fig. 70: Cross section at 1065 mm bundle elevation (QUE-08-11); overview from top.

Bottom of cross section slab, 1135 mm elevation, inverted to top view

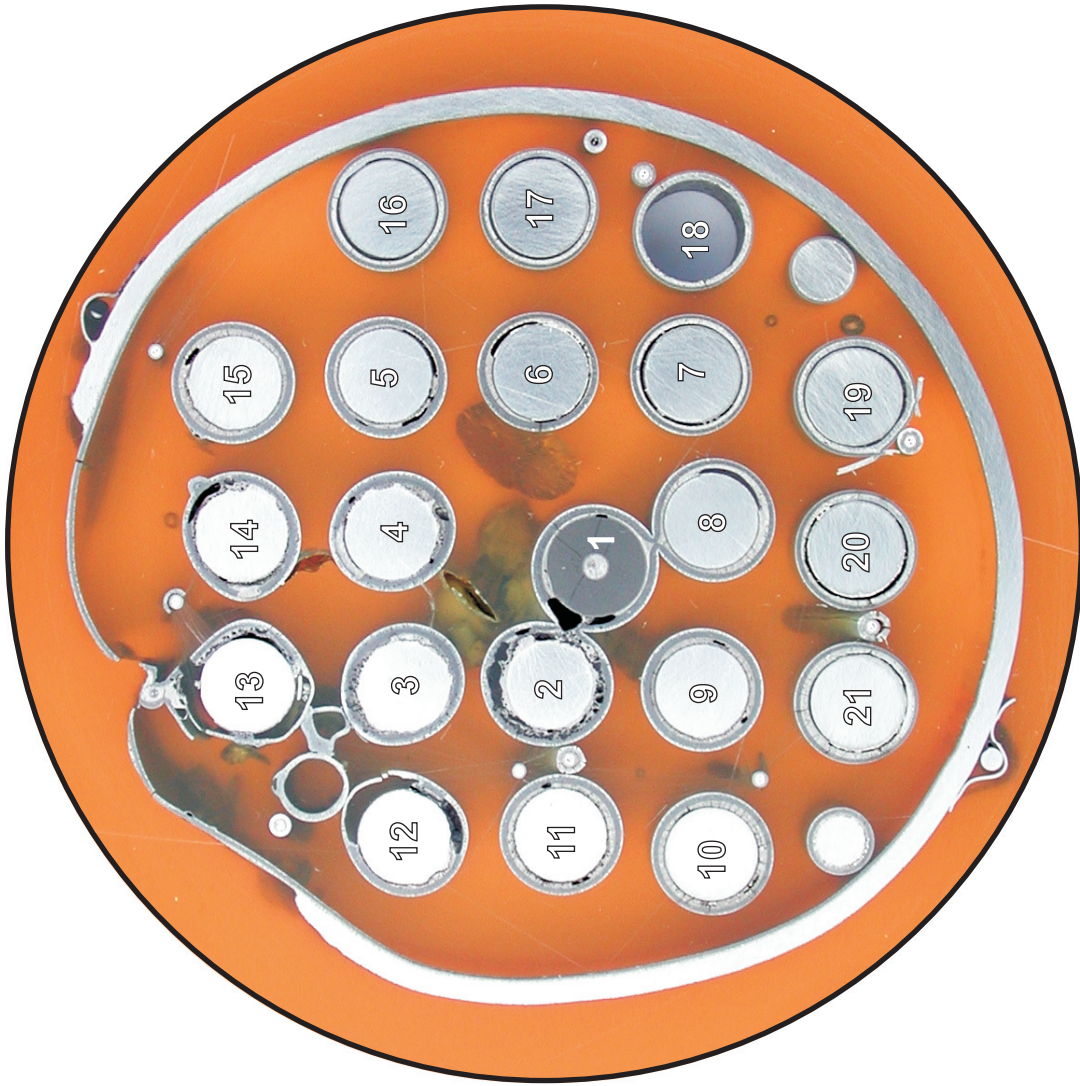


Fig. 71: Cross section at 1150 mm bundle elevation (QUE-08-12); overview from top.

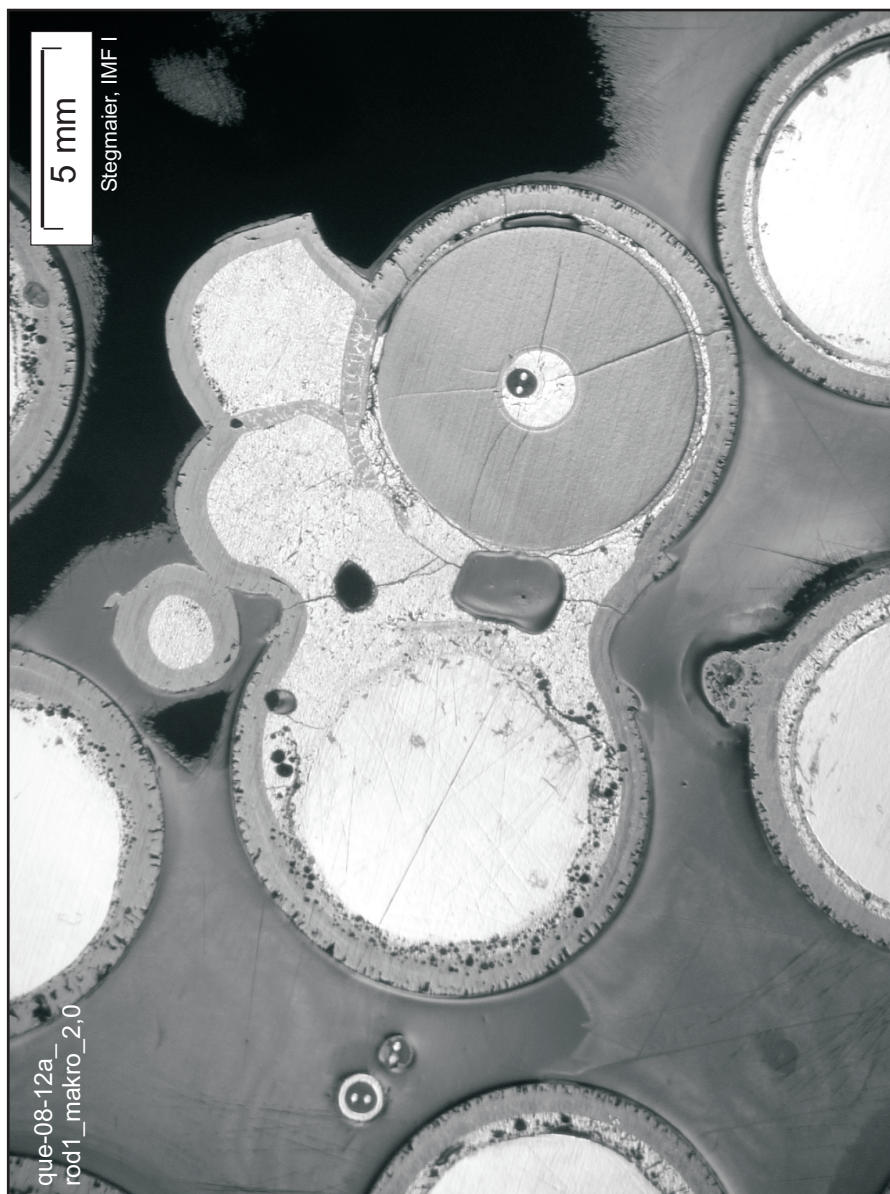
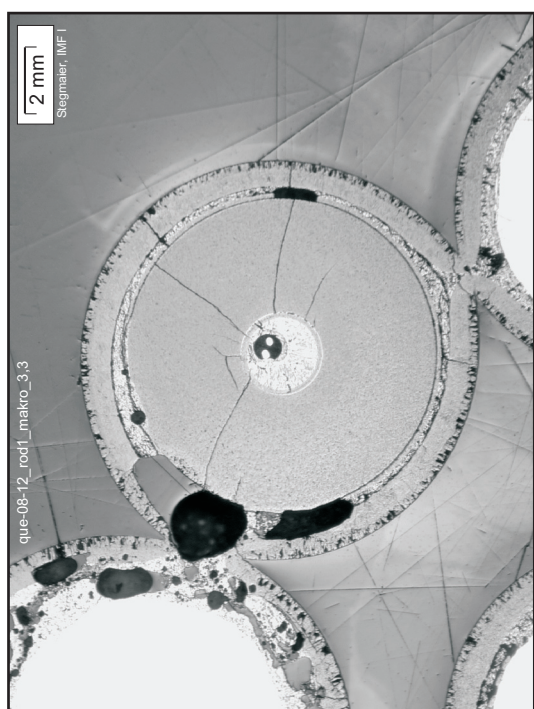


Fig. 72: Cross sections at 1150 and 1135 mm (QUE-08-12); central rod and areas around, in comparison of top (left) and bottom (right) elevations.

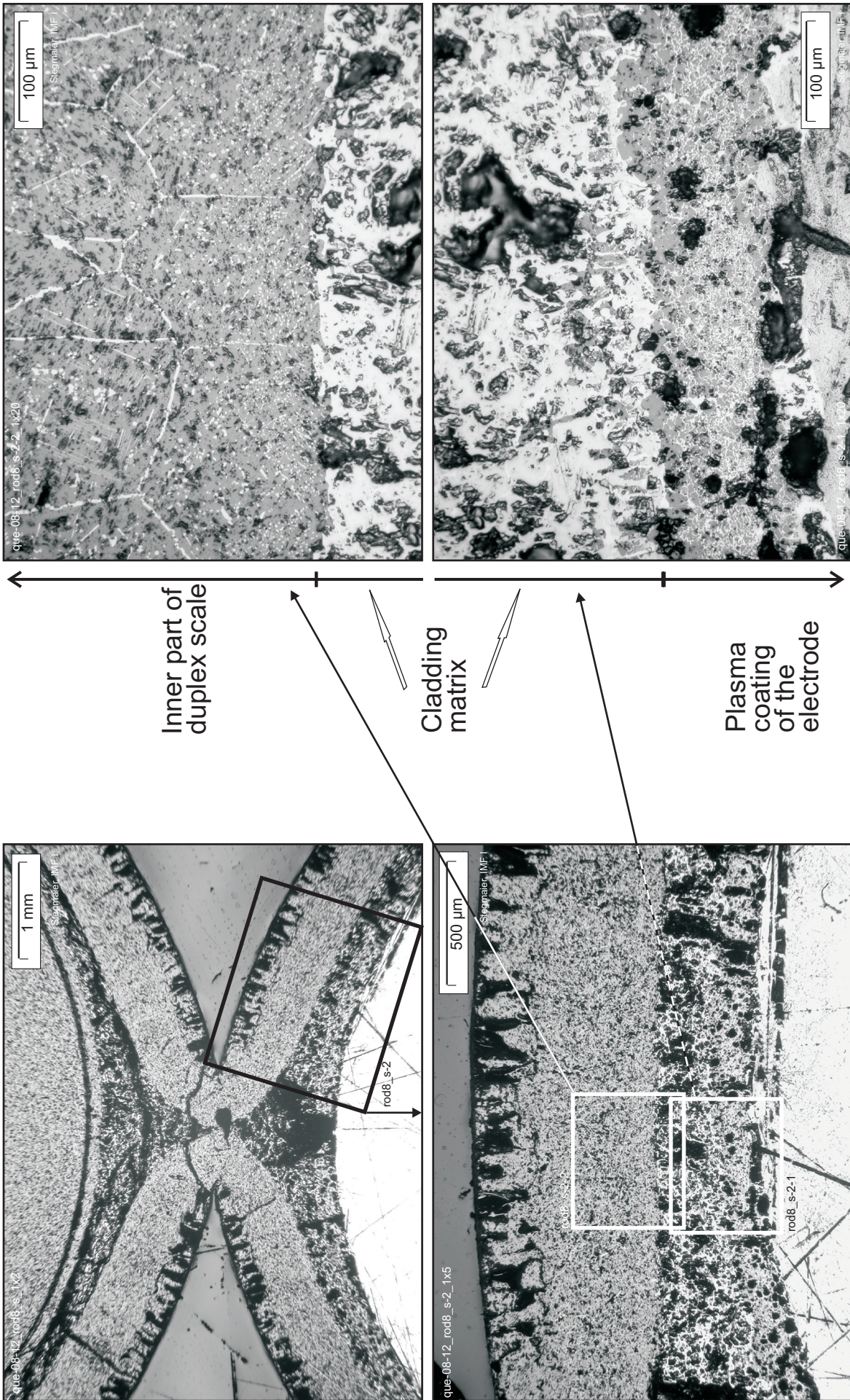


Fig. 73: Cross section at 1150 mm (QUE-08-12); neck formation between central rod and rod 8, and state of cladding and molybdenum electrode of rod 8.

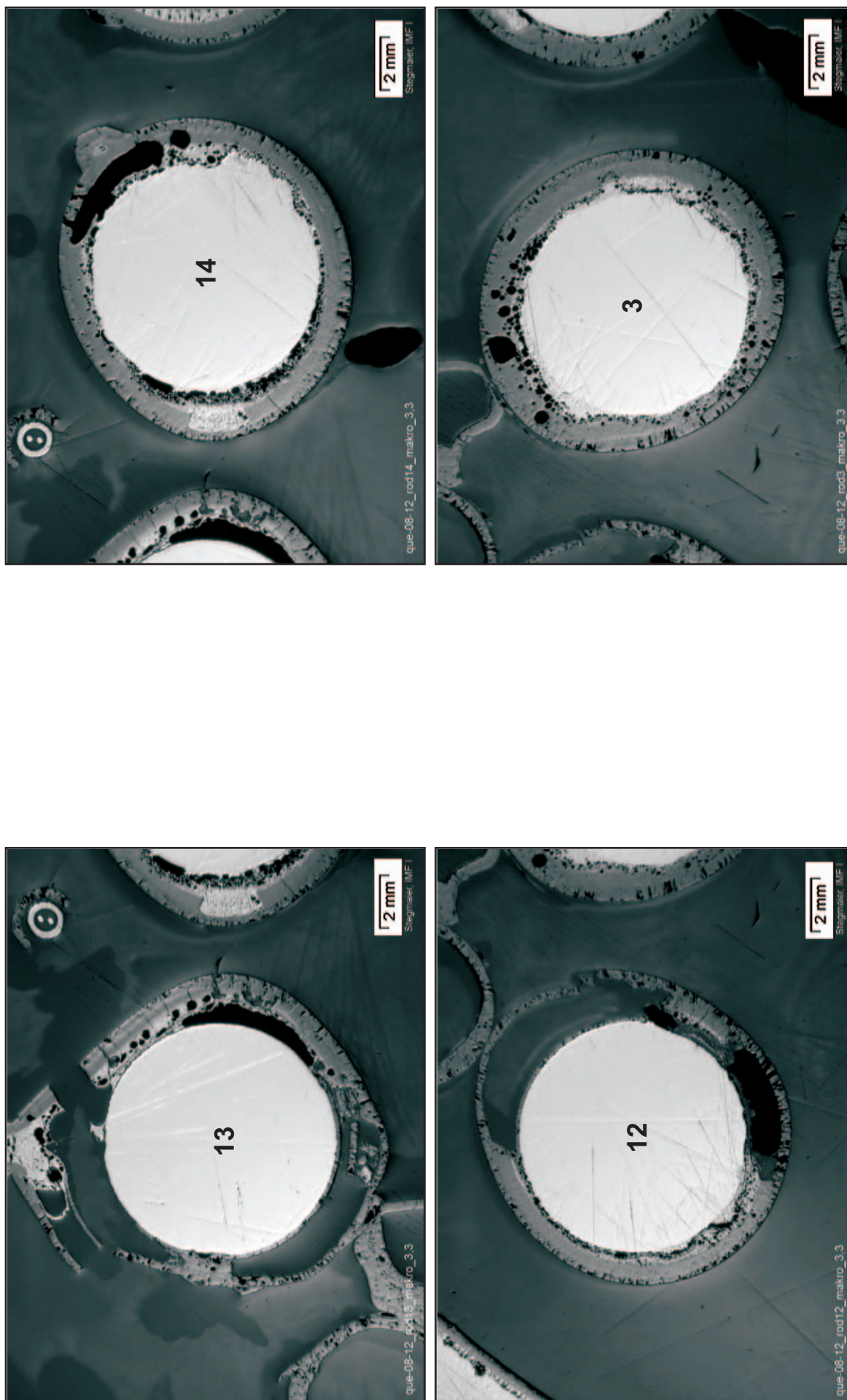


Fig. 74: Cross section at 1150 mm (QUE-08-12); state of cladding / molybdenum electrode interaction for different rods.

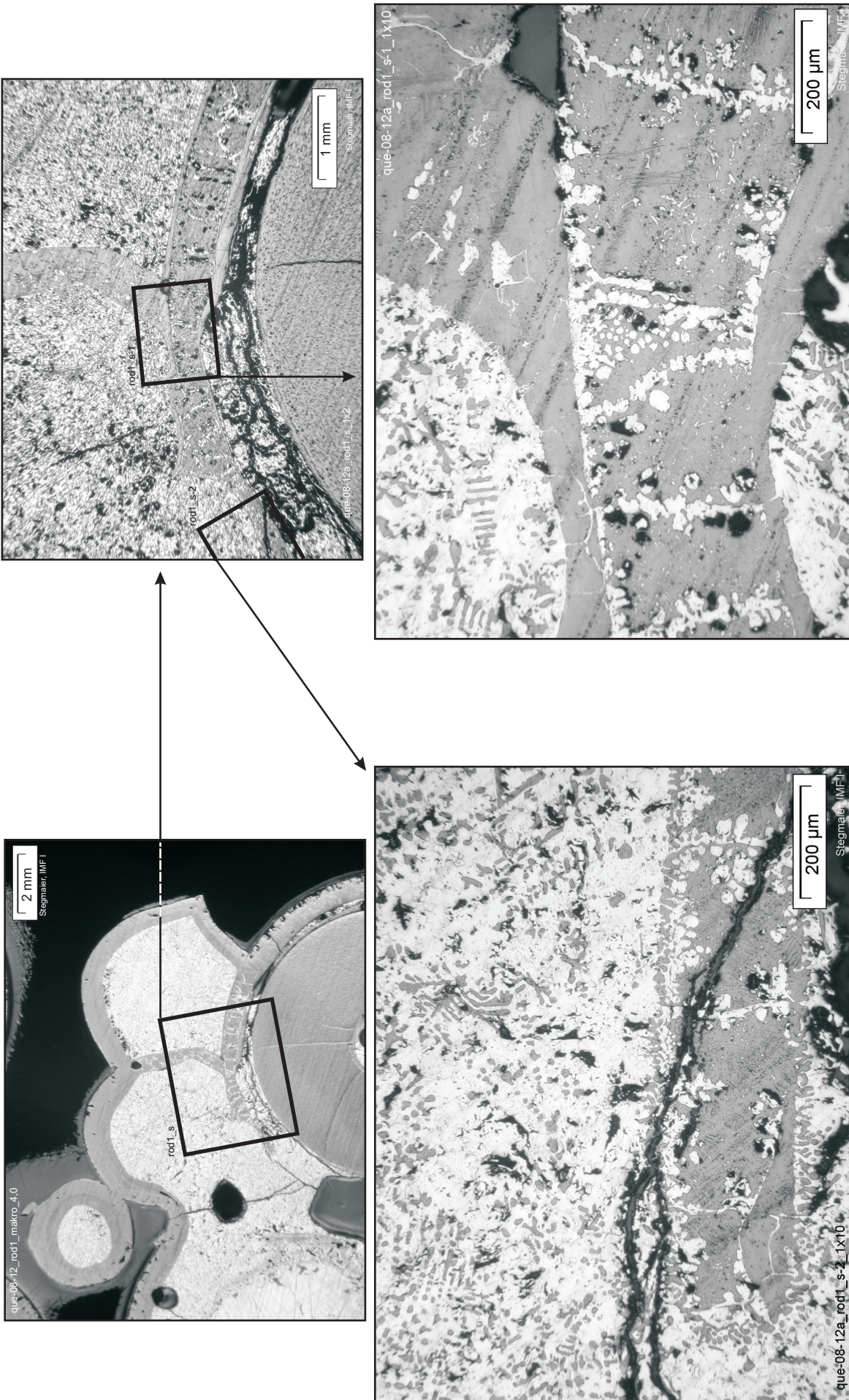


Fig. 75: Cross section at 1135 mm (QUE-08-12, slab bottom); melt pool in contact to central rod, and details of trend towards dissolution of embedded scale.

Bottom of cross section slab, 1307 mm elevation, inverted to top view



Fig. 76: Cross section at 1320 mm bundle elevation (QUE-08-14); overview from top.

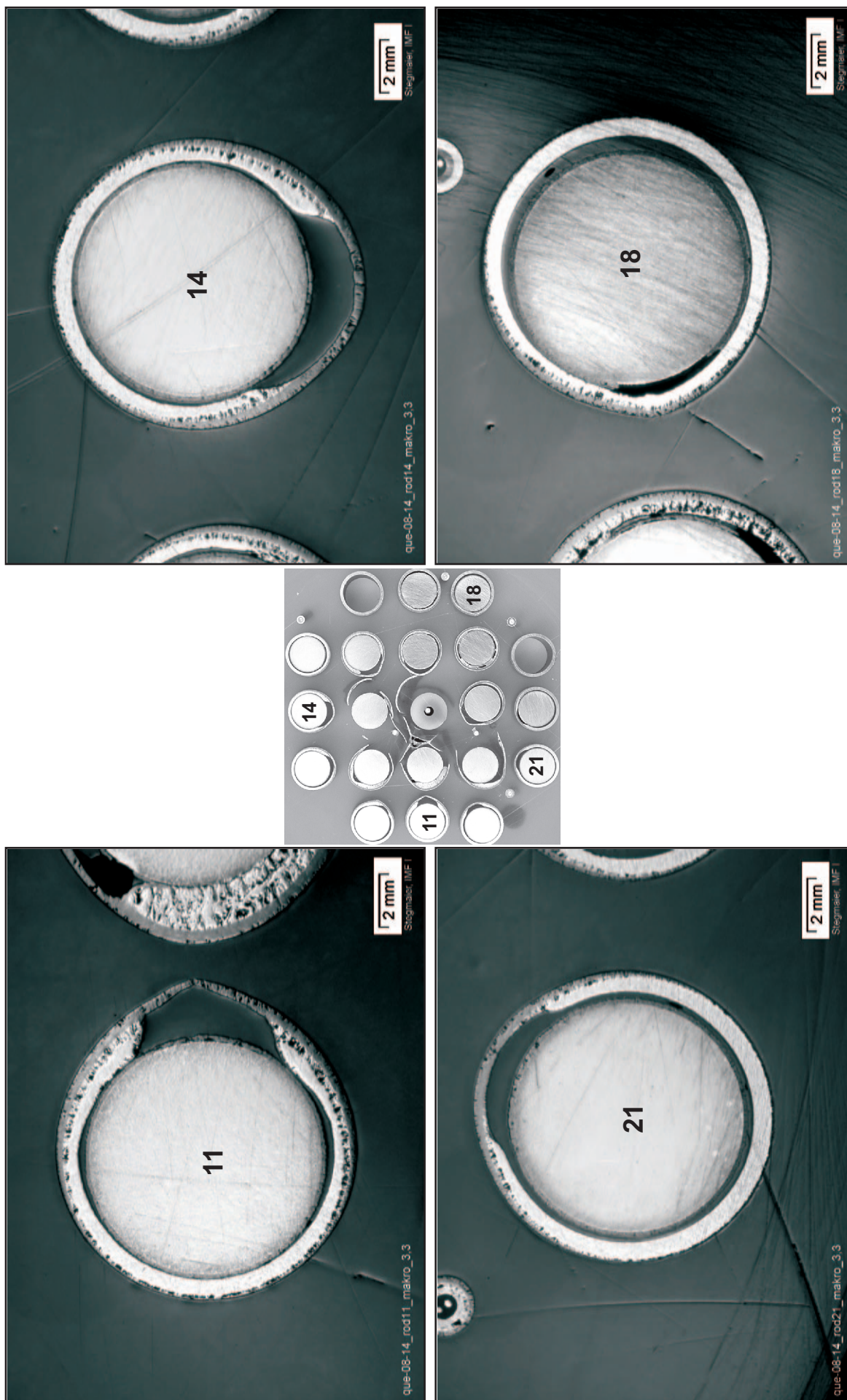


Fig. 77: Cross section at 1320 mm (QUE-08-14); rods at bundle periphery, showing strongest oxidation and melting of cladding towards bundle center, indicating remarkable temperature history variations.

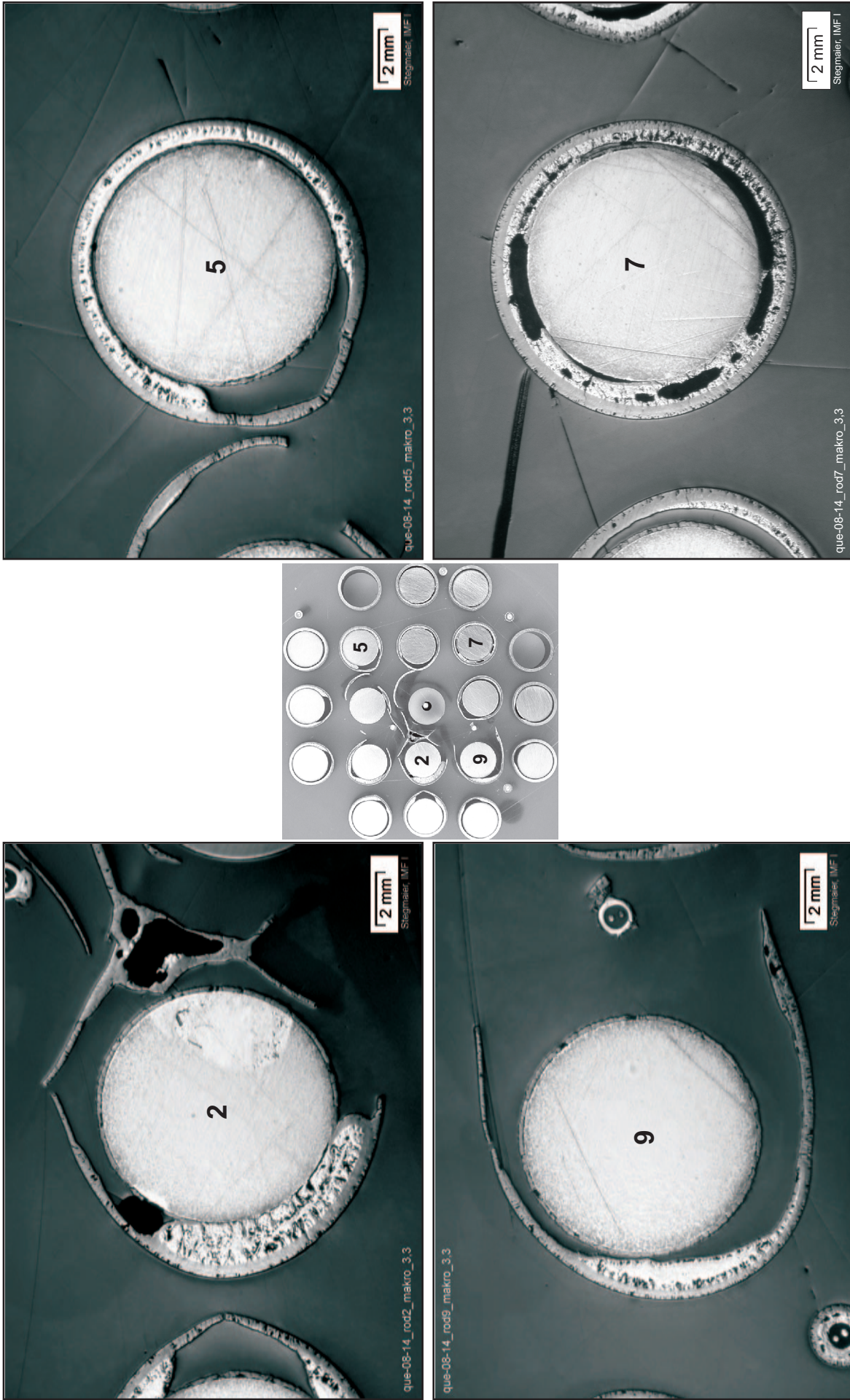


Fig. 78: Cross section at 1320 mm (QUE-08-14); rods of the inner ring, showing cladding melt redistribution and relocation. Mo electrodes not attacked during cooldown-initiated temperature escalation.

Bottom of cross section slab, 1410 mm elevation, inverted to top view

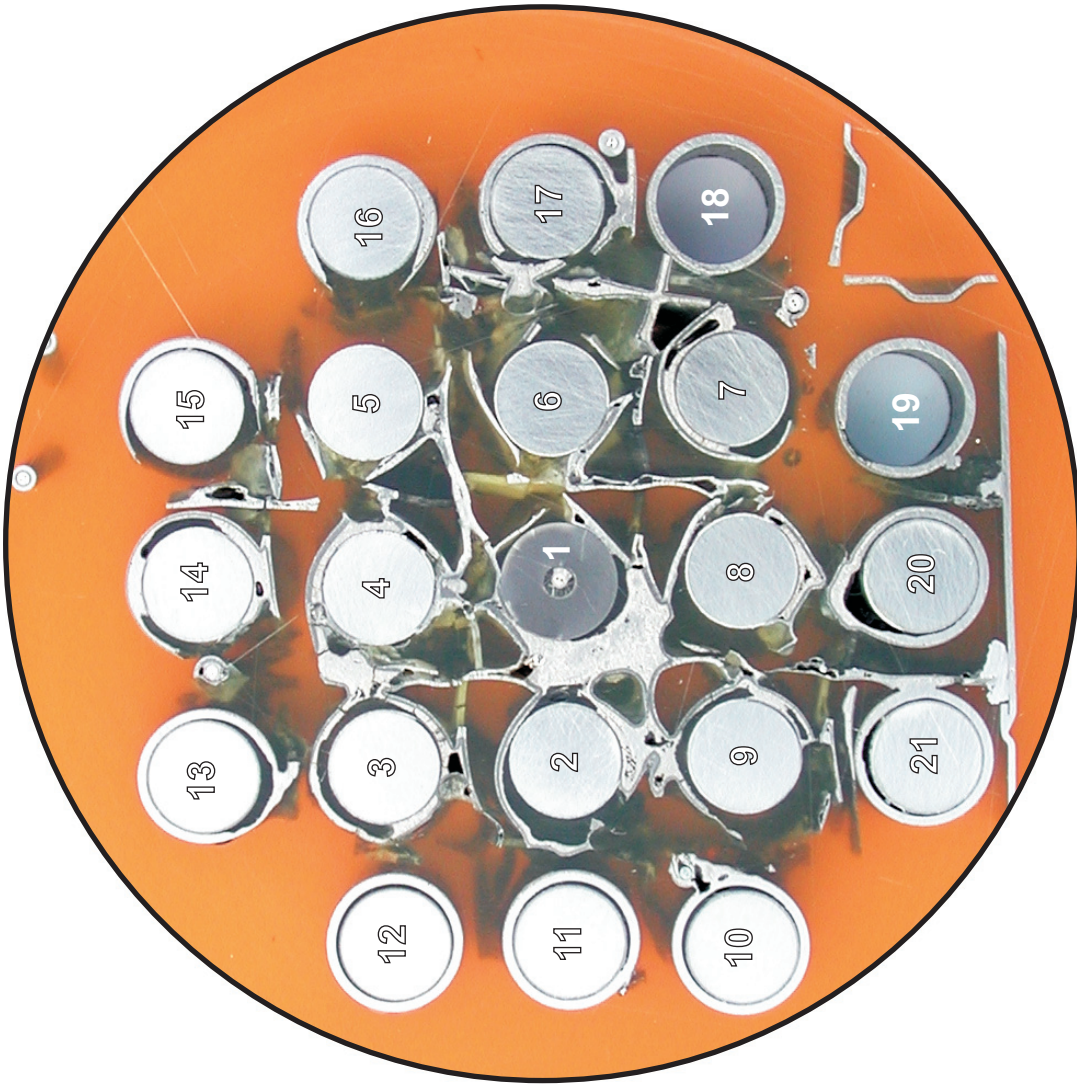


Fig. 79: Cross section at 1425 mm bundle elevation (QUE-08-15); overview from top.

Bottom of cross section slab, 1465 mm elevation, inverted to top view



Fig. 80: Cross section at 1480 mm bundle elevation (QUE-08-16); overview from top.

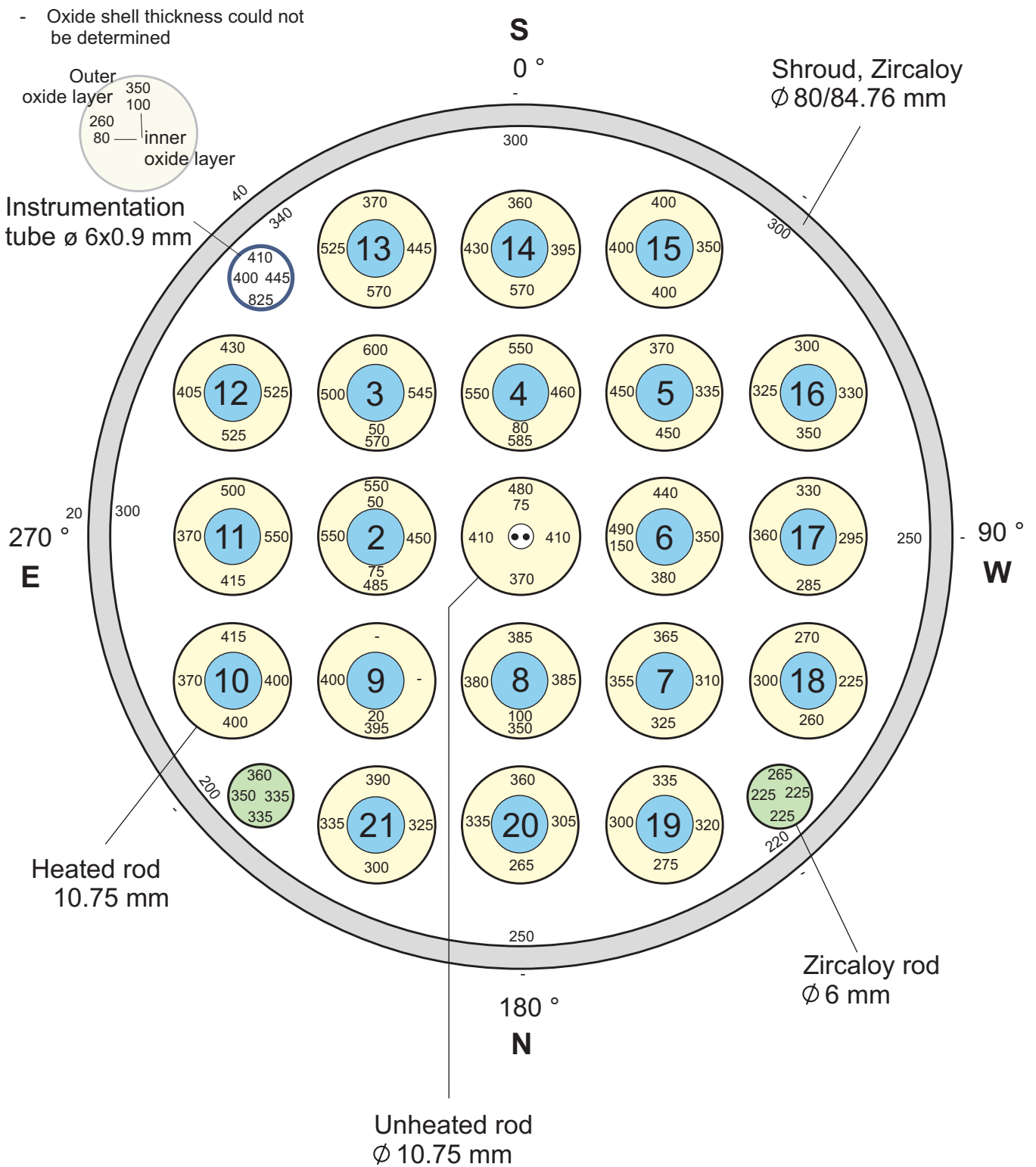


Fig 83-QUE08-Cross section QUE-08-8.cdr
21.04.05 - IMF

Fig. 83: QUENCH-08; Oxide layer thicknesses at bundle elevation 860 mm (Cross section QUE-08-8).

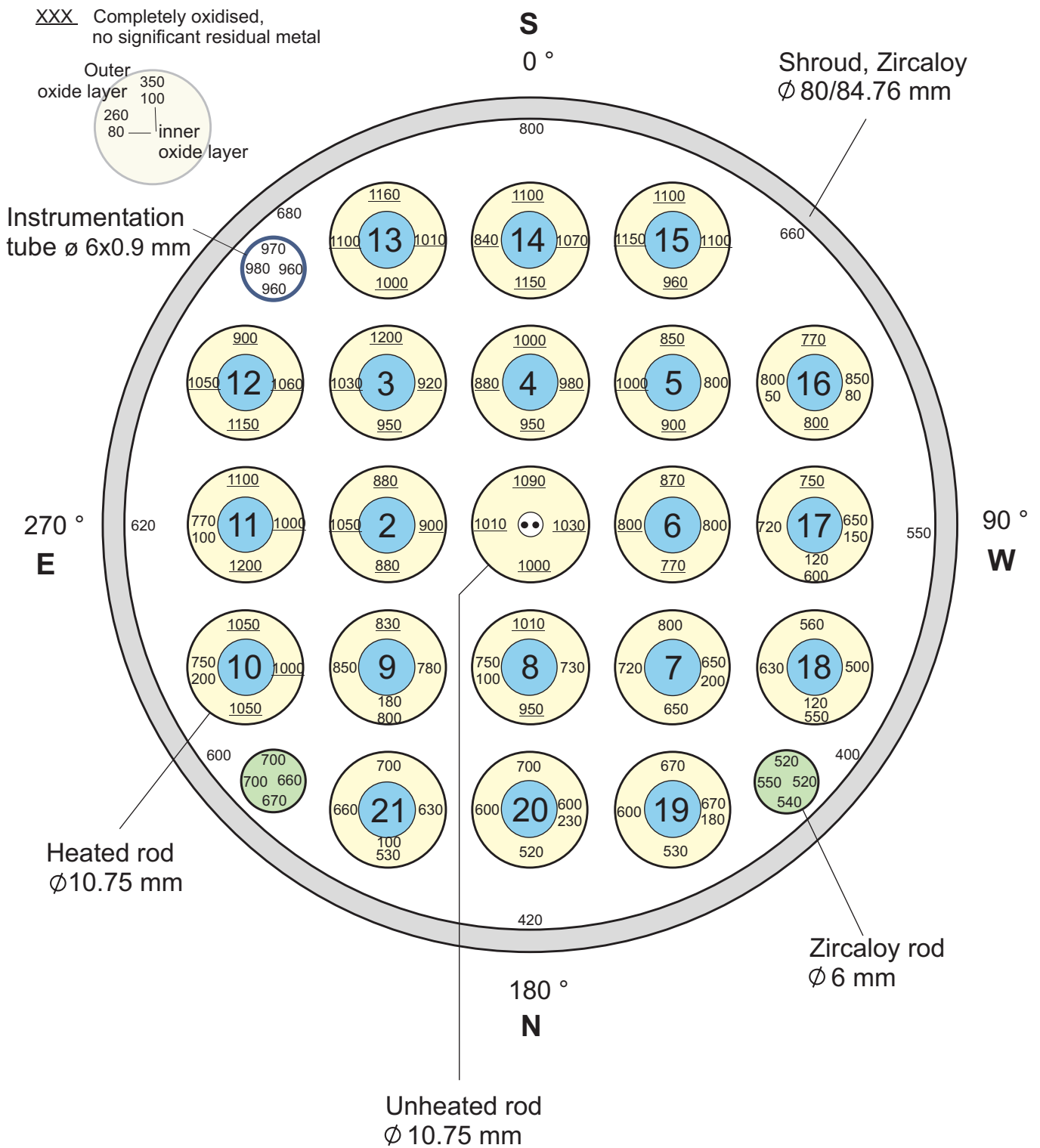


Fig 84-QUE08-Cross section QUE-08-9.cdr
21.04.05 - IMF

Fig. 84: QUENCH-08; Oxide layer thicknesses at bundle elevation 900 mm (Cross section QUE-08-9).

XXX Completely oxidised,
no significant residual metal

- Oxide shell thickness could not be determined

Instrumentation tube
Ø 6x0.9 mm

Shroud, Zircaloy
Ø 80/84.76 mm

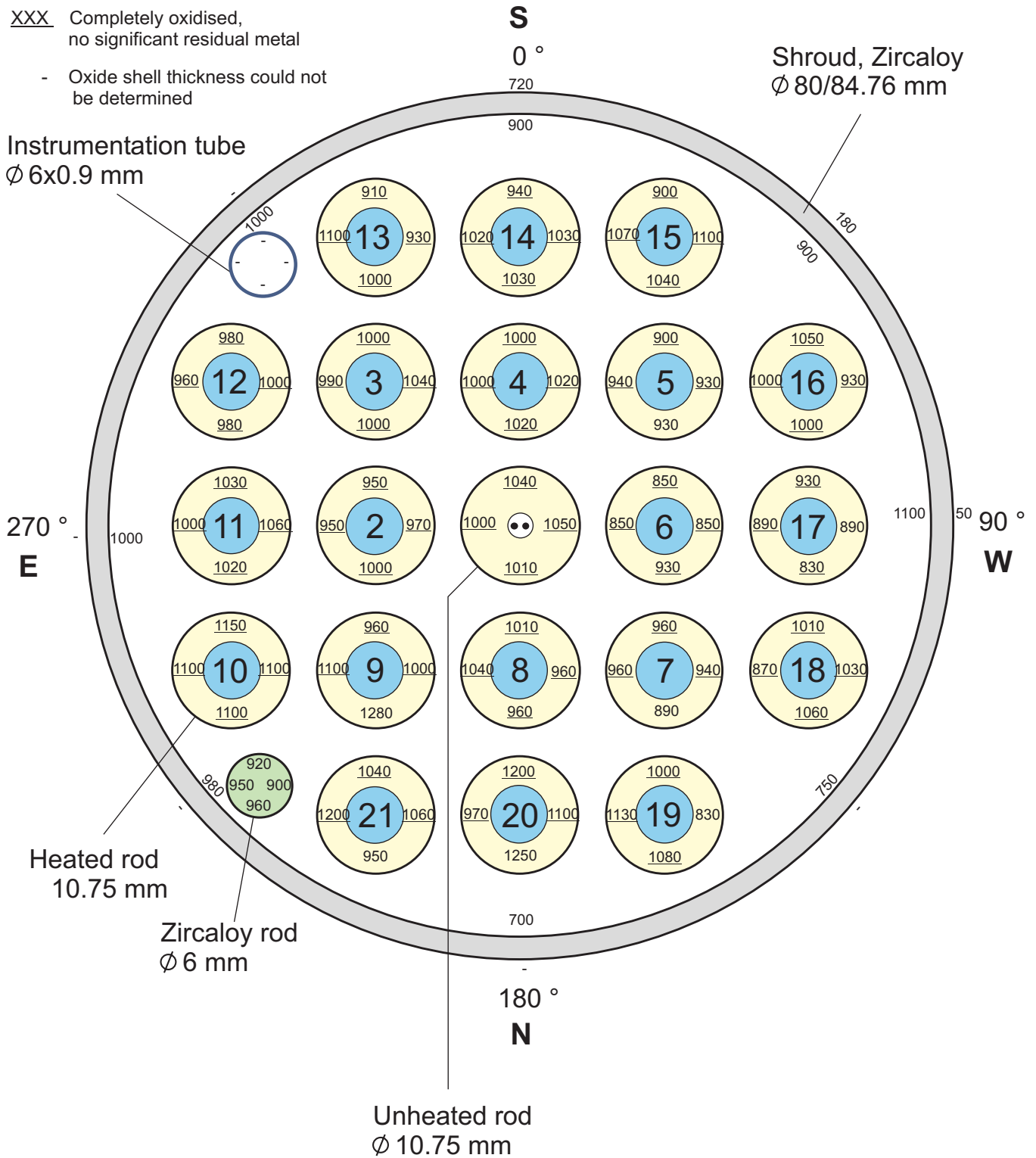


Fig 85-QUE08-Cross section QUE-08-6.cdr
21.04.05 - IMF

Fig. 85: QUENCH-08; Oxide layer thicknesses at bundle elevation 950 mm (Cross section QUE-08-6).

XXX Completely oxidised,
no significant residual metal

- Oxide shell thickness could not be determined

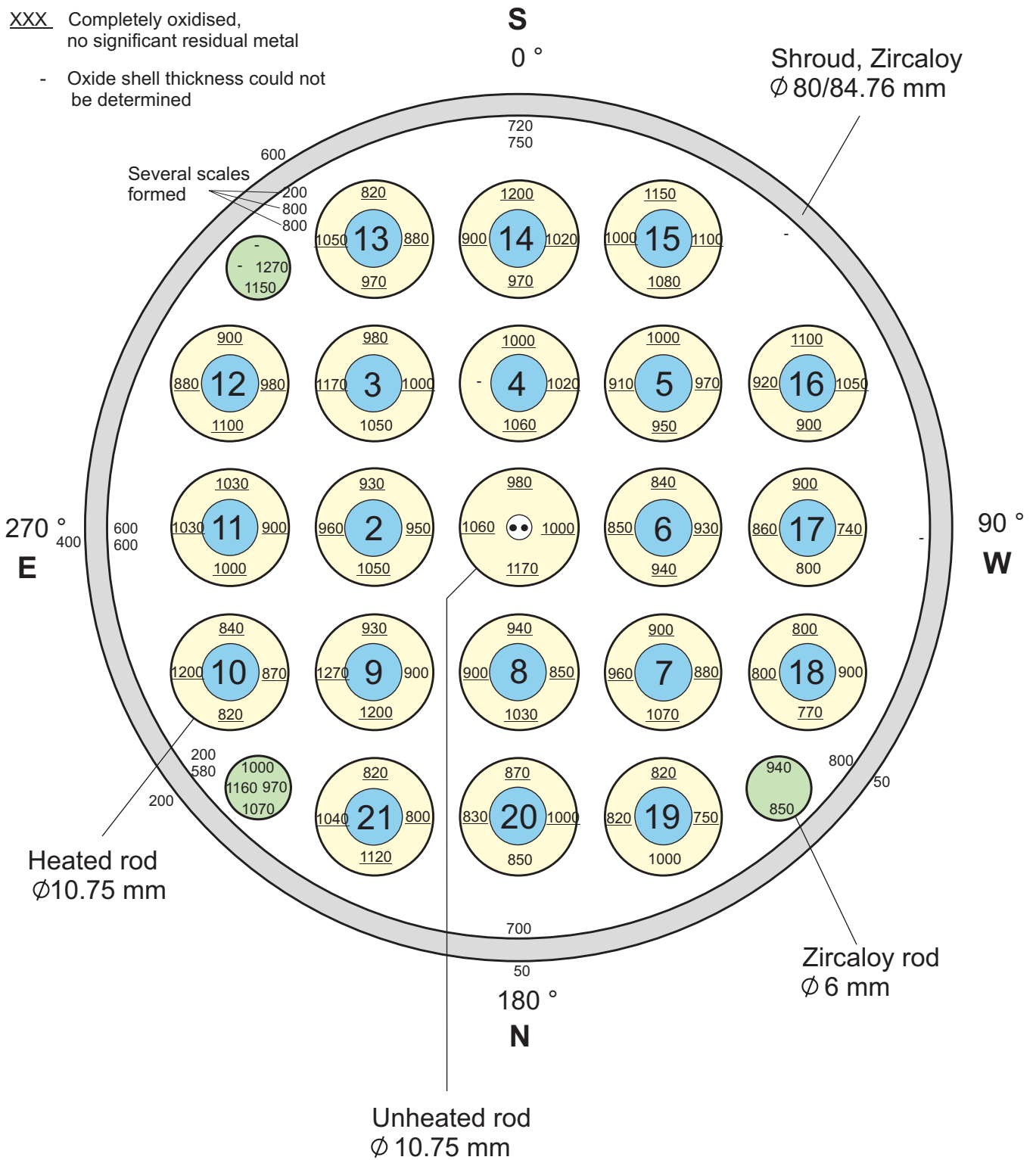


Fig 86-QUE08-Cross section QUE-08-10.cdr
21.04.05 - IMF

Fig. 86: QUENCH-08; Oxide layer thicknesses at bundle elevation 1000 mm (Cross section QUE-08-10).

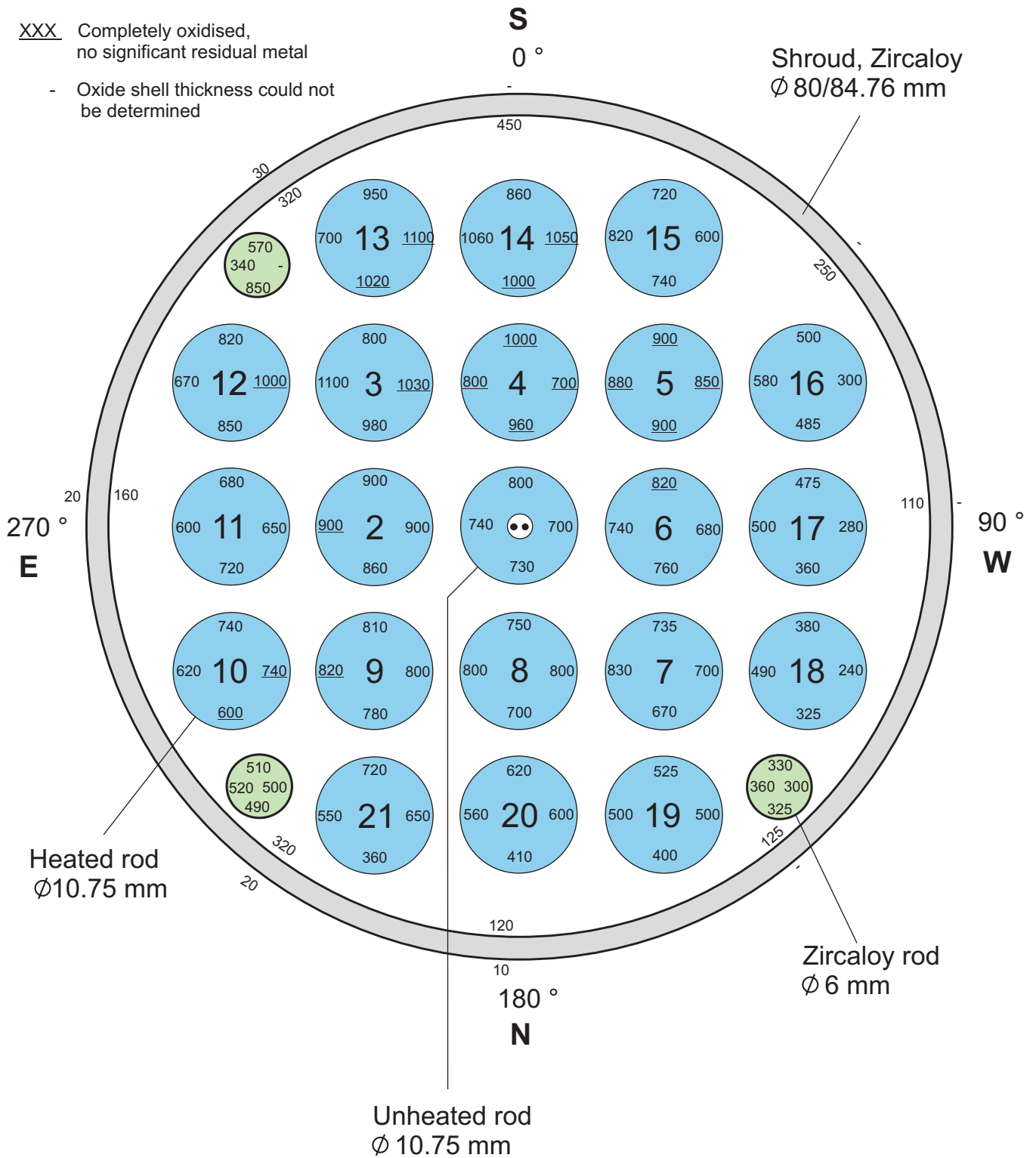


Fig 87-QUE08-Cross section QUE-08-11.cdr
16.07.05 - IMF

Fig. 87: QUENCH-08; Oxide layer thicknesses at bundle elevation 1065 mm (Cross section QUE-08-11).

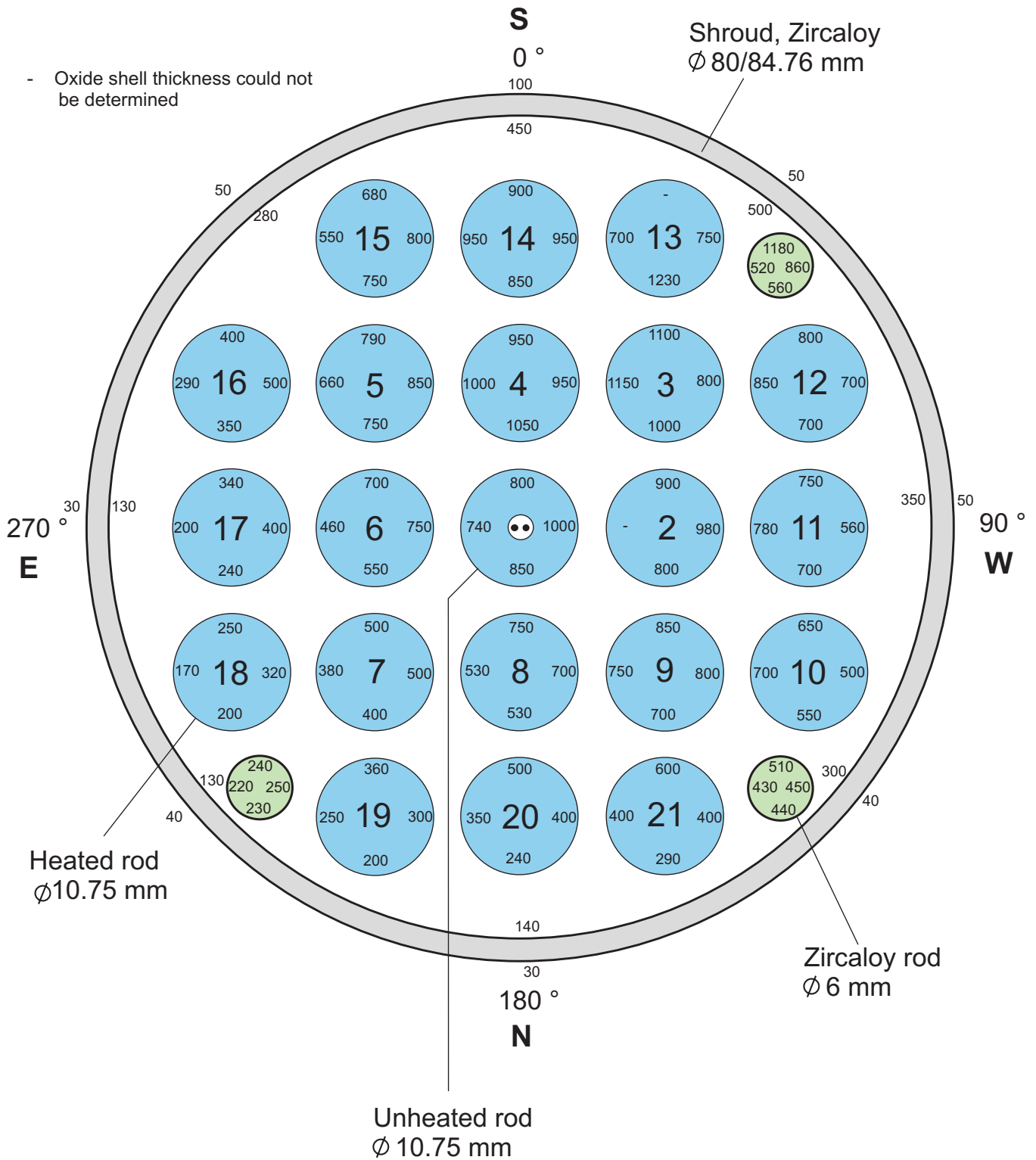


Fig 88-QUE08-Cross section QUE-08-12.cdr
21.04.05 - IMF

Fig. 88: QUENCH-08; Oxide layer thicknesses at bundle elevation 1135 mm (Cross section QUE-08-12).

XXX Completely oxidised,
no significant residual metal

- Oxide shell thickness could not be determined

S
0 °

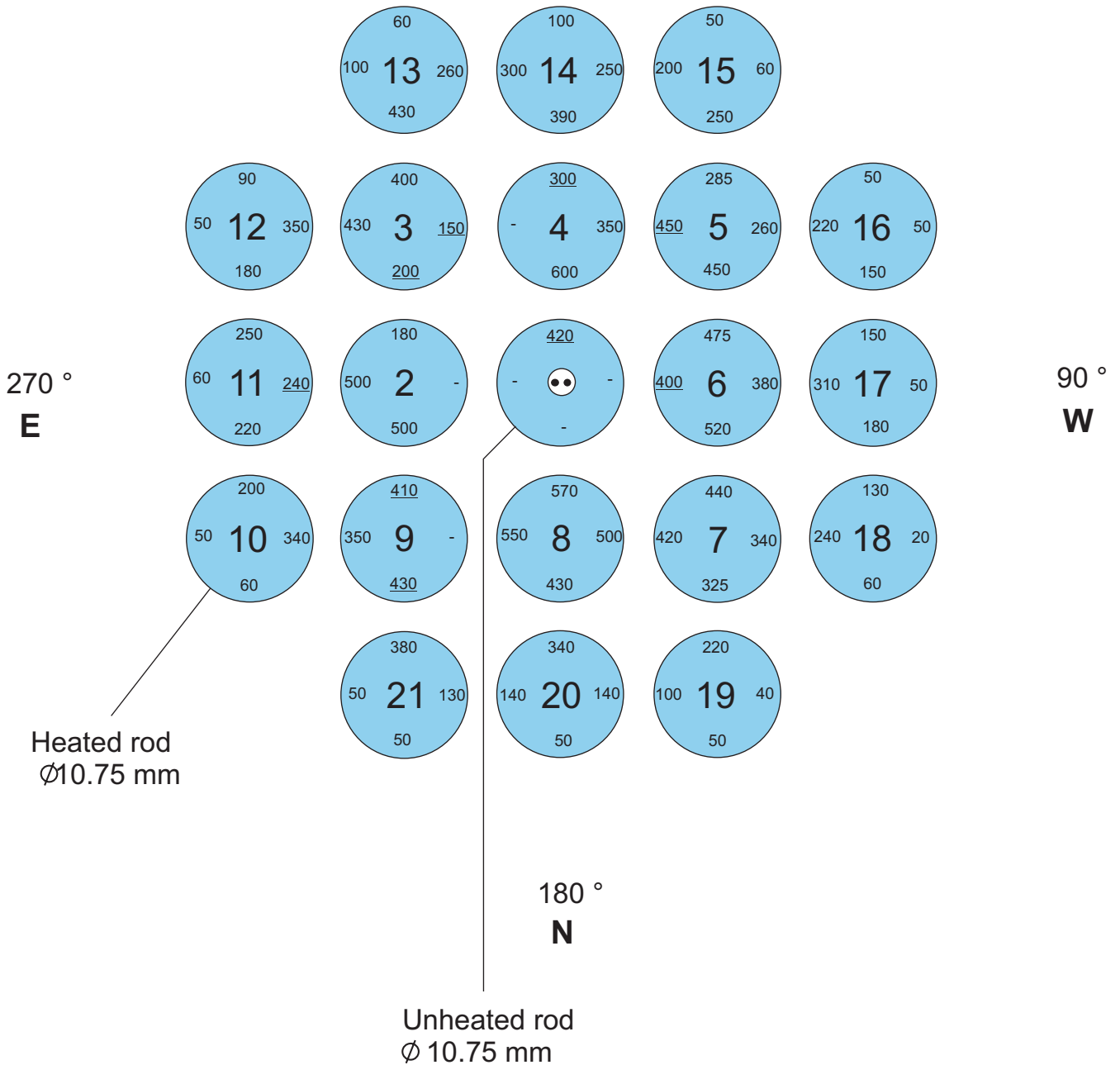


Fig 89-QUE08-Cross section QUE-08-14.cdr
21.04.05 - IMF

Fig. 89: QUENCH-08; Oxide layer thicknesses at bundle elevation 1320 mm (Cross section QUE-08-14).

S
0°

- Oxide shell thickness could not be determined

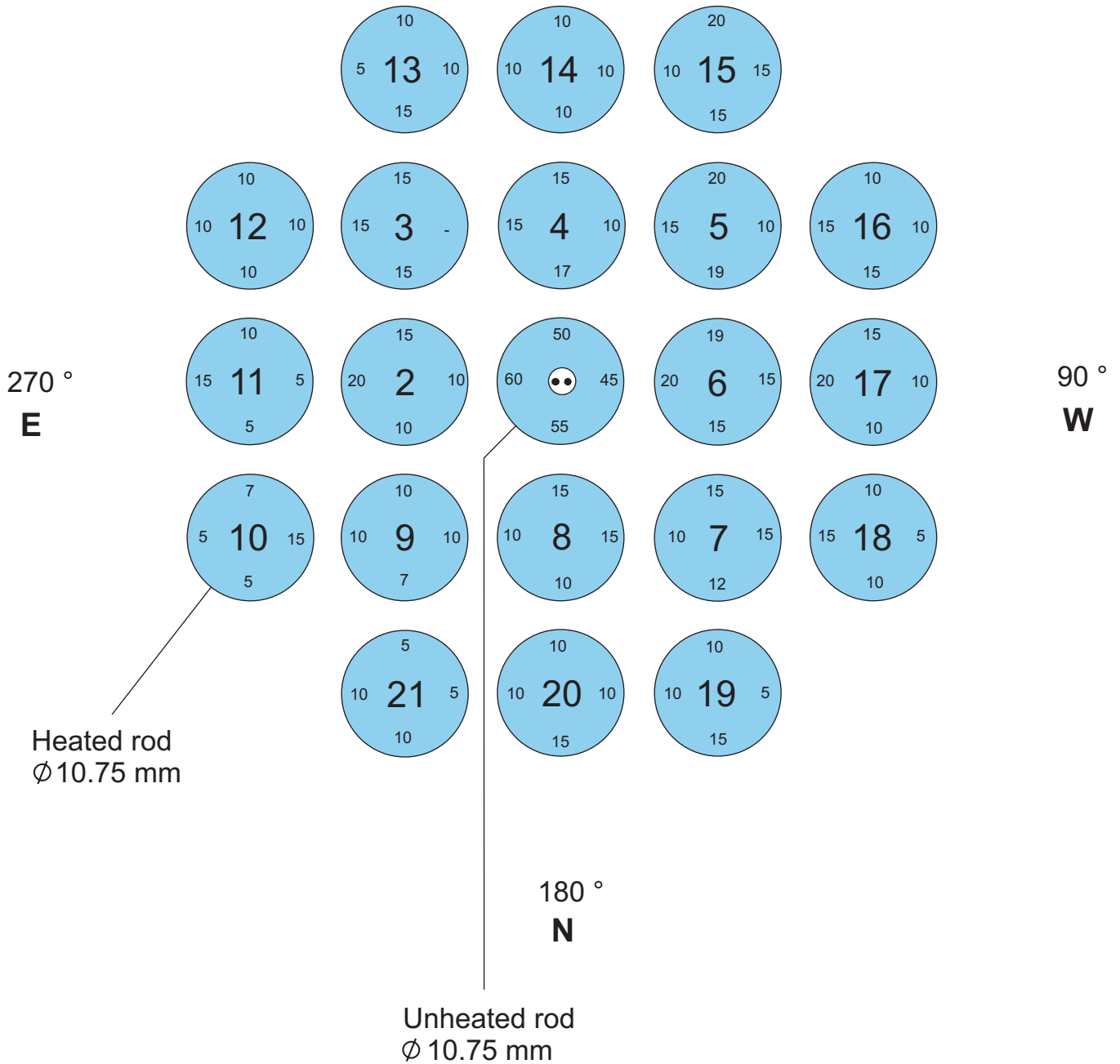


Fig 90-QUE08-Cross section QUE-08-16.cdr
21.04.05 - IMF

Fig. 90: QUENCH-08; Oxide layer thicknesses at bundle elevation 1480 mm (Cross section QUE-08-16).

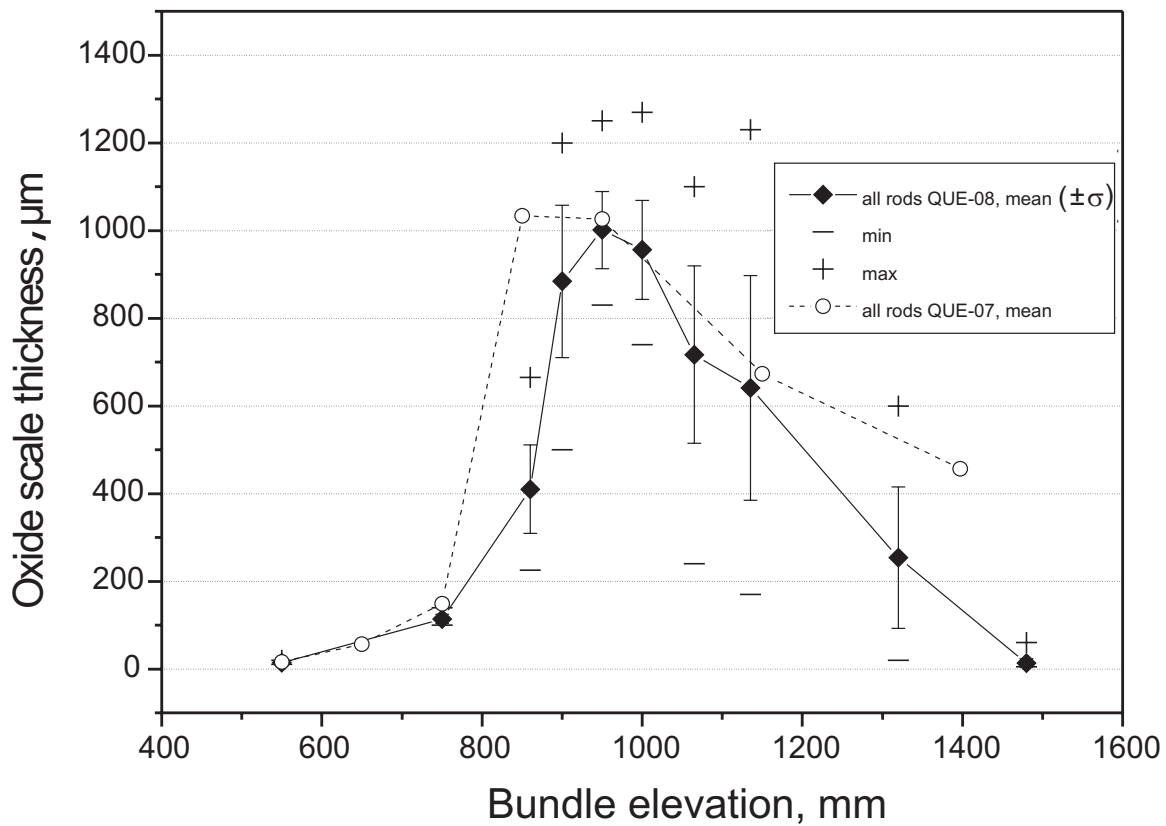
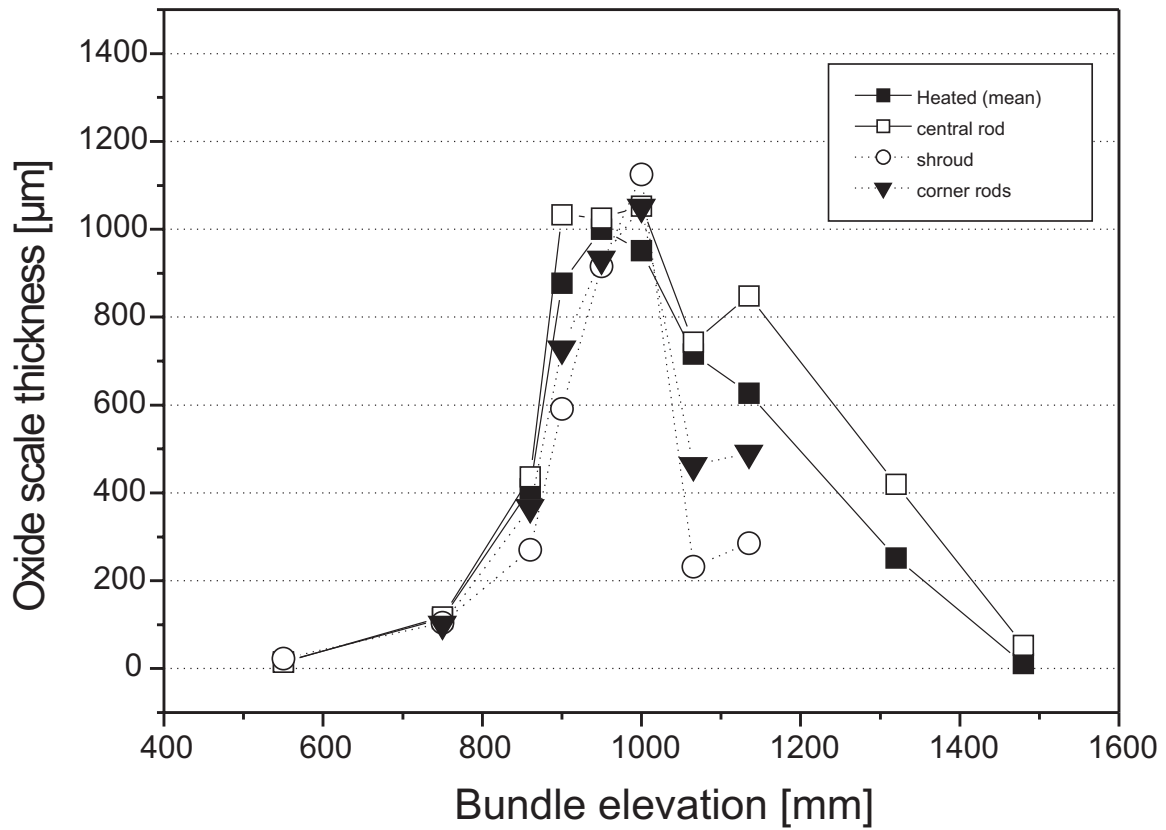


Fig 91-QUE08-oxide scale.cdr
21.04.05 - IMF

Fig. 91: QUENCH-08; Axial distribution of the oxide scale, top, and comparison of the mean data with experiment QUENCH-07, bottom.

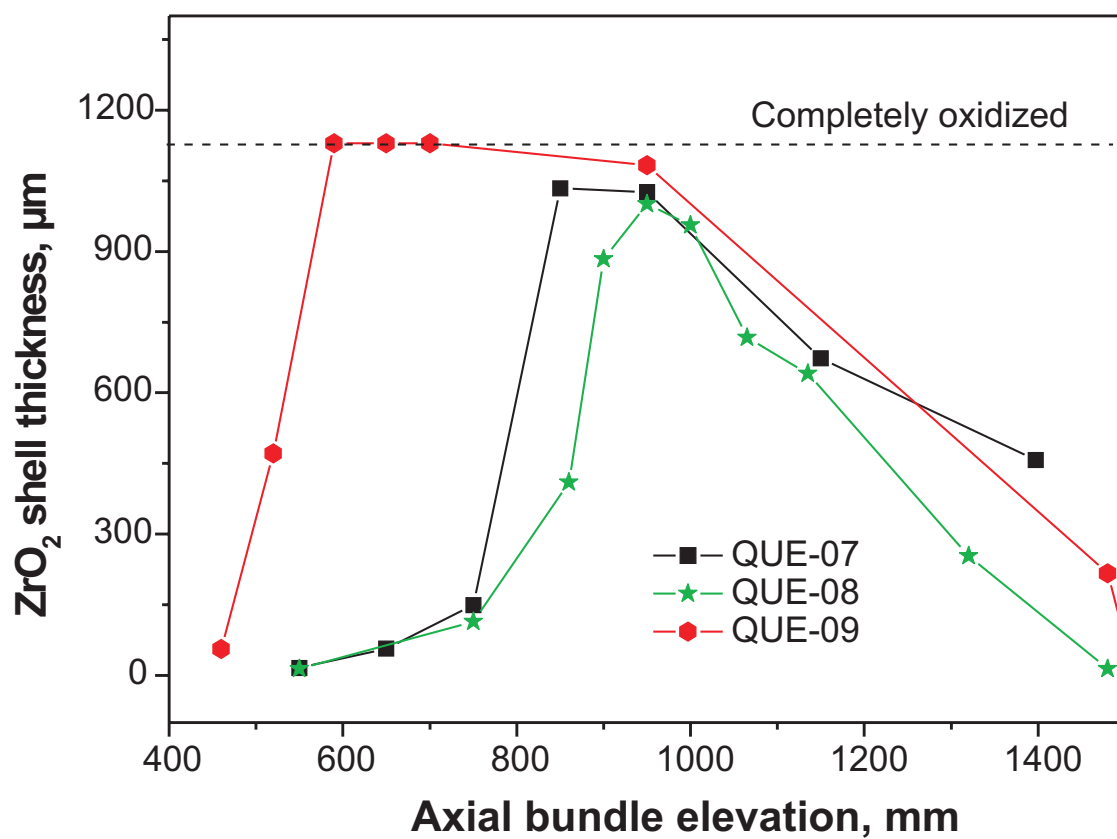


Fig 92-QUE08+07+09 oxide scale.cdr
22.04.05 - IMF

Fig. 92: Axial oxide scale profiles of experiments QUENCH-07, QUENCH-08, and QUENCH-09.

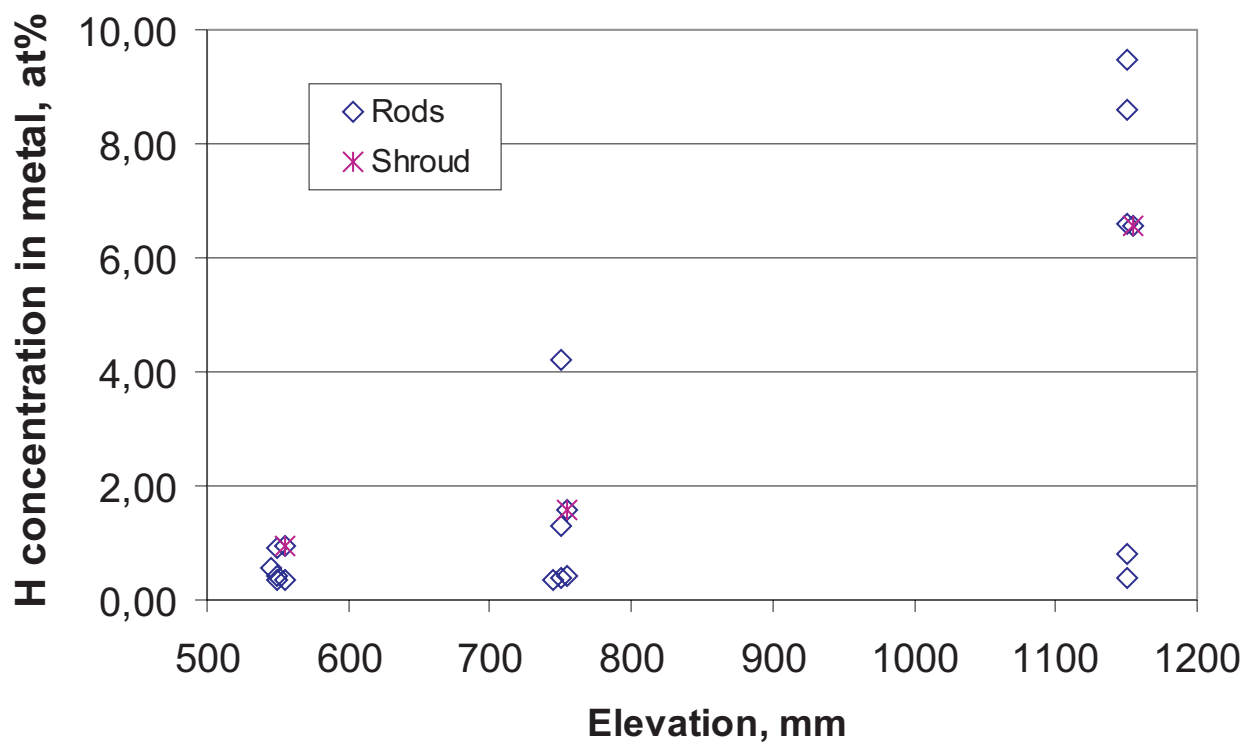


Fig 93-QUE08-absorbed Hydrogen.cdr
22.04.05 - IMF

Fig. 93: QUENCH-08; Hydrogen absorbed by the remaining Zr(O) metal phases.

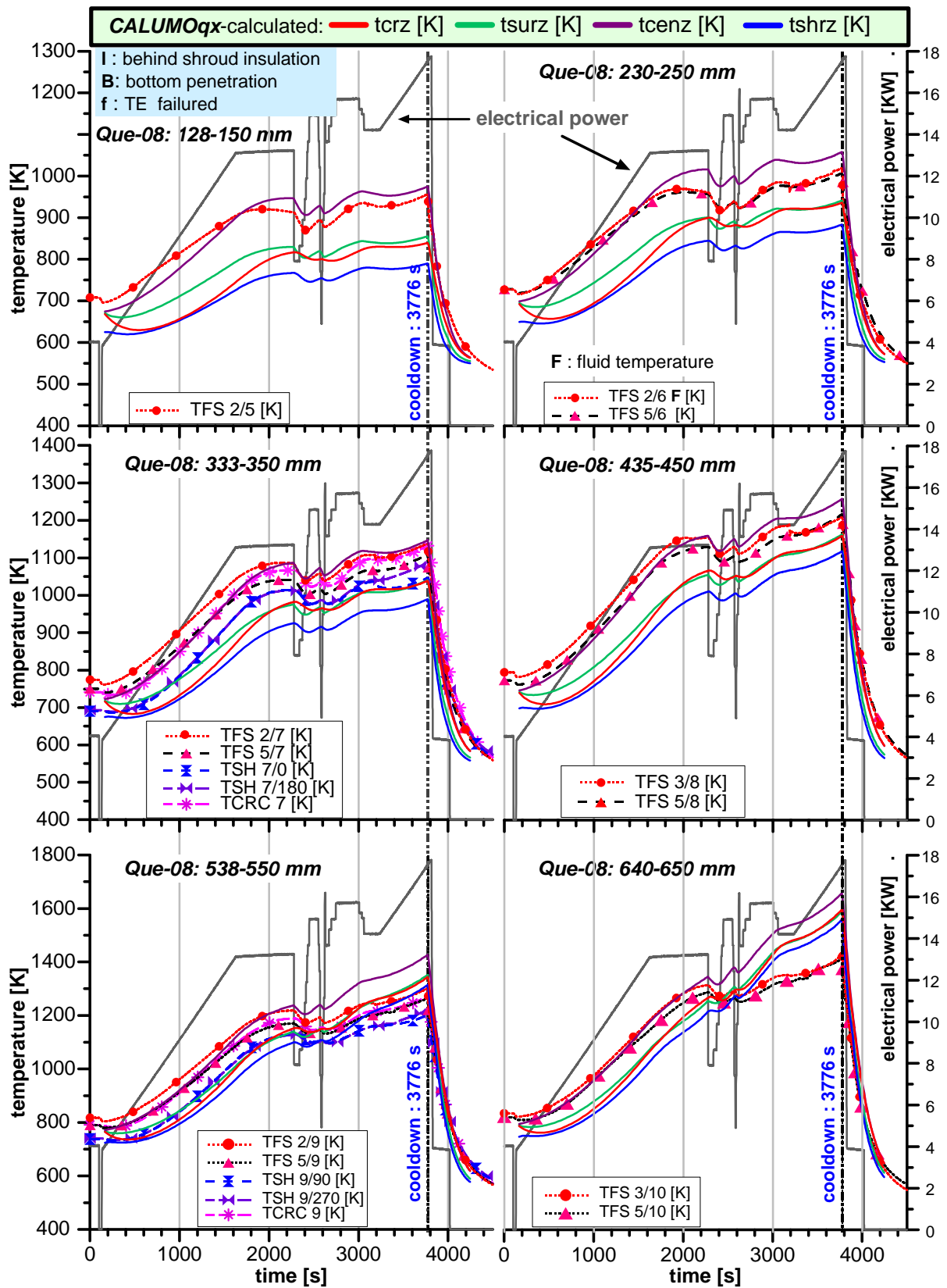


Fig 94-QU08 Steiner.doc
 21.04.05 - IMF

Fig. 94: Evolution of rod and shroud temperatures of QUENCH-08 at different axial locations, CALUMOqx-calculated data in comparison with experimental values.

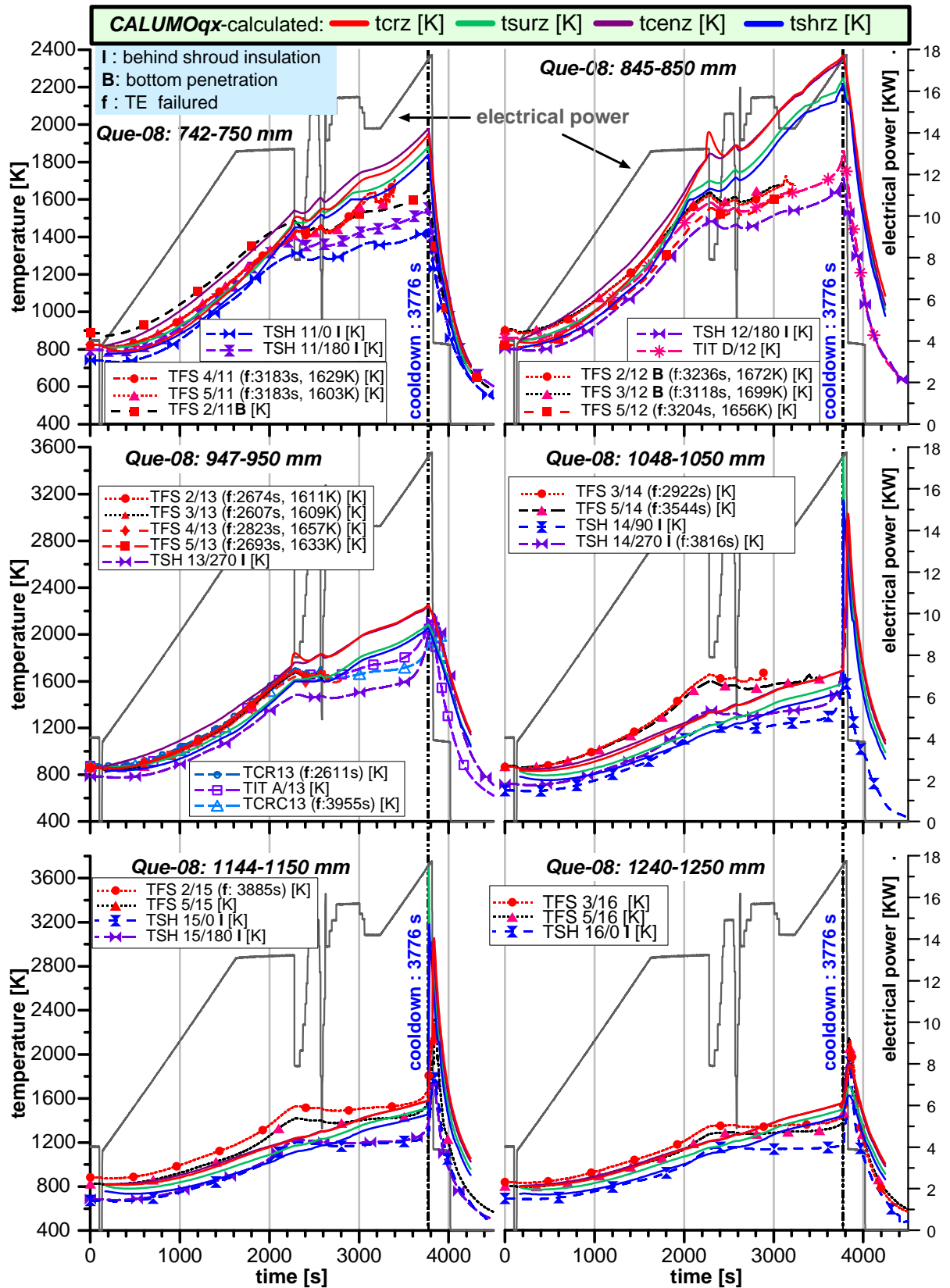


Fig 95-QU08 Steiner.doc
21.04.05 - IMF

Fig. 95: Evolution of rod and shroud temperatures of QUENCH-08 at different axial locations, CALUMOqX-calculated data in comparison with experimental values.

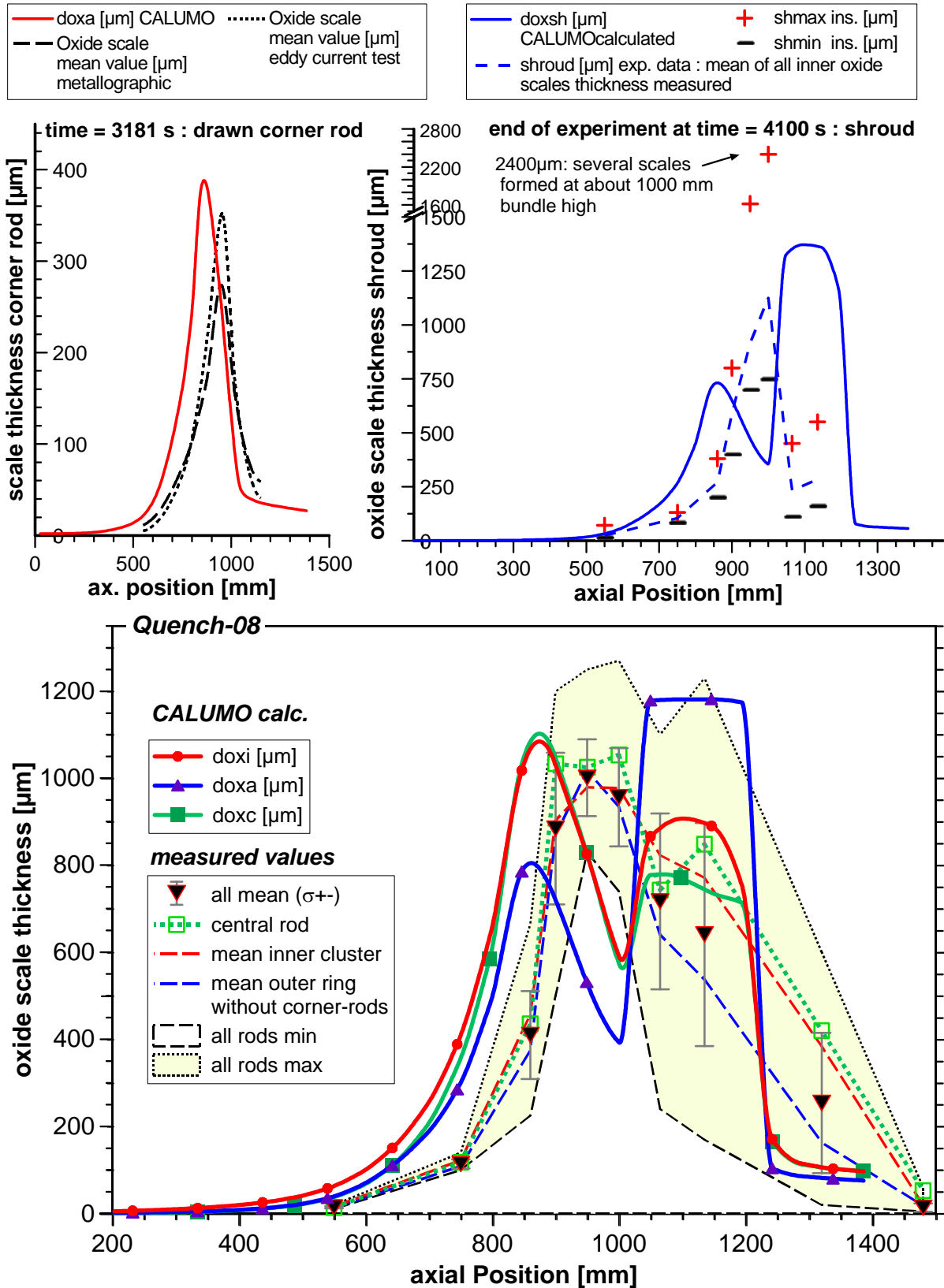


Fig 96-QU08 Steiner.doc
21.04.05 - IMF

Fig. 96: Axial distribution of the oxide scale thickness for the drawn corner rod (top, left), at the end of QUENCH-08 for the shroud (top, right) and all rods (bottom).

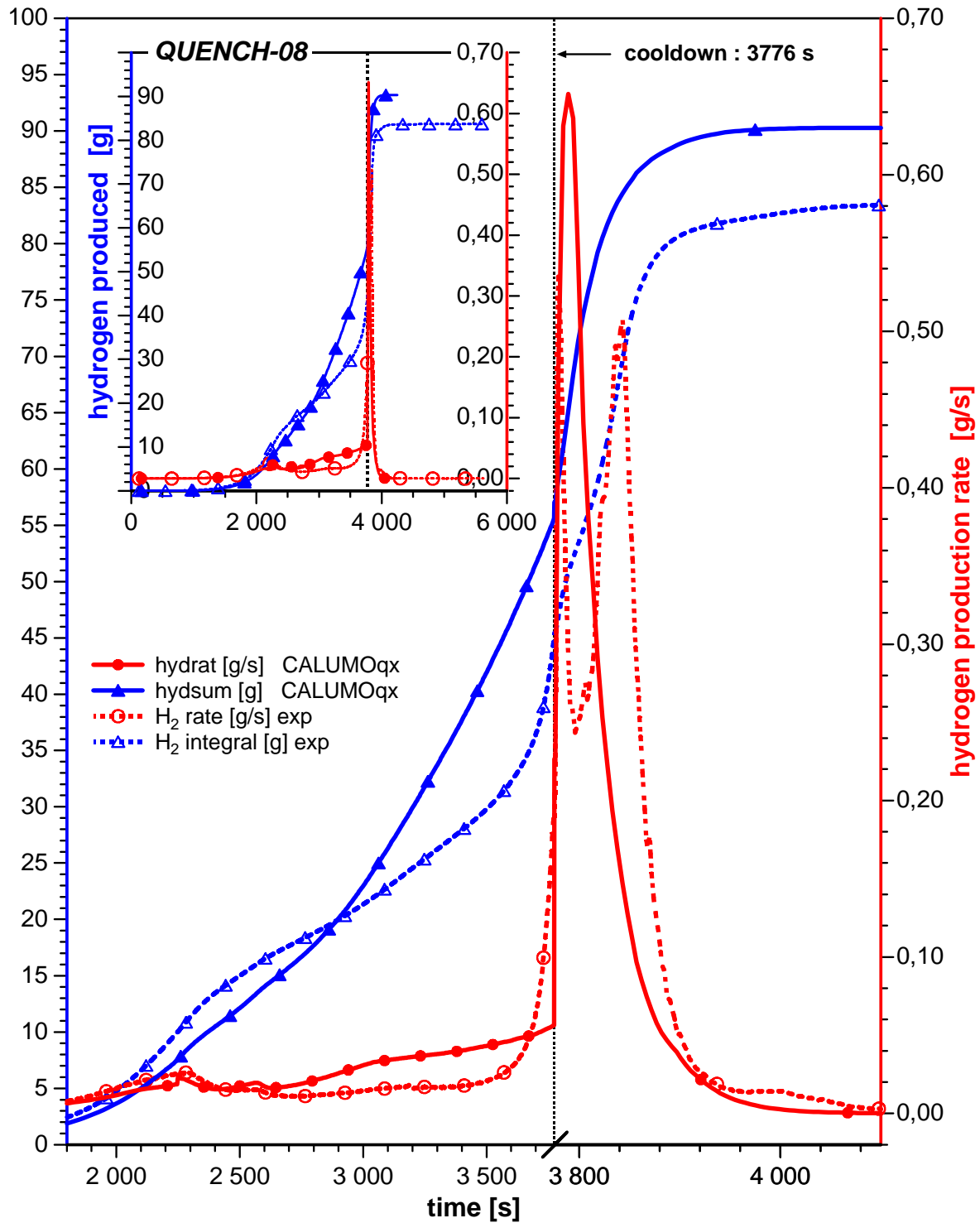


Fig 97-QU08 Steiner.doc
21.04.05 - IMF

Fig. 97: Evolution of the hydrogen production rate and the overall produced hydrogen for QUENCH-08 calculated with CALUMOqx.

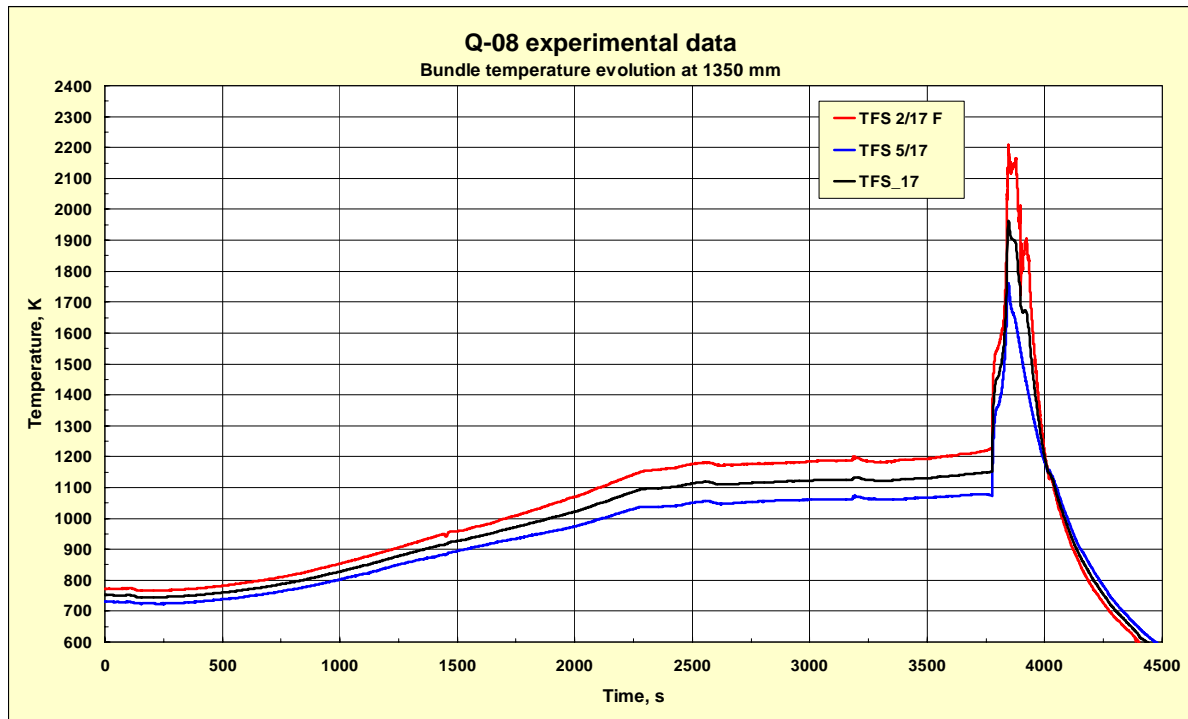


Fig. 98: QUENCH-08 bundle temperature evolution at the elevation 1350 mm measured by thermocouples TFS 2/17 (red), TFS 5/17 (blue) and averaged temperature used in the calculations (black).

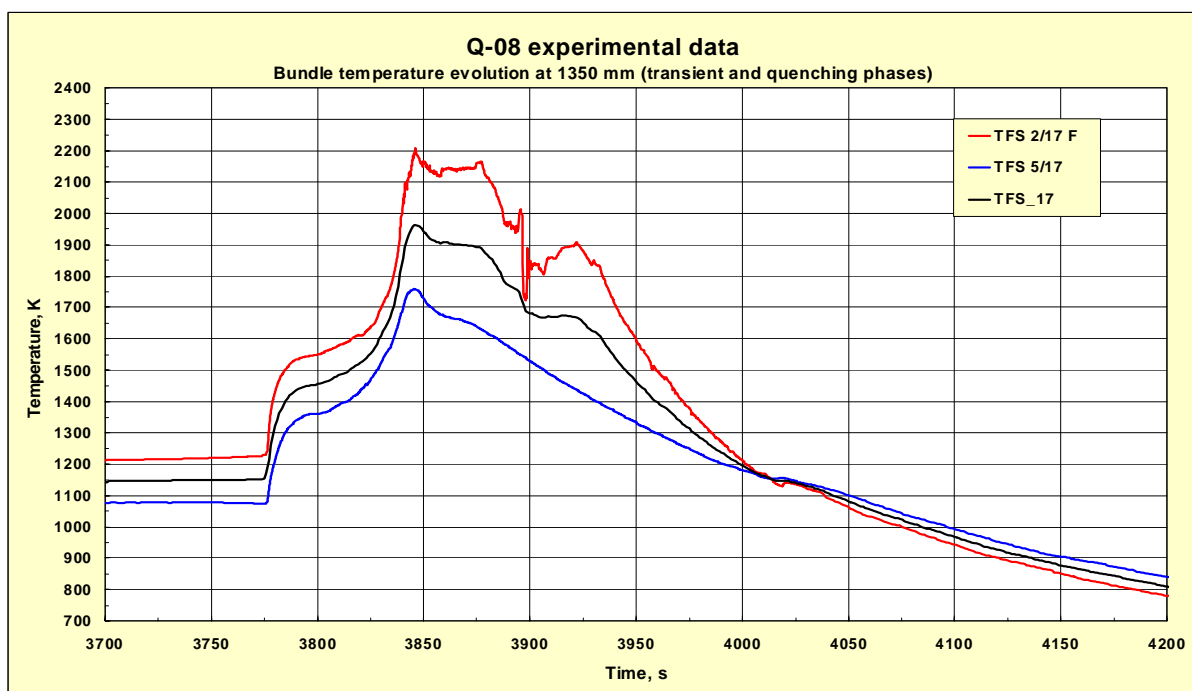


Fig. 99: QUENCH-08 bundle temperature evolution at the 1350 mm elevation during transient and cooling phases (3700-4200 s) measured by thermocouples TFS 2/17 (red), TFS 5/17 (blue) and averaged temperature used in the calculations (black).

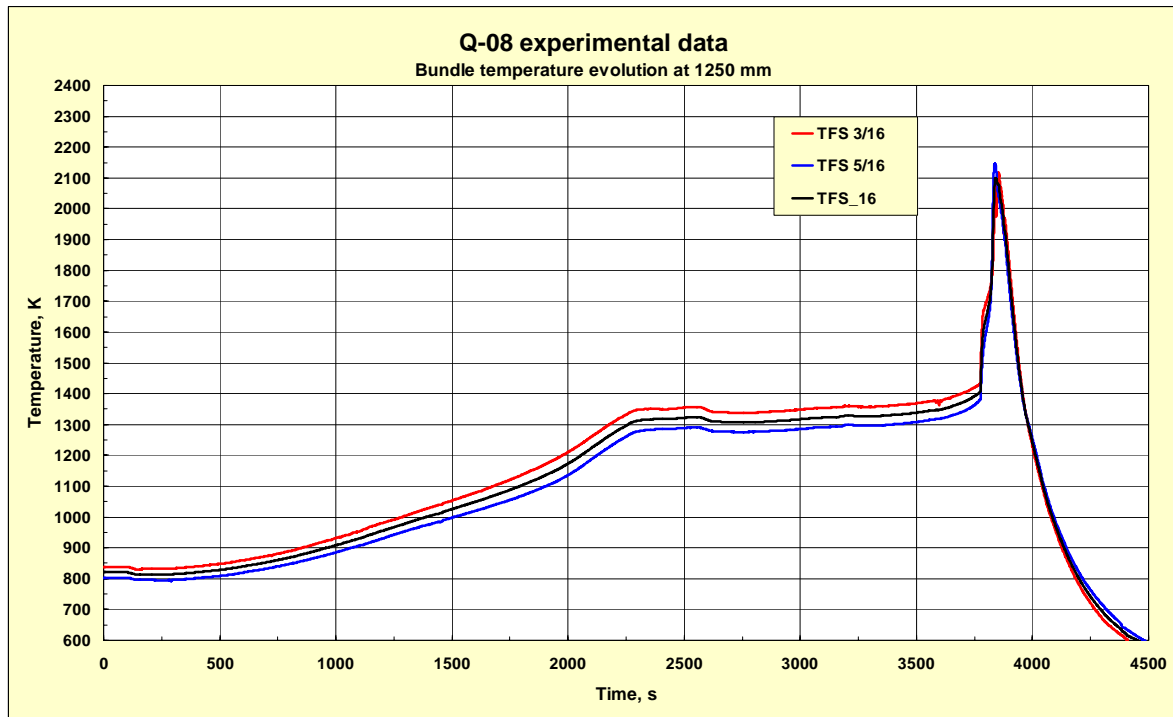


Fig. 100: QUENCH-08 bundle temperature evolution at the elevation 1250 mm measured by thermocouples TFS 3/16 (red), TFS 5/16 (blue) and averaged temperature used in the calculations (black).

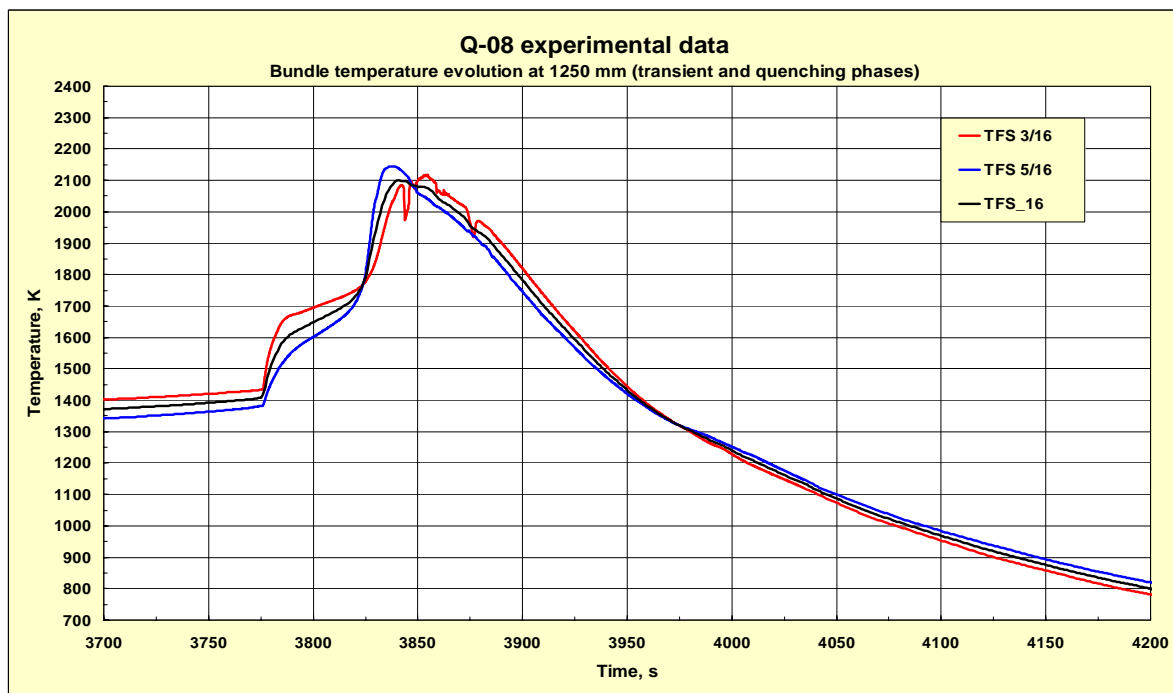


Fig. 101: QUENCH-08 bundle temperature evolution at the elevation 1250 mm during transient and cooling phases (3700-4200 s) measured by thermocouples TFS 3/16 (red), TFS 5/16 (blue) and averaged temperature used in the calculations (black).

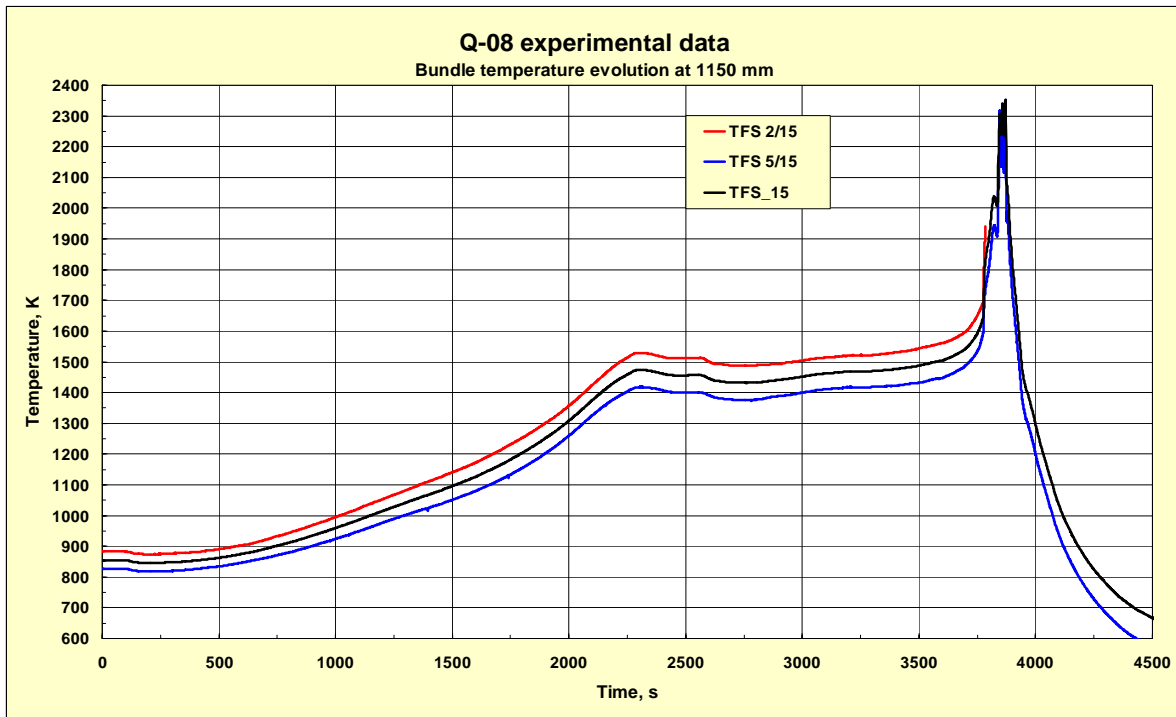


Fig. 102: QUENCH-08 bundle temperature evolution at the elevation 1150 mm measured by thermocouples TFS 2/15 (red), TFS 5/15 (blue) and averaged temperature used in the calculations (black).

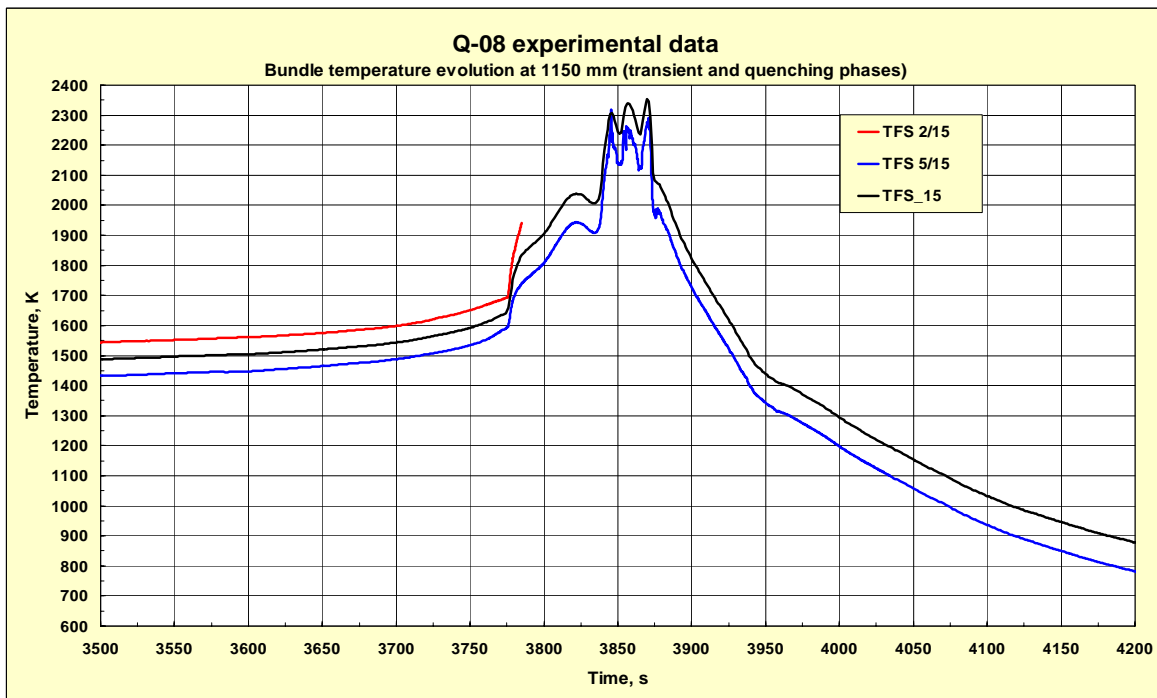


Fig. 103: QUENCH-08 bundle temperature evolution at the elevation 1150 mm during transient and cooling phases (3500-4200 s) measured by thermocouples TFS 2/15 (red), TFS 5/15 (blue) shroud and averaged temperature used in the calculations (black).

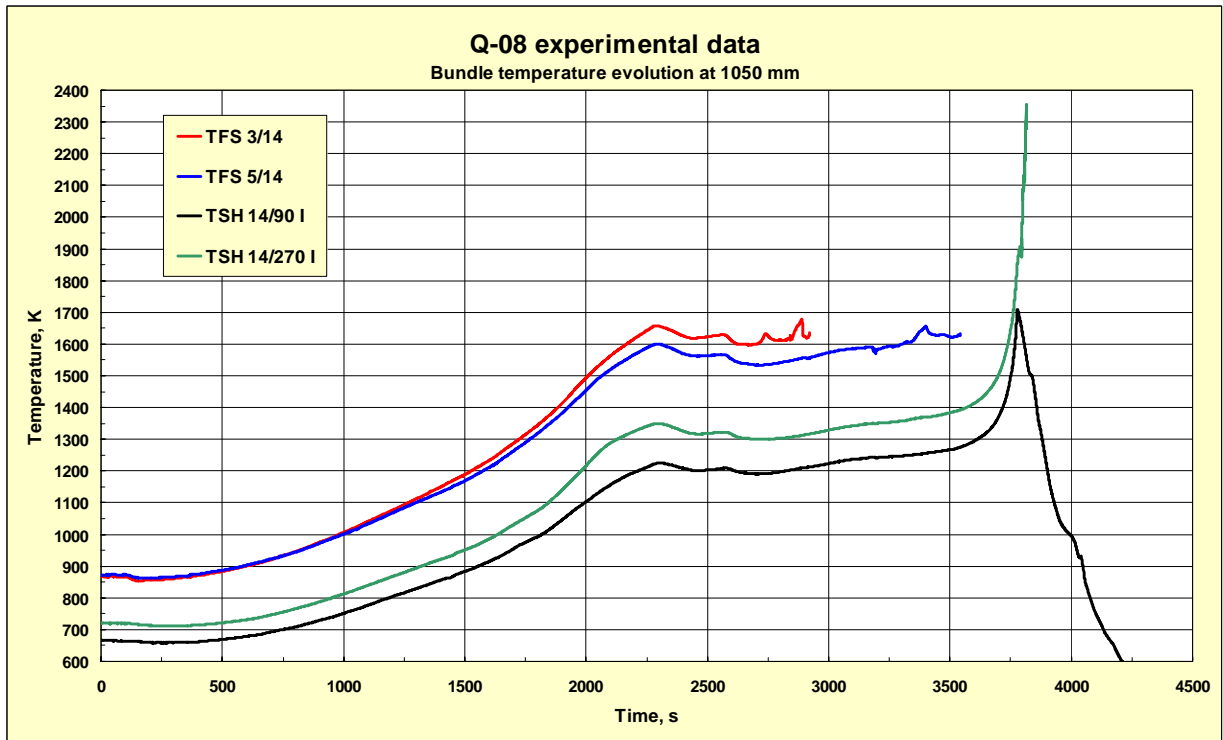


Fig. 104: QUENCH-08 bundle temperature evolution at the elevation 1050 mm measured by thermocouples TFS 3/14 (red), TFS 5/14 (blue), shroud thermocouples TSH 14/90 I (black), TSH 14/270 I (green).

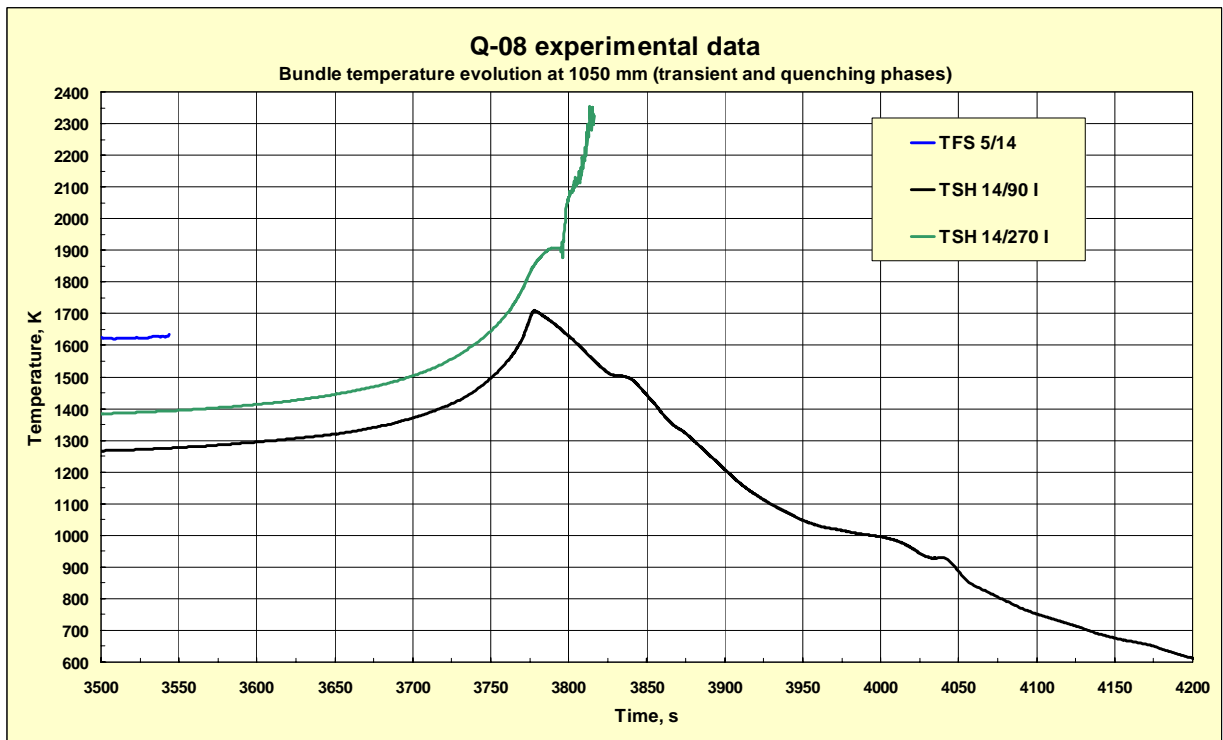


Fig. 105: QUENCH-08 bundle temperature evolution at the elevation 1050 mm during transient and cooling phases (3500-4200 s) measured by thermocouples TFS 5/14 (blue), shroud thermocouples TSH 14/90 I (black), TSH 14/270 I (green).

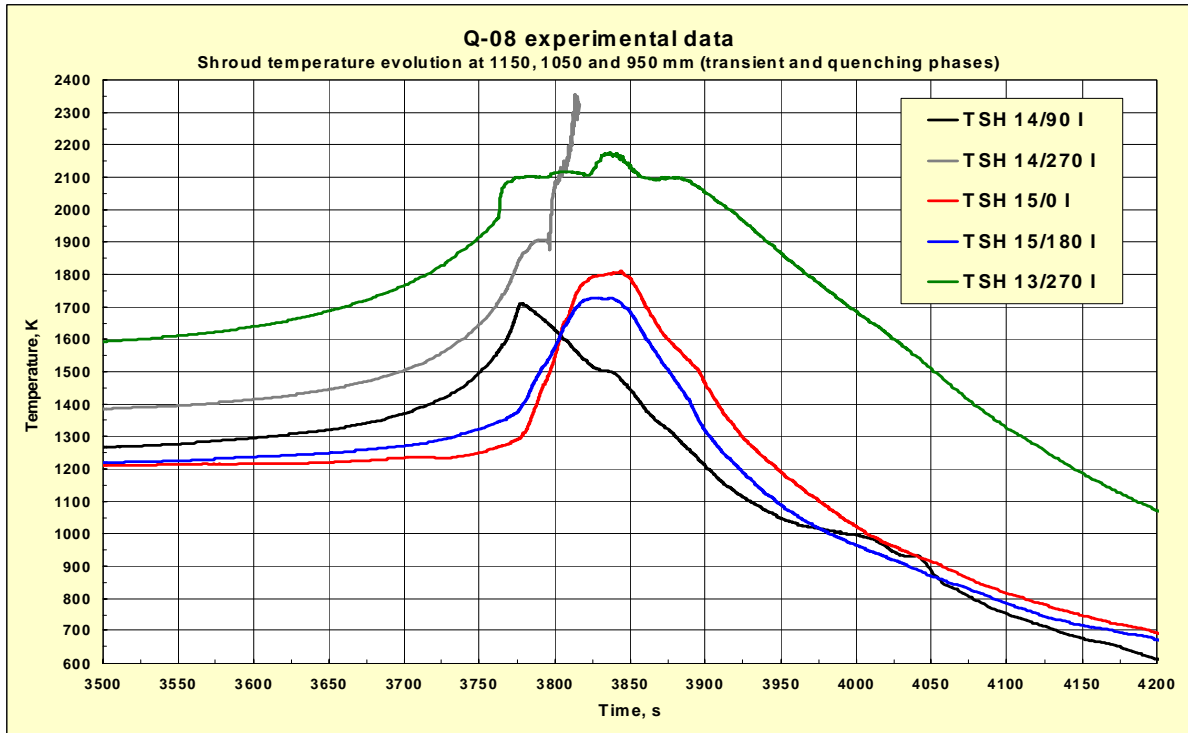


Fig. 106: Shroud temperature evolution at the elevations 950, 1050 and 1150 mm measured by thermocouples TSH14/90 I (black), TSH14/270 I (grey), TSH15/0 I (red), TSH15/180 I (blue) and TSH13/270 I (green) for the time period 3500-4200 s of QUENCH-08.

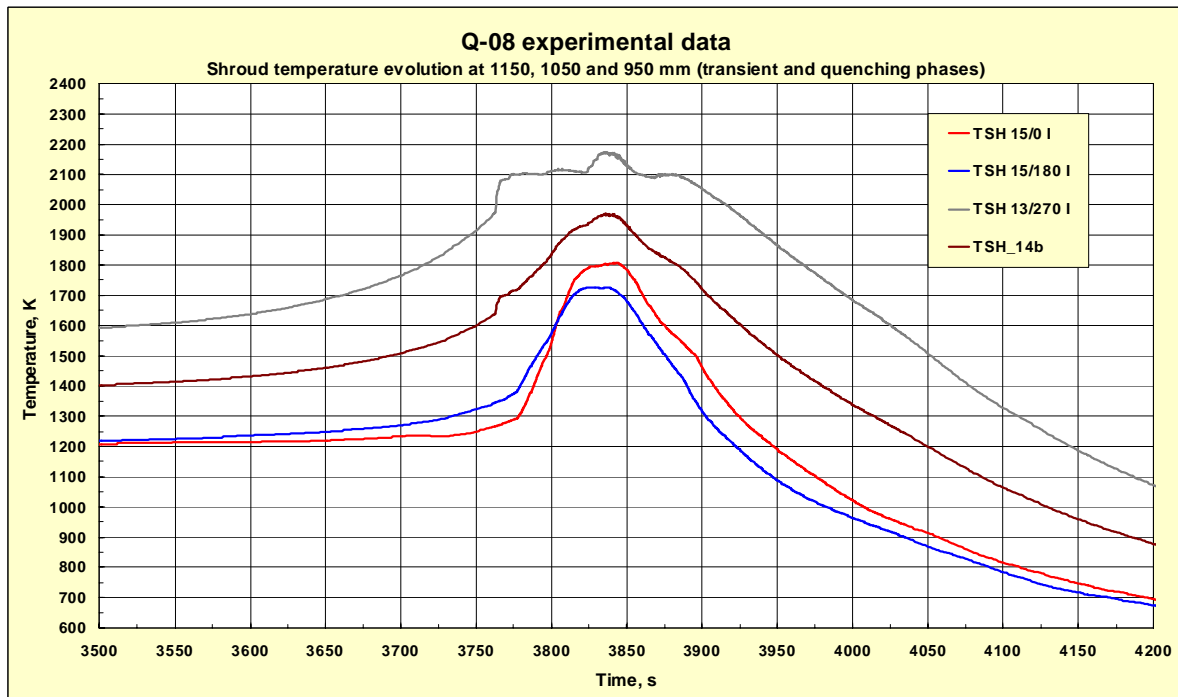


Fig. 107: Shroud temperature evolution at the elevations 950 and 1150 mm during pre-oxidation, transient, and cooling phases of QUENCH-08 (3500-4200 s) measured by thermocouples TSH13/270 I (grey), TSH15/0 I (red) and TSH15/180 I (blue) and the estimated basis for the shroud temperature at 1050 mm TSH 14b.

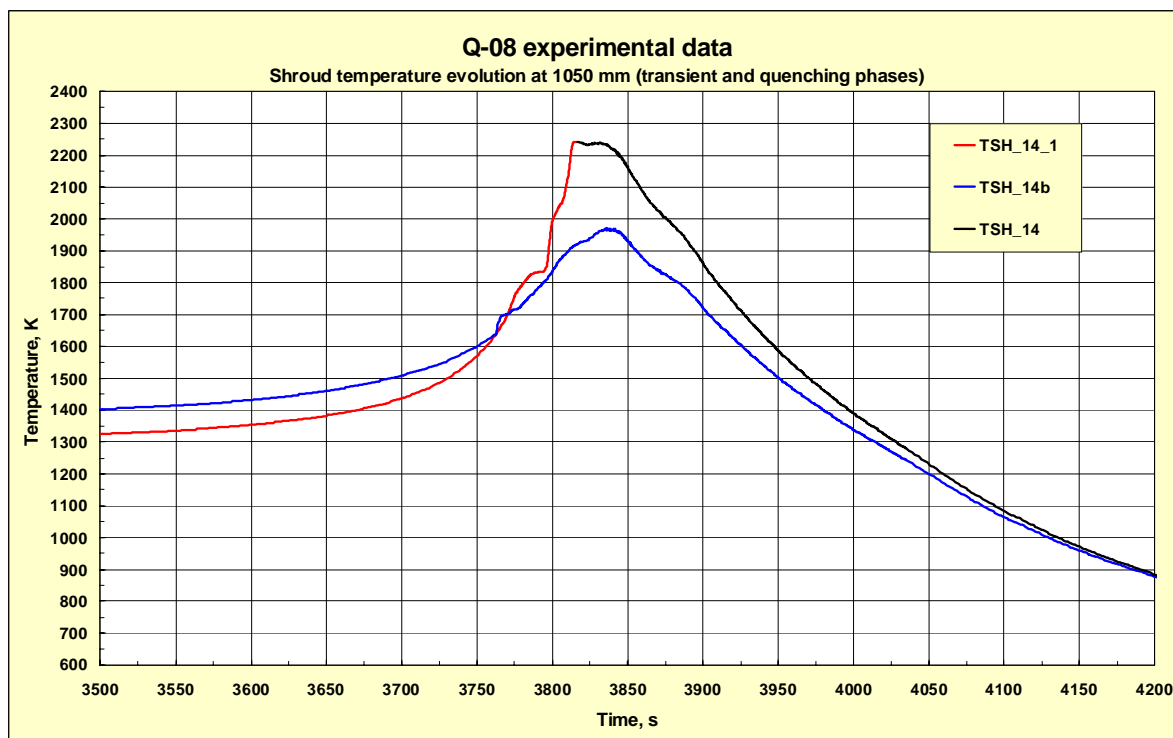


Fig. 108: Estimated basis for the shroud temperature evolution at the elevation 1050 mm during QUENCH-08 with TSH_14b (blue), TSH 14_1 (red) plotted up to 3816.4 s, and TSH_14 (black) reconstructed after 3816 s.

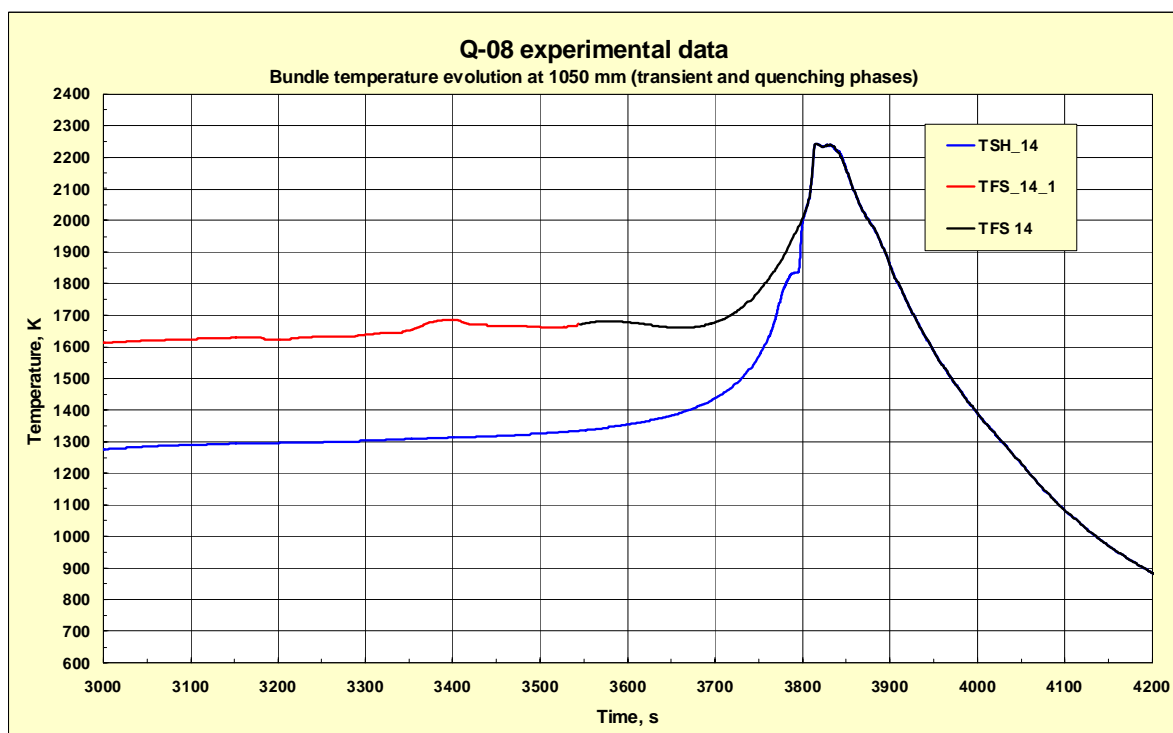


Fig. 109: Averaged QUENCH-08 bundle temperature evolution at the elevation 1050 mm during pre-oxidation, transient and cooling phases (3000-4200 s): TFS_14_1 measured up to 3544 s (red), TSH_14 reconstructed (blue), and TFS 14 averaged temperature used in the calculations (black).

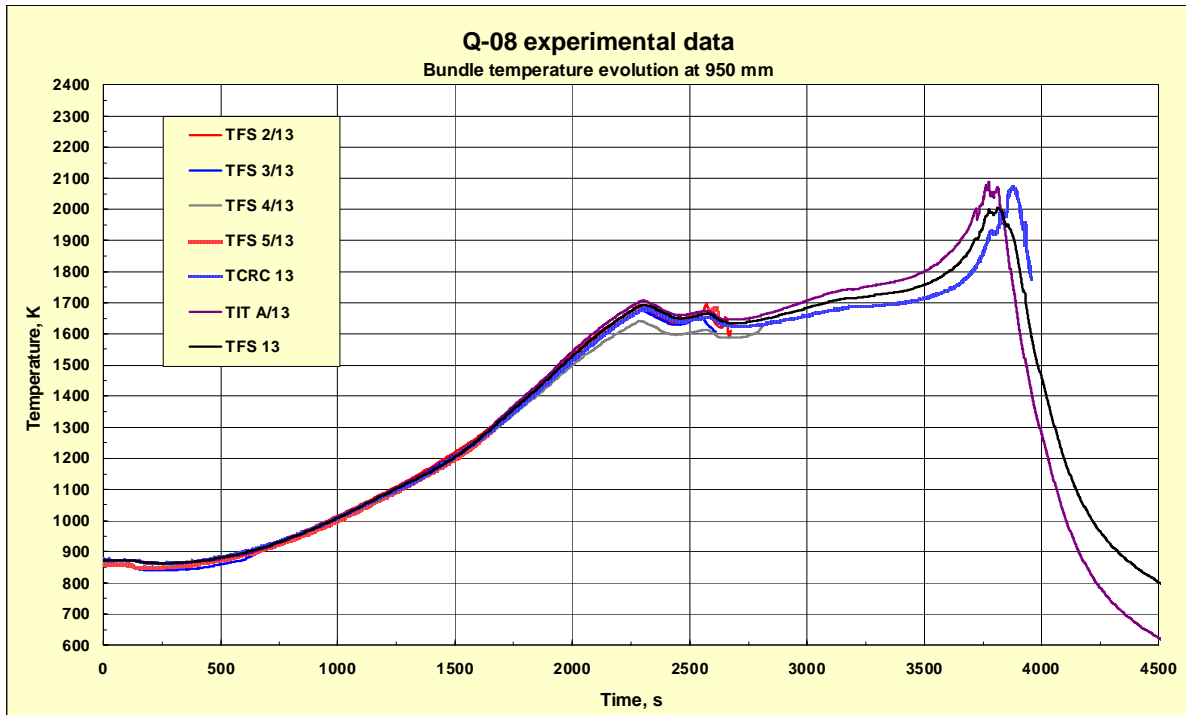


Fig. 110: QUENCH-08 bundle temperature evolution at the elevation 950 mm measured by thermocouples TFS 2/13 (red), TFS 3/13 (blue), TFS 4/13 (grey), TFS 5/13 (light red), central rod thermocouple TCRC 13 (light blue), corner rod thermocouple TIT A/13 (violet) and averaged temperature used in the calculations (black).

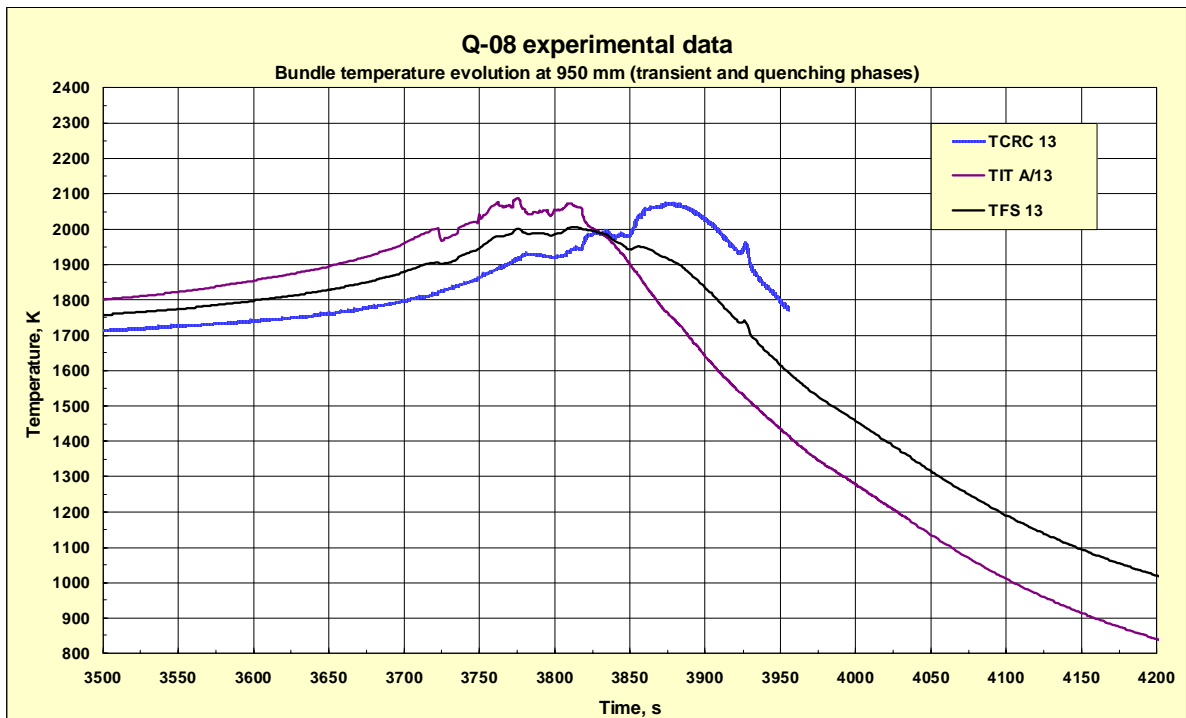


Fig. 111: QUENCH-08 bundle temperature evolution at the elevation 950 mm during pre-oxidation, transient, and cooling phases (3500-4200 s) measured by central rod thermocouple TCRC 13 (blue), corner rod thermocouple TIT A/13 (violet) and averaged temperature used in the calculations (black).

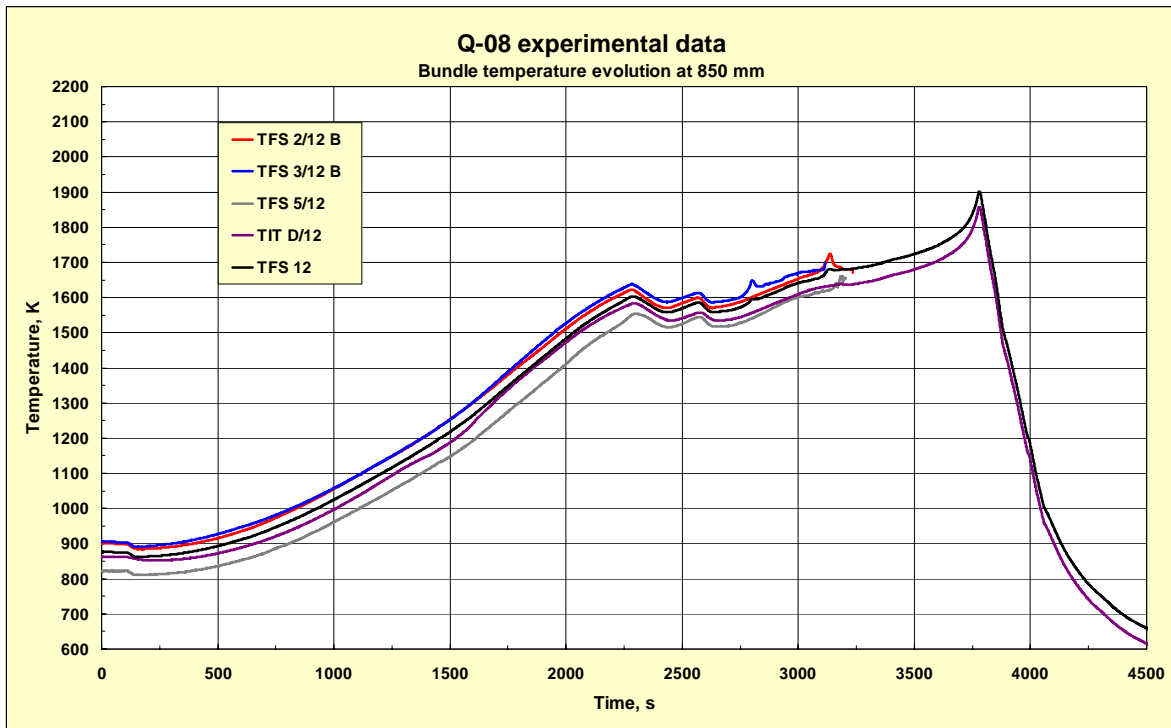


Fig. 112: QUENCH-08 bundle temperature evolution at the elevation 850 mm measured by thermocouples TFS 2/12B (red), TFS 3/13B (blue), TFS 5/12 (grey), TIT D/12 (violet) and averaged temperature used in the calculations (black).

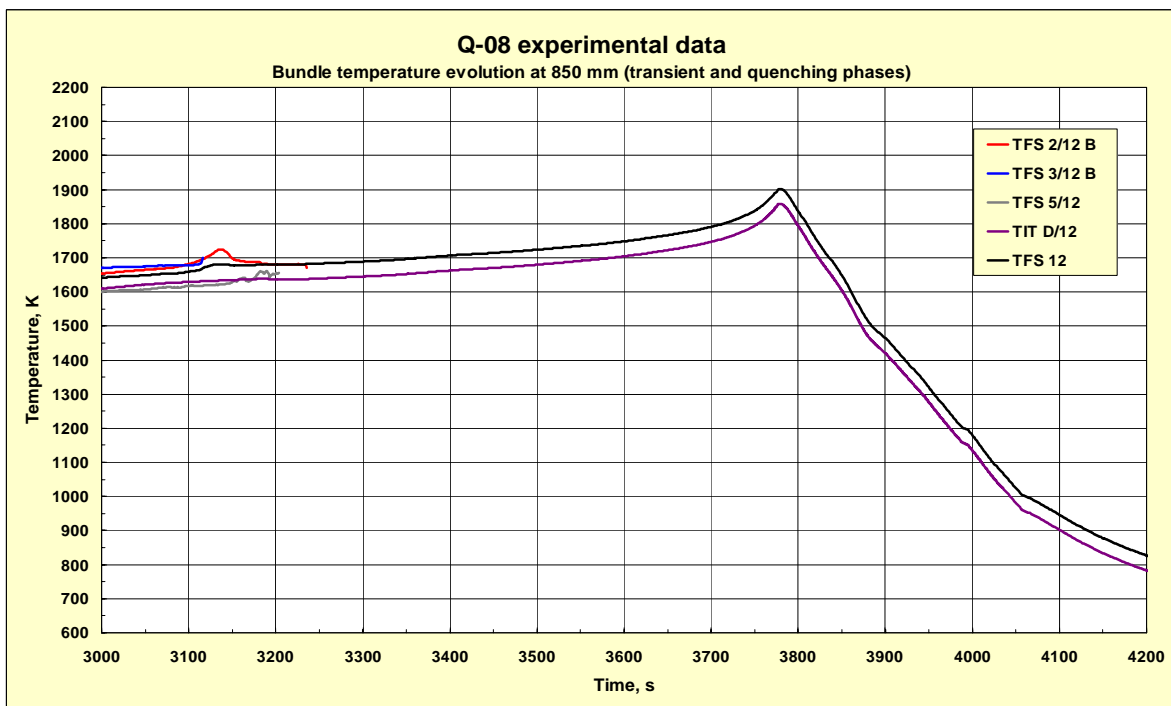


Fig. 113: QUENCH-08 bundle temperature evolution at the elevation 850 mm during pre-oxidation, transient and cooling phases (3000-4200 s) measured by thermocouples TFS 2/12B (red), TFS 3/13B (blue), TFS 5/12 (grey), TIT D/12 (violet) and averaged temperature used in the calculations (black).

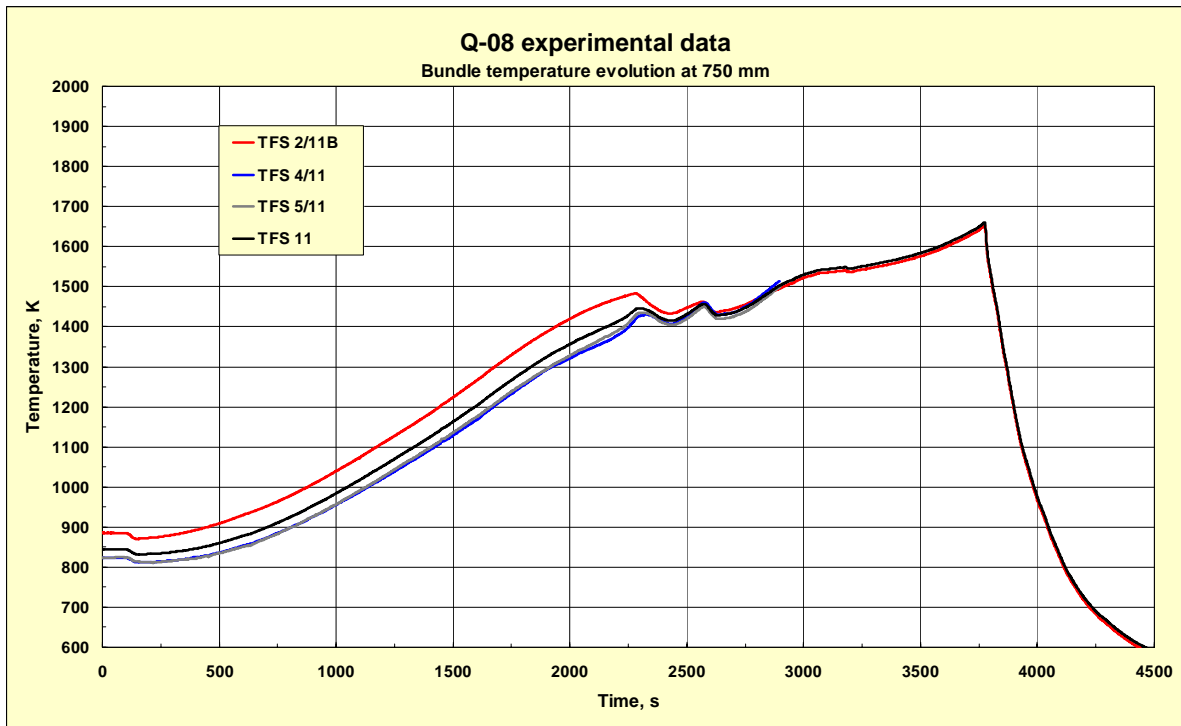


Fig. 114: QUENCH-08 bundle temperature evolution at the elevation 750 mm measured by thermocouples TFS 2/11B (red), TFS 4/11 (blue), TFS 5/11 (grey) and averaged temperature used in the calculations (black).

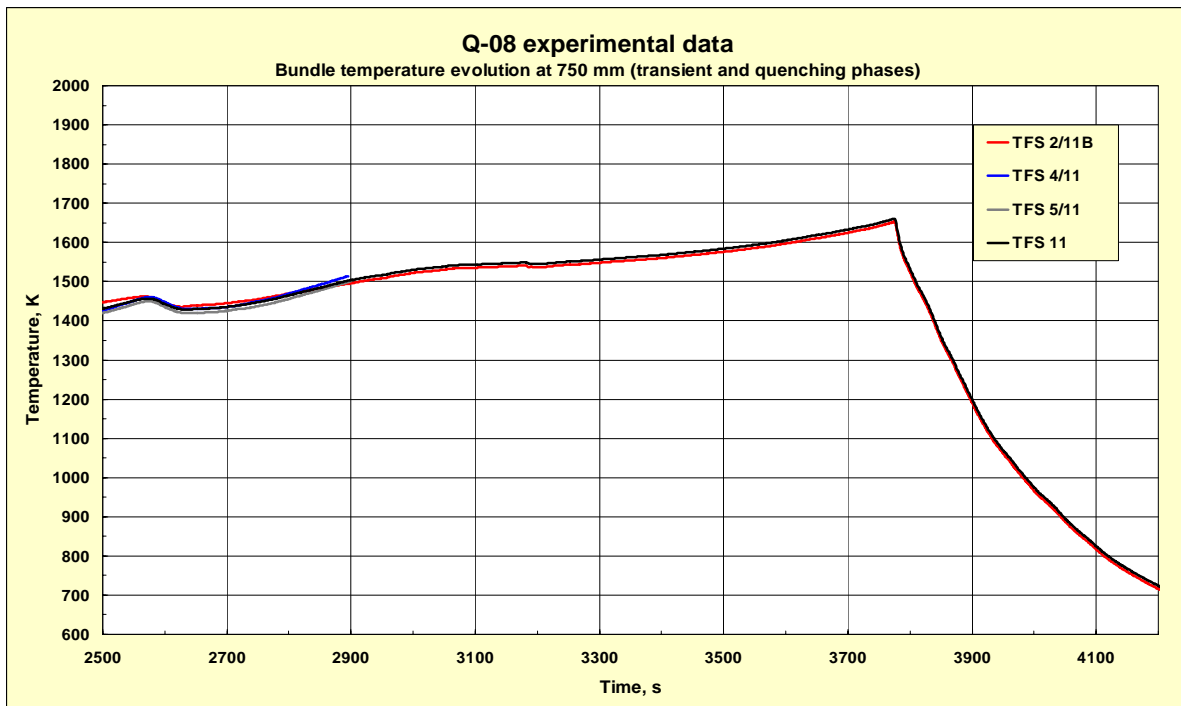


Fig. 115: QUENCH-08 bundle temperature evolution at the elevation 750 mm during pre-oxidation, transient and cooling phases (2500-4200 s) measured by thermocouples TFS 2/11B (red), TFS 4/11 (blue), TFS 5/11 (grey) and averaged temperature used in the calculations (black).

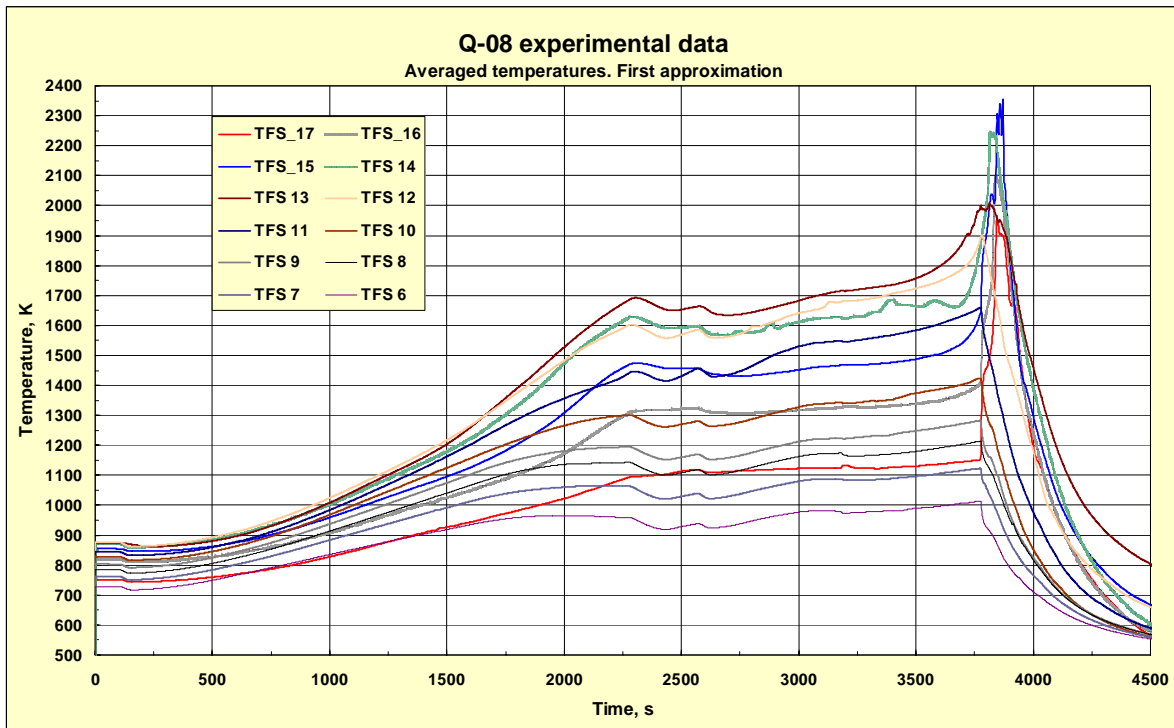


Fig. 116: Averaged and smoothed curves representing the temperature evolution of the QUENCH-08 bundle at the elevations from -250 to 1350 mm.

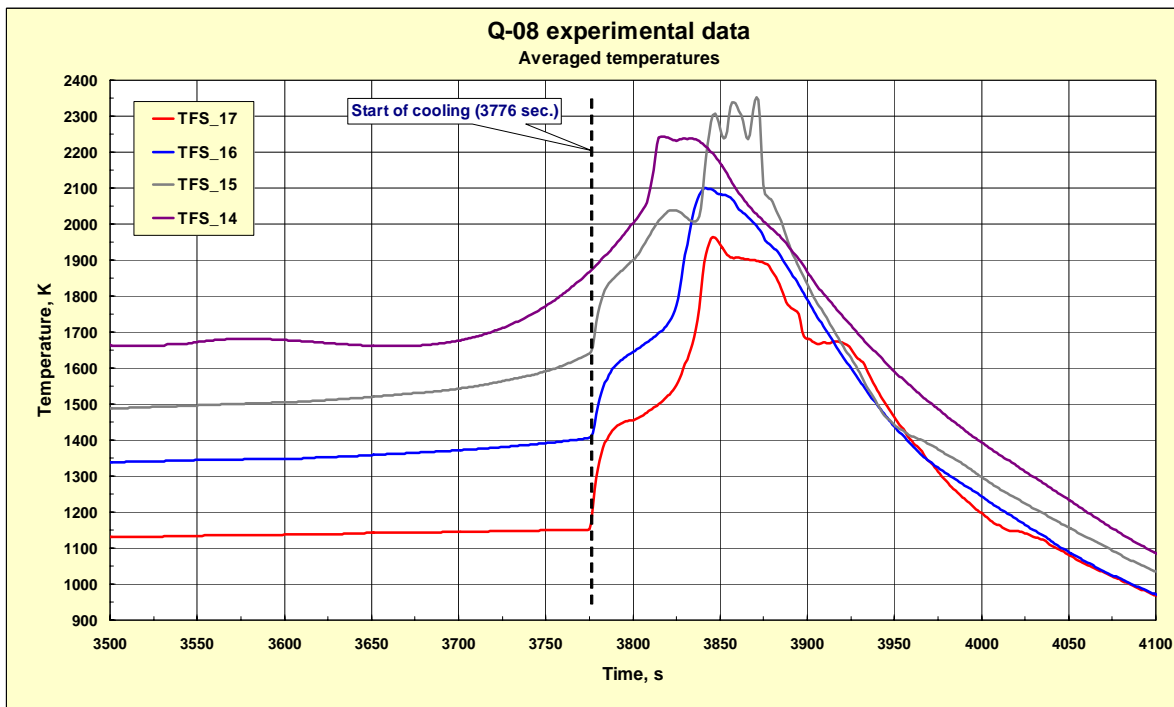


Fig. 117: Averaged and smoothed curves representing temperature evolution during pre-oxidation, transient, and cooling phases (3500-4100 s) of the QUENCH-08 bundle at the elevations from 1050 to 1350 mm.

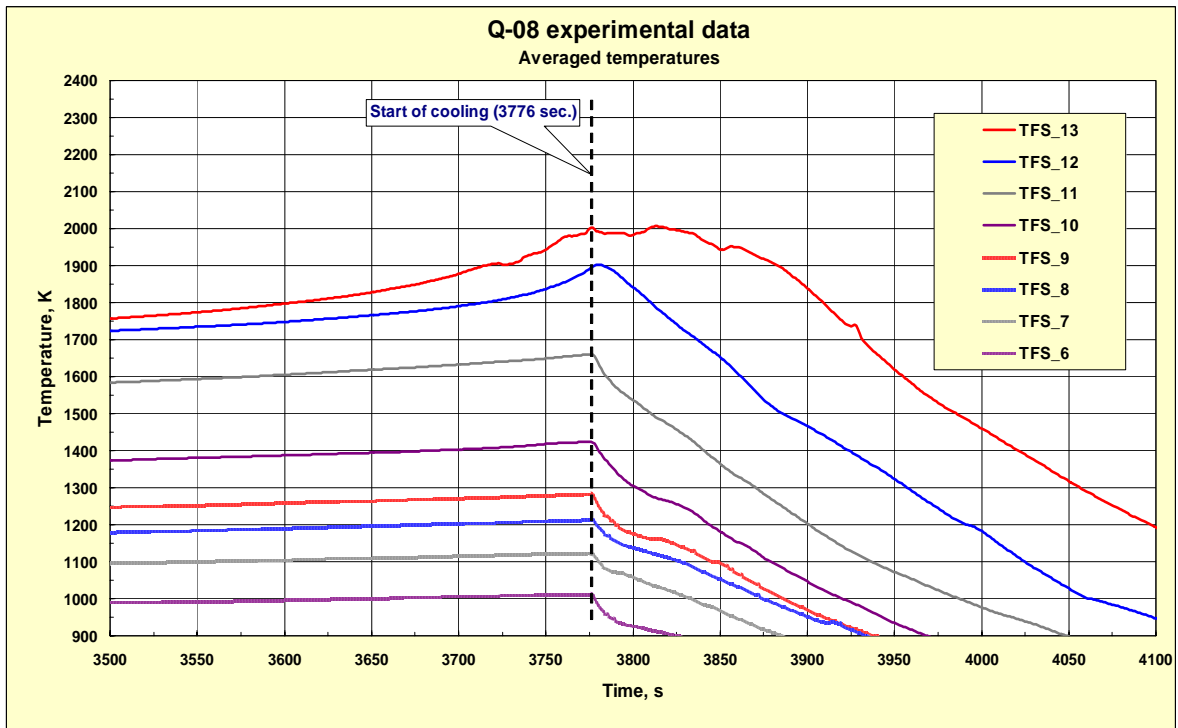


Fig. 118: Averaged and smoothed curves representing temperature evolution of the QUENCH-08 bundle during pre-oxidation, transient, and cooling phases (3500-4100 s) at the elevations from 250 to 950 mm.

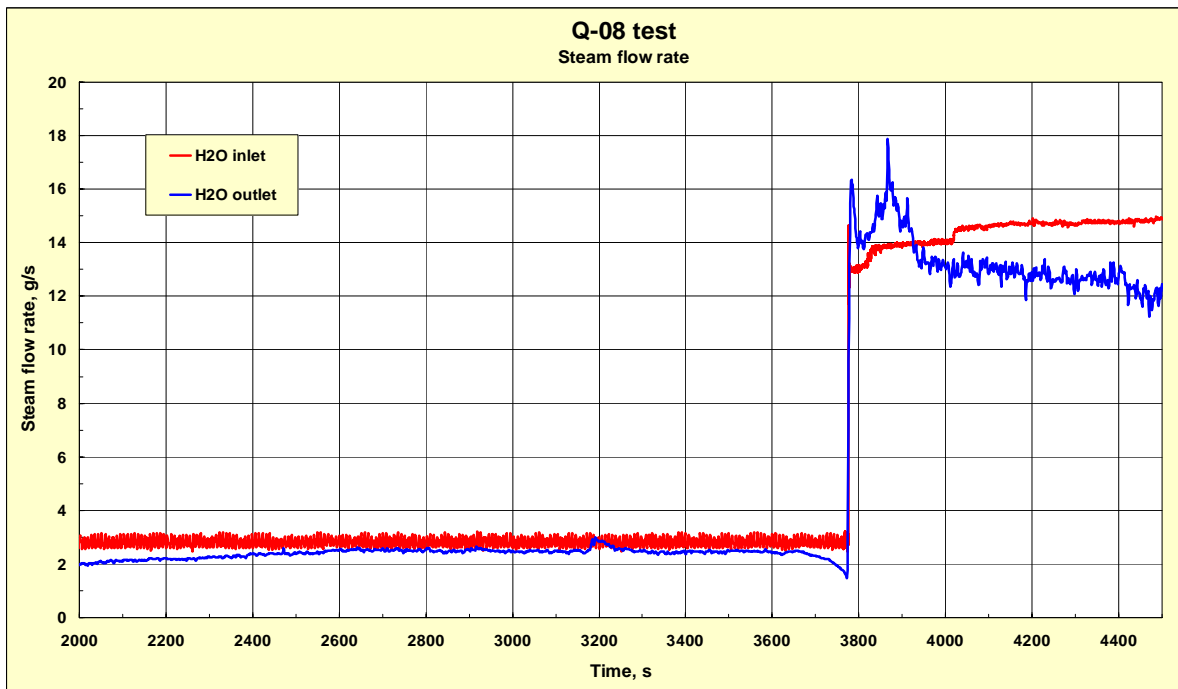


Fig. 119: QUENCH-08 steam flow rate at the bundle inlet measured by F 204/F 205 flow meters (red) and at the bundle outlet (MS GAM300 data; blue).

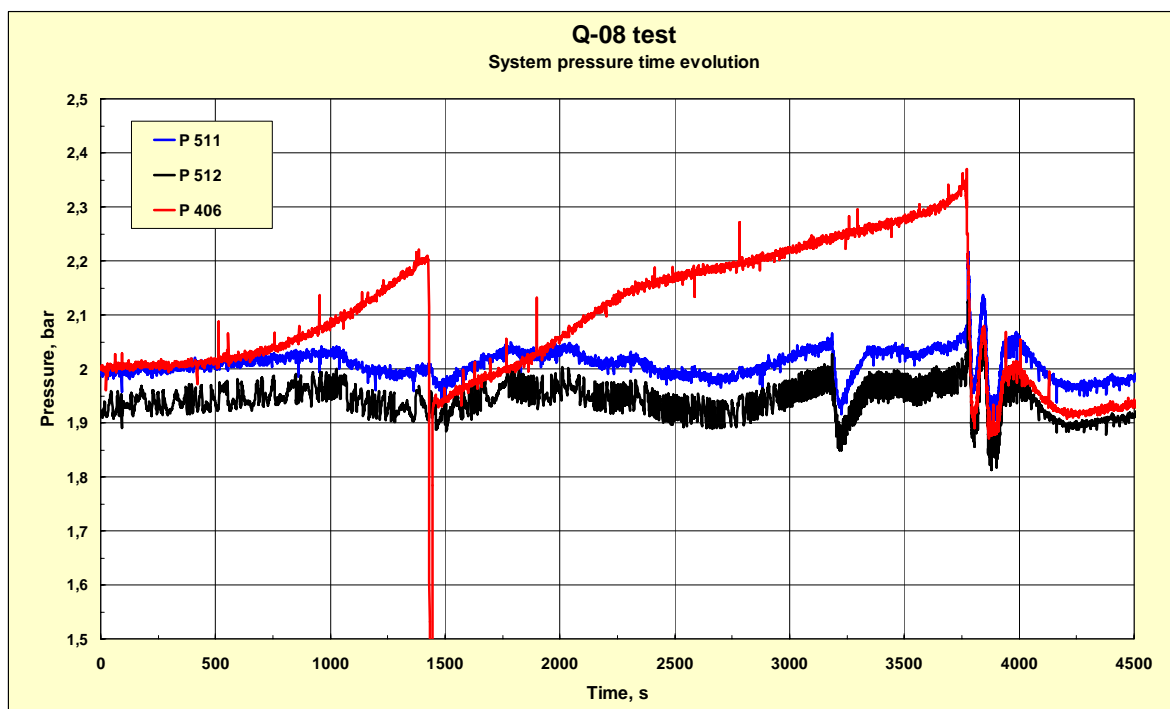


Fig. 120: QUENCH-08 system pressure evolution at bundle inlet measured by P 511 (blue), at bundle outlet measured by P 512 (black), and at the annulus shroud/cooling jacket measured by P 406 (red).

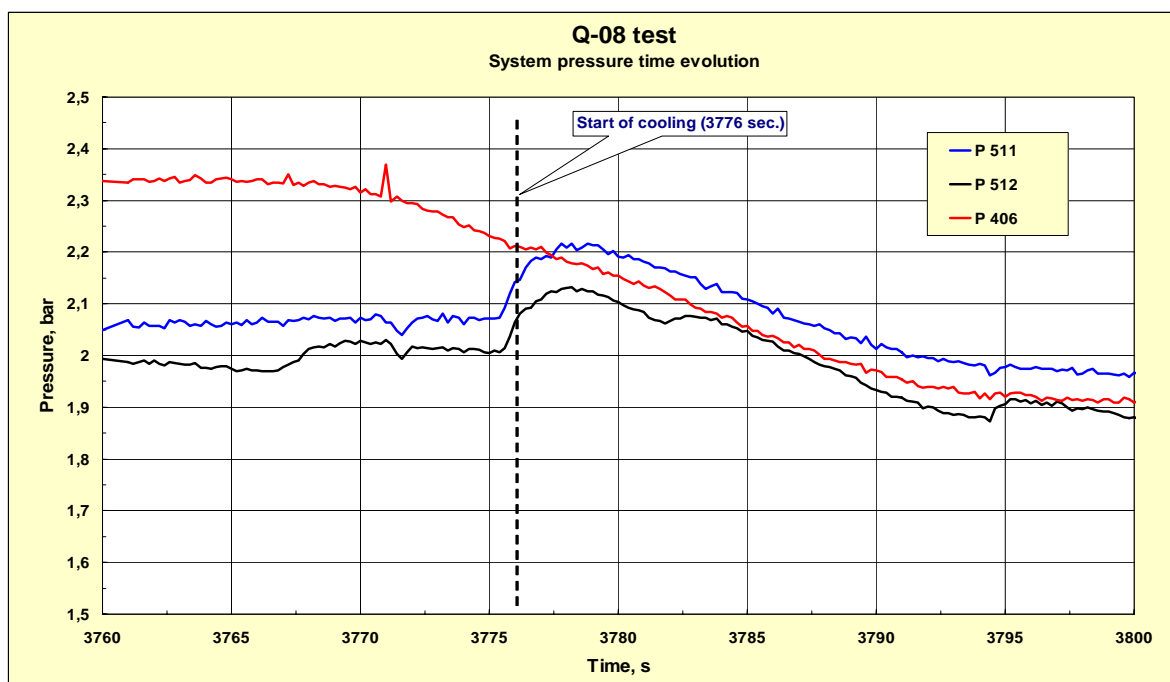


Fig. 121: QUENCH-08 system pressure evolution during the time period 3760-3800 s at bundle inlet measured by P 511 (blue), at bundle outlet measured by P 512 (black), and at annulus shroud/cooling jacket P 406 (red).

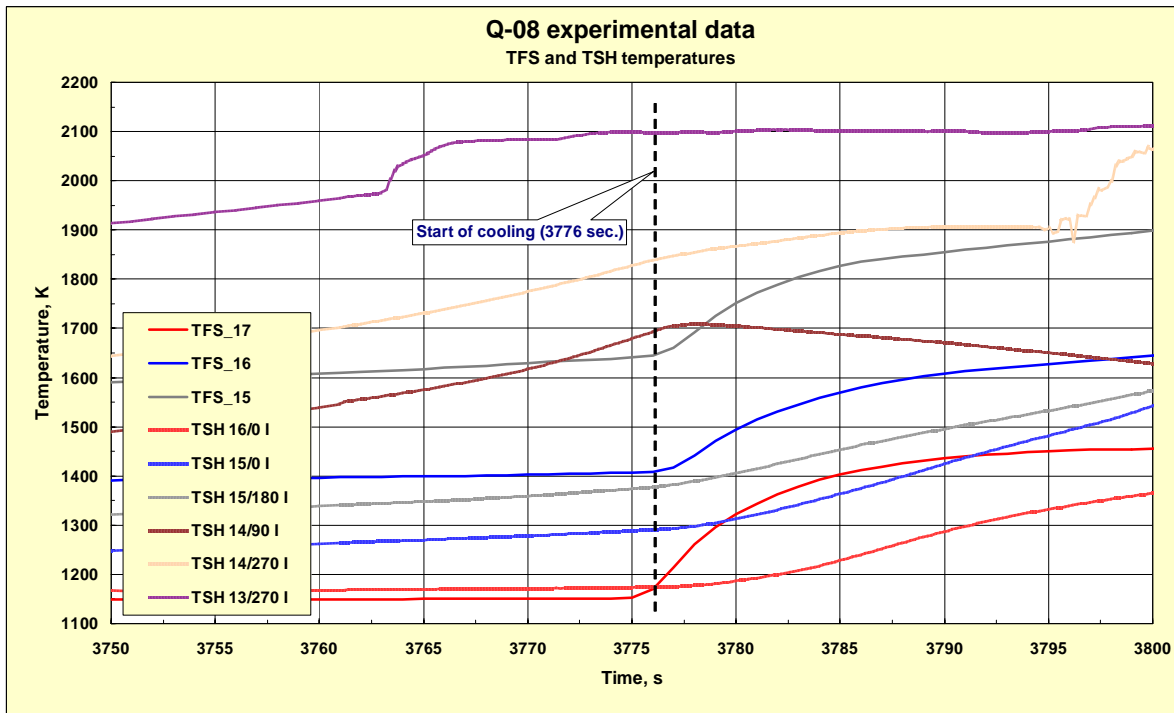


Fig. 122: The averaged TFS curves of QUENCH-08 at the elevations 1350, 1250, and 1150 mm together with TSH thermocouple curves at 1250, 1150, 1050 and 950 mm.

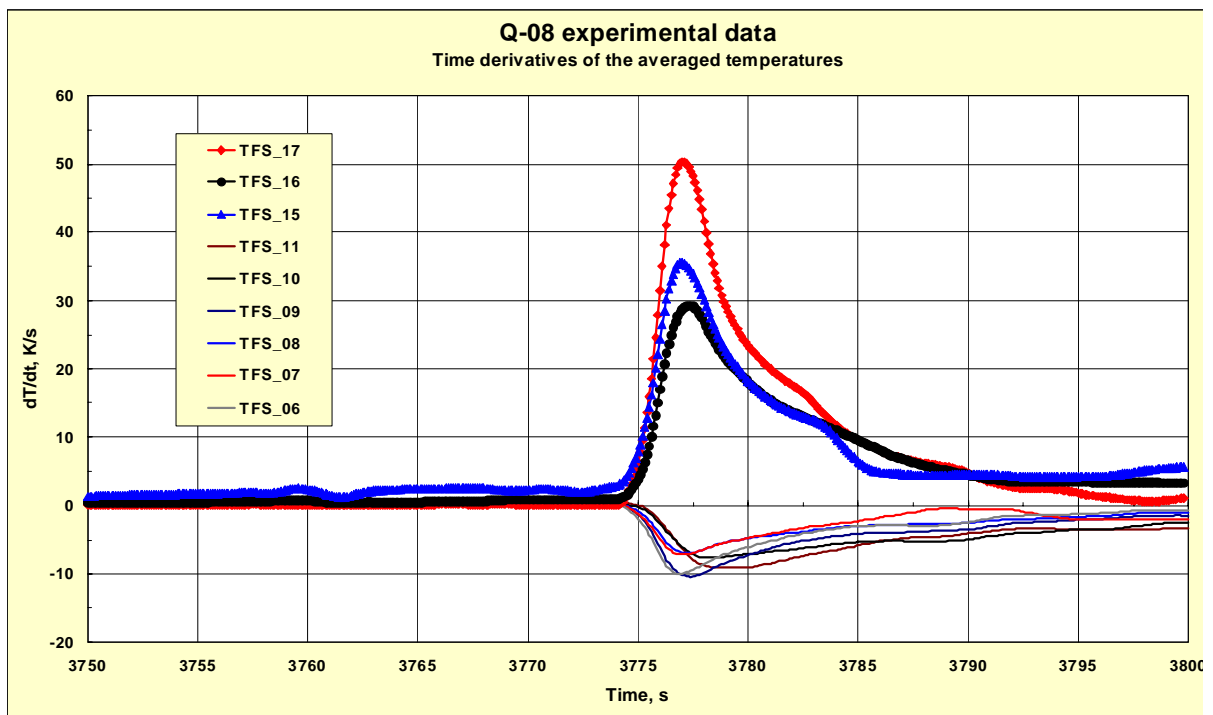


Fig. 123: Derivatives dT/dt of the averaged temperatures of QUENCH-08 at different elevations, K/s (upper elevations: lines with symbols, lower elevations: thin lines).

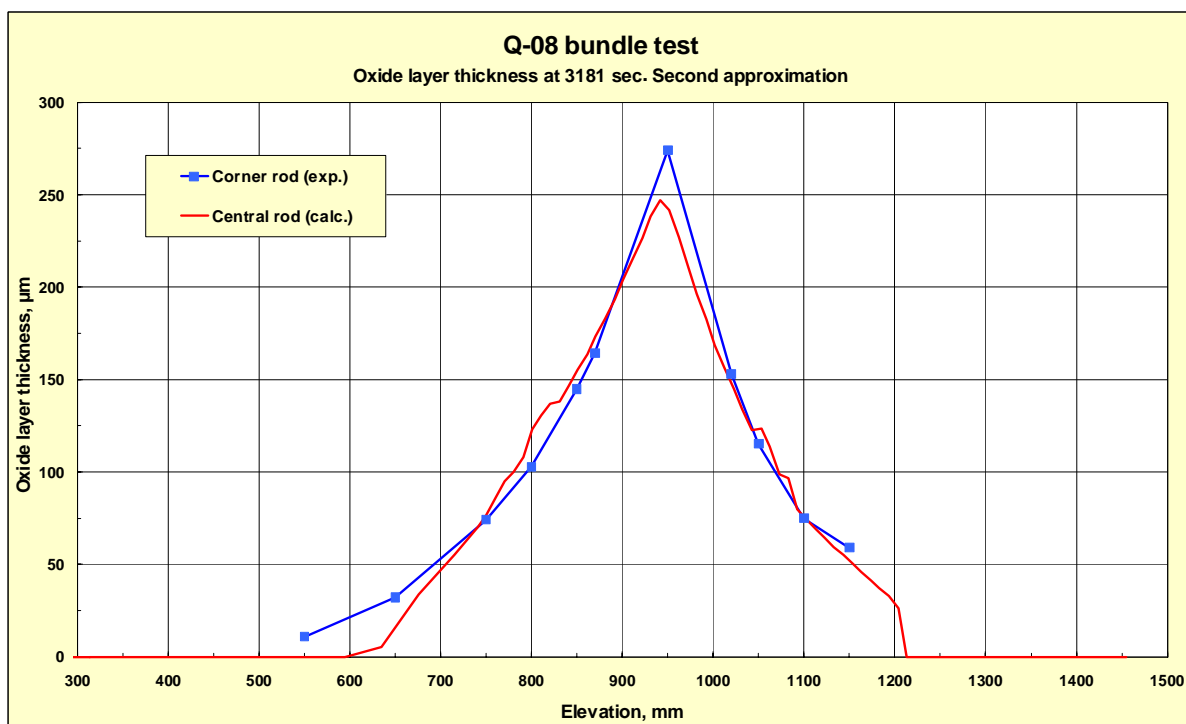


Fig. 124: Oxide layer thickness axial profile of corner rod B (withdrawn from the QUENCH-08 bundle at 3181 s) compared to the calculated one of the central rod for the same time.

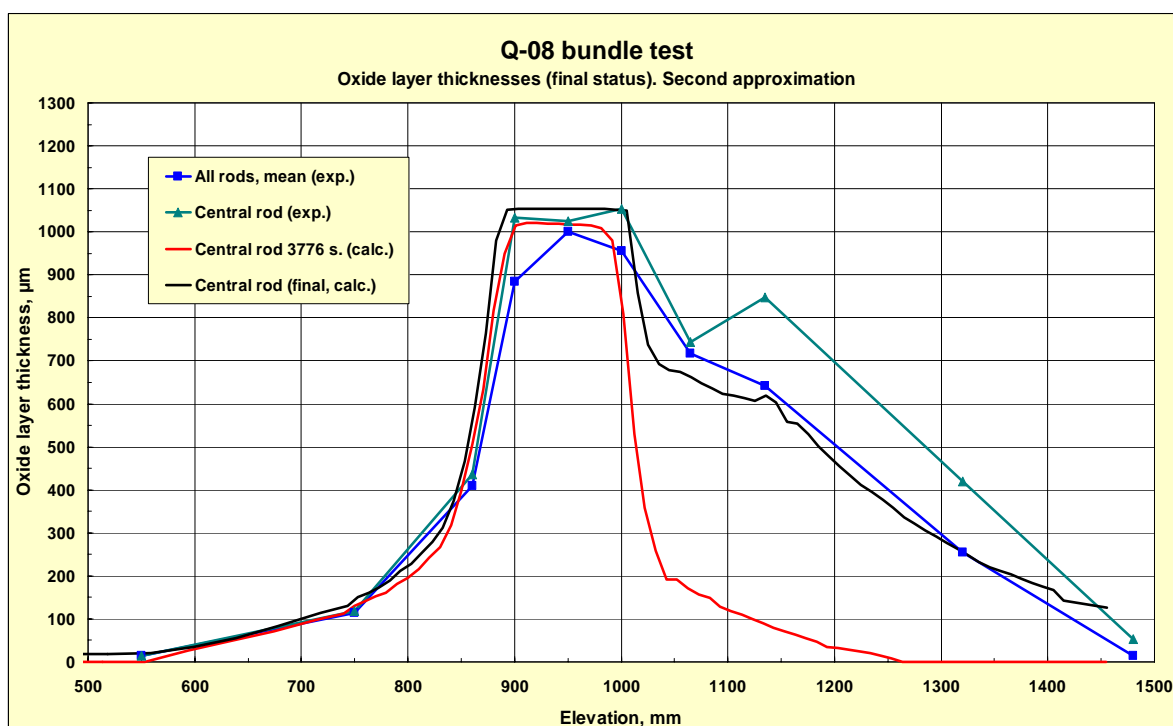


Fig. 125: QUENCH-08 measured oxide layer thickness profiles of the heated rods (average) and of the central rod (both at final state), compared to the calculated oxide layer thickness profiles of the central rod at 3776 s (initiation of cooldown) and of the central rod (final state).

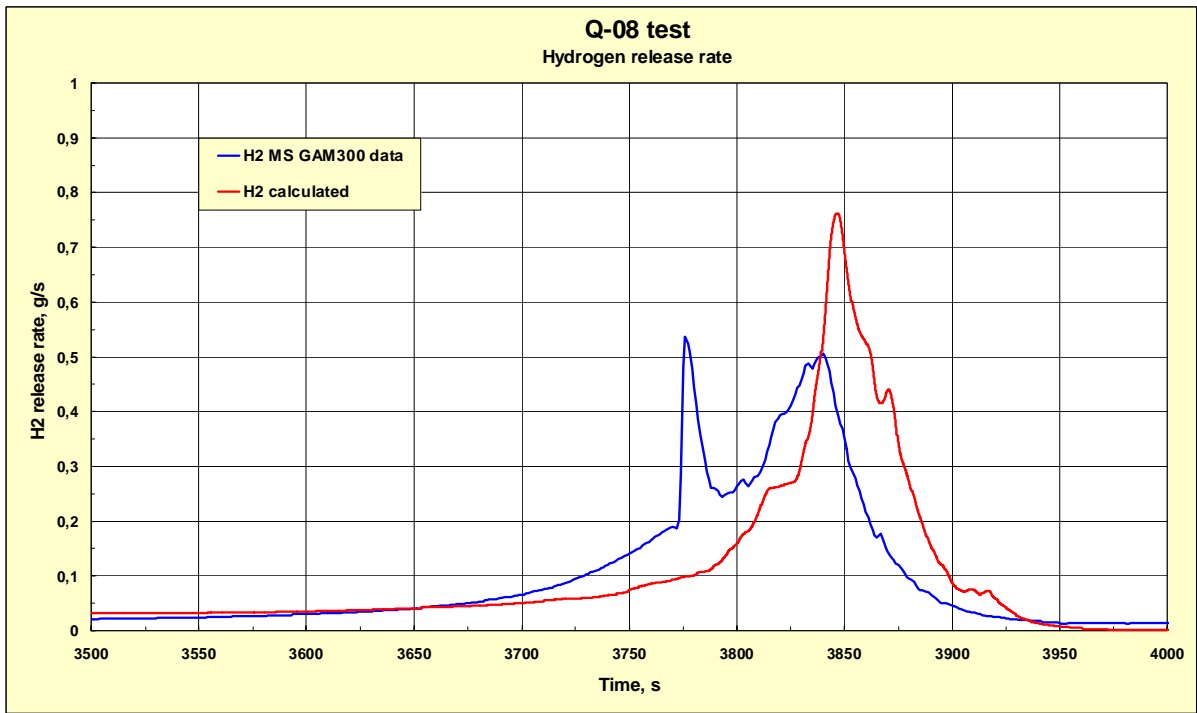


Fig. 126: QUENCH-08 hydrogen production rate calculated by the S/Q code (red) and compared to the experimental data of MS GAM300 (blue).

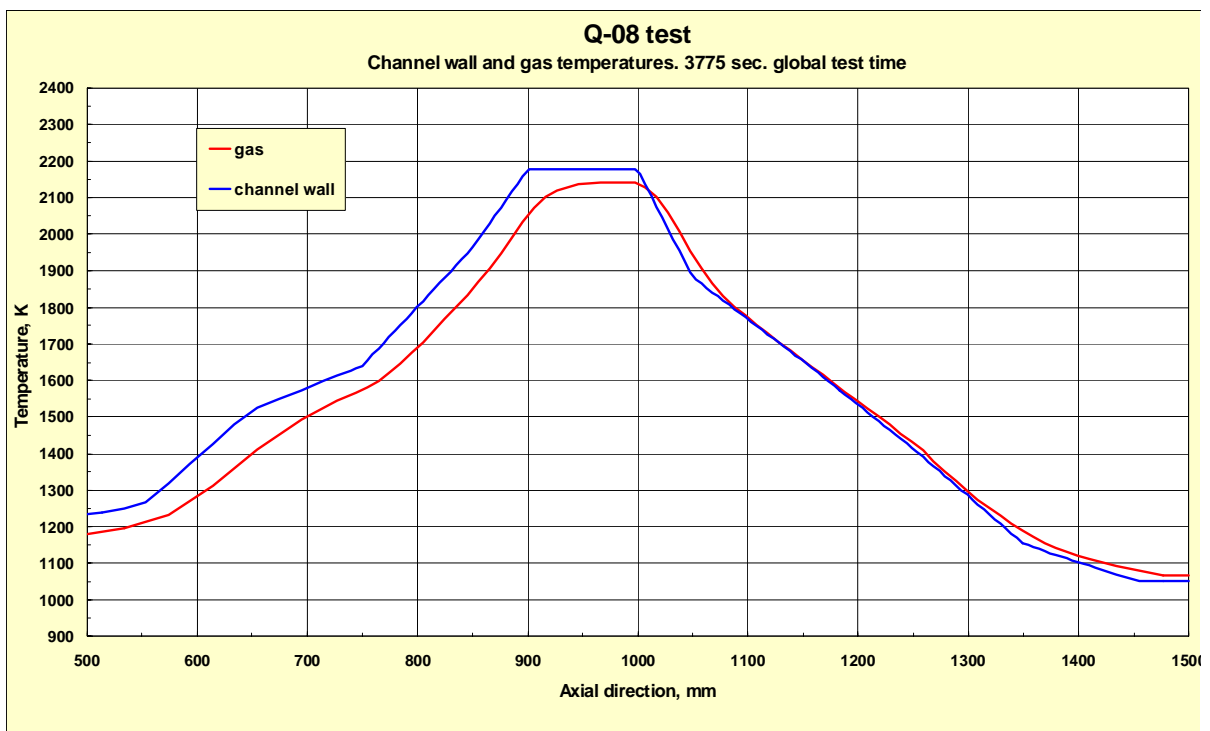


Fig. 127: Axial profiles of channel wall and gas temperature at 3775 s (1 s before QUENCH-08 cooldown initiation).

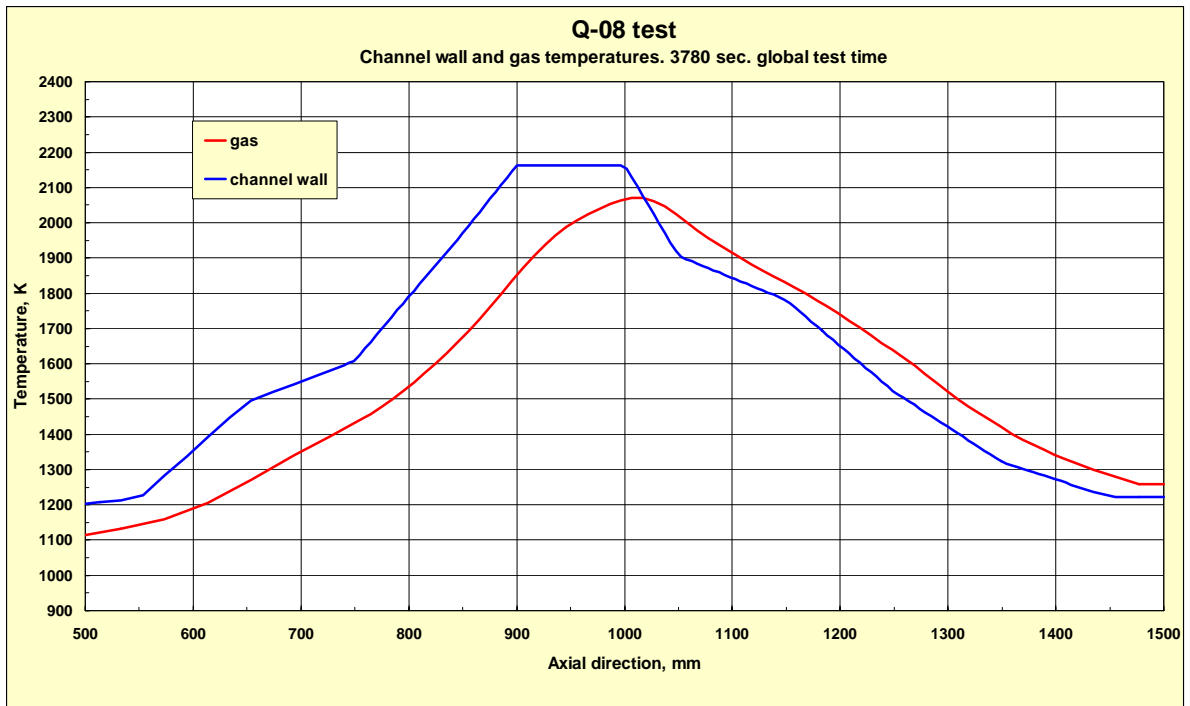


Fig. 128: Axial profiles of channel wall and gas temperature at 3780 s (4 s after QUENCH-08 cooldown initiation).

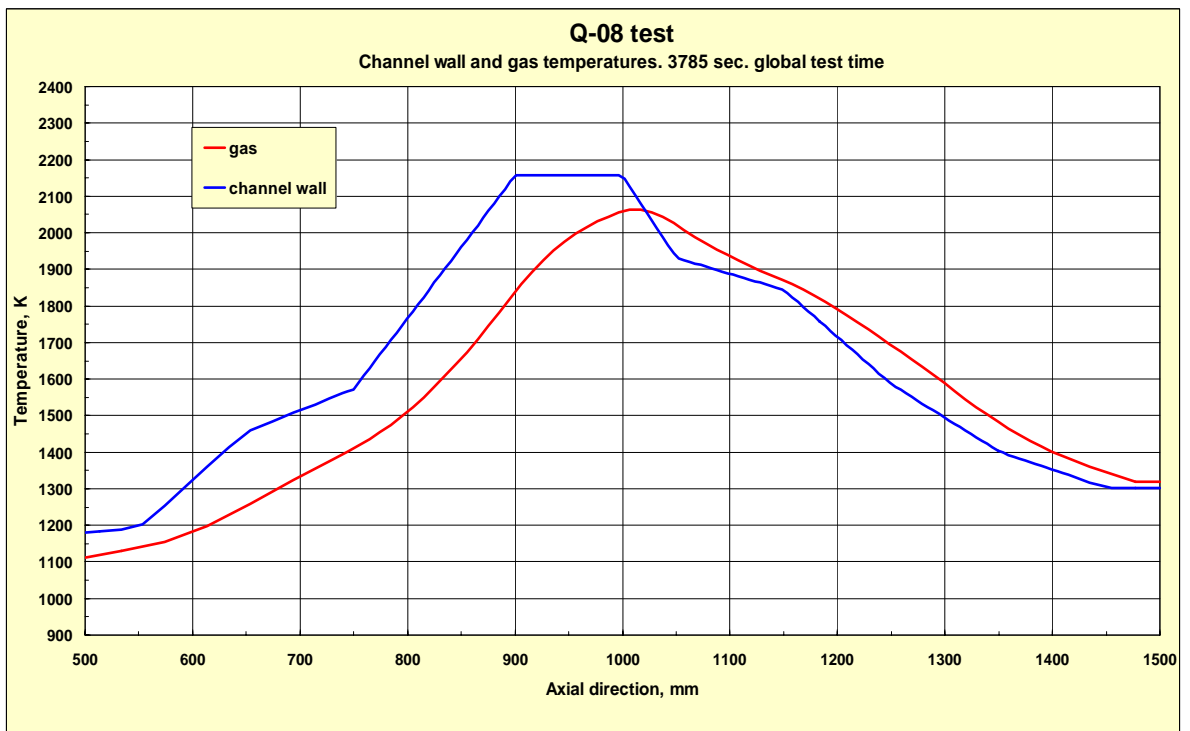


Fig. 129: Axial profiles of channel wall and gas temperature at 3785 s (9 s after QUENCH-08 cooldown initiation).

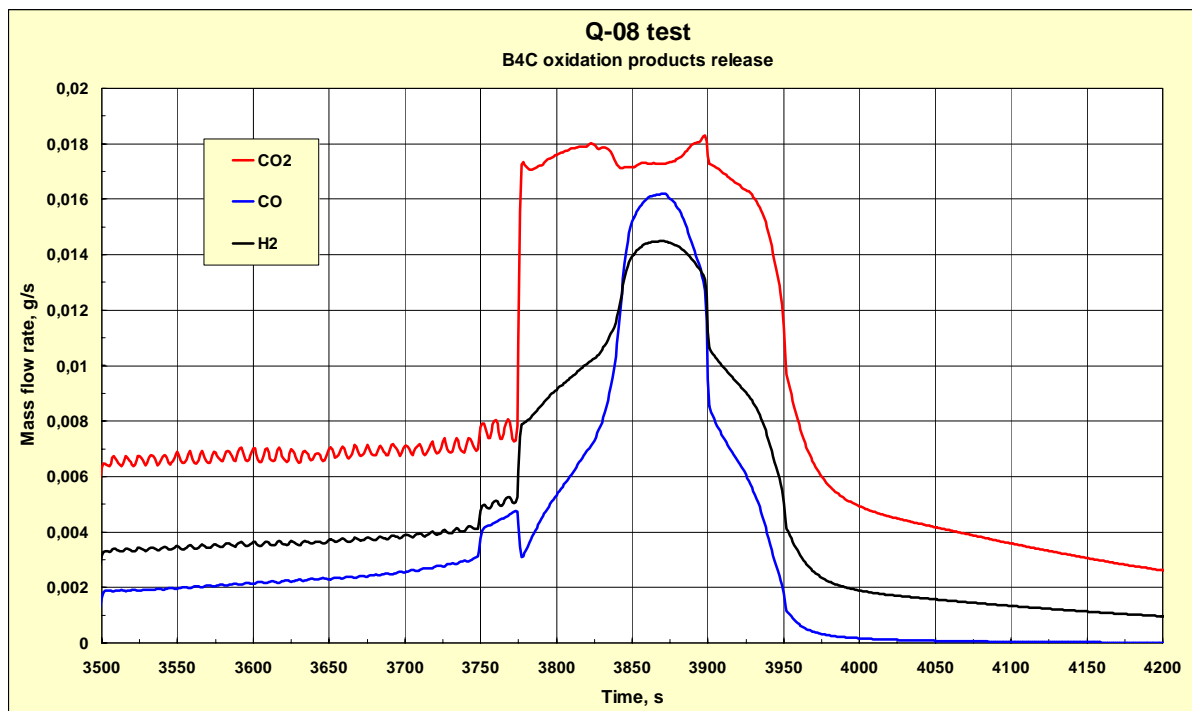


Fig. 130: Calculated CO₂, CO, and H₂ mass flow rates of virtual experiment QUENCH-08.

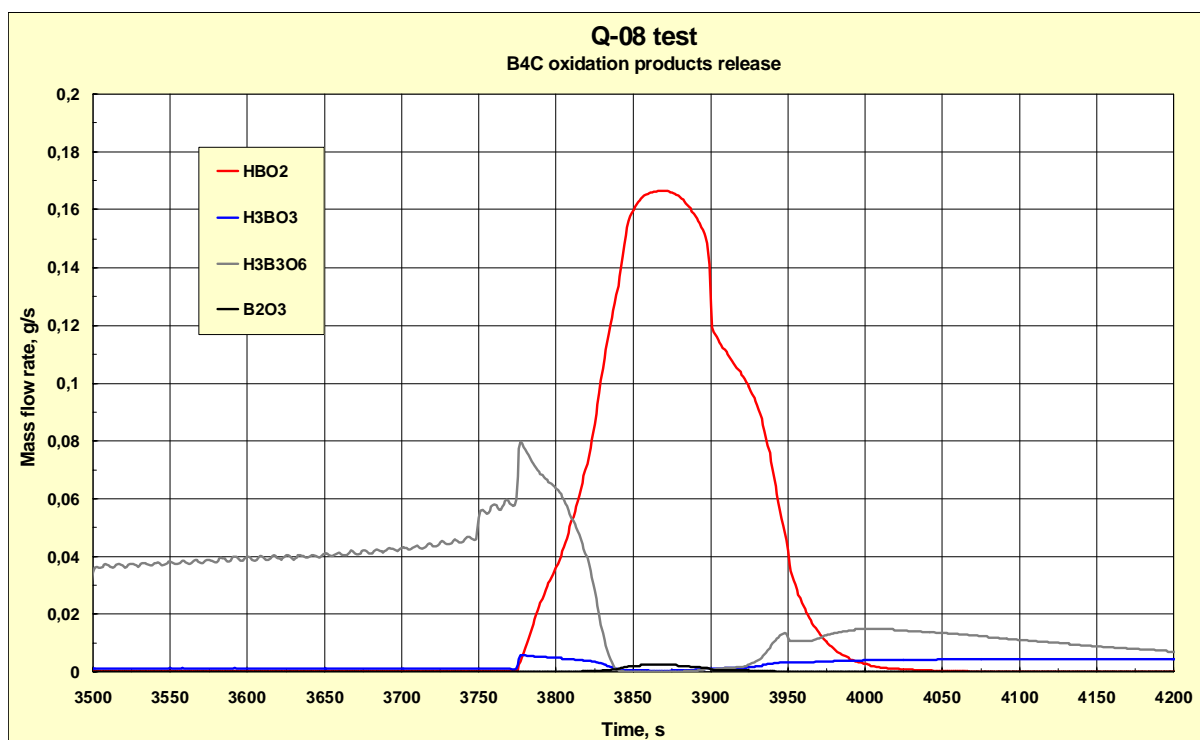


Fig. 131: Calculated B₂O₃, HBO₂, H₃BO₃ and H₃B₃O₆ mass flow rates of virtual experiment QUENCH-08.

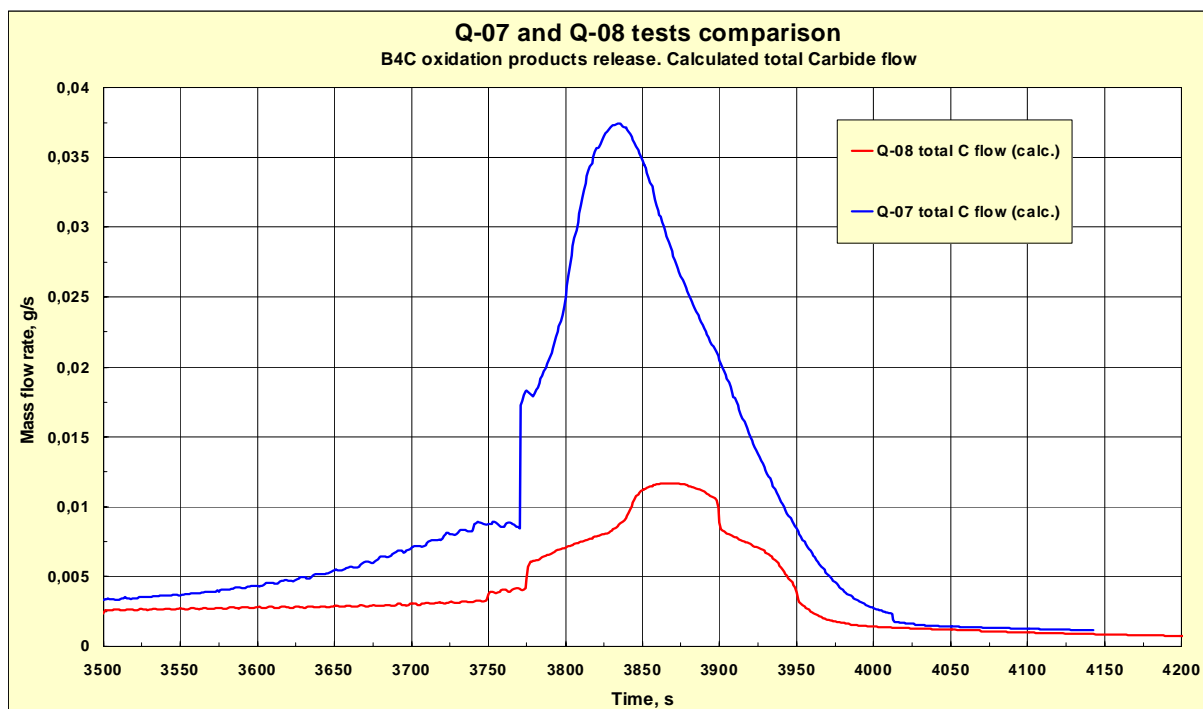


Fig. 132: Calculated C mass flow rate (CO_2 , CO , CH_4) for the QUENCH-07 and virtual QUENCH-08 tests. Time scale of the QUENCH-07 data was shifted by 212 s to match cooldown initiation (3564 s in Q-07 and 3776 s in Q-08).

Appendix

Correction of time offsets for QUENCH-07 test

The additional analysis of the QUENCH-07 data set showed that there is some temporary inconsistency between the bundle characteristic data (temperature, pressure, flow rate etc.) and the mass spectrometer data. Two events, which were typical only for this test, determined the pronounced temporary offset between the thermocouple response and hydrogen increase at the onset of quenching.

The first problem concerns the synchronization of the test controlling computer and different measurement computers. Usually, all computers of the QUENCH facility should be synchronized before the beginning of the test with help of a radio-controlled clock. This action takes place once and is not repeatable after starting to record data. Obviously this operation was not properly executed so that the system time of different facility computers worked with different times at the beginning of the test. The analysis of the stored protocol files resulted in time differences of 15 s between the system clocks of the main measurement computer and the mass spectrometer computer. So, all time values of the mass spectrometer data set should be changed by minus **15 s**. I.e., mass spectrometer plots (Figs. 25-31) presented in the report FZKA 6746 on QUENCH-07 [14] have to be shifted to the left by 15 s.

The second problem is connected to the thermal conditions inside of the quenching steam feed-in pipe, i.e. the pipe with a length of about 4 m located between the quench valve and the connection to the bundle inlet tube. Since test QUENCH-05 this pipe is equipped with an electrical auxiliary heating at the outer surface, which is usually activated during all test phases. For test QUENCH-07 it was decided to deactivate this heating aiming to keep the cooling steam at saturated conditions. But the rate of the quenching steam (15 g/s) was not enough to heat the pipe fast enough, so that the steam was more or less completely condensed on the inner pipe surface for a certain time period. This is to explain a time *delay* of **7 s** between quench initiation and steam injection into the inlet tube (T 303, F 303 given in Fig. A-1, top) and in the bundle (TFS 2/1, see also Fig. A-1, top). During this time period the feed-in pipe was heated to a temperature corresponding to the boiling point so that the fluid exists the feed-in pipe at two phase conditions during the whole quenching phase. The two-phase conditions are likely to cause oscillations seen in the steam rate measurements of the mass spectrometer (Fig. A-2, top). In report FZKA 6746 (QUENCH-07) the dashed lines in Fig. 17, Figs. 19-21, Figs. 24-32 are to be shifted by 7 s to right and the legend "cooldown initiation" should be thereby be substituted by "start of bundle flooding". In addition, the time cooldown initiation (3557 s) should be complemented with the time of start of bundle flooding at 3564 s (FZKA 6746: Table 5, Figs. 16 and 17).

As a result of the time corrections described above the integral value of hydrogen generated should be corrected for the QUENCH-07 experiment: The best-estimate value of the total H₂ mass should be changed from 182 g [16] to 186 g, and the corrected H₂ mass generated up to cooldown is 66 g instead of 62 g.

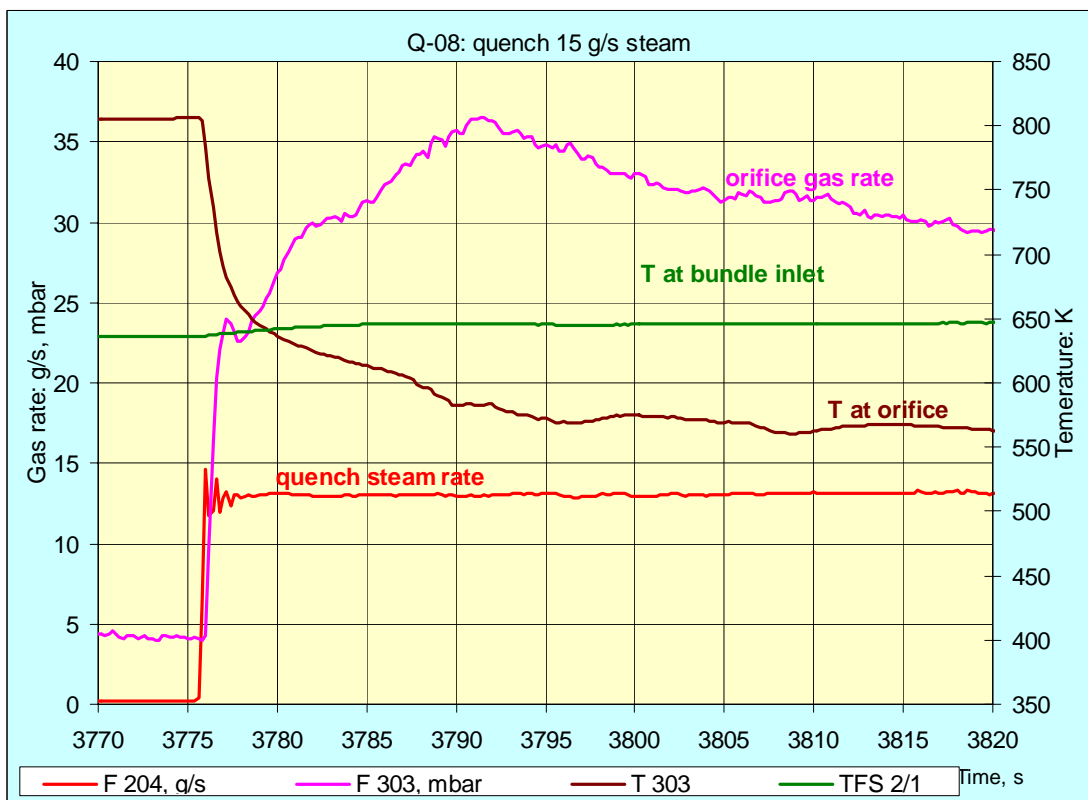


Fig. A-1. Comparison of the quench initiation for QUENCH-07, top, and QUENCH-08, bottom.

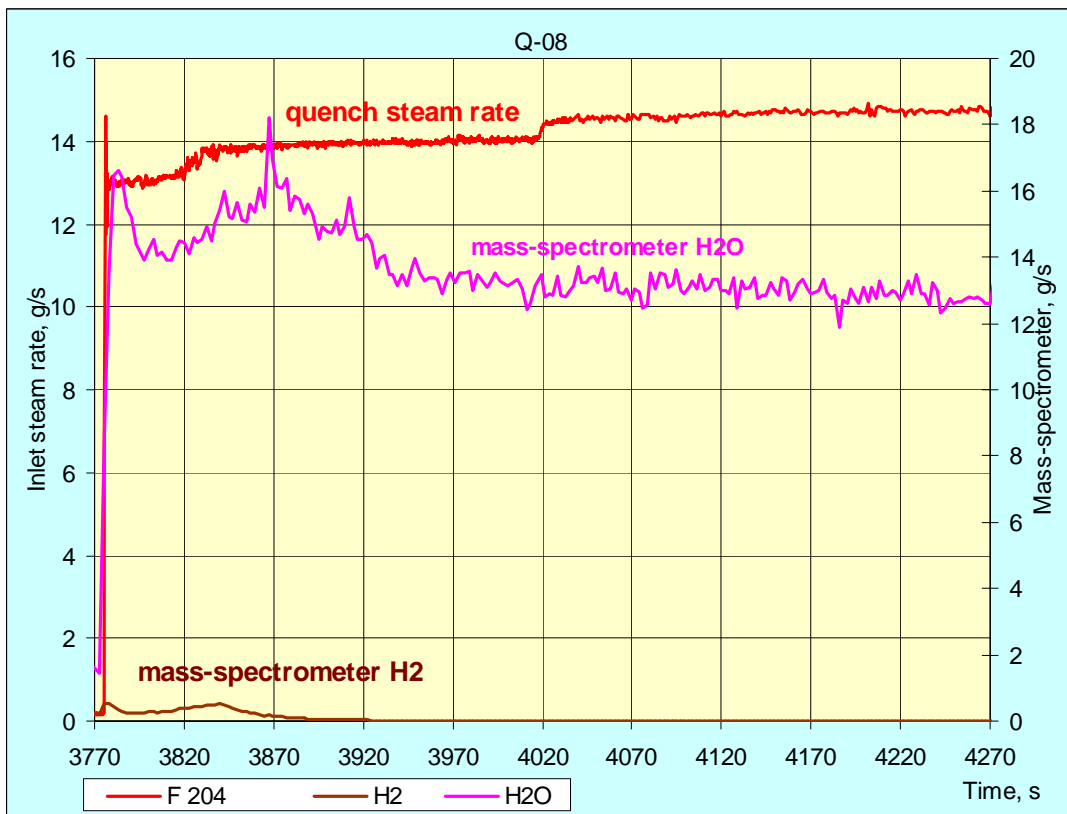
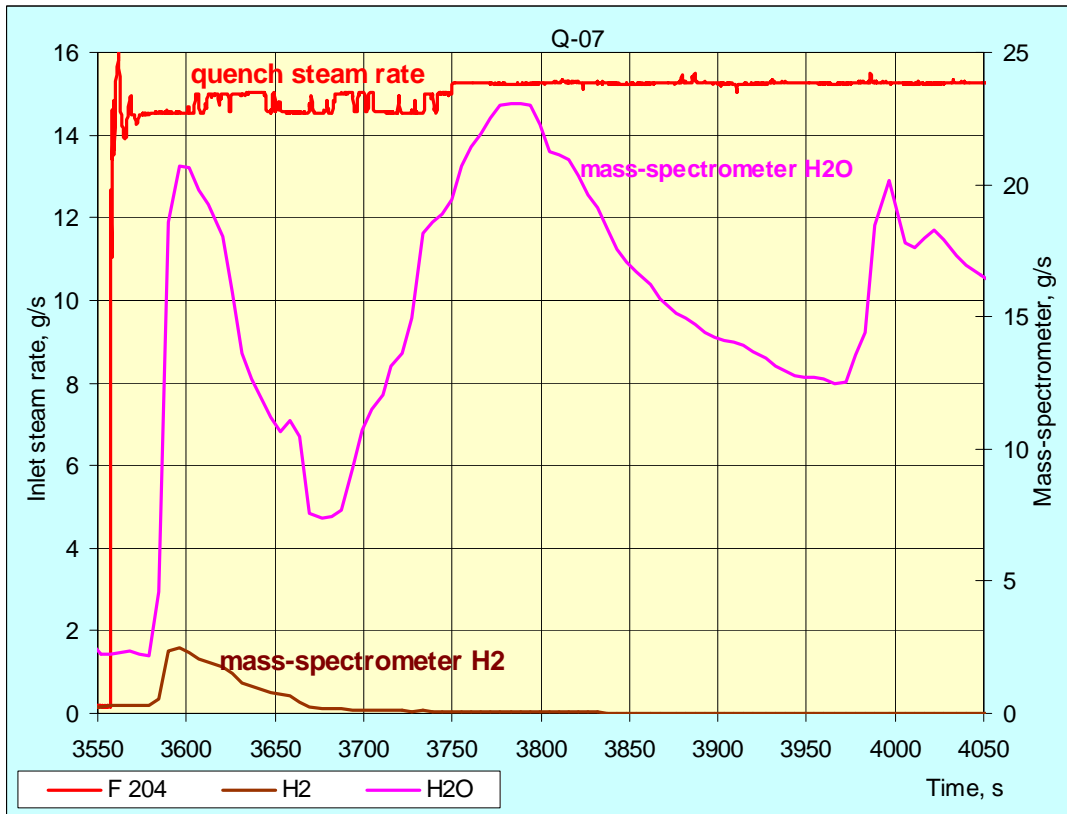


Fig. A-2. Comparison of the steam and hydrogen outlets during the quenching for QUENCH-07, top, and QUENCH-08, bottom.